Synthesis, Structural, Spectroscopic and Electrochemical characterization of Nanoscale Pristine & Doped $LiFePO_4$

A thesis submitted in partial fulfillment for the degree of

Doctor of Philosophy

By

Y. SUNDARAYYA

School of Physics
University of Hyderabad
Hyderabad – 500 046, INDIA
September 2008

DECLARATION

I hereby declare that the matter embodied in this thesis, entitled "**Synthesis, Structural, Spectroscopic and Electrochemical characterization of Nanoscale Pristine & Doped $LiFePO_4$**" is the result of investigation carried out by me in School of Physics, University of Hyderabad, Hyderabad – 500 046, under the supervision of Prof. C. S. Sunandana.

Place: Hyderabad

Date: (Y. SUNDARAYYA)

CERTIFICATE

This is to certify that the research work contained in this doctoral thesis entitled "**Synthesis, Structural, Spectroscopic and Electrochemical characterization of Nanoscale Pristine & Doped $LiFePO_4$**", has been carried out by Mr. Y. SUNDARAYYA under my direct supervision and the same has not been submitted for the award of Ph. D. degree of any University.

Place: Hyderabad,

Date: Supervisor

(Prof. C. S. SUNANDANA)

DEAN

School of Physics

We departed yesterday to meet tomorrow
That tomorrow never comes
He proved his Bolsheviek discipline

My dear

Comrade ***Prasad*** *ku…*

Acknowledgements

It is with great pride and high regard, I express my profound gratitude to my supervisor, **Prof. C S Sunandana**, a person of who could manage to retain the sense of wonder in life. When the world is heading to search the small 'GOD' particle with big machines, he explores for big wonders through nano world. His way of looking and discovering at the fascinating world with the eyes of a child, breaks the barriers of thought that we habituated, as we grew. I sincerely thank him for his encouraging cooperation and infinite patience.

I owe my thanks to **Dr. M Ghanashyam Krishna**, my Doctoral committee member for his enlightening comments and suggestions on my work.

I would like to thank the **Prof. Vipin Srivastava**, Dean, School of Physics, **Prof. V S S Sastry**, former dean for providing all the necessary facilities.

I thank **Prof. K C Kumaraswamy** for the fruitful discussions and timely help, a person who keeps me to stand by my word.

I wish to thank **Prof. C Bansal**, for introducing me the science of Mössbauer spectroscopy and allowing me to use the facility. I wish to thank **Dr. P S R Prasad**, NGRI, Hyderabad for allowing me to use the HTIR facility.

Prof. S N Kaul, from whom I learnt the art and science of research. I sincerely thank him for being with me all the times.

The one and only one person with out whom the thesis would not have been in the present form is **Dr. Ajay K Mishra**. I owe special thanks for giving me a helping hand towards submission.

I remember still the days when I was introduced to the world of battery research, a promising but necessary area for mankind through **Dr. T Mohan** and **Dr. Janakiraman**, HBL-NIFE Power Systems (Pvt.) Ltd., Hyderabad. I am grateful for their encouragement.

I wish to thank **Dr. P Balaya** and **Dr. Y Srinivasa Rao** for their timely help being in busy schedules. I thank **Dr. S Srinath** for his timely help and discussions.

I wish to thank my lab mate M. Gnanavel for his help and kind concern towards my work. I wish to thank Dr. Bharathi Mohan and Dr. K V R for their cooperation.

I am thankful to the Mr. C S Murthy, Principal Scientific Officer and staff members of CIL for their cooperation and help. In particular, I am thankful to Dr. Manjunath, Suresh and Mr. Nageswararao for their assistance. I express my sincere thanks to Mr. Vincent and Mr. Prasadarao, Glass blower for their timely help. I wish to thank Abraham, Gaddam Srinivas, Poornachandrarao, Saramma and Chandrapal for their help.

I thank Vikram (Chemistry) and who helped me in not allowing the painful situations during my research project.

I sincerely thank my friends on the campus, particularly Baavagaru, Baachi, Gopal, Kishore, Srikanth, Arun, Pradeep, and John, for bearing and spending with me the campus evenings.

I thank all the research scholars in the school, Sudhee, Ajith, Chaitanya, Trivikram, Tejal and Pamu for their timely help and concern.

I thank all my family members for having faith and waiting to discharge my responsibilities. I sincerely thank my parents for being so patient and also not disturbing me through out my doctoral program. The help from Chinna and Rajani is unforgettable. Sudha's comapanion could make me to work in a fruitful manner. Special thanks to all these three people.

Any work, for instance a research project cannot be done without a strong support of financial resources. I acknowledge and thank CSIR, UGC and HBL-NIFE for financial assistance.

--- O ---

Table of Contents

--- O ---

Abstract

The present thesis work was undertaken to study in detail, the novel material $LiFePO_4$, a potential cathode material for Li-ion batteries. Carbon coated Fe^{3+} phase free nanocrystalline $LiFePO_4$ has been synthesized from a non-aqueous sol-gel synthesis route. The material has been studied extensively by XRD for crystal structure, SEM for microstructure, EDAX for elemental analysis, FTIR for the internal modes phosphate ion and Mössbauer spectroscopy for the environment at Fe site.

Two-phase systems namely $(x)LiFePO_4$**:**$(1-x)Fe^{2+}PO_4$ and $Na_xLi_{1-x}FePO_4$ have been synthesized and studied to understand the environment at the Fe-site and variation of infrared modes due to the absence of lithium and also substitution of sodium for lithium. The chemical stability of the interlock of the FeO_6 octahedra and PO_4 tetrahedra has been probed by substituting the phosphate ion of $LiFePO_4$ with the vanadate ion.

An exhaustive investigation of Fourier transform of Infrared (FTIR) spectra to ascertain the dependence of different stretching and bending modes of the phosphate ion with temperature. Low temperature Mössbauer measurements were carried out from room temperature to 20K with a very close scan around 50K to understand this magnetic transition in detail and also different relaxation phenomena involved in this transition. This is supported by the susceptibility measurements from SQUID. Finally Electrochemical experiments performed with $LiFePO_4$ material synthesized in our laboratory for its electrochemical behavior.

--- O ---

Chapter 1
Introduction

1.1 Introduction

In carrying out the piece of research described in this PhD Thesis, we are motivated by the current energy scenario especially by the urgent need to develop nanomaterials for use as components for Li-ion micro-power sources and allied devices. The fact that energy consumption/production that relies on the combustion of fossil fuels is forecast to have a severe future impact on world economics and ecology. Electrochemical energy production is under serious consideration as an alternative energy/power source, as long as this energy consumption is designed to be more sustainable and more environmentally friendly **[1]**. The exponential growth in portable electronic devices such as cellular phones and laptop computers during the past decade has created enormous interest in compact, light-weight batteries offering high energy densities. Also, growing environmental concerns around the globe are driving the development of advanced batteries for electric vehicles.

Systems for electrochemical energy storage and conversion include batteries, fuel cells, and electrochemical capacitors (ECs). In batteries and fuel cells, electrical energy is generated by conversion of chemical energy via redox reactions at the anode and cathode. As reactions at the anode usually take place at lower electrode potentials than at the cathode, the terms negative and positive electrode (indicated as minus and plus poles) are used. The more negative electrode is designated the anode, whereas the cathode is the more positive one.

1.2 Storage Battery the Prime Mover

A *battery* is one or more electrically connected electrochemical cells with contact terminals/to supply electrical energy. A *primary battery* is a cell, or group of cells, for the generation of electrical energy intended to be used until exhausted and then discarded. Primary batteries are assembled in the charged state; discharge is the primary process during operation. A *secondary battery* is a cell or group of cells for the generation of electrical energy in which the cell, after being discharged, may be restored to its original charged condition by an electric current flowing in the direction opposite to the flow of current when the cell was discharged. A familiar example is the charging of the exhausted battery of the mobile phone. The *anode* is the negative electrode of a cell associated with oxidative chemical reactions that release electrons into the external circuit. The *cathode* is the positive electrode of a cell associated with reductive chemical reactions that gain electrons from the external circuit. An *electrolyte* is a material with good ionic conductivity that provides for a facile passage of ions between the positive and negative electrodes of a cell. A *separator* is a physical barrier between the positive and negative electrodes incorporated into most cell designs to prevent electrical shorting.

Separators must be permeable to the ions while being inert in the battery environment. The electrodes interchange ions in a cell through an electronically insulating electrolyte (liquid/ solid) that has high ionic conductivity to minimize internal battery resistance. The amount of electrical charge stored by an electrode is referred as the *electrical capacity*, typically expressed in units of amp-hours per kilogram (Ah/kg) or amp-hours per liter (Ah/l). Electrical capacity is multiplied by the electrochemical potential of the battery to obtain its *total available energy* on a weight or volume basis, typically expressed in units of Watt-hour per kilogram (Wh/kg) or Watt-hour per liter (Wh/l) respectively.

1.3 Basic concepts of rechargeable lithium batteries

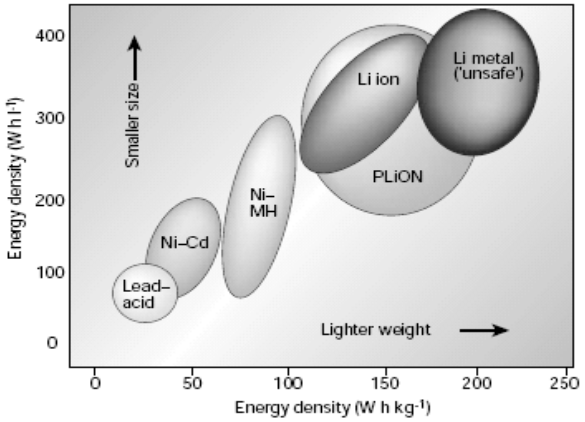

Figure 1. Comparison of different battery technologies in terms of volumetric and gravimetric density. (Coutesy: Tarascon et al)

Lithium-ion batteries are particularly appealing for micro/milliwatt power level applications as they provide higher energy density compared to the other rechargeable battery systems such as lead-acid, nickel-cadmium, and nickel-metal hydride batteries as shown in figure 1. The higher volumetric and gravimetric energy densities of the lithium ion cells shown in the figure are due to the high cell voltages (~4 V) achievable by the use of non-aqueous electrolytes, which also allow a wider temperature of operation. Lithium-ion cells became a commercial reality after the initial announcement by Sony in the early 1990s because of an intense world-wide activity on lithium insertion compounds for electrode materials during the past three decades.

The motivation for using a battery technology based on Li metal as anode relied initially on the fact that Li is the most electropositive metal (~3.04 V versus standard hydrogen electrode) as well

as the lightest (equivalent weight M = 6.94 gm/mole, and specific gravity ρ = 0.53 gm/cm^3) metal, thus facilitating the design of storage systems with high energy density **[2]**.

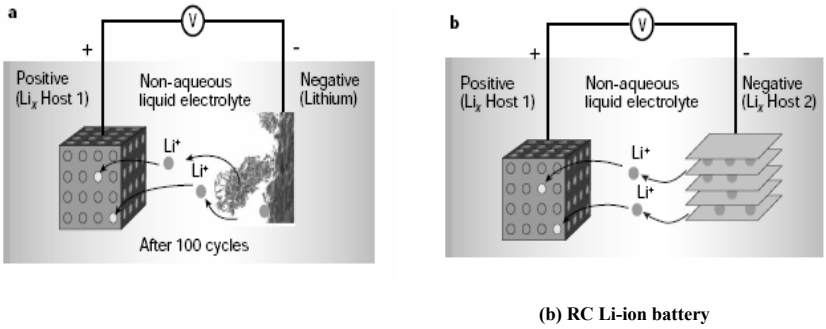

Figure 2. Schematic representation and operating principles of Li batteries. (a) Rechargeable Li-metal battery and (b) Rechargeable Li-ion battery. (Courtesy: Tarascon et al)

Because of the presence of Li in its ionic rather than metallic state, Li-ion cells solve the dendrite problem (figure 2) **[2]** and are, in principle, inherently safer than Li-metal cells. To compensate for the increase in potential of the negative electrode, high-potential insertion compounds are needed for the positive electrode, and emphasis shifted from the layered-type transition-metal disulphides to layered or three-dimensional-type transition-metal oxides **[3]**.

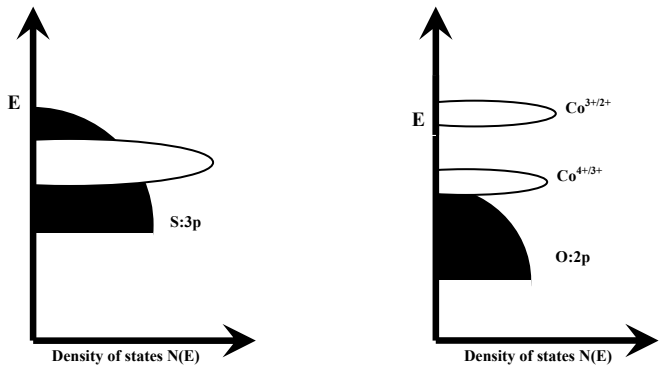

Figure 3. Relative energies of metal:d and nonmetal:p levels in (a) a sulphide and (b) an oxide.

This concept of rechargeable lithium batteries was first illustrated with a transition metal sulphide, TiS_2, as the cathode, metallic lithium as the anode, and a non-aqueous electrolyte **[4]**. During discharge, the lithium ions are inserted into the van der Waals gap between the sulphide layers and the charge balance is maintained by a reduction of the Ti^{4+} ions to Ti^{3+}. During charging, exactly the reverse process involving the extraction of lithium from the van der Waals gap and an oxidation of

Ti^{3+} to Ti^{4+} occurs. During the lithium insertion/ extraction process, the layer structure is maintained, resulting in good reversibility.

Following this layered TiS_2, several other sulphides and chalcogenides were pursued during the 1970s and 1980s as cathodes. However, most of them exhibit a lower cell voltage (of < 2.5 V versus metallic lithium anode). This limitation in the cell voltage is due to an overlap of the higher valcency M^{n+}: d band with the top of the nonmetal p band –for example, with the top of the S(3p) band. Such an overlap results in an introduction of holes into (or removal of electrons from) the S^{2}:3p band and the formation of molecular ions such as S_2^{2-} which in turn leads to an inaccessibility of higher oxidation state for M^{n+} in a sulphide $Li_xM_yS_z$. The stabilization of higher oxidation state is essential to maximize the cell voltage. Recognizing this difficulty with chalcogenides, Goodenough's group focused on oxide cathodes during 1980s **[3, 5, 6]**. The location of the top of the O^{2-}:2p band much below the top of the S^{2-}:3p band and a larger raising of the M^{n+}:d energies in an oxide compared to that in a sulphide due to a large Madelung energy make the higher valent states accessible in oxides. For example, while Co^{3+} can be readily stabilized in an oxide, it is difficult to stabilize Co^{3+} in a sulphide since the $Co^{2+/3+}$ redox couple lies within the S^{2-}:3p band as seen in figure 3. Accordingly, several transition metal oxide hosts crystallizing in a variety of structures (2-D layered and 3-D framework structures) have been pursued during the past two decades.

1.4 Criteria for a successful cathode material

Although the concept is simple, the lithium insertion compound (LIC) $Li_xM_yX_z$ (X = anion) should satisfy several stringent criteria in order for it to be a successful cathode material in a rechargeable lithium cell:

1. A high lithium chemical potential ($\mu_{Li(C)}$) to maximize the cell voltage. This implies that the transition metal ion M^{n+} in $Li_xM_yX_z$ should have a high oxidation state.
2. It (LIC) should allow an insertion/extraction of a large amount of lithium, x, to maximize the cell capacity. This depends on the number of available lithium sites and the accessibility of multiple valances for M in the insertion host. A combination of high capacity and cell voltage can maximize the energy density, which is given by a product of the capacity and voltage.
3. The lithium insertion/extraction process should be reversible with no or minimal changes in the host structure over the entire range x of lithium insertion/extraction in order to provide a good cycle life for the cell. This implies that the insertion compound $Li_xM_yX_z$ should have good structural stability without breaking any M–X bonds.
4. It (LIC) should support mixed conduction. It should have good electronic conductivity σ_e and lithium-ion conductivity σ_{Li} to minimize polarization losses during the discharge/charge

process and thereby to support a high current density and power density. This depends on the crystal structure, the arrangement of the MX_n polyhedra, the geometry and interconnection of the lithium sites, nature and electronic configuration of the M^{n+} ion, and, the relative positions of the M^{n+} and X^{m-} energies.

5. It (LIC) should be chemically stable without undergoing any reaction with the electrolyte over the entire range, x, of lithium insertion/extraction.
6. The redox energy of the cathode in the entire range, x, of lithium insertion/extraction should lie within the bandgap of the electrolyte to prevent any unwanted oxidation or reduction of the electrolyte.
7. From a commercial point of view, the insertion compound should be inexpensive, environmentally benign, and light weight. This implies that the M^{n+} ion should preferably be from the 3d transition series.

1.5 Advantages

Lithium-ion batteries can be formed into a wide variety of shapes and sizes so as to efficiently fill available space in the devices they power. They are lighter than other equivalent secondary batteries-often much lighter. The energy is stored in these batteries through the movement of lithium ions. However, the bulk of the electrodes are effectively "housing" for the ions and add weight, and in addition "dead weight" from the electrolyte, current collectors, casing, electronics and conductivity additives reduce the charge per unit mass to little more than that of other rechargeable batteries. A key advantage of using Li-ion chemistry is the high open circuit voltage that can be obtained in comparison to aqueous batteries (such as lead acid, nickel metal hydride and nickel cadmium).

Li-ion batteries do not suffer from the memory effect. They also have a low self-discharge rate of approximately 5% per month, compared with over 30% per month in common nickel metal hydride batteries (Low self-discharge Ni-MH batteries have much lower values, around 1.25% per month) and 10% per month in nickel cadmium batteries.

According to one manufacturer, Li-ion cells (and, accordingly, "dumb" Li-ion batteries) do not have any self-discharge in the usual meaning of this word **[7]**. What looks like a self-discharge in these batteries is a permanent loss of capacity, described in more detail below. On the other hand, "smart" Li-ion batteries do self-discharge, due to the small constant drain of the built-in voltage monitoring circuit. This drain is the most important source of self-discharge in these batteries.

1.6 Disadvantages

In spite of interesting and advantageous effects observed in the nano-crystalline state, there are also drawbacks. One of the major difficulties stems from the fact nano-crystallinity inherently introduces a perceptible excess energy and, thus, stability problems into the system.

In order for Li-batteries to exhibit a stationary performance, the nanocrystalline materials have to rely on kinetic (rather than on thermodynamic) stability. For an elementary material (such as Li) this is an impossible task due to the high Li-mobility **[8]**.

Another important drawback of the Li-ion battery is that its life span is dependent upon aging from time of manufacturing (shelf life) regardless of whether it was charged, and not just on the number of charge/discharge cycles. This drawback is not widely published **[9].** However, the time to get a fully charged battery is also reduced in proportion to the capacity. This is due to the increase in internal resistance of the battery, which causes the voltage at the terminals to drop under load, reducing the maximum current that can be drawn from them.

Li-ion cells must never be discharged below a certain voltage to avoid the possibility of irreversible damage. Therefore all Li-ion battery systems are equipped with a circuit that shuts down the system when the battery is discharged below the predefined threshold **[7].**

1.7 Need for Nanostructured Battery Materials

The use of nanomaterials for energy storage and conversion in electrochemical power sources is rapidly growing field with tremendous potential. Even though the use of nanomaterials in power sources is not new, the science at the Nanoscale has still not been fully exploited **[10]**.

Certain phenomena are only possible on the Nanoscale due to the dominance of interfacial physics and chemistry at large surface-to-volume ratios, such as the quantum interactions between Nanoscale material phases. By learning to control the physics and chemistry at these small length scales, one can envision nanoarchitectured materials engineered to exhibit properties and performance that far exceed the “sum of the parts”.

It is well known that electronic transport properties can be tuned by interfacial design and by varying the spacing of interfaces down to the nano-regime. For that reason, nano-electronics has become a well-established field in physics and materials science. Ionic transport properties are of similar significance (chemical kinetics of solids, electrochemical devices), for the physical chemistry of solids and for materials science, and essentially over the last two decades many experiments and

theoretical considerations have shown the impact of interfaces and of the spacing of interfaces on ionic transport properties **[11]**.

Nanostructured materials offer the possibility to make use of small transport lengths and small separation distances like in fluids, but unlike fluids, the higher structural stability of the solid state can be exploited. At smaller sizes, edge and corner effects become increasingly important. They do not significantly change the overall energy unless we go below –typically- a few nanometers. At such small sizes structural changes influence properties and performance. At such extremely small sizes, it is better to use a bottom-up approach than a top-down approach.

The state-of-art storage mechanism in modern Li-batteries ("Li-ion batteries") occurs via insertion into the host electrode structure. A high capacity can be achieved by storage that makes use of heterogeneous solid state reactions **[12, 13]**. Both mechanisms are distinctly affected by grain size as far as kinetics and surface thermodynamics are concerned. The specific storage capacity is not expected to be greatly altered. Besides this absorptive mechanism (insertion reaction) and this reactive mechanism (heterogeneous) there is a third one, adsorptive mechanism (reversible interfacial reaction), the capacity of which depends on the grain size in the first place and indeed relies on the presence of nano-particles. Different possibilities of interfacial reactions have been mentioned in the literature; one is under-potential deposition **[14]** where typically a monolayer of Li is bonded on a metal associated with a partial charge transfer. A second possible mechanism is the lithium storage by reaction with the grain boundary phase **[15]** in poly crystalline materials or by reaction with the liquid electrolyte at the solid/liquid interface **[12, 13]**. The third mechanism **is** the charge separation at phase boundaries.

Charge storage via heterogeneous reaction**(s)**, in principle, includes all storage modes discussed. In the first stage Li is homogeneously inserted into the bulk and the charge/discharge curve exhibits the well-known characteristics of an insertion electrode (usually slightly sloped with additional possible anomalies due to structural transitions). After having reached the solubility limit (which also depends on the particle size), new phases and hence new interfaces are formed. The corresponding charge/discharge curve profile is expected to be nearly flat (non-vanishing slope due to nanocrystallinity effects). Even if these phases no longer dissolve Li, further storage is possible via interfacial of metallic lithium. As pointed out above, electron injection occurs at the surface of the non-alloying metal M while ion injection is probable at the Li_2O/M surface. In all these cases of interfacial storage resembles the characteristic of a capacitor. Such interfacial charging has been suggested to be very reversible unlike Li storage in the passivating layer that might also occur **[13]**.

Generally, there is a reduction or oxidation ('redox') reaction in the lithium insertion/extraction (discharge/charge) process, where Li ion and electron transport take an important route, especially in high-rate charging and discharging. Nanostructured materials can provide short path lengths for both Li ion and electron transport. In contrast, commercial batteries are mostly based on micro-meter sized electrode materials, i.e. powders containing particles in the micrometer range and having a low surface area (<10 m^2/gm) **[16]**. From the point of view of Li-ion diffusion, these micrometer-sized electrode materials are not beneficial for high-rate charge/discharge because of the long path length for Li ion transport and low contact area between the electrode and electrolyte.

Indeed, the size (and its distribution), morphology and density of particles play a fundamental role on their performance as electrodes **[17]**. Compounds based on nanoparticles constitute a relatively new class of cathodes with, at least, one excellent characteristic, i.e., elevated cyclability. This comes from much shorter diffusion paths for Li ions diffusion and the occurrence of smaller dimensional changes upon cycling.

1.8 Oxide cathodes

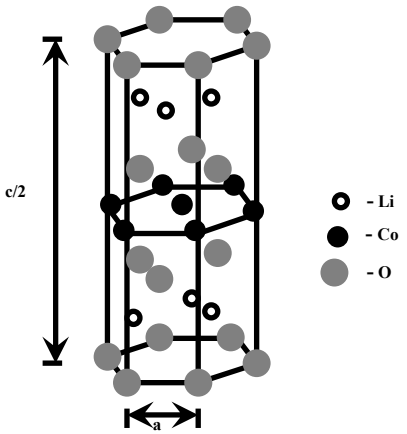

Figure 4. Crystal structure of $LiCoO_2$ having the O3 layered structure.

Several oxides with a general formula $LiMO_2$ (M = V, Cr, Co, and Ni) crystallize in a layered structure in which the Li^+ and M^{3+} ions occupy the alternate (1 1 1) planes of the rock salt structure to give a layer sequence of O-Li-O-M-O- along the c axis as shown in figure 4 for $LiCoO_2$. The structure has an oxygen stacking sequence along the c-axis and the Li^+ and M^{3+} ions occupy the octahedral interstitial sites of the cubic close-packed oxygen array. This structure is designated as the O3 layer structure since the Li^+ ions occupy the octahedral sites and hence there are three MO_2 sheets per unit cell. The structure with a strongly (covalently) bonded MO_2 layers allows a reversible extraction/

insertion of lithium ions from/ into the lithium planes. The interconnected Li-ion sites through the edge-shared LiO_6 octahedral arrangement between MO_2 layers provide the fast 2-D Li-ion diffusion leading to high ionic conductivity σ_{Li}. On the other hand, the edge-shared MO_6 octahedral arrangement with a direct M-M interaction can provide good electronic conductivity σ_e depending on the electronic configuration of the M^{3+} ion. As a result, the $LiMO_2$ oxides crystallizing in the O3 structure have become attractive candidate cathodes.

1.9 Layered $LiCoO_2$

Goodenough recognized that $LiCoO_2$ has a structure similar to the layered structures of the dichalcogenides and showed that the lithium could be removed electrochemically, thus making it a viable cathode material **[18]**. $LiCoO_2$ has the α-$NaFeO_2$ structure with the oxygens in a cubic close-packed (ccp) arrangement. On complete removal of the lithium, the oxygen layers rearrange themselves to give hexagonal close packing of the oxygens in CoO_2 **[19]**. Between these composition limits several phases are formed with varying degrees of distortion of the ccp oxygen lattice. The composition $Li_{0.5}CoO_2$ can also be formed in the spinel form **[20]**, though it appears to be metastable and is not normally formed during the cycling of the Li_xCoO_2 electrode. However, a recent TEM study **[21]** has identified the spinel phase originating on the surface of heavily cycled $LiCoO_2$ cathodes. Apart from $LiCoO_2$, several other oxides have been developed as cathode materials for Li-ion batteries. Layered $LiNiO_2$, $LiMnO_2$, $LiFeO_2$ and spinel $LiMn_2O_4$ are a few among them, which were examined looking to maximize the cell voltage and energy density.

1.10 Limitations of oxide cathodes

The majority of fundamental and technological investigations in the search for better positive electrode materials has been devoted to transition metal oxides such as $LiMO_2$ (M = Co, Ni, Mn), $LiMn_2O_4$, LiV_2O_5, or LiV_3O_8 **[22]**. The first two classes of materials built on close-packed oxygen stacking adopt 2-D and 3-D crystal structures, respectively. Lithium ions may easily be intercalated into or extracted from these structures in a reversible manner. These oxides are reasonably good ionic and electronic conductors and lithium insertion/extraction proceeds while operating on the M^{4+}/ M^{3+} redox, located at around 4V vs. Li^+/Li. Cost considerations brought some special attention to the possible use of $LiFeO_2$ that may be prepared in the same crystallographic arrangement as of $LiCoO_2$ through ion exchange from α-$NaFeO_2$ **[23]**. Electrochemical extraction of lithium would give access to the Fe^{4+}/ Fe^{3+} redox couple but no sustained stability of $Li_{1-x}FeO_2$ has been demonstrated yet.

The peculiar structure of the 2-D oxides $Li_{1-x}MO_2$ (M = Co, Ni, Fe, Mn) lead to structural instabilities when the number x of extracted lithium is high (complete charge). Irreversible motion of transition metals within the lithium layers may occur and lead to important capacity loss on cycling. In practical use, for instance, only 150 mAh/gm out of the theoretical 273 mAh/gm is used for $LiCoO_2$ in commercial Li-ion batteries **[24]**. For this reason, Goodenough **[25]** and Thackeray **[26–28]** envisioned in the early 1980s the possible use of 3-D oxides such as the spinel $LiMn_2O_4$. In such spinel structures, MnO_6 octahedra are strongly connected to each other through edge-sharing and bind a three-dimensional network of conduction paths for lithium motion. One of the major problems with the spinel $LiMn_2O_4$ is that there is a ~1 V difference for the same Mn^{4+}/ Mn^{3+} couple between the extraction of lithium from the tetrahedral 8a sites (~4 V for Li^+ vs. Li) and the insertion of lithium in the octahedral 16c sites (~3 V for Li^+ vs. Li). This limits the theoretical capacity at 4V on lithium extraction from $LiMn_2O_4$ to values similar to the practical capacities delivered by $LiCoO_2$ or $LiNiO_2$.

1.11 Polyanionic Frameworks

The concept of 3-D insertion/ extraction positive electrodes was examined in the late 1980s to new families of 3-D framework structures, by Goodenough's group **[29, 30]** and by Delmas **[31, 32]**. These framework structures are not built from close-packing of oxygen atoms but built on polyanions such as tetrahedral XO_4^{n-} groups (X = P, Mo, W, S). In 1989, Manthiram and Goodenough of the University of Texas at Austin showed that cathodes containing polyanions, e.g., sulphates produce higher voltage than oxides due to the inductive effect of the polyanion **[30]**. The influence of the chemical nature of the XO_4^{n-} groups (X = P, Mo, W, S) on the position of a given $M^{n+}/ M^{(n-1)+}$ redox couple vs. $Li^+/$ Li was addressed in their paper.

Later the NASICON (NAtrium Super Ionic CONductor) was considered as particularly attractive from structural stability and fast ion transport considerations. The originality of the idea of using this class of materials as insertion electrodes comes from the fact that previous studies had been focusing on developing NASICON compositions as solid electrolytes in Na/S type batteries. The chemical and structural characteristics responsible for the fast ion transport in the NASICON structure were clearly addressed in a fundamental contribution of Goodenough **[33]** and are summarized as follows:

1. Highly covalent 3-D framework generating a large interstitial space,
2. Elasticity of the framework for better accommodation of local compositional changes,
3. Weak framework – alkali cation interactions,
4. Electrostatic interactions between neighboring alkali cations,
5. 3-D network of interconnected conduction pathways,

6. Non reducible transition element when in contact with metallic alkali cation.

Although metal phosphates have been studied for more than 20 years since the discovery of fast ion transport in NASICON, it is only recently that they have been considered as candidate materials for cathodes **[34, 35]** or anodes **[35-37]** of lithium batteries.

1.12 $LiFePO_4$, the material under consideration

Olivines belong to a general class of 'polyanion' compounds containing compact tetrahedral 'anion' structural units $(XO_4)^{n-}$ (X = P, As, Mo or W) with strong covalent bonding, networked to produce higher-coordination sites such as oxygen octahedra that are occupied by other metal ions **[38]**. Sparked by the work from Goodenough's laboratory **[39–41]**, there is a great interest in polyanion compounds as lithium storage electrodes for rechargeable batteries **[42–49]**. $LiFePO_4$ is one among the many polyanionic framework extensively studied by Goodenough's research group, for its electrochemical behavior.

$LiFePO_4$ has a high lithium intercalation voltage (~3.5V relative to lithium metal), high theoretical capacity (170mA/gm, higher than that obtained by $LiCoO_2$ and comparable to stabilized $LiNiO_2$), ease of synthesis, and stability when used with common organic electrolyte systems **[45, 46]**. This is the first cathode material with potentially low cost and plentiful elements and also environmentally benign that could have a major impact in electrochemical energy storage **[50]**.

Insertion of lithium into $FePO_4$ was found reversible over several cycles and Li_xFePO_4 represents a cathode of good capacity. However, a nearly close-packed hexagonal oxide-ion array that is bonded strongly in three dimensions provides a relatively small free volume for Li-ion motion, so the electrode supports only relatively small current densities at room temperature. Nevertheless, increasing the current density does not lower the open-circuit voltage V_{oc}: rather it decreases, reversibly, the cell capacity. Reducing the current restores the capacity. This is due to the diffusion limited phenomenon associated with the two-phase character of the insertion process **[39]**.

1.13 Crystal structure of $LiFePO_4$

The crystal structure of $LiFePO_4$ had been determined by Santoro et al **[43]** from neutron diffraction data during late 1960s. The tryphilite $LiFePO_4$ adopts the olivine structure-type, built on oxygen hexagonal packing into which Li^+ and Fe^{2+} occupy one half of the octahedral sites and P one-eighth of the available tetrahedral sites. The peculiar distribution of Li^+ and Fe^{2+} within the octahedral sites generates LiO_6 and FeO_6 octahedra as shown in figure 5. This connectivity has a special impact on both electronic and ionic conductivity in $LiFePO_4$. FeO_6 edge shared octahedra shares corners between each other, not edges, and electronic delocalization is thus rendered difficult. The lithium

ions residing in tunnels formed by chains of edge-shared octahedra become mobile during charging and discharging cycles, thus making the lithium conductivity one-dimensional.

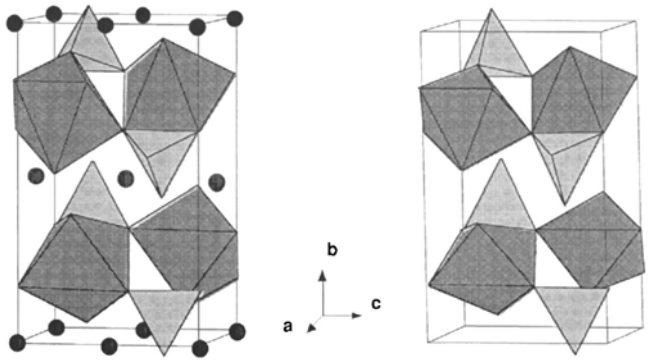

Figure 5. Crystal structures of (a) $LiFePO_4$ and (b) $FePO_4$. (Courtesy: Padhi et al)

The excellent reversibility of the cells on repeated cycling is due to the striking similarity of the $LiFePO_4$ and $FePO_4$ structures, which are compared in figure 5. $FePO_4$ is isostructural with heterosite, $Fe_{0.65}Mn_{0.35}PO_4$, for which several bond lengths have been refined. $LiFePO_4$ undergoes a contraction of *a* and *b* parameters but a small increase in the parameter *c* upon chemical extraction of lithium. Both $LiFePO_4$ and the delithiated form $FePO_4$ belong to the same space group *Pbnm* with slightly higher values of the lattice parameters of the former **[39]**. We have shown in our previous publications **[52]** that $LiFePO_4$ crystallizes into orthorhombic phase with space group *Pnma*, and the calculated cell parameters for orthorhombic $LiFePO_4$ crystallites are found to be a = 9.436 Å, b = 5.944 Å, and c = 4.650 Å.

1.14 Mechanism for Insertion/ Extraction of Lithium to/ from $LiFePO_4$

Lithium insertion proceeds from the surface of the particle moving inward behind a two-phase interface, a Li_xFePO_4/ $Li_{1-x}FePO_4$ interface in this system, as shown in figure 6. As the lithiation proceeds, the surface area of the interface shrinks. For a constant rate of lithium transport per unit area across the interface, a critical surface area is reached where the rate of total lithium transported across the interface is no longer able to sustain the current; the cell performance then becomes diffusion-limited. The higher the current, the greater is the total critical interface area and, hence, the smaller the concentration x of inserted lithium before the cell performance becomes diffusion-limited. On extraction of lithium, the parent phase at the core of the particle grows back toward the particle surface, which is why the parent phase is retained on repeated cycling and the loss in capacity is reversible on lowering the current density delivered by the cell. This loss of capacity is not due to a

breaking of the electrical contact between particles as a result of volume changes, a process that is normally irreversible **[39]**.

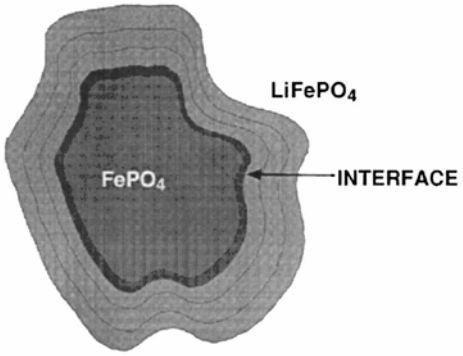

Figure 6. Schematic representation of the motion of $LiFePO_4/FePO_4$ interface on lithium insertion to a particle of $FePO_4$.

1.15 Electronic structure of octahedral transition metal ions

The ability of $LiFePO_4$ to undergo large variations in lithium concentrations is attributable to the flexibility of the valance electronic structure formed by the octahedral FeO_6 and tetrahedral PO_4. Lithium is generally completely ionized with in this structure, having donated its valance electron to the host. The electronic properties of $LiFePO_4$ are dictated by the number of valance electrons and by the interaction of the *d*-orbitals of the Fe with the *p*-orbitals of phosphorus and oxygen.

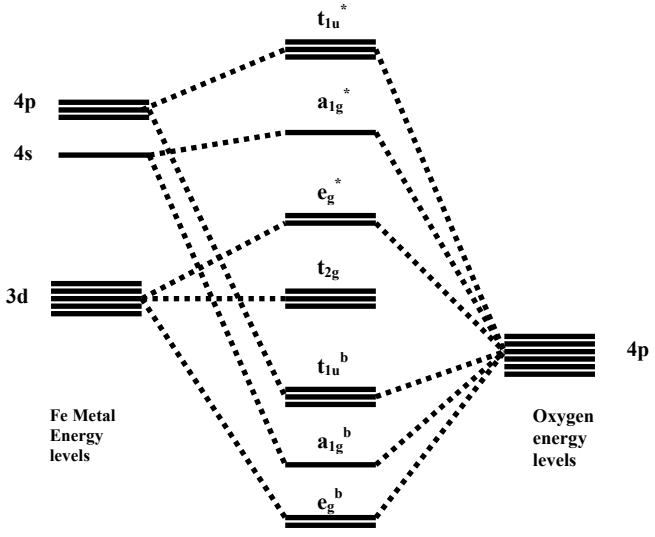

Figure 7 Schematic illustration of the bonding and antibonding levels that arises for a transition metal in an oxygen octahedral environment.

In olivine $LiFePO_4$, the Fe ion is octahedrally coordinated by oxygen. The five *d*-orbitals when occupied by a single electron outside of a closed shell core are degenerate in a free Fe ion, but in an octahedral environment (figure 7), this degeneracy is broken. Crystal field theory **[53–56]**, for example, shows that the interaction of the *d*-orbitals with the electrostatic potential due to the negatively charged oxygen ions of the octahedron produces an increase in the energy of the $d_{3z^2-r^2}$ and $d_{x^2-y^2}$ orbitals with respect to the energy of the d_{xy}, d_{xz} and d_{yz} orbitals. This occurs because the $d_{3z^2-r^2}$ and $d_{x^2-y^2}$ orbitals have lobes pointing toward the negatively charged oxygen ions while the lobes of the d_{xy}, d_{xz} and d_{yz} orbitals point between oxygen ions.

Only the effect of the electrostatic field of the oxygen ions is considered in the above treatment. The important role of covalency that can exist between the iron and oxygen orbitals has been ignored. A more accurate picture of the interaction between the ferrous ion with the surrounding oxygen ions arises from molecular orbital theory **[53–56]**. The $d_{3z^2-r^2}$ and $d_{x^2-y^2}$ orbitals directly overlap with the p_x, p_y and p_z orbitals of oxygen forming bonding and antibonding σ levels referred to as $e_g^{\,b}$ and $e_g^{\,*}$. These levels are illustrated in figure 7. Since the energies of the *p* orbitals lie below those of the *d* orbitals, the bonding $e_g^{\,b}$ levels consist mainly of metal *d* states. This dichotomy in character between the bonding and antibonding levels becomes more pronounced as the difference in the energy of the metal *d*-levels and the oxygen *p*-levels widens. The d_{xy}, d_{xz} and d_{yz} orbitals which do not directly overlap with oxygen *p* orbitals to form *σ* bonds, are frequently said to form a set of nonbonding levels denoted by t_{2g} **[53–56]**. A band gap Δ_o separates the t_{2g} levels are below the e_g levels. Although the d_{xy}, d_{xz} and d_{yz} orbitals do not form σ bonds with the oxygens, they do form *π* bonds with the oxygen p orbitals **[53]**.

Instead of being non-bonding levels, the t_{2g} energy levels of figure 7, more accurately correspond to the bonding levels of the *π* overlap between the metal d_{xy}, d_{xz} and d_{yz} and the oxygen *p* levels. Increased covalency of this *π* bond will result in a lowering of the energy of the t_{2g} levels and hence an increase in the band gap Δ_o **[53]**.

Other levels arise from the overlap of the oxygen *p*-levels with the Fe *4s* and *4p* levels. These are referred to as t_{1u} and a_{1g}. Since the energy of the oxygen *p* levels are again below the energy of the metal *4s* and *4p* levels, the bonding t_{1u} and a_{1g} levels are predominantly of oxygen character.

In a crystal, the levels of figure 7 become bands. Furthermore, although the transition metal ions reside in octahedral interstitial sites, the remainder of the crystal outside of the octahedral site generally does not exhibit the symmetry of a perfect octahedron. Hence the degeneracy of the levels is lifted further. Nevertheless, the schematic picture of figure 7 is usually still identifiable in the band structure.

While general trends can be rationalized with simple crystal field and molecular orbital models, more accurate numerical methods based on density functional theory are necessary to understand and predict the relationship between the electronic structure of a compound and its specific electrochemical properties. We now focus on the wavefunctions of Fe^{++}.

1.16 Spin Hamiltonian of Fe^{2+} in the trigonal crystal field; Energy diagram:

For Fe^{2+} $[(3d)^6]$, the ground state is the orbital triplet, for which case, we need to determine the energy diagram by taking both the crystal field and the spin orbit interaction into account **[57]**.

The free-ion $(3d)^6$, ^5D state ($L = 2$, $S = 2$) of the Fe^{2+} is split by the cubic crystal field into the orbital doublet (E) and orbital triplet ($T2$), the latter being the lowest one. The orbital wavefunction of the ground orbital triplet are represented by

$$|-1\rangle = |\Psi_{d1}\rangle = \sqrt{\frac{2}{3}}|\phi_{-2}\rangle + \frac{1}{\sqrt{3}}|\phi_1\rangle$$

$$|0\rangle = |\Psi_s\rangle = |\phi_0\rangle$$

$$|1\rangle = |\Psi_{d2}\rangle = \sqrt{\frac{2}{3}}|\phi_2\rangle - \frac{1}{\sqrt{3}}|\phi_{-1}\rangle$$

where we use the notation, $|l = 3, m\rangle = |\phi_m\rangle$ and we have the relation $\hat{L}_z|\phi_m\rangle = m|\phi_m\rangle$ (m = -3, -2, -1, 0, 1, 2, 3). Here after we do not use the operators in quantum mechanics for convenience. We consider the splitting of the orbital triplet by the perturbing Hamiltonian given by

$$H_0 = -k\lambda \vec{l}.\vec{S} - \delta(l_z^2 - \frac{2}{3}).$$

Where k (≈ 1) is constant, λ (= -100 cm^{-1} for Fe^{2+}) is a spin-orbit coupling constant, and S is the spin angular momentum of the magnitude 2. The second term is the tetragonal field. A fictitious angular

momentum l of the magnitude 1 represents the triplet state (l is antiparallel to the real orbital angular momentum $L(=-kl)$).

Since $l_z + S_z$ is a constant of the motion, its eigenvalue m can be used to classify the various states, where $m = l_z' + S_z'$, $l_z \left| l_z' \right\rangle = l_z' \left| l_z' \right\rangle$ $(l_z' = 1,0,-1)$ and $S_z \left| S_z' \right\rangle = S_z' \left| S_z' \right\rangle$ $(S_z' = 2,1,0,-1,-2)$. There are 15 states. A notation $\left| l_z', S_z' \right\rangle$ is used to specify these states.

$m = l_z' + S_z'$	Eigen functions
3	$\left\|l_z' = 1, S_z' = 2\right\rangle$
2	$\left\|1,1\right\rangle$, $\left\|0,2\right\rangle$
1	$\left\|1,0\right\rangle$, $\left\|0,1\right\rangle$, $\left\|-1,2\right\rangle$
0	$\left\|1,-1\right\rangle$, $\left\|0,0\right\rangle$, $\left\|-1,1\right\rangle$
-1	$\left\|1,-2\right\rangle$, $\left\|0,-1\right\rangle$, $\left\|-1,0\right\rangle$
-2	$\left\|0,-2\right\rangle$, $\left\|-1,-1\right\rangle$
-3	$\left\|-1,-2\right\rangle$

The ground orbital triplet is split by the spin–orbit coupling λ' and the trigonal field δ (>0). The energy levels are denoted by $E_3 (m = \pm 3)$, $E_2^{(\pm)} (m = \pm 2)$, $E_1^{\,i} (i = 1,2,3)(m = \pm 1)$, $E_0^{(0)}$ and $E_0^{(\pm)}$ *(m=0)*. Here we use $x = \dfrac{\delta}{\lambda'}$.

(i) $m = \pm 3 (E_3)$

$$\frac{E_3}{\lambda'} = -\frac{x}{3} - 2$$

(ii) $m = \pm 2 (E_2)$

$$\frac{E_2}{\lambda'} = \frac{x}{6} - \frac{1}{2} \pm \frac{1}{2}\sqrt{9 + 2x + x^2}$$

(iii) $m = \pm 1 [E_1^{(1)}, E_1^{(2)}, E_1^{(3)}]$

$$\frac{E_1^{(i)}}{\lambda'} = -\frac{x}{3} + 1 + \xi_i \qquad (i = 1, 2, 3).$$

where

$$x = \xi_1 + 1 - \frac{3}{\xi + 1} - \frac{2}{\xi_i - 1}$$

(iv) $m = 0[E_0^{(0)}, E_0^{(\pm)}]$

$$\frac{E_0^{(0)}}{\lambda'} = -\frac{x}{3} + 1, \qquad (\frac{E_0^{\pm}}{\lambda'} + \frac{x}{3} - 1)(\frac{E_0^{\pm}}{\lambda'} - \frac{2x}{3}) = 6$$

The ground level is either $E_0^{(+)} or E_1^{(1)}$, depending on the sign of x. All the energy states except for $E_1^{(1)} and E_0^{(+)}$ might be neglected in the first approximation, since these lowest levels lie 100 cm^{-1} below the others. Thus we may use a fictitious spin s = 1 for the lowest three states denoted by the eigen kets $|\Psi_0\rangle$ for the singlet and $|\Psi_\pm\rangle$ for the doublet. From this discussion we move on to consider the electronic structure of $LIFePO_4$.

1.17 Electronic Structure of $LiFePO_4$

The electronic structure of $LiFePO_4$ underpins transport properties important to use as a lithium storage electrode. In a rechargeable lithium battery, during extraction/intercalation of Li ions from/to cathode, vacancies are created/refilled at the Li sites. Removal and insertion can lead to several phenomena that can significantly affect the electrochemical properties of the compound. For one, variations in lithium concentration alter the electronic properties of the host. The valance electron of each lithium ion is generally donated to the host where it can either change the valance state of the transition metal ion and/or alter the nature of the bonds between the transition metal and the anion. Simultaneously, lithium removal from the host may structurally destabilize the host or may lead to order-disorder phase transitions between lithium and vacancies once a critical vacancy concentration is reached. These phenomena often affect the voltage characteristic or the lattice parameters of the cathode.

The stability of crystal structure of $LiFePO_4$ especially the stable ordered lithium-vacancy arrangements and charge-ordered and magnetic-ordered electronic states are more difficult to predict or rationalize with simple electronic structure models. It is here that first-principles electronic structure methods for $LiFePO_4$ have been proved in understanding this material.

Ab initio studies focusing on the band gap and effective hole or electron mass have found a small gap, or no gap at the Fermi level, which seems to be in contradiction to experiment **[58–62]**. For example, Xu et al. **[62]** found that $LiFePO_4$ is a semi-metal, which seems surprising, given the experimentally observed lack of electrical conductivity. However, there is significant evidence that the local density approximation (LDA) and generalized gradient approximation (GGA), used in

almost all previous studies on the electronic structure of these phosphates, cannot accurately reproduce their electronic structure, due to the very approximate treatment of the electron correlation in transition metal orbitals by LDA/GGA. In order to clarify the electronic structure of $LiFePO_4$, Zhou et al **[63]** have applied the more accurate GGA+U method to determine the density of states (DOS) of $LiFePO_4$.

Computed results are compared with the optical gap of $LiFePO_4$, as measured using UV–Vis-NIR diffuse reflectance spectroscopy. The results obtained from experiment (3.8–4.0 eV) and GGACU computations (3.7 eV) are in very good agreement. However, standard GGA, without the same level of treatment of electron correlation, is shown to lead to large errors in the electronic structure parameters. It is argued that olivines are likely to be polaronic conductors with extrinsically determined carrier levels and that their electronic conductivity is therefore not simply related to the band gap.

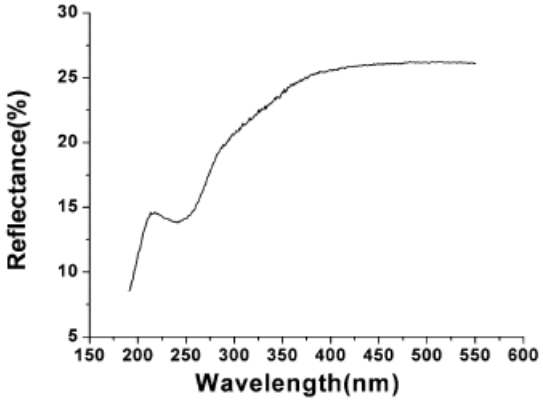

Figure 8. The diffuse reflectance spectrum for $LiFePO_4$.

A polaron conduction mechanism for $LiFePO_4$ is supported by the measured temperature dependence of the conductivity, which suggests that in the pure material electronic conductivity has an Arrhenius type behavior, with activation energy of about 0.39 – 0.5 eV **[64, 65]**. If this temperature dependence is due to exciting delocalized carriers over the gap, then based on the gap determined in the work of Fei Zhou et al **[63]**, the activation energy should be about 1.95 eV. Therefore, the measured activation energy is more likely a measure of the carrier mobility alone, with the carrier density set extrinsically, and independent of temperature.

Zhou et al **[63]** have obtained the diffuse reflectance spectrum of $LiFePO_4$, as shown in figure 8. The large drop in reflectance below about 375 nm is due to the absorption across the band gap of the material. Using the Kubelka – Munk remission function **[66]**, $F = (1 - R)^2/2R$, where R is the

diffuse reflectance, the gap can be determined as the energy at which F starts to increase linearly **[67]**. This gives 4.0 eV for the gap. An alternative way to determine the band gap is by extrapolating the onset of absorption to the wavelength axis (Shapiro's method), which gives a value of 3.8 eV **[68]**. This value is in good agreement with the GGA+U result of 3.7 eV, reported in the literature **[58]**.

1.18 Magnetic structure of $LiFePO_4$

The magnetic properties of $LiMPO_4$ (M= Mn, Fe, Co, Ni) systems have been studied since the early 1960s **[69–71]**. They all undergo a paramagnetic –to- antiferromagnetic phase transition at low temperatures to a similar magnetic arrangement differing only in the orientation of the staggered spins. Nearest-neighbor (NN) spins in the *b-c* plane are antiparallel and the stacking along the *a* axis is such that ferromagnetic sheets perpendicular to the *b* axis are formed; nearest-neighbor sheets are antiparallel, giving rise to a (0,1,0) fundamental magnetic reflection that, depending on the direction of the magnetic moment, can be intense or extinct. Earlier neutron diffraction studies of polycrystalline samples showed that the magnetic space group of $LiFePO_4$ and LiCoPO4 is *Pnma*' with the spins oriented along the *b* crystallographic direction (i.e., the (0,1,0) reflection is absent), and *Pnm'a* magnetic space group for $LiNiPO_4$ and $LiMnPO_4$ with the spins aligned parallel to the *c* axis (i.e., strong intensity at the (0,1,0) reflection) **[69, 72–76]**. Recent neutron diffraction studies of single crystal $LiCoPO_4$ have reported finite intensity for the (0,1,0) reflection, interpreted in terms of a ground state with a spin direction that is slightly rotated from the *b* axis. Weak ferromagnetism has been reported for $LiMnPO_4$ **[76]** and $LiNiPO_4$ **[77]** at temperatures below T_N.

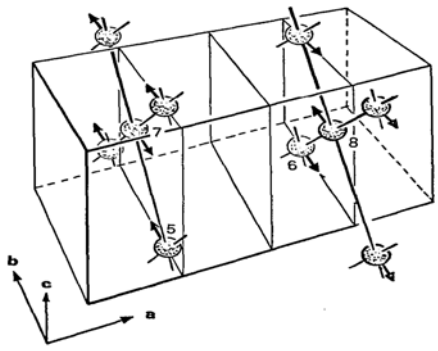

Figure 9. Magnetic structure of $LiFePO_4$. Only the iron positions are shown. (Courtesy: R. P. Santoto et al)

In particular, Santoro and Newnham **[69]**-in a pioneering effort- determined the magnetic structure of olivine polycrystalline $LiFePO_4$ from neutron diffraction data, as early as in 1967. They find that $LiFePO_4$ undergoes a magnetic phase transition from paramagnetic to antiferromagnetic state at 50±2 K, the Néel temperature. This type of magnetic ordering was indicated by minima of

reciprocal susceptibility (χ^{-1}) of $LiFePO_4$ as a function of temperature. They have also claimed only M–O–M superexchange interactions occur in the $LiMPO_4$ (M=Mn, Fe, Co, Ni), which give rise to antiferromagnetic puckered-planes orthogonal to **a**, as shown in figure 9. There are no direct or a superexchange linkage between these planes and it is necessary to postulate long-range interactions, such as the Mn–O–P–O–Mn triple exchange suggested by Mays **[78]**.

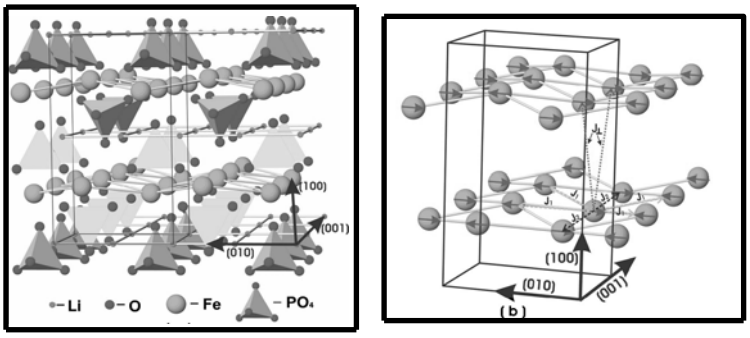

Figure 10. (a) Atomic structure of $LiFePO_4$. The Fe^{2+} ions form buckled layers stacked perpendicular to the [100] crystallographic direction. The ground state of $LiFePO_4$ is collinear antiferromagnetic with the average moment along b direction. (b) Spin arrangement of the two Fe^{2+} layers, the in-plane nearest and next-nearest-neighbor interactions J_1 and J_2 and interplane nearest neighbor inaction $J\perp$ are labeled. (Courtesy: Jiying Li et al)

After Goodenough's group **[39]** proposed the electrochemical nature of the material, the research activity on this material has increased enormously. Particularly, extensive work by Julien's group **[79–81]** on magnetic measurements has given a picture of magnetic structure of $LiFePO_4$. Luo Zhi et al **[82]** have done the low temperature Mössbauer measurements of $LiFePO_4$ and evaluated the hyperfine parameters above and below the Néel temperature. Rousse et al **[83]** have solved the magnetic structures using neutron diffraction on polycrystalline samples of $LiFePO_4$. A comparison has been made between the magnetic structures of $LiFePO_4$ and $FePO_4$ and discussed the difference in Néel temperatures of the both in terms of super and super-super exchange interactions and anisotropy of Fe^{2+}.

Because of the intriguing magnetic properties, in particular, the strong magnetoelctric (ME) effect it exhibits **[84]**, $LiFePO_4$ has attracted the attention of the global research community. The Fe^{2+} ion occupies the center of a slightly distorted FeO_6 octahedron that shares oxygen anions with a PO_4 tetrahedron forming a closely packed oxygen framework. The Fe^{2+} ions (S = 2) form corrugated layers that are stacked along the [100] crystallographic axis, as shown in figure 10. Nearest neighbors in the b-c plane are coupled magnetically by a relatively strong exchange interaction, J_1 through a Fe-O-Fe oxygen bond, where as in-plane next-nearest-neighbors are coupled (J_2) via Fe-O-O-Fe **[85]**. Interlayer magnetic coupling is mediated by a phosphate ion via Fe-O-P-O-Fe bonding **[78]**. Thus the

olivine family of $LiMPO_4$ exhibits highly anisotropic properties which are between those of two- (2D) and three-dimensional (3D) systems **[72, 73]**.

In 1969, Hang Nam Ok **[86]** had shown the antiferromagnetic ferrous carbonate undergoes slow electron relaxation, spin-lattice relaxation phenomena, with Mössbauer spectra recorded at low temperatures. Also, electron-spin relaxation phenomena have been observed by many investigators **[87–92]**. However, most of these studies in iron compounds were restricted to the ferric (Fe^{3+}) ions. Though, Luo Zhi et al **[82]** have done the Mössbauer studies of $LiFePO_4$, they were not focused on an investigation of possible relaxation effects. And to the best of our knowledge, no relaxation effects in the Fe^{2+} ions in the antiferromagnetic $LiFePO_4$ have been discussed.

1.19 Importance of Carbon Coating

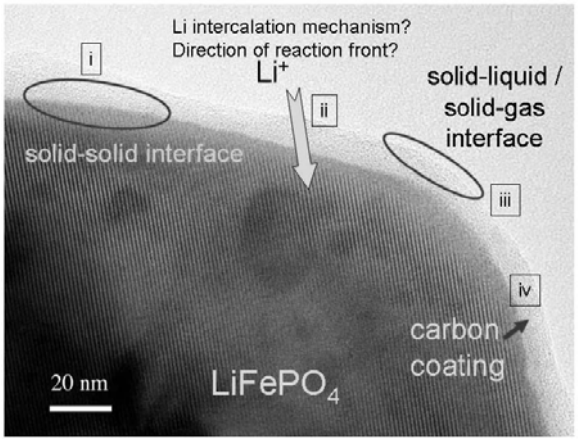

Figure 11. A battery system involves interactions among various states of matter. Transmission electron microscopy data (Courtesy of H. Gabsrisch).

Padhi et al **[39]** showed that $LiFePO_4$ can-in spite of its poor electronic conductivity – be used as a cathode material. It has been accepted **[93–97]** by and large that $LiFePO_4$ has fundamentally low electronic conductivity, desirable for solid electrolytes but not for applications as ion-storage or fuel-cell electrodes. At the lattice scale, mixed electronic-ionic conductivity is necessary for preservation of overall charge neutrality during lithium ion transport, the chemical (ambipolar) diffusion coefficient being rate-limited by the slower species. At meso- and microscale, a high electronic conductivity is desirable to prevent the impedance of a typical storage battery electrode, composed of a percolating network of storage and a conductive additive such as carbon, from becoming excessive.

It is known that surface carbon coatings help prevent irregular particle growths and ensure sub-micrometer size and uniform size distribution of the $LiFePO_4$ particles formed **[101]**. Synthesis of

nanocomposites consisting of submicron particles of $LiFePO_4$ and an electronic conductive phase, typically carbon, in intimate contact with each other **[98]** would help in getting enhanced performance of a cathode formed with $LiFePO_4$. The electronic conductive phase would help to alleviate limitations of slow electronic transport in the composite electrode caused by the poor electronic conductivity of active material, namely $LiFePO_4$, and the small particle size of $LiFePO_4$ would help ensure short diffusion length for its reaction with lithium, both factors contributing to enhance the rate capability. In this regard, different interactions involved during charge-discharge are shown in figure 11.

The efficiency of $LiFePO_4$ can be considerably improved if, e.g., a few nm thick carbon coating of individual $LiFePO_4$ particles can be formed in-situ during the $LiFePO_4$ synthesis **[98]**. The carbon coating provides an efficient electronically conductive network but it is still permeable enough for Lithium ions. As far as the role of the size of the phosphate particles is concerned, there are different opinions in the literature **[102–104]**.

Ravet et al **[105]** showed a seven-order-of-magnitude increase in the electronic conductivity of $LiFePO_4$ by adding carbon in raw materials, while Zaghib et al **[106]** demonstrated that better performance can be achieved at high-rate discharge (3C) with 6% carbon additive in the $LiFePO_4$ electrode. This material is suitable for large-scaled applications such as hybrid electric vehicles (HEV). The carbothermal effect proposed by Ait-Salah et al **[107]**, showed that addition of 5% carbon coating reduces Fe, preventing the formation of ferromagnetic nanoparticles, withdraws traces of the Fe^{3+} phase such as Fe_2P and/or Fe_2O_3, in which iron is in the trivalent state.

1.20 Aim and Scope of the thesis

From the foregoing assessment of the literature on Li-ion cathode materials, $LiFePO_4$ in particular, it is obvious that the material has been synthesized by different routes and it's electrochemically characterized thoroughly because of its excellent electrochemical behavior. One major limitation in synthesis is the formation of Fe^{3+} bearing phase (like $Li_3Fe_2(PO_4)_3$), which destabilizes the olivine structure during charge – discharge cycle. However, the different synthesis techniques for Fe^{3+} free $LiFePO_4$ have received very little attention. Another problem is the undesirable particle growth which leads to slow electronic transport in the cathode caused by fairly low electronic conductivity of the active cathode material.

$LiFePO_4$ has also been studied for its magnetic behavior below liquid nitrogen temperatures and Para – Antiferromagnetic transition by magnetisation studies. Many basic differences in the

magnetisation processes have been observed when a nanocrystalline material is compared with its crystalline counterpart. Most of the above-mentioned properties are also expected to undergo fundamental changes particularly due to the sizeable magnetic contributions to them.

Lithium in $LiFePO_4$ is constrained to diffuse in 1D due to the interlock of the FeO_6 octahedra and PO_4 tetrahedra, which makes the material more stable for thermal and chemical fluctuations. The thermal behavior of $LiFePO_4$, in particular at high temperatures has somehow failed to attract the attention of the research groups. It is expected that interesting and important changes occur in the local environment at the Fe site and also the bonding with in FeO_6 and PO_4.

As chemical/electrochemical delithiation of $LiFePO_4$ results in lithium deficient $LiFePO_4$, it is reasonably expected that the concentration of Li-ions would change the electron field gradient (EFG) at the Fe site. Similar changes may also be expected with the substitution of Li by bigger alkali ions Na^+ and/or K^+, which occupies more space, creates more free volume and affects the Fe-O bonding and spin alignment and EFG at Fe-site.

With these points in mind, an elaborate synthesis of nanocrystalline $LiFePO_4$ free from ferric phase or ions was undertaken. The material has been characterized by XRD for crystal structure, SEM for morphology, EDAX for elemental analysis, FTIR for internal modes of phosphate ion and Mössbauer spectroscopy for the nature and valency of the ferrous ion of the FeO_6 octahedra.

Two-phase systems namely $(x)LiFePO_4$**:**$(1\text{-}x)Fe^{2+}PO_4$ and $Na_xLi_{1-x}FePO_4$ have been synthesized and studied to understand the environment at the Fe-site and variation of infrared modes due to the absence of lithium and also substitution of sodium for lithium. The chemical stability of the interlock of the FeO_6 octahedra and PO_4 tetrahedra has been probed by substituting the phosphate ion of $LiFePO_4$ with the vanadate ion.

An exhaustive investigation of Fourier transform of Infrared (FTIR) spectra to ascertain the dependence of different stretching and bending modes of the phosphate ion with temperature. Low temperature Mössbauer measurements were carried out from room temperature to 20K with a very close scan around 50K to understand this magnetic transition in detail and also different relaxation phenomena involved in this transition. This is supported by the susceptibility measurements from SQUID.

Finally Electrochemical experiments performed with $LiFePO_4$ material synthesized in our laboratory for its electrochemical behavior.

References

1. Winter, M., and Brodd, R. J., *Chemical Reviews, **104**, p4245 (2004)*.
2. Tarascon, J. -M., and Armond, M., *Nature, **414**, p359 (2001)*.
3. Mizushima, K., Jones, P. C., Wiseman, P. J., and Goodenough, J. B., *Materials Research Bulletin, **15**, p783 (1980)*.
4. Whittingham, M. S., *Science, **192**, p1126 (1976)*.
5. Gooenough, J. B., Mizushima, K., and Takeda, T., *Japanese Journal of Applied Physics, **19**, p305 (1983)*.
6. Thackeray, M. M., David, W. I. F., Bruce, P. G., and Gooenough, J. B., *Materials Research Bulletin, **18**, p461 (1983)*.
7. *Li-ion Technical Handbook*, Gold Peak Industries (Taiwan), Ltd., Taipei, Taiwan.
8. Maier, J., *Programs of Solid State Chemistry, **23**, p171 (1995)*.
9. Buchmann, Isidor. "*Will Lithium-Ion batteries power the new millennium?*". Isidor Buchmann (CEO of Cadex Electronics Inc.).
10. Carlin, R. T., and Swider-Lyons, K., *The AMPTIAC newsletter, **6 (1)**, p25 (2002)*.
11. Maier, J., *Prog Solid State Chemistry, **23**, p171 (1995)*.
12. Gurgeon, S., Laruelle, S., Herrera-Urbina, R., Dupont, L., Poizot, P., and Tarascon, J. M., *Journal of Electrochemical Society, **148**, pA285 (2001)*.
13. Li, H., Richter, G., and Maier, J., Advances in Materials, **15**, p735 (2002).
14. Conway, B. E., *Electrochimica Acta, **38**, p1249 (1993)*.
15. Beaulieu, L. Y., Larcher, D., Dunlap, R. A., and Dahn, J. R., *Journal of Electrochemical Society, **147**, p3206 (2000)*.
16. Jiang, C., Hosono, E., and Zhou, H., *Nanotoday, **1(4)**, p28 (2006)*.
17. Nazri, G, -A., (Ed.), *Lithium batteries Science and Technology*, kluwer Academic Publishers, Massachusetts, USA (2004).
18. Mitzushima, K., Jones, P. C., Wiseman, P. J., and Goodenough, J. B., *Materials Research Bulletin, **15**, p783 (1980)*.
19. Amatucci, G. G., Tarascon, J. M., and Klein, L. C., *Journal of Electrochemical Society, **143**, p1114 (1996)*.
20. Rossen, E., Reimers, J. N., and Dahn, J. R., *Solid State Ionics, **62**, p53 (1993)*.
21. Gabrisch, H., Yazimi, R., and Fultz, B., *Journal of Electrochemical Society, **151**, pA891 (2004)*.

22. Guoymard, G., *New trends in Electrochemical Technology: Energy storage systems for Electronics*, Osaka, T., Datta, M., (Ed.), Gordon & Breach Science Publishers, p253 (2000).
23. Nalbandyan, V. B., Shukaev, I. L., *Russian Journal of Inorganic Chemistry, **32**, p3 (1987)*.
24. Nazri, G, -A., and Pistoia, G., (Eds.), *Lithium Batteries: Science and Technology*, Kluwer academic publishers, Massachusetts, USA (2004).
25. Goodenough, J. B., Thackeray, M. M., David, W. I. F., and Bruce, P. G., *Revue De Chimie Minerale, **21**, p435 (1984)*.
26. Thackeray, M. M., David, W. I. F., and Goodenough, J. B., *Materials Research Bulletin, **17**, p785 (1983)*.
27. Thackeray, M. M., David, W. I. F., Goodenough, Bruce, P. G., and J. B., *Materials Research Bulletin, **18**, p461 (1983)*.
28. Thackeray, M. M., David, Johnson, P. J., dePicciotto, L. A., Bruce, P. G., and Goodenough, and J. B., *Materials Research Bulletin, **19**, p179 (1984)*.
29. Manthiram, A., and Goodenough, J. B., *Journal of Solid State Chemistry, **71**, p349 (1987)*.
30. Manthiram, A., and Goodenough, J. B., *Journal of Power Sources, **26 (3-4)**, p403 (1989)*.
31. Delmas, C., Cherkaoui, F., Nadiri, A., and Hagenmuller, P., *Materials Research Bulletin, **22**, p631 (1987)*.
32. Delmas, C., and Nadiri, A., *Materials Research Bulletin, **23**, p65 (1988)*.
33. Goodenough, J. B., Hong, H. Y. –P., and Kafalas, J. A., *Materials Research Bulletin, **11**, p203 (1976)*.
34. Masquelier, C., Padhi, A. K., Nanjundaswany, K. S., and Goodenough, J. B., *Journal of Solid State Chemistry, **135**, p228 (1998)*.
35. Morcrette, M., Wurm, C., and Masquelier, C., *Solid State Sciences, **4**, p239 (2002)*.
36. Chen, J.-M., Li, Y. J., Hurng, W.-M., Whittingham, M. S., (Industrial Technology Research Institute, Chutung, Taiwan) *U.S. Patent 5,514,490 (1996)*.
37. Li, Y. J., and Whittingham, M. S., *Solid State Ionics, **63**, p391 (1993)*.
38. Chung, S, -Y., Bloking, J. T., Chiang, Y. –M., *Nature Materials, **1**, p123 (2002)*.
39. Padhi, A. K., Najundaswamy, K. S., and Goodenough, J. B., *Journal of Electrochemical Society, **144**, p1188 (1997)*.
40. Padhi, A. K., Najundaswamy, K. S., Masquelier, C., Okada, S. and Goodenough, J. B., *Journal of Electrochemical Society, **144**, p1609 (1997)*.
41. Nanjundaswamy, K. S., Padhi, A. K., Goodenough, J. B., Okada, S., Ohtsuka, H., Arai, H., and Yamaki, J., *Solid State Ionics, **92**, p1 (1996)*.
42. Tarascon, J.-M., and Armand, M., *Nature, **414**, p359 (2001)*.

43. Gaubicher, J., Le Mercier, T., Chabre, Y., Angenault, J., and Quarton, M., *Journal of Electrochemical Society, **146**, p4375 (1999)*.
44. Amine, K., Yasuda, H., and Yamachi, M., *Electrochemistry and Solid State Letters, **3**, p178 (2000)*.
45. Yamada, A., Chung, S. C., and Hinokuma, K., *Journal of Electrochemical Society, **148**, pA224 (2001)*.
46. Andersson, A. S., Thomas, J. O., Kalska, B. and Häggström, L., *Electrochemistry and Solid State Letters, **3**, p66 (2000)*.
47. Ravet, N., Goodenough, J. B., Benser, S., Simoneau, M., Hovington, P., and Armand, M., *Abstract **127**, the 1999 Joint International Meeting Abstracts, Honolulu, HI, Oct. 17-22, 1999*.
48. Huang, H., Yin, S.-C., and Nazar, L. F., *Electrochemistry and Solid State Letters, **4**, pA170 (2001)*.
49. Prosini, P. P., Zane, D., and Pasquali, M., *Electrochimica Acta, **46**, p3517 (2001)*.
50. Whittingham, M. S., *Chemical Reviews, **104 (10)**, p4271 (2004)*.
51. Santoro, R. P., and Newnham, R. E., *Acta Crystallography, **22**, p344 (1967)*.
52. Sundarayya, Y., Kumara Swamy, K.C., and Sunandana, C.S., *Materials Research Bulletin, **42**, p1942 (2007)*.
53. Day, M. C., Selbin, J., *Theoretical Inorganic Chemistry*, Reinhold Publishers (1962).
54. Ballhausen, C. J., *Introduction to Ligand Field Theory*, MaGraw-Hill (1962).
55. Dunn, T. M., McClure, D. S., Pearson, R. G., *Crystal Field Theory*, Harper and Row (1965).
56. Hall, L. H., *Group Theory and Symmetry in Chemistry*, McGraw-Hill (1969).
57. Inomata, K., and Oguchi, T., *Japanese Journal of Physical Society, **23**, p765 (1967)*.
58. Yamada, A., Chung, S. -C., *Journal of the Electrochemical Society, **148**, pA960 (2001)*.
59. Yamada, A., Hosoya, M., and Chung, S. C., *Journal of Power Sources, **119**, p232 (2003)*.
60. Tang, P., Holzwarth, N. A. W., *Physical Review B, **68**, p165107 (2003)*.
61. Shi, S. Q., Liu, L. J., Ouyang, C. Y., et al., *Physical Review B, **68**, p195108 (2003)*.
62. Xu, Y. -N., Chung, S. -Y., and Bloking, J. T., *Electrochemical and Solid-State Letters, 7, p A131 (2004)*.
63. Zhou, F., Kang, K., Maxisch, T., Ceder, G., and Morgan, D., *Solid State Communications, **132**, p181 (2004)*.
64. Chung, S. -Y., Bloking, J. T., Chiang, Y. -M., *Nature Materials, **1**, p123 (2002)*.
65. Xu, Y. -N., Chung, S. -Y., Bloking, J. T., et al., *Electrochemical and Solid-State Letters, **7**, p A131 (2004)*.

66. Wendlandt, W.W., and Hecht, H.G., *Reflectance Spectroscopy*, Interscience Publishers, New York, 1966.
67. Tandon, S.P., and Gupta, J.P., *Physica Status Solidi,* ***38****, p363 (1970)*.
68. Shapiro, I.P., *Optika i Specktroskopiya,* ***4****, p256 (1958)*.
69. Santoro, R. P., and Newnham, R. E., *Acta Crystallography,* ***22****, p344 (1967)*.
70. Mercier, M., Gareyte, J., Bertaut, E. F., and Seances, C. R., C. R. Seances, *Acad. Sci., Ser. B,* ***264****, p979 (1967)*.
71. Santoro, R. P., Segal, D. J., and Newnham, R. E., *Journal of Physics and Chemistry of Solids,* ***27****, p1192 (1966)*.
72. Vaknin, D., Zarestky, J. L., Ostenson, J. E., Chakoumakos, B. C., Goñi, A., Pagliuso, P., Rojo, T., and Barberis, G. E., *Physical Reviews B,* ***60****, p1100 (1999)*.
73. Vaknin, D., Zarestky, J. L., Miller, L. L., Rivera, J.-P., and Schmid, H., *Physical Reviews B,* ***65****, p224414 (2002)*.
74. Goňi, A., Lezama, L., Barberis, G. E., Pizarro, J. L., Arriortua, M. I., and Rojo, T., *Journal of Magnetism and Magnetic Materials,* ***164****, p251 (1996)*.
75. Arčon, D., Zorko, A., Dominko, R., and Jaglicic, Z., *Journal of Physics and Chemistry of Solids,* ***16****, p5531 (2004)*.
76. Kharchenko, Y., Kharchenko, N., Baran, M., and Szymczak, R., *Low Temperature Physics,* ***29****, p579 (2003)*.
77. Arčon, D., Zorko, A., Cevc, P., Dominiko, R., Bele, M., Jamnik, J., Jaglicic, Z., and Golosocsky, I., *Journal of Physics and Chemistry of Solids,* ***65****, p1773 (2004)*.
78. Mays, J. M., *Physical Reviews,* ***131****, p38 (1963)*.
79. Ait-Salah, A., Zaghib, K., Mauger, A., Gendron, F., and Julien, C. M., *Physica Status Solidii (A)* ***203(1)****, R1 (2006)*.
80. Zagbib, K., Ravet, N., Gauthier, M., Gendron, F., Mauger, A., Goodenough, J. B., and Julien, C. M., *Journal of Power Sources,* ***163****, p560 (2006)*.
81. Ravet, N., Gauthier, M., Zagbib, K., Goodenough, J. B., Mauger, A., Gendron, F., and Julien, C. M., *Chemistry of Materials,* ***19****, p2595 (2007)*.
82. Luo Zhi, Di Nai-Li, Kou Zhi-Qi, Cheng Zhao-Hua, Liu Li-Jun, Chen Li-Quan, and Huang Xue-Jie, *Chinese Physics,* ***13(12)****, p2158 (2004)*.
83. Rousse, G., Rodriguez-Carvajal, J., Patoux, S., and Masquelier, C., *Chemistry of Materials,* ***15****, p4082 (2003)*.
84. Fiebig, M., *Journal of Physics D,* ***38****, pR123 (2005)*.
85. Dai, D., Whangbo, M. H., Koo, H. J., Rocquefelte, X., Jobic, S., and Villesuzanne, A., *Inorganic Chemistry,* ***44****, p2407 (2005)*.

86. Hang Nam Ok, *Physical Review, **185(2)**, p472 (1969)*.

87. Wertheim, G. K., and Remeika, J. P., *Physics Letters, **10**, p14 (1964)*.

88. Blume, M., *Physical Review Letters, **14**, p96 (1965)*.

89. Blume, M., and Tjon, J. A., *Physical Review, **165**, p446 (1968)*.

90. Campbell, L. E., and Debenedetti, S., *Physical Review, **167**, p556 (1968)*.

91. Wichman, H. H., Klein, M. P., and Shirley, *Physical Review, **152**, p345 (1966)*.

92. Vander Woode, F., and Dekker, A. J., *Physica Stayus Solidi, **9**, p977 (1965)*.

93. Tarascon, J.-M., and Armand, M., *Nature, **414**, p359 (2001)*.

94. Gaubicher, J., Le Mercier, T., Chabre, Y., Angenault, J., & Quarton, M., *Journal of Electrochemical Society, **146**, p4375 (1999)*.

95. Amine, K., Yasuda, H., and Yamachi, M., *Electrochemistry and Solid State Letters, **3**, p178 (2000)*.

96. Huang, H., Yin, S.-C., and Nazar, L.F., *Electrochemistry and Solid State Letters, **4**, pA170 (2001)*.

97. Yang, S., Song, Y., Zavalij, P.Y., and Whittingham, M. S., *Electrochemistry Communications. **4**, p239 (2002)*.

98. Ravet, N., Goodenough, J. B., Benser, S., Simoneau, M., Hovington, P., and Armand, M., *Abstract **127**, the 1999 Joint International Meeting Abstracts, Honolulu, HI, Oct. 17-22, 1999*.

99. Huang, H., Yin, S.-C., and Nazar, L.F., *Electrochemistry and Solid State Letters, **4**, pA170 (2001)*.

100. Prosini, P.P., Zane, D., and Pasquali, M., *Electrochimica Acta, **46**, p3517, (2001)*.

101. Yang, J., and Xu, J. J., *Electrochemical and Solid State Letters, **7(12)**, pA515 (2004)*.

102. Li, H., Huang, J., Chen, L. Q., Zhou, G. W., Zhang, Z., Yu, D. P., Mo, Y. J., and Pei, N., *Solid State Ionics, **135-137**, p181 (2000)*.

103. Chen, Z. H., and Dahn, J. R., *Journal of Electrochemical Society, **149**, pA1184 (2002)*.

104. Beaulieu, L. Y., Larcher, D., Dunlap, R. A., and Dahn, J. R., *Journal of Electrochemical Society, **147**, p3206 (2000)*.

105. Ravet, N., Chouinard, Y., Magnan, J. F., Besner, S., Gauthier, M., and Armand, M., *Journal of Power Sources, **97**, p503 (2001)*.

106. Zaghib, K., Striebel, K., Guerfi, A., Shim, J., Armand, M., and Gauthier, M., *Electrochimca Acta, **50**, p263 (2004)*.

107. Ait-Salah, A., Zaghib, K., Mauger, A., Gendron, F., Julien, C. M., *Physica Status Solidi (a), **203(1)**, R1 (2006)*.

--- O ---

Chapter 2

Experimental Techniques

2.1 Introduction

In this chapter, the experimental techniques and working principles of the various instruments used in carrying out this piece of research work are described. The structural characterization was performed by X-ray diffractometry (XRD) and microstructure studies were carried out using scanning electron microscopy (SEM). The composition of the sample, $LiFePO_4$ in particular was determined by energy dispersive X-ray analysis (EDAX). Mössbauer Spectroscopy and Fourier Transform of Infrared Spectroscopy (FTIR) were used to analyze the phase purity at the Fe site, and the spectroscopic properties of the phosphate group respectively. The magnetic properties of the synthesized $LiFePO_4$ at low temperatures have been studied using Superconducting Quantum Interference Device (SQUID) and Mössbauer spectroscopy, while the high temperature behavior of the sample, order – disorder phase transition in particular has been studied by Fourier transform of Infrared Spectroscopy.

2.2 X-Ray Diffraction

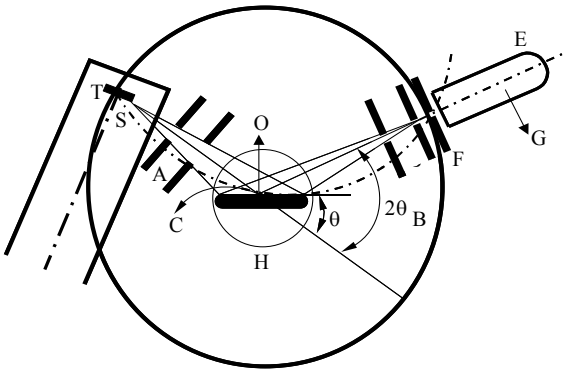

A & B - collimator slits	G – Counter
C- Sample	S – The line focal spot on the target
E & H - Supporting table	T- Target of the X-ray tube
F – receiving slit	O –Axis perpendicular to the plane of drawing

Figure 2.1 A Schematic diagram of X-ray diffractometer

One of the simplest tools to obtain the structural details (e.g., average crystallite size and crystallite composition) about the nanocrystalline $LiFePO_4$ is the X-ray diffraction technique. Diffraction of X-ray beam from a lattice can occur only when the Bragg condition for diffraction,

$$2d_{hkl}Sin\theta = n\lambda \qquad (2.1)$$

is satisfied, where d_{hkl} is the interplanar spacing between parallel planes.

θ is the Bragg angle

λ is the incident wavelength and

n is order of diffraction.

The powder X-ray diffraction technique involves the diffraction of monochromatic X-rays by a powder specimen. Since single crystals are not always available, this technique is preferred to Laue method (wherein the wavelength of the X-rays is varied, keeping the incident angle constant) and polycrystalline samples may be examined nondestructively without any special preparation.

When X-rays of known wavelength are used, the diffractometer can measure the positions and line intensities of diffraction lines simultaneously and quickly. This method is especially suited for determining lattice parameters with high precision and for the identification of phases.

In this study we used PHILLPS X-ray diffractometer with a source providing Ni-filtered Cu-K_α radiation (λ=1.54056 A^0). Bragg angle was varied by rotating the specimen. A radiation detector with associated electronic equipment forms the detector module.

The principle of operation **[1]** of this diffractometer is illustrated in the figure 2.1. The sample C is supported on a table which can be rotated about an axis O perpendicular to the plane of drawing and therefore parallel to the diffractometer axis O. X-rays diffracted from the sample are collected in the GM counter G after being focused at the slit F. A and B are special slits (soller slits) which define and collimate the incident and diffracted beams respectively. The beam from the x-ray tube contains not only K_α radiation but also weak K_β line and some other components. The intensity of these weak and unwanted components is suppressed by passing the beam through a Ni filter. This filter is also used in a special holder in the diffracted beam to help decrease the background radiation originating in the specimen. The diffracted beam passes through another set of Soller slits (Fig.2.2) and the receiving slit F before entering the counter. Since the receiving slit defines the width of the beam admitted to the counter, an increase in its width will optimize the intensity of any diffraction line being measured. The intensity of the diffracted beam is measured directly by an electronic counter which converts the incoming X-rays into electric pulses counted by X-ray detector placed on the circumference of a circle centered on the thin film specimens as shown in fig (2.1) **[1]**.

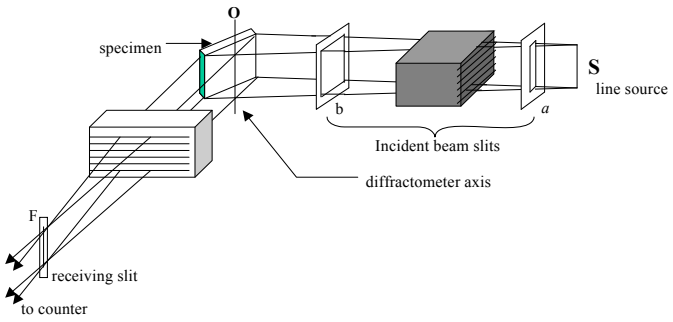

Figure 2.2 Arrangements of Soller slits in a diffractometer

The counter is power driven at a constant angular velocity about diffractometer axis. It is connected to a scaler and set at a fixed value of 2θ for a time, sufficient to make an accurate count of pulses from the counter. It is then moved to a new position and the operation repeated. The range of interest in 2θ is covered in this fashion, and the curve of intensity (I) versus 2θ plotted. When the continuation background between diffraction lines is being measured, the counter may be moved in steps of several degrees.

The receiving slits and counter are supported on the carriage E, which may be rotated about the axis O. The supports E and H are mechanically coupled so that the rotation of the counter through 2θ degrees is automatically accompanied by rotation of the specimen through θ degrees. To preserve focusing conditions, the angles of incidence and reflection are made equal to one another and equal to the half the total angle of diffraction, using this 2θ-θ coupling.

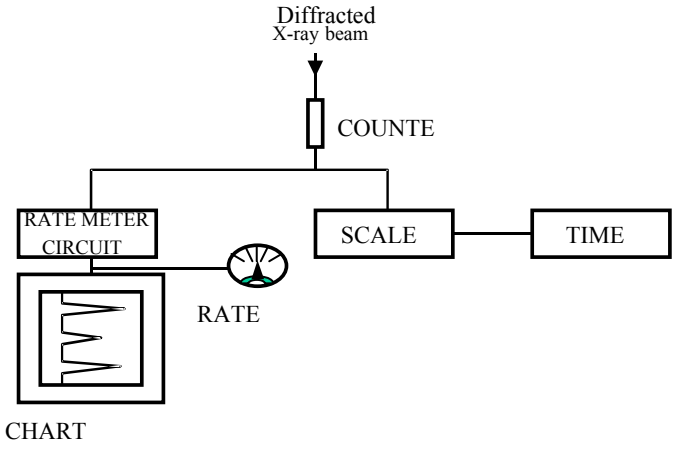

Figure 2.3. Detection system in a X-ray diffraction

Because of the focusing of the diffracted rays and the relatively large radius of the diffractometer circle (about 15 cm in commercial instruments), a diffractometer can resolve very

closely spaced diffraction lines. Indicative of this is the fact that the resolution of the Cu K_α can be obtained. Such resolution can only be achieved with a properly adjusted instrument, and it is necessary to so align the component parts so that the following conditions are satisfied for all diffraction angles:

1. Line of source, specimen surface and receiving slit axis are parallel.
2. The specimen surface contains the diffractometer axis and
3. The line source and receiving slit both lie on the diffractometer circle.

Figure 2.3 shows the block diagram of the detection system of a diffractometer **[1]**.

The following information can be obtained from diffraction peak positions and the shape of XRD:

1. Position of the peak measured (2θ) yields size i.e., d spacing and crystal lattice parameter (size of the unit cell)
2. The shape (Full width Half Maximum, FWHM) of the XRD peak gives information regarding crystallite size and lattice imperfect ions.

The average crystallite sizes *t* of very small crystals (< 100 nm in diameter) can be measured from FWHM of their diffraction peaks by the Scherrer's **[1]** formula,

$$t = \frac{0.94\lambda}{B\cos\theta_B} \qquad (2.2)$$

where θ_B is the Bragg angle

λ is incident wavelength(nm)

B- FWHM (radians)

2.3 SEM and EDAX

The morphology of the samples was examined by Scanning Electron Microscope (SEM). For this purpose, pellets were prepared by compacting powder samples (prepared by Sol-gel synthesis) in a die. The morphology of the samples, as-prepared, was imaged to estimate the average size of the nano crystalline sample. The composition of the as-prepared samples was determined using Energy-dispersive analysis by X-rays (EDAX). The EDAX detector and electronics assembly was attached to SEM, from Hitachi series environmental SEM which works at an accelerating voltage of 20 kV, for chemical compositions of the sample (except for Lithium). During EDAX Analysis, the specimen is bombarded with an electron beam inside the scanning electron microscope. The bombarding electrons collide with the specimen atoms' own electrons, knocking some of them off in the process. A position vacated by an ejected inner shell electron is eventually occupied by a higher-energy electron from an

outer shell. To be able to do so, however, the transferring outer electron must give up some of its energy by emitting an X-ray photon. The amount of energy released by the transferring electron depends on which shell it is transferring from, as well as which shell it is transferring to. Furthermore, the atom of every element releases X-rays with unique amounts of energy during the transferring process. Thus, by measuring the amounts of energy present in the X-rays being released by a specimen during electron beam bombardment, the identity of the atom from which the X-ray was emitted can be established. The energy scale of the spectrometer was calibrated by recording ultra pure Au and Co samples spectra and the spectrum thus recorded was analyzed with software.

2.4 Fourier Transform of Infrared (FTIR) Spectroscopy:

Infrared spectroscopy is an important technique in materials physics and chemistry. It is an easy way to identify the presence of certain functional groups in a molecule. Also, one can use a library of absorption bands to confirm the identity of a pure compound or to detect the presence of specific impurities. Two types of instrumentation are widely used to obtain infrared spectra:

1. Dispersive spectrophotometers, which use a monochromatic source of infrared radiation to produce a spectrum with one resolution element at a time.
2. Michelson interferometers, which use a moving mirror to create an interference pattern, or interferogram, from which all resolution elements are determined simultaneously.

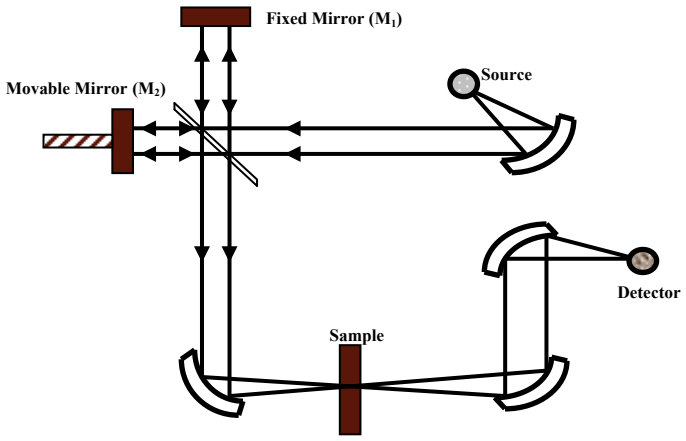

Figure 2.4. Schematic diagram of a FTIR spectrometer

2.4.1 Theory of Interferometer operation

The interferometer requires two mirrors, an infrared light source, a detector, and a beam splitter as shown in figure 2.4. The beam splitter is the heart of the interferometer. Essentially a half-silvered mirror, the beam splitter reflects about half of an incident light beam while simultaneously transmitting the remaining half. One half of this split beam travels to the interferometer's moving

mirror while the other half travels to the interferometer's stationary mirror. The two mirrors reflect both beams back to the beam splitter where each of the two beams is again half reflected and half transmitted. Two output beams result one travels to the detector as the other travels to the source.

Note each output beam is composed half of the light that traveled from the moving mirror and half traveled from the stationary mirror. Also, the two output beams contain equivalent, but not necessarily identical information. This fact results from reflection-induced phase shifts at the beam splitter and subsequent interference. When the two beams return to the beam splitter, an interference pattern is generated. This pattern varies with the displacement of the moving mirror, that is, with the difference in path length in the two arms of the interferometer. The pattern, detected by the infrared detector as variations in the infrared energy level, ultimately yields spectral information. In the present work, the FTIR spectra have been recorded on JASCO FTIR (ModelFT/IR-5300) and NEXUS FTIR (from Thermo–Nicolet) spectrometers. The spectra are recorded in the wavenumber range 400–2000 cm^{-1} in the absorbance mode using KBr pellet method.

2.5 Mössbauer spectroscopy

Mössbauer spectroscopy is a method for measuring small shifts in nuclear energy levels with high precision. This method involves the 'recoilless' emission and absorption of gamma rays and utilizes the Doppler effect in order to use these gamma rays as a sensitive probe. The Mössbauer effect was discovered in 1958 by R. L. Mössbauer **[2]**. He showed that nuclear radiation can be emitted and absorbed recoilless if the atoms are in a solid state environment.

The Mössbauer spectrometer basically consists of a radioactive source, a drive to provide the relative Doppler velocity between the source and absorber (the material under investigation), a detector which counts the gamma radiation (in the transmission geometry) or the conversion electrons (in the backscattering geometry) and needful electronics for precise control and data acquisition.

The objective behind carrying out the Mössbauer experiments lies in its ability to probe shifts and splitting of the nuclear energy levels because of its exceptionally high intrinsic resolving power (10^{-10} to 10^{-14}) when compared with the other spectroscopic techniques. The information is extracted by writing the total Hamiltonian as a sum of a Hamiltonian H_o exclusively for the atom and three more terms known as hyperfine interactions: E_0 which refers to Coulombic interactions between the nucleus and electrons, M_1 for magnetic interactions between the nuclear magnetic moment and the internal field at the nuclear site created by the atomic electrons, and E_2 for the electric quadrupole

interactions between the quadrupole moment of the nucleus and the electric field gradient created by the atomic electrons. Other higher order terms are neglected **[3–5]**.

2.5.1 Isomer shift

In the process of γ-transition, the size of the nuclear volume alters which gives rise to the change in the nucleus–electron interaction energy. This change depends on the chemical environment that is the total surrounding electron charge density of the probed nucleus of the absorber. As this energy cannot be measured directly, it is always compared to a suitable reference. Figure 2.5 illustrates isomer shift in Mössbauer spectroscopy.

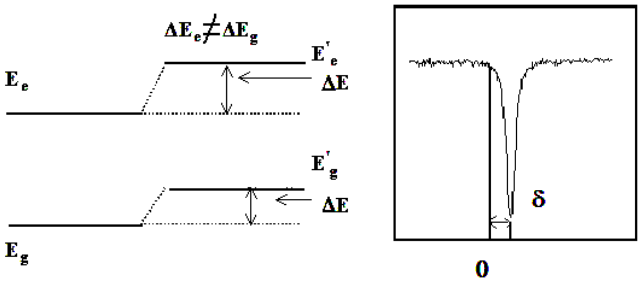

Figure 2.5. Illustrating Isomer shift in Mössbauer spectroscopy.

A simplified expression for the isomer shift, δ is written as a product of nuclear term (practically constant for a given transition) and a chemical term:

$$\delta = \text{constant} \square \{|\psi_s(0)_A|^2 - |\psi_s(0)_B|^2\} \qquad (2.2)$$

where A and B stand for the absorber and source and $|\psi_s(0)|^2$ is the *s*-electron density at the nucleus including the indirect effect of *p*, *d*, and *f* electrons on the s electron density. The isomer shift also gets affected with a change in temperature and pressure. The effect of pressure depends on the details of the electronic structure of the material.

2.5.2 Electric quadrupole interactions

If a nucleus has a spin quantum number $I > 1/2$, it has a non-spherical charge distribution given by

$$eQ = ! \rho r^2(3\cos^2\theta - 1)\, d\tau \qquad (2.3)$$

where *e* is the charge of proton, ρ is the charge density in a volume element $d\tau$, which is at a distance *r* from the center of the nucleus and making an angle θ to the nuclear spin quantization axis. The sign of *Q* depends upon the shape of the deformation, negative if oblate and positive if prolate along the spin axis. An asymmetric charge distribution around the nucleus causes an asymmetric electric field at the nucleus, characterized by the electric field gradient $J E$ **[6]**. There are two contributions to $J E$: lattice contributions from charges on distant ions, and valence contributions due to incompletely filled

electron shells. The electric quadrupole interaction between these two quantities gives rise to a splitting in the nuclear energy levels. ⅃ *E* does not work on the *I*=1/2 ground state, instead, it removes degeneracy in the excited state, splitting it into two sub states $m_I = \pm 1/2$ and $m_I = \pm 3/2$.

The energy lines now overlap with each other and give rise to a doublet in the Mössbauer spectrum. The separation between the energy levels is known as the quadrupole splitting and is given by

$$\Delta E_Q = e^2 qQ\sqrt{(1 + \eta^2/3)}/2 \qquad (2.4)$$

where $eq = d^2V/dz^2$ with V being the electrostatic potential,
$\eta = (d^2V/dx^2 - d^2V/dy^2)/(d^2V/dz^2)$, and Q is the magnitude of charge deformation. The electric quadrupole interaction provides useful information about bond properties, molecular and electronic structure.

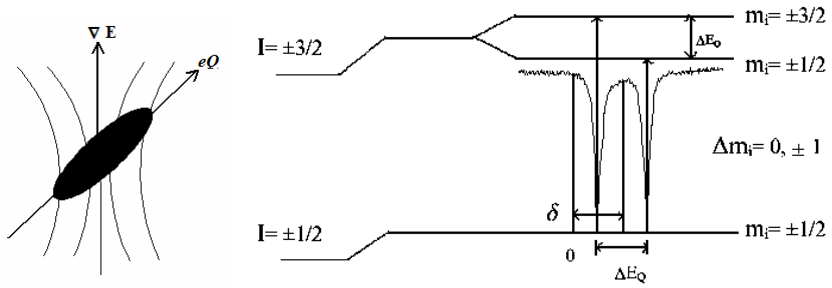

Figure 2.6. The diagram showing Electric quadrupole interactions.

2.5.3 Magnetic hyperfine interactions

If the nucleus of the probe atom in the absorber is in a magnetic field caused by the electrons of the atom, or by an externally applied field, then magnetic dipole interactions occur. The Hamiltonian can be written as

$$H = -\mu.H = -g\mu_N I.\, H \qquad (2.5)$$

where I is the nuclear spin, H is the total magnetic field, μ_N is the nuclear magneton, and g is the nuclear g factor. Since both of the nuclear energy levels of the 14.4-keV (in case of iron) transition have spin and associated magnetic moments, they experience hyperfine splitting caused by the interaction of the magnetic moment of the nucleus with the magnetic field. These new levels are the magnetic sub states of the energy levels, which are degenerate in the absence of a magnetic field, and this result in more possible nuclear transitions. The transitions that are allowed are determined by the quantum selection rule, which states that $\Delta m_I = 0, \pm 1$ as illustrated in figure 2.7.

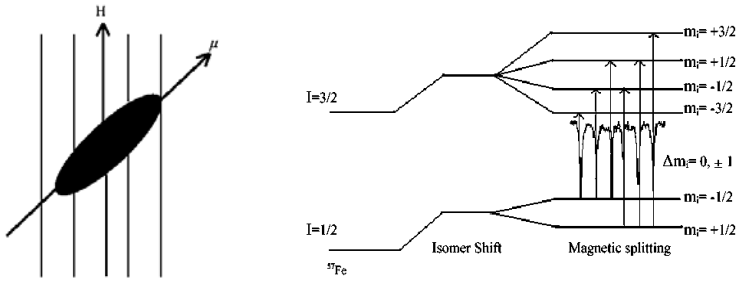

Figure 2.7. Magnetic hyperfine interactions.

2.5.4 Combined magnetic and quadrupole interactions

The magnetic and quadrupole interaction are direction dependent. If the asymmetry parameter $\eta = 0$ and H is along the principal z axis of the electric Field gradient tensor, then the Hamiltonian is diagonal in I_z. Then

$$E(I_z) = -g\mu_N H I_z + E_Q (I_z) \qquad (2.6)$$

If the electric field gradient is axially symmetric and its principal axis makes an angle θ with the magnetic axis and provided that $e^2qQ \square \mu H$ then the eigen values are

$$E_Q(I_z) = -g\mu_N H m_I + (-1)^{|m_I|+\frac{1}{2}}[(e^2qQ/4)\{(3\cos^2\theta - 1)/2\}] \qquad (2.7)$$

The separation of the outer lines in the HMF spectrum will be different from the inner lines **[5]**.

2.5.5 Mössbauer Spectrometer

Mössbauer spectra can be recorded most commonly in two ways: 1) Employing a single line source with an absorber having different hyperfine interactions generated nuclear energy level splitting or 2) Employing a single line absorber with source having nuclear energy level shift. In either of the two ways the nuclear energy level splitting have to be matched with the recoil free γ-ray energy to record the resonance spectra. One immediate and convenient way of matching these energies is to impart a Doppler velocity to the single line source or absorber and hence giving a first order energy shift (ΔE_γ) to the incident γ-ray energy (E_γ) equals to $\Delta E_\gamma = (v/c)\, E_\gamma$, where ν is the relative velocity between source and absorber. Depending on the variations of the Mössbauer natural line widths (FWHM) and energy level splitting. The range and precision of the Doppler velocities has to be selected. For example for the standard Mössbauer absorbers such as pure Fe (where Hyperfine Magnetic Field (HMF) ≈ 330 kOe at RT), Fe_2O_3 (HMF ≈ 515 kOe at RT), Fe_3O_4 (HMF ≈ 455 kOe at 495 kOe at RT), Sodium Nitropruside or stainless steel a velocity range of ±9, ±12, ±12, ±4 and ±2 respectively will be sufficient to record a spectra with good baseline and ^{57}Fe source. Some other ways of recording Mossbauer spectra and designs of spectrometer depending on specific application are summarized in.

In our laboratory the Mössbauer spectrometer is operated in the constant acceleration mode and it has the following four basic building blocks

1. Mössbauer source
2. Velocity drive and associated feedback systems
3. γ-Radiation detector system with associated electronics and
4. PC based Mössbauer data acquisition system.

a) Mössbauer Source:

The Mössbauer source was prepared by Du Pont Pharmaceuticals, USA by electrodepositing Co^{57} nuclei in 6μm thick Rhodium matrix and annealing at 1050^{o}C for 72 hours under hydrogen atmosphere. The source has been sprayed with an acrylic coating. The strength of the source was 25.9mCi (958.3MBq) with a half life of 270 days.

b) Velocity drive and feed back system:

The velocity drive unit was fabricated locally by Nucleonix (model MD575) following the design of Kankeleit. It is an electromechanical transducer and consists of a coil connected to a rod, carrying the source. This coil is made of phosphor-bronze. This coil carries the driving velocity signal and is the energizing coil. The coil and rod assembly moves in a magnetic field produced by two permanent magnets. Another phosphor-bronze coil, known as the pick-up coil is also connected rigidly to the rod, and the rod is held with the transducer at either end with springs.

The magnetic flux (φ) linked with the pick-up coil is given by $\varphi = \int_A nB.dA$, where n is the number of turns in the coil, B is the magnetic flux density and A is the area of the loop. When this coil moves in the magnetic field, then according to Lenz's law, an induced emf is produced which is proportional to the rate of change of flux (dφ/dt) linked with the coil. This induced emf is a replica of the driving waveform and this is fed to the error stage of the feedback and power amplifier where it is compared with the reference velocity waveform. The reference velocity waveform is triangular (constant accelaration) in shape and is obtained by integrating the square input to the Mössbauer drive unit. The feedback network adjusts to produce zero difference between the driving waveform and the reference waveform. Apart from triangular waveform the other form possible is saw-tooth wave to produce constant acceleration. The specific velocity range required for different absorbers is obtained by changing the amplitude of the velocity waveform.

c) γ-Radiation detection system and associated electronics:

A gas-filled proportional counter from LND.INC, USA was used as the Mossbauer γ-ray detector. The gas mixture used was 97% Xe +3% CO_2 at a pressure of 2 atmosphere with a Beryllium window 0.005" thick and having areal density 22.5 mg/cm^2. A high voltage unit produced the detector bias; model HV 211 from ECIL, India. A preamplifier with very high input impedance and low output impedance was used, which was acting as a buffer (impedance matcher) between the detector and the spectroscopy amplifier. This FET input charge sensitive preamplifier was made by EG & G, ORTEC, USA. Spectroscopy amplifier, model PA572 from ECIL-India, was used for amplifying and shaping the detector output pulses. The output pulses from the spectroscopy amplifier were fed to a single channel analyzer (SCA), model SC6048 from ECIL-India, and the TTL output pulses of the SCA were fed to the ADC card for counting purpose. The detector bias, which was fed through the preamplifier, was selected from the plateau region of the number of counts (pulses) from the detectors vs. applied voltage curve with the Mössbauer source directly facing the detector. The bias voltage was set between 2600–2700 volts. This high voltage is achieved by using an oscillator coupled step-up transformer – a voltage multiplier – in the output stage and a feedback system to maintain the oscillator current and hence secondary voltage.

Mössbauer spectra were recorded in transmission geometry with γ-rays, collimated using lead block. The radiations emitted from the Mössbauer source were 6.3 keV X-rays, 14.4 keV and 136 keV γ-rays. The high-resolution proportional counter was detecting all these three radiation and corresponding pulses were produced. However we were interested only in the 14.4 keV γ-rays. So for obvious reasons we had to block the pulses produced by other radiations to enter in to the counting system. This was achieved by setting the SCA input voltage gates appropriately. Before setting these gates we recorded the so-called pulse height spectrum (PHS) without putting any absorber between the source and the detector and by keeping the SCA in the 'WINDOW' mode, in which the difference between the upper and lower level voltages are fixed. The spectroscopy amplifier gain, pulse shaping time, base line restoration and polarity were properly set by observing the amplified detector pulses on the oscilloscope. Care was taken in choosing these parameters of the spectroscopy amplifier so that there were not many saturated output pulses. In the PHS we observed well-resolved two peaks (apart from the low voltage escape peak) in different voltage intervals proportional to the 6.3 and 14.4 keV incident radiations. The sum peak corresponding to the (6.3 keV + 14.4 keV) was also observed with low intensity. The SCA lower and upper voltage levels were set to the voltage values close to starting of 14.4 keV peak and ending of the sum peak respectively and it was put in the NORMAL mode (where pulses between the upper and lower level only were accepted and all other pulses were rejected). In this way 14.4 keV γ-rays pulses were chosen and hence the signal to noise was improved.

d) PC based Mössbauer data acquisition system

In designing the Mössbauer data acquisition system one need to use a multi channel analyzer (MCA) operating in the multi channel scaling (MCS) mode, the mode in which different channels are accessed at different time intervals. The time intervals correspond to the times during which the drive is moving with velocity 'v' to 'v+dv'. In implementing this operation it is convenient and cost effective to use a microprocessor based data acquisition system (MPDS) rather than a conventional MCA with involved hardware. What all one has to do is to open a memory bank (channels) to store the counts (standard pulses from the output of the SCA) in synchronization with the velocity of the drive. Different channels correspond to different velocities of the source and in turn different energies. Thus the counts vs. channel number data represent the Mössbauer spectrum. Standard samples (e.g. pure Fe) Mössbauer data are recorded to calibrate the channel numbers to velocities from the known separations of the Mössbauer lines in terms of velocity from other sources **[15]**. In principle we can increase the number of channels to have better resolution of velocity but not up to ad-infinitum as it may detoriate the spectrum quality due to even marginal non-linearity in the drive velocity waveform. Most commonly 256, 512, or 1024 channels are addressed.

Our design of the data acquisition system was based on the PCL208 High Performance Data Acquisition Card (or ADC card) of Dynalog Microsystems, India. The card was plugged into the expansion slot of a PC to implement MCS function of a MCA. The I/O card has an AD converter, an Intel 8254 programmable interval timer, and DA converter on board. The timer IC has three 16 bit down counters/timers. The counters were set to binary counting mode to enable them to count from 0 to 65535. The counter registers and the counters control register were configured to get the following counter operations. Counter 1 was internally coupled with a clock of frequency 1MHz and is used to generate the dwell time of 100 μ-seconds. We organized 1024 (512 + 512) channels for our spectrometer. To implement this, Counter 2 was set to down count by 1024 and give the current channel position by reading its contents on the fly to reduce the dead time in the MCS to the order of 0.5 μ-seconds. The third timer (Counter 0, internally coupled with 100 kHz clock) keeps track of the number of SCA TTL output pulses that come from the radiation detector. For the purpose of synchronization the square wave to drive the Mössbauer velocity drive is obtained by software checking the counter, which divides the dwell time by 1024. If there is a channel advances then the DAC is output with zero for a current timer value greater than 512 and FF for a value less than 512. The frequency of this square wave, fed to the Mössbauer drive unit, was 10 Hz.

Mössbauer spectra with good counting statistics (~0.5M counts/channel) were recorded. The spectrum recorded in the first 512 channels was the mirror image of the spectrum recorded in the next

512 channels. Therefore the spectra in these two halves were added by folding the overall spectrum with respect to the zero velocity channels in both the halves to increase the statistics of each spectrum (~1M counts/channel in the folded spectrum). SCA gates were set to get very good signal – to – noise ratio.

2.5.6 Mössbauer absorber preparation

There are various ways of preparing Mössbauer absorber. It can be in the form of a foil or in the form of powder – either compacted in the form of pellet or as it is. In our studies, absorbers were prepared by spreading the fine powder as uniformly as possible in the central hole (~9mm diameter) of a copper plate fixed on a cello tape; in this way the sample was also stuck to the cello tape. Another piece of cello tape was fixed from top so that there was no chance of the sample to fall and the copper plate with sample were firmly stuck to cello tape pieces from both sides. The amount of powder for the absorber was calculated so that the natural Fe contents in the absorbers were closed to 10 mg/cm^2, which is ideally required according to Margulies and Ehrman **[16]**. Hence we could safely assume no correction in the lines due to thickness broadening and that all our absorbers were with in the thin absorber limit.

2.6 Superconducting Quantum Interference Device (SQUID)

The sensitivity of a Josephson junction to an applied magnetic field increase with the area of the junction, which justifies making the devices arge so that the control currents can be reduced to a minimum. The switching speed of the junction, however, decreases as the area increases. In recent devices, the conflicting demands of speed and sensitivity are met by replacing a single junction with two or more junctions connected by a continuous superconducting loop. Such a multi-junction device is called a Josephson interferometer or a Superconducting Quantum Interference Device (SQUID). Using a SQUID, the minutest changes in magnetic fields can be measured with more sensitivity than with any other device.

2.6.1 Principle

In the case of two Josephson junctions, connected in parallel, as the magnetic flux Φ threading a superconducting loop is changed, the critical current of two junctions oscillates with a period equal to the flux quantum Φ_o. These oscillations are a result of the interference between the macroscopic wave functions at the two junctions. This phenomenon of "superconducting quantum interference" forms the basis of a SQUID.

2.6.2 Requirement

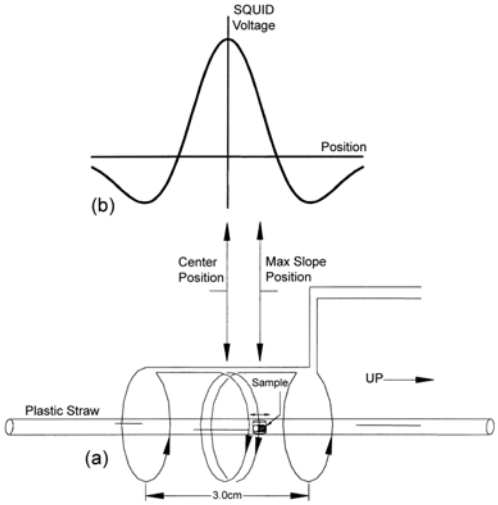

Figure 2.8. (a) Second-derivative coil-configuration and
(b) pick-up coil response as the sample is moved through the coils.

The I–V characteristics of a dc-SQUID must be non-hysteric which is ensured by adding an external shunt with a sufficiently low resistance. When the flux through SQUID is changed, the I–V characteristics oscillate between two extreme values. If the SQUID is biased with a constant current, the voltage across the SQUID becomes periodic in the applied flux.

2.6.3 Working of a SQUID

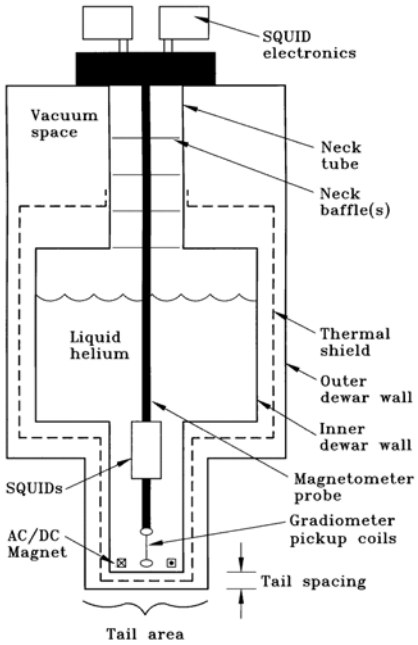

Figure 2.9. A cross sectional schematic of a simple low-Tc SQUID gradiometer system.

SQUID, a device which makes use of flux quantization and Josephson tunneling, is a flux-to-voltage transducer that converts a change in magnetic flux to a change in voltage which can be easily detected with conventional electronics. It can operate at temperatures below the superconducting transition temperature and is a magnetic-flux detector of incomparable sensitivity. A typical response curve for a SQUID magnetometer is shown in figure 2.8.

In practical SQUID measuring instruments, the flux through the SQUID loop is hold constant by means of a negative feedback with an additional coil. The strength of the feedback current necessary for this is then a measure of the magnetic flux to be measured. A particularly high sensitivity is achieved if a low frequency signal is superpose-moded on the feedback current, the low frequency voltage thereby caused is detected by a lock-in amplifier. With the help of superconducting flux transformers, one can also measure magnetic fields which do not lie at the location of the SQUID loop. With an optimally designed SQUID, such high sensitivities are possible that they correspond to an energy resolution of the magnetic field of about 1 x 10^{-33} Joules per Hertz of measured band width, which is about two times the Planck constant (h) **[8]**.

2.7 Electrochemical Characterization

The sample $LiFePO_4$ synthesized in our laboratory has been tested for its electrochemical activity and the details have been given elsewhere in this thesis.

References

1. Cullity, B. D., Elements of X-ray diffraction, 2nd Ed., Addison-Wesley Publishing Co., Inc. (1978).
2. Mössbauer, R. L., *Z. Physik*, **151**, 124 (1958).
3. Boyle, J. F., and Hall, H. E., *Reports on the progress of Physics*, p441- 524 (1962).
4. Greenwood, N. N., Gibb, T. C., *Mössbauer Spectroscopy*, Chapman and Hall, London (1971).
5. Gutlich, P., Link, R., Trautwein, A., *Mössbauer Spectroscopy and Transition Metal Chemistry*, Springer Verlag, Berlin (1978).
6. Stevens, J. G., and Stevens, V. E., (Eds.), Mössbauer Effect data index, Plenum Press, New York, (1966-1975).
7. Margulies, S., and Ehrman, J. R., Nuclear Instruments and Methods, **71**, p285 (1969).
8. Johann H Hunken, “Superconductor Electronics”

--- O ---

Chapter 3

Synthesis and Characterization of $LiFePO_4$

3.1 Synthesis of $LiFePO_4$

Whittingham et al prepared Olivine $LiFePO_4$ by hydrothermal synthesis **[1].** It has also been synthesized by hydrothermal synthesis **[2–4]**, solid state synthesis **[5, 6–14]**, sol-gel synthesis **[15–19]**, microwave processing **[20, 21]**, aqueous precipitation technique **[22]**, organogel synthesis **[23]**, emulsion drying synthesis **[24]** and ultrasonic spray pyrolysis **[25]**. In all the above methods, the precursor mixture is treated under Nitrogen, Argon or reducing atmosphere. Lithium iron phosphate has also been synthesized by Meng li etal **[26]** adopting the vacuum as environment for heating the starting materials.

Though $LiFePO_4$ has many advantages over the other lithium cathode materials from commercial point of view, one of the limitations is its low electronic conductivity, which directly influences the rate performance of the material **[6]**. The other two drawbacks in synthesis that limit high performance of $LiFePO_4$ are the formation of Fe^{3+} phase during the synthesis and the undesirable particle growth **[14].** While the former destabilizes the olivine structure during charge – discharge cycle, the latter leads to slow electronic transport in the cathode caused by fairly low electronic conductivity of the active cathode material. In this context, synthesizing nanoparticles of $LiFePO_4$ assumes considerable importance, to help ensure short diffusion length for its reaction with lithium. One way to increase the intrinsic electronic conductivity is through cation doping **[27]**. The other is synthesizing an electronic conductive phase of carbon coated sub-micron particles of $LiFePO_4$ **[14, 28–31]**.

In our laboratory, we have synthesized the nanoparticles of in-situ surface carbon coated $LiFePO_4$ using non-aqueous sol-gel route. The flowchart for the synthesis is given in figure 1. Initially Lithium acetate dihydrate (Loba chemicals), Ferrous oxalate dihydrate (Riedel-de Haën) and Ammonium dihydrogen phosphate (Merck) were taken in the stoichiometric ratio of Li:Fe:P = 1:1:1 and were thoroughly stirred in minimum amount of Ethylene Glycol (Ranbaxy, Mol.wt. = 62.07) to form a gel with the precursor materials mixed at the microscopic level. A certain amount (90mg) of the gel so obtained was transferred to an alumina crucible. Dynamic calcinations were carried out in the furnace of a thermo-gravimetric analysis (TG) device (NETZSCH STA 409 PC/PG). The precursor mixture was dynamically heated up to 1000^oC with a heating rate of 10^oCmin^{-1}.

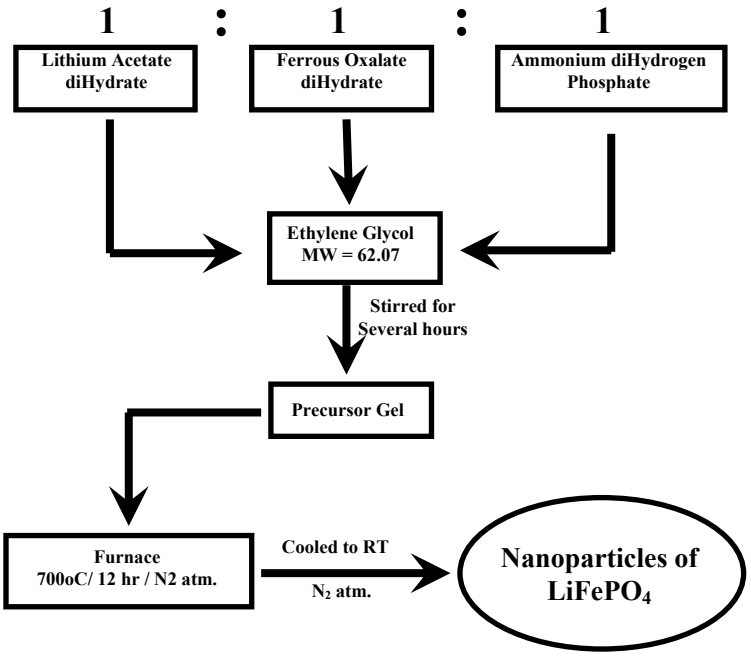

Figure 1. Flow chart of the Sol-gel synthesis route adopted for nanoparticles of $LiFePO_4$.

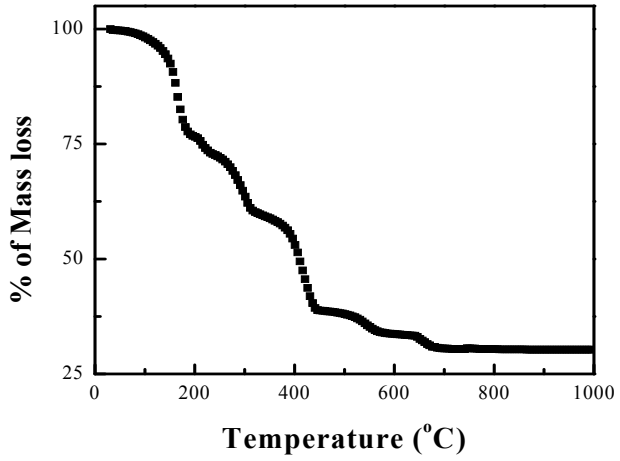

Figure 2. TG recorded on the precursor mixture of $LiFePO_4$ under N_2 atmosphere at a heating rate of 10°C/min.

Figure 2 shows the TG record on the precursor mixture of $LiFePO_4$, which hints us to heat the precursor mixture at around 700°C. To prevent the oxidation of the precursor, a continuous flow of nitrogen was maintained in the furnace during heating. Now the precursor gel taken in an alumina crucible is kept in a furnace and dry nitrogen gas flushed for 2 hours, followed by heat treatment at 700°C for 12 hours. The sample was cooled to room temperature under nitrogen atmosphere and ground thoroughly in dry air.

The selection of materials in our synthesis route differs from that of Jingsi Yang et al **[18]** due to the following reasons. Lithium acetate and ferrous oxalate were selected as starting materials (Fe^{2+} oxalate in particular) as they belong to a select group of materials employed in solid-state chemistry for thermally induced synthesis of various nanocrystalline metal oxides **[32–37]**. The selection of ammonium dihydrogen phosphate also ensures the availability of sufficient amount of $(PO_4)^{3-}$ ions required for the reaction. Besides the decomposition of lithium oxalate and ferrous oxalate (in particular) in dynamic nitrogen atmosphere allows full participation-in the reaction(s)- of the gaseous intermediates (CO, CO_2), yielding only Fe^{+2} ions at temperatures as high as above 535^{o}C, as reported by Martin et al **[38]**. Figure 2 represents the TG recorded on the precursor mixture in the temperature range from 30^{o}C to 1000^{o}C at 10^{o}C per minute. From this figure, it is clearly evident that ~ 700^{o}C, is the optimal temperature for the formation of monophasic $LiFePO_4$, The steps involved in this synthetic strategy are delineated in the mass losses suffered by the reactants. The mass lost at different stages due to heating the gel in the TG furnace could be ascribed to the following processes **[38]**:

1. Release of crystal water proceeding within the temperature range of 170 – 230^{o}C:

$$FeC_2O_4.\ 2H_2O \rightarrow FeC_2O_4 + 2H_2O$$

2. Thermal decomposition of ferrous oxalate to magnetite at temperature around 306^{o}C:

$$3FeC_2O_4 \rightarrow Fe_3O_4 + 4CO + 2CO_2$$

3. Reduction of ferrous oxalate by CO to Fe_3C at temperatures above 360^{o}C:

$$3FeC_2O_4 + 2CO \rightarrow Fe_3C + 7CO_2$$

4. Thermal conversion of Fe_3C at temperatures above 423^{o}C:

$$Fe_3C \rightarrow 3Fe + C$$

5. Thermally induced reduction of magnetite to FeO by CO above 550^{o}C:

$$Fe_3O_4 + CO \rightarrow 3FeO + CO_2$$

Upon heating the precursor mixture in a dynamic nitrogen atmosphere at elevated temperatures (above 600^{o}C), the decomposition of precursor mixture takes place releasing the Fe(+2) ions only. The continuous availability of the gaseous products (CO, CO_2) promotes the complete reductive decomposition of acetate and oxalate (iron oxalate in particular) and ensures the complete absence of Fe(+3) ions (or phases). It may be reasonably assumed that during the initial stage of heating, the decomposition of oxalates takes place slowly. At this stage of the synthesis, decomposed, undecomposed materials, and the gaseous products co-exist so that the release of Fe^{++} ions is dynamically controlled. This controlled release of Fe^{2+} ions would lead to their movement towards the already existing PO_4 tetrahedra to form FeO_6 octahedra and to enhance the formation of nucleation centers for the nanocrystalline growth. The Li^+ ions also released meanwhile go through the tunnels

formed by the interlocking of FeO_6 octahedra and PO_4 tetrahedra to form nanoparticles of phase pure $LiFePO_4$, as shown below.

$$Li^{+} + Fe^{+2} + (PO_4)^{-3} \rightarrow LiFePO_4$$

3.2 Characterization

3.2.1 Crystal structure

The sample was characterized by X-ray diffraction (XRD) using PHILLIPS X-ray diffractometer with Cu-K_α radiation (λ=1.54056Å). The diffraction patterns were recorded in the angle range (2θ) range 15^o-60^o with a step size of 0.02^o, as shown in figure 3.

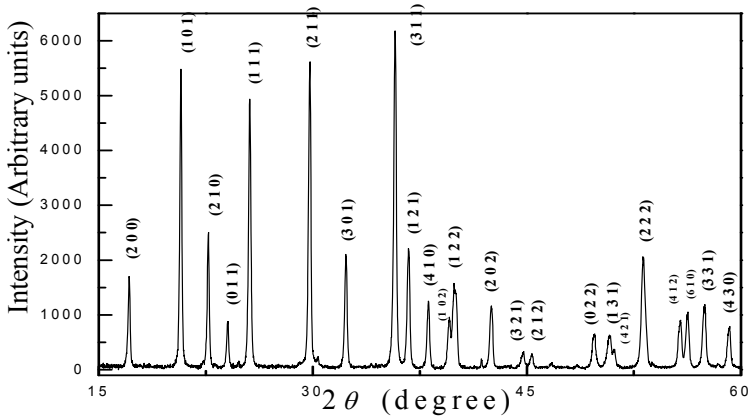

Figure 3. XRD pattern of the synthesized $LiFePO_4$ for 2θ values from 15^o-60^o, with identified hkl planes.

A careful comparison of the as recorded X-ray pattern with the JCPDS cards of the possible lithium iron phosphate permitted the identification of tryphilite $LiFePO_4$ with orthorhombic phase and space group *Pnma* **[39]**. A detailed crystallite-size analysis of the X-ray diffracted pattern using Scherrer formula **[40]**.

$$t = \frac{0.94\lambda}{B\cos\theta_B}$$

reveals that crystallites of $LiFePO_4$ with average sizes 45(5) nm are present. The calculated cell parameters obtained from *method of least squares* **[40]** for orthorhombic $LiFePO_4$ crystallites, a = 10.3427Å, b = 6.01814 Å, and c = 4.6972 Å, are in good agreement with previously reported values **[39]** thus validating our product.

3.2.2 Micro structure

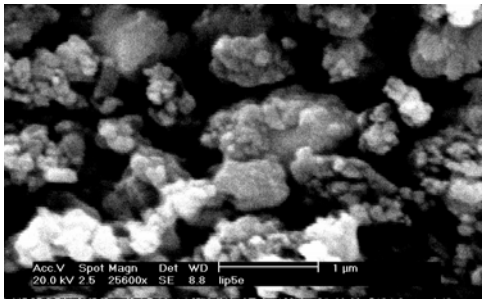

Figure 4. SEM image of $LiFePO_4$ powder.

To visualise the particle size distribution, $LiFePO_4$ powder under investigation was dispersed in acetone. A drop of it was taken on a stub, dried in air and sputtered with gold. This sample was subjected to a SEM examination to probe the distribution of particle size. Figure 4 shows SEM image of the gold sputtered $LiFePO_4$ powder. The picture exhibits particles with size distribution of 100-150 nm with few irregular growths.

3.2.3 Elemental Analysis

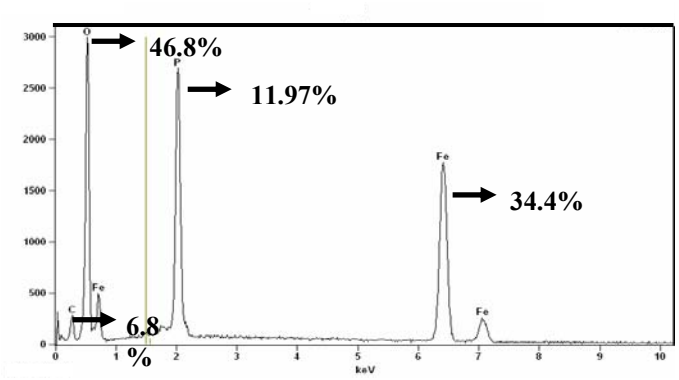

Figure 5. EDAX spectrum of $LiFePO_4$.

A pellet made of $LiFePO_4$ powder synthesized at 700^oC is subjected to EDAX (Hitachi series environmental SEM at an accelerating voltage of 20 kV mode) for chemical compositions of the sample (except for Lithium) and to evaluate the in-situ surface carbon coated over $LiFePO_4$. The EDAX spectrum recorded on a pellet of $LiFePO_4$ is shown in figure 5, which shows that approximately 6.8% carbon is present in the sample.

3.2.4 Local structure

The local molecular structural features and different vibrational modes of carbon-coated $LiFePO_4$ have been extensively studied by infrared spectroscopy **[41–44]**. To understand the location of phosphate group, the 2–3 mg of the $LiFePO_4$ sample was made into a pellet after mixing with few

milligrams (3–5) of potassium bromide (KBr) and infrared (IR) spectrum was recorded using JASCO FT/IR-5300 in the wave number range (υ) 2000 – 400 cm^{-1} in the absorption mode with a resolution of 4 cm^{-1}. Figure 6 shows the as-recorded FTIR spectrum of C-$LiFePO_4$.

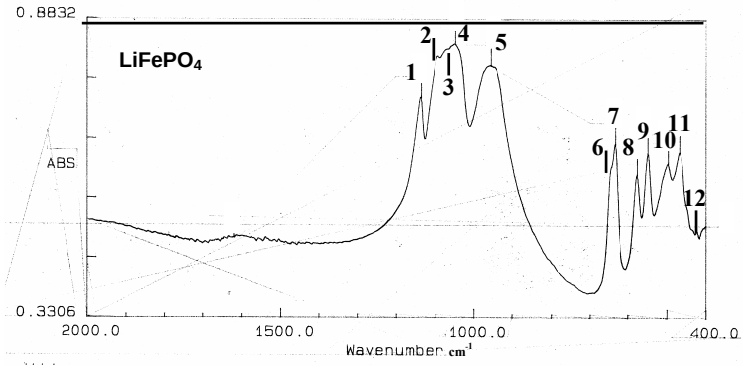

Figure 6. Infrared absorption spectrum of the in-situ carbon coated nano particles of $LiFePO_4$.

The vibrational motions in $LiFePO_4$ can be divided in to two classes that originate from the intramolecular vibrations of the PO_4^{3-} oxo-anion and the external optical modes of PO_4 **[44]**. While the earlier lie in the range of 1200-400 cm^{-1}, the latter is observed below 400cm^{-1} (not shown in the figure). The FTIR spectrum of $LiFePO_4$ sample in the low-wave number region (400–700cm^{-1}) involves bending modes and in the high-wave number region (700–1300cm^{-1}) involves stretching vibrations. In $LiFePO_4$, the FeO_6 and PO_4 are part of a 'train' a molecular ions train providing a framework for the structure. While bending modes (υ_2 & υ_4) are more susceptible to small structural changes–being less localized than stretching modes (υ_1 & υ_3), the latter modes show order–disorder transition in the form of variations in the bond lengths of the phosphate ion. The bending and stretching modes of phosphate ion in $LiFePO_4$ observed have been tabulated in table1.

In the low-wave number region, the bands 428cm^{-1}, 468cm^{-1}, 498cm^{-1}, 549cm^{-1}, 577cm^{-1}, 635cm^{-1} and 660cm^{-1} are observed due to active symmetric and asymmetric (ν_2–ν_4) bending modes of P–O bonds. The first four modes are due to mixed bending vibrations of symmetric and anti symmetric bending modes (υ_2+υ_4), while the remaining two modes i.e., 635cm^{-1} and 660cm^{-1} are due to the anti symmetric bending modes (υ_4). These low-frequency modes are thus particularly sensitive to the local environment and structure of the olivine lattice. In the high-wave number region, the band 957cm^{-1} is due to symmetric stretching mode (ν_1) and the bands observed at 1049cm^{-1}, 1064cm^{-1}, 1102cm^{-1}, and 1138cm^{-1} are assigned to the antisymetric stretching mode(ν3). The factor group splitting of asymmetric stretching vibrations (ν_3) for $LiFePO_4$ is $\Delta\nu_3$ = 89 cm^{-1}. The vibrations of the phosphate units are split into many components due to the correlation effect induced by the coupling

with of Fe–O units in the material. This rich spectrum thus gives the evidence that this sample is well crystallized.

Table 1: Observed FTIR bands in nanoparticles of C-$LiFePO_4$.

S. No.	Different modes (cm^{-1})	Assignment
1	1138	ν_3
2	1102	ν_3
3	1064	ν_3
4	1049	ν_3
5	957	ν_1
6	660	ν_4
7	635	ν_4
8	577	$\nu_4+\nu_2$
9	549	$\nu_4+\nu_2$
10	498	$\nu_4+\nu_2$
11	468	$\nu_4+\nu_2$
12	428	$\nu_4+\nu_2$

3.2.5 Phase Purity

It is a well known that any Fe^{3+} phase evolved during the synthesis of $LiFePO_4$ would destabilize the olivine structure during charge – discharge cycle **[8]**. Mössbauer spectroscopy was utilized to demonstrate this aspect of the material in discussion. The room temperature (RT) Mössbauer spectrum was recorded in transmission mode using ^{57}Co γ-ray source in a Rhodium matrix and multi-channel analyzer. The sample thickness was adjusted so that the Fe content was approximately 10 mg/cm^2. The calibrations for velocity and isomer shift were performed using iron (Fe) foil.

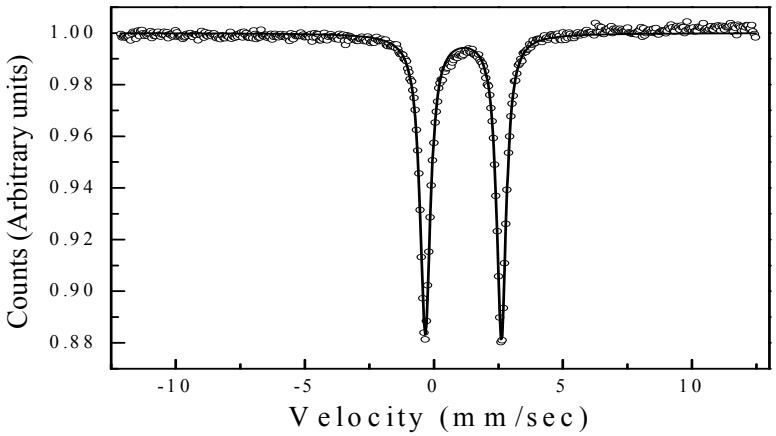

Figure 7. Room temperature Mössbauer spectrum of the $LiFePO_4$ sample (The circles show the experimental data and the black line shows Lorentzian fit).

The ^{57}Fe Mössbauer spectrum of the $LiFePO_4$ recorded at room temperature is shown in figure 7. The doublet is analysed by fitting to two Lorentzians. The spectrum reveals a symmetric doublet alone with isomer shift (IS) = 1.2468 mm/sec and quadrupole shift (QS) = 2.950(3) mm/sec. These values are typical for Fe^{2+} in ferrous compounds as they exhibit lower electron density due to *six* 3d electrons on Fe^{2+} as compared to Fe^{3+} with *five* 3d electrons. These values are in agreement with those reported in the literature **[45]**. Significantly, Fe^{3+} is conspicuous by its absence, which attests to the exclusively divalent nature of Fe in $LiFePO_4$. (Any incidence of Fe^{3+} would result in a weak, easily detectable and distinguishable,and closely spaced doublet located in between the very strong Fe^{2+} doublets, as was seen in the work of Prince et al **[45]**). At this stage it is pertinent to mention the very recent Mossbauer spectroscopic studies on orthorhombic $K_4MgFe_3(PO_4)_5$ with an intense closely spaced doublet- the unmistakable signature of Fe^{3+} **[46]**.

The very large QS (nearly five times greater than that of Fe^{3+}) value observed is due to high spin configuration of 3d electrons and the asymmetric local environment at the Fe in $LiFePO_4$ as explained by Yamada et al **[13]**. The IS and QS values are quite different from the IS = 0.435 mm/sec and QS = 0.68 mm/sec of Fe^{3+} in $FePO_4$ **[47]**. The obtained IS and QS values are also substantially different from those of Fe^{2+} in $FeC_2O_4.2H_2O$ (one of the precursors), given as 1.20 mm/sec and 1.72 mm/sec respectively. This clearly reveals the drastic change in the microscopic environment at Fe^{2+} in the synthesized $LiFePO_4$ relative to that of the iron oxalate precursor.

3.2.6 Conclusions

Sub-micron sized particles of $LiFePO_4$ with average crystallite size of 45(5) nm were prepared from oxalate precursors employing a non-aqueous sol-gel route. A uniform particle size distribution with grain size 100 – 150nm was observed using SEM with few irregular growths. The synthesis route that we have adopted has shown that the formation of Fe^{3+} impurities has been scrupulously avoided. This was confirmed by the presence of only a well-separated symmetric doublet characteristic of Fe^{+2} in the Mössbauer spectrum. The IS and QS values obtained from the symmetric doublet reveals the high spin configuration of 3d electrons and the asymmetric local environment at the Fe in phase-pure $LiFePO_4$. The observed FTIR spectrum was assigned to stretching and bending modes of the phosphate group.

References

1. Yang, S., Zavalij, P.Y., Whittingham, M. S., *Electrochemistry communications, **3** (2001) 505*.
2. Tucker, M. C., Doeff, M. M., Richardson, T. J., Fiñones, R., Reimer, J. A., and Cairns, E. J., *Electrochemistry and Solid State letters, **5(5)**, pA95, 2002*.
3. Yang, S., Song, Y., Zavalij, P. Y., and Whittingham M. S., *Electrochemistry Communications, **4(3)**, p239, 2002*.
4. Ellis, B., Kan, W. H., Makahnouk, W. R. M., and Nazar, L. F., *Journal of Material Chemistry, **17**, p3248, 2007*.
5. Padhi, A. K., Nanjundaswamy, K. S., and Goodenough, J. B., *Journal of Electrochemical Society, **144** (1997) p1188*.
6. Goñi, A., Bonagamba, T. J., Silva, M. A., Panepucci, H., Rojo, T. and Barberis, G. E., *Journal of Applied Physics, **84(1)**, p416, 1998*.
7. Prosini, P. P., Lisi, M., Zane, D., and Pasquali, M., *Solid State Ionics, **148**, p45, 2002*.
8. Prince, A. A. M., Mylswamy, S., Chan, T. S., Liu, R.S., Hannoyer, B., Jean, M., Shen, C.H., Huang, S. M., Lee, J. F., and Wang, G. X., *Solid State Communications, **132**, p455, 2004*.
9. Zhou, F., Kang, K., Maxisch, T., Ceder, G., and Morgan, D., *Solid State Communications, **132**, p181, 2004*.
10. Shi, Z., Liu, M., and Gole, J. L., *Electrochemistry and Solidstate letters, **3**, p316, 2000*.
11. Amine, K., Liu, J., and Belharouak, I., *Electrochemistry communications, 7, p669, 2005*.
12. Andersson, A. S., Kalska, B., Häggström, L., and Thomas, J. O., *Solid State Ionics, **130**, p41, 2000*.
13. Yamada, A., Chung, S. C., Hinokuma, K. J., *Journal of Electrochemical Society, **148(3)**, pA224, 2001*.
14. Zaghib, K., Ravet, N., Gauthier, M., Gendron, F., Mauger, A., Goodenough, J. B., and Julien, C. M., *Journal of Power sources, **163**, p560, 2006*.

15. Lerf, A., *Journal of Physics and Chemistry of Materials, **65**, p553, 2004*.
16. Sanchez, M. A. E., Brito, G. E. S., Fantini, M. C. A., Goya, G. F., and Matos, J. R., *Solid State Ionics, **177**, p497, 2006*.
17. Giorgetti, M., and Berrettoni, M., *Inorganic Chemistry, **45** (2006) p.2750*.
18. Yang, J., and Xu, J. J., *Electrochemical and Solidstate lettes, **7(12)**, pA515, 2004*.
19. Piana, M., Cushing, B. L., Goodenough, J. B., and Penazzi, N., *Solid State Ionics, **175**, p233, 2004*.
20. Higuchi, M., Katayama, K., Azuma, Y., Yukawa, M., Suhara, M., *Journal of Power Sources, **119-121**, p258, 2003*.
21. Park, K. S., Son, J. T., Chung, H. T., Kim, S. J., Lee, C. H., and Kim, H. G., *Electrochemistry communications, **5**, p839, 2003*.
22. Arnold, G., Hemmer, G. R., Ströbele, S., Vogler, C., and Wohlfahrt-Mehrens, M., *Journal of power sources, **119-121**, p247, 2003*.
23. Yang, S. T., Zhao, N. H., Dong, H. Y., Yang, J. X., and Yue, H. Y., *Electrochimica Acta, **51**, p166, 2005*.
24. Myung, S, -T., Komaba, S., Hirosaki, N., Yashiro, H., and Kumagai, N., *Electrochimica Acta, **49**, p4213, 2004*.
25. Teng, T, -H., Yang, M, -R., Wu, S, -H., and Chiang, Y, -P., *Solid State Communications, **142**, p389, 2007*.
26. Li, M., Xie, K., Li, D., and Pan, Y., *Journal of Materials Science, **40**, p2639, 2005*.
27. Chung, S. Y., Blocking, J. T., and Chiang, Y. M., *Nature Materilas, **1** (2002) p123*.
28. Huang, H., Yin, S. C., and Nazar, L. F., *Electrochemistry and Solid State letters. **4** (2001) pA170*.
29. Croce, F., Epifanio, A. D., Hassoun, J., Deptuia, A., Olczac, T., and Scros, B., *Electrochemistry and Solid state letters, **5** (2002) pA47*.
30. Chen, Z., and Dahn, J. R., *Journal of Electrochemical Society, **149** (2002) pA1184*.
31. Yamada, A., Hosoya, M., Chung, S. C., Kudo, Y., Hinokuma, K., Liu, K. -Y., and Nishi, Y., *Journal of Power sources, **119-121** (2003) p232*.
32. Cong, C. J., Liao, L., Li, J. C., Fan, L. X., and Zhang, K. L., *Nanotechnology, **16(6)** (2005) 981*.
33. Mendoza, M. E., Donado, F., Silva, R., Perez, M. A., and Carrillo, J. L., *Journal of Physics and Chemistry of Solids, **66(6)** (2005) 927*.
34. Zhang, K. F., Sun, X. Z., Lou, G. W., Liu, X., Li, H. L., and Su, Z. X., *Materials letters **59(22)** (2005) 2729*.
35. Drouet, C., and Alphonse, P., Journal *of Materials Chemistry, **12(10)** (2002) 3058*.

36. Li, X. S., Chen, L. Y., Xie, C. Y., Miao, Y. F., Li, D. M., and Xin, Q., *Thermochim. Acta,* ***260*** *(1995) 115*.
37. Dutta, P. K., Gallagher, P. K., and Twu, J., *Chemistry of Materials,* ***5(12)*** *(1993) 1739*.
38. Hermanek, M., Zboril, R., Mashlan, M., Machala, L., and Schneeweiss, O., *Journal of Materials Chemistry,* ***16*** *(2006) 1273*.
39. Yakubovich, O. V., Simonov, M. A., Belov, N. V., *Akad. Nauk. SSSR,* ***93*** *(1997) 235*. JCPDS (Joint committee on powder diffraction standards) XRD data base 83-2092 of PCPDFWIN version 2.02 May 1999, ©JCPDS-ICDD, 1999.
40. Cullity, B. D., *Elements of X-ray diffraction, Addisson-Wiley, Massachusetts (1978)*.
41. Zaghib, K., Ravet, N., Gauthier, M., Gendron, F., Mauger, A., Goodenough, J. B., and Julien, C. M., *Journal of power sources,* ***163*** *(2006) p560*.
42. Julien, C. M., Zaghib, K., Mauger, A., Massot, M., Ait-Salah, A., Selmane, M., and Gendron, F., *Journal of Applied Physics,* ***100****, p063511, 2006.*
43. Lemos, V., Guerini, S., Filho, J. M., Lala, S. M., Montoro, L. A., and Rosolen, J. M., *Solid State Ionics,* ***177*** *(2006) p1021*.
44. Ravet, N., Gauthier, M., Zaghib, K., Goodenough, J. B., Mauger, A., Gendron, F., and Julien, C. M., *Chemistry of Materials,* ***19*** *(2007) p.2595*.
45. Prince, A. A. M., Mylswamy, S., Chan, T. S., Liu, R. S., Hannoyer, B., Jean, M., Shen, C. H., Huang, S. M., Lee, J. F., and Wang, G. X., *Solid State Communications,* ***132*** *(2004) 455*.
46. Hidouri, M., Sendi, N., Wattiaux, A., Amara, M. B., *Journal of Physics and Chemistry of Solids,* ***69****, p2555 (2008)*.
47. Champion, A. R., Vaughan, R. W., and Drickamer, H. G., *Journal of Chemical Physics,* ***47*** ***(8)*** *(1967) 2583*.

--- O ---

Chapter 4

(1-x)$Fe^{2+}PO_4$:(x)$LiFePO_4$ System

4.1 Introduction

A previous X-ray diffraction (XRD) and Mössbauer spectroscopy study **[1]** of $LiFePO_4$ in an electrochemical cell clearly showed that $LiFePO_4$ and $FePO_4$ coexist as two-phase (1-x)$LiFePO_4$**:**(x)$FePO_4$ at various stages of lithium extraction (charge) and/or insertion (discharge). This two-phase nature of this system is believed to be a fundamentally important property in relation to its electrochemical performance as a Li-ion battery cathode. Therefore it is essential to gain a measure of this fundamental understanding of the $LiFePO_4$ system at fully charged state (x = 0) and fully discharged state (x = 1), respectively. Recently, Yamada et al. **[2]** suggested that Li_xFePO_4 is a mixture of $Li_{0.05}FePO_4$ and $Li_{0.89}FePO_4$. At temperatures around 350^oC, a new disordered phase appears, having the same olivine structure but with lattice parameters intermediate between those of heterosite and tryphilite **[3]**. Lithium atoms are distributed uniformly in this new solid solution phase at high temperatures. This Li_xFePO_4 solid solution is referred to as disordered, since it forms only at high temperatures, where entropy plays a major role in phase stability. This seems consistent with a random mixture of lithium throughout the $FePO_4$ structure. Dodd et al **[4]** have studied the transformation of the two-phase mixture, x $LiFePO_4$ plus (1-x)$FePO_4$, to the single phase Li_xFePO_4 for several compositions (x), and the results are summarized in the form of a phase diagram of Li_xFePO_4 showing temperatures where the mixing-unmixing transition occurs at different lithium concentrations.

Theoretical and experimental work has been done to understand the electronic structure and phase transitions in $LiFePO_4$ during lithium insertion and extraction. The charge compensation and phase separation in the electrochemical lithiation reaction are generally attributed to the reduction of Fe^{3+} to Fe^{2+} **[5–7]**. It has been suggested that the phosphate polyanion lowers the Fermi level and hence raises the cell potential and maintains a stable structural framework through strong P–O covalent bonds **[6–10]**. In all the previously mentioned literature, a *top to bottom* study has been done in the sense the starting material considered is $LiFePO_4$, and a successive removal has been done to get Li_xFePO_4. Our previous study **[11]** showed that **a** progressive evolution of olivine structure occurs by the gradual interlock of FeO_6 octahedra and PO_4 tetrahedra with Li concentration by introducing lithium in to Li_xFePO_4 ($0.0 \leq x \leq 1.0$). A fairly abrupt phase transformation from monoclinic $Fe_3(PO_4)_2$ to orthorhombic $LiFePO_4$ shows up for x~0.2 accompanied by structural disorder which gets stabilized at $x \approx 0.35$. A systematic study of X-ray diffractograms shows nanocrystal nucleation and growth from an unstable low symmetry crystalline phase with considerable disorder. Here we present a *bottom to top* systematic study of Li_xFePO_4 ($0.00 \leq x \leq 1.00$) and the phase transition from

monoclinic ferrous phosphate to orthorhombic liFePO_4 using X-ray diffraction, Infrared spectroscopy and Mössbauer spectroscopy.

4.2 Synthesis

Stoichiometric amounts of Lithium acetate dihydrate, Ferrous oxalate dihydrate and Ammonium dihydrogen phosphate were mixed in minimum amount of Ethylene glycol and samples of Li_xFePO_4 (x = 0.00, 0.25, 0.50, 0.75 and 1.00) were synthesized by non-aqueous sol-gel synthesis as was explained in chapter 2. The samples were examined by X-ray diffraction for characterization of the crystal structure, Infrared spectroscopy to observe the variation in the local structure, and Mössbauer spectroscopy to explore the valence and symmetry changes at the Fe site as x is progressively increased from 0.00 to 1.00.

4.3 Structural details of $Fe_3(PO_4)_2$:

When x = 0.00, the synthesized product is purely ferrous phosphate, which will be described in the next section. As the Fe sites are different from those in $LiFePO_4$, it would be instructive to look at the crystal structure of ferrous phosphate. Ferrous phosphate is isotypic **[12]** with graftonite. The two isolated phosphate tetrhedra are fairly regular with average bond lengths of 1.534 Å for P(1) and 1.535 Å for P(2) and an average bond angle of 109.3^o. Ferrous phosphate contains three distinct iron-oxygen polyhedra. Fe(2) and Fe(3) are irregularly coordinated by five oxygen atoms while Fe(1) has six nearest oxygen atoms in the shape of a highly distorted octahedron. The Fe(1) site in $Fe_3(PO_4)_2$ is generated by removing the seventh oxygen from the pentagonal basal plane to a distance of 3.12 Å in $Fe_3(PO_4)_2$. The second longest M(1)–O bond in graftonite is to O(7) at 2.58Å which is the oxygen in question in $Fe_3(PO_4)_2$. A coordination number of 5 for Fe(1) gives a bond strength sum of 1.84; going to coordination number 6 raises it to 1.95, while a coordination number of 5 for Fe(2) and Fe(3) gives bond strength sums of 1.98 and 1.97 respectively. Using six-coordination for Fe(1) gives an average Fe^{2+} - oxygen distance of 2.23 Å as compared to an average distance of 2.13 and 2.10 Å for five-coordinated Fe(2) and Fe(3), respectively. This assignment of coordination (6:5:5) results in each oxygen being bonded to one phosphorus and two iron atoms.

4.4 Structural characterization by XRD:

All the samples Li_xFePO_4 were characterized by X-ray diffraction using PHILLIPS X-ray diffractometer with Cu-K_α radiation (1.54056Å). The diffraction patterns were recorded in the angle (2θ) range 20^o – 60^o with a step size of 0.02^o. Figure1 shows the as recorded X-ray diffractograms of Li_xFePO_4 (x = 0.00 to 1.00). A comparison of the as recorded X-ray diffractograms with the JCPDS cards of the possible combinations of Li, Fe, P and O permitted the identification of tryphilite

$LiFePO_4$ with orthorhombic phase and space group Pnma **[13]** for the sample with x = 1, while $Fe_3(PO_4)_2$ with monoclinic phase and space group $P2_{1/c}$ (14) **[14]** could be assigned for the sample with x = 0. And both the phases have been observed for intermediate compositions of Li_xFePO_4 for which x = 0.25, 0.50 and 0.75. A phase transformation from monoclinic $Fe_3(PO_4)_2$ to orthorhombic $LiFePO_4$ was indeed observed as x varies from 0 to 1.

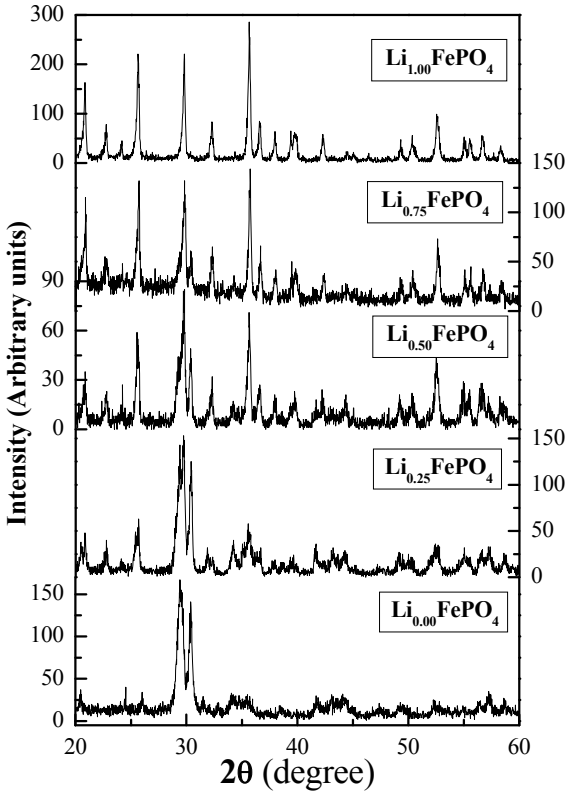

Figure 1. As-recorded X-ray diffractograms of $Na_xLi_{1-x}FePO_4$ (x = 0.00 to 1.00).

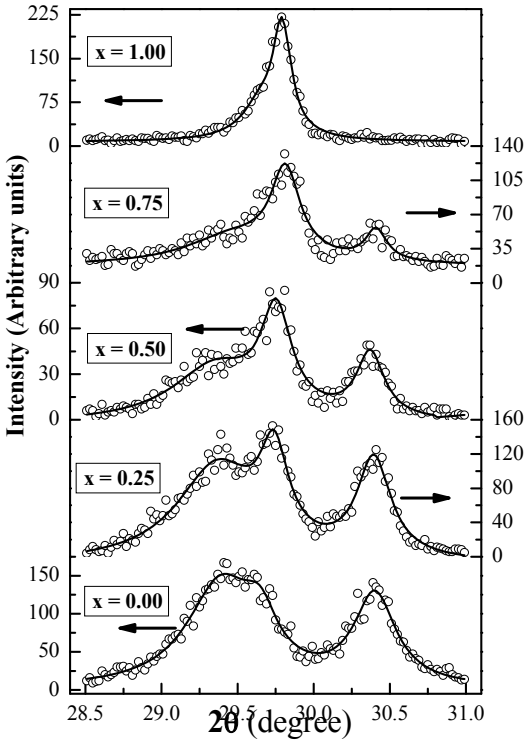

Figure 2. X-ray diffractograms of Li_xFePO_4 (x = 0.00 to 1.00) and the respective non-linear least square fits in the angle (2θ) range 28.5^o – 31^o.

Fig. 2, 3 shows the X-ray diffractograms of Li_xFePO_4 (x = 0.00 to 1.00) and the corresponding non-linear least square fits in the angle (2θ) range 28.5^o–31^o, and 33^o–38.7^o respectively. The phase transformation from monoclinic $Fe_3(PO_4)_2$ to orthorhombic $LiFePO_4$ observed is delineated as follows. The peak with maximum intensity at the scattering angle 30.42^o (2θ) in $Fe_3(PO_4)_2$ diminishes with the variation of 'x' from 0.00 to 1.00, while a new peak develops with the increase in 'x' and it attains maximum intensity at 2θ = 35.65^o (for x = 1), in $LiFePO_4$. And for 0.00 ‹ x ‹ 1.00, there exists a two-phase system of (1-x)$Fe_3(PO_4)_2$: (x)$LiFePO_4$. This two-phase system contains the reflections from both the monoclinic and orthorhombic phases. The observed values of '2θ' and lattice parameter 'd' obtained from the X-ray diffractograms of Li_xFePO_4, for all x (= 0 to 1) are processed by 'method of least squares' **[15]** to prove that all the reflections are from either orthorhombic $LiFePO_4$ phase or monoclinic $Fe_3(PO_4)_2$. The calculated values of '2θ' and 'd', are compared with the observed values and found to be in good agreement with the literature **[13, 14]**.

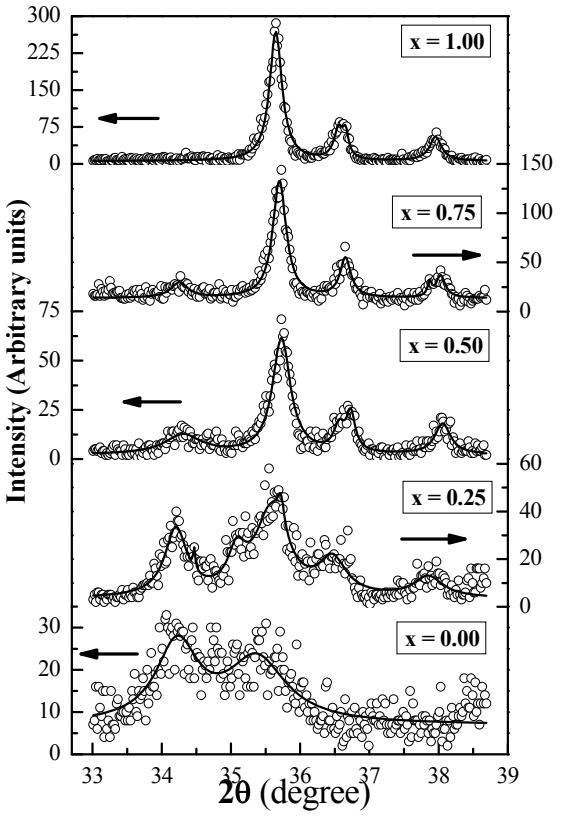

Figure 3. X-ray diffractograms of Li_xFePO_4 (x = 0.00 to 1.00) and the respective non-linear least square fits in the angle (2θ) range 33^o – 38.7^o.

Table 1: The calculated unit cell parameters of Li_xFePO_4 (x = 0 to 1).

S. No.	'x' in Li_xFePO_4	Calculated cell parameters for $Fe_3(PO_4)_2$ phase			Calculated cell parameters for $LiFePO_4$ phase			Volume of the Unit cell (nm^3)	
		a (Å)	b(Å)	c (Å)	a (Å)	b(Å)	c (Å)	Mono-clinic	Ortho-rhombic
1	0.00	8.0184	11.1788	7.0287	–	–	–	0.6217	–
2	0.25	8.2607	11.1100	7.0248	10.3133	6.0098	4.6982	0.6361	0.2912
3	0.50	8.1357	11.1526	7.0263	10.2929	5.9784	4.6732	0.6375	0.2876
4	0.75	8.1820	11.1841	7.0245	10.3117	5.9927	4.6830	0.6482	0.2894
5	1.00	–	–	–	10.3154	5.9966	4.6858	–	0.2899

The values of 'Δ2θ' and 'Δd' are also calculated and found to be with in the experimental limits. All the values of $2\theta_{obs}$, $2\theta_{cal}$, d_{obs}, d_{cal}, Δ2θ and Δd for all Li_xFePO_4 ($0 \leq x \leq 1$) are tabulated and are given in an appendix. The calculated cell parameters obtained from 'method of least squares' for all the samples under discussion are given in table1. The average crystallite size calculated using Scherrer's formula **[15]** for Li_xFePO_4 are 19(10), 26(13), 34(22), 34(23), and 39(16) nm for x = 0.00, 0.25, 0.50, 0.75 and 1.00 respectively.

4.5 Vibrational spectroscopy of Li_xFePO_4 System:

It is already established from the analysis of XRD data on Li_xFePO_4 that as 'x' is varied from '0 to 1' in Li_xFePO_4, a structural phase transition has been observed from monoclinic $Fe_3(PO_4)_2$ to orthorhombic $LiFePO_4$. And it is known that the IR modes observed for tetrahedral phosphate ion are effected by it's presence in different environments like pure compounds, solution, solid solution, glasses etc. **[16]**. With this background, it **is** expected that the local (molecular) structure of $LiFePO_4$ changes with the changes in the presence (amount) and/or absence of Lithium during charging and discharging (An in-situ measurement of IR bands during charging and discharging would of course give better results). To understand these variations in the surroundings around phosphate ion ideally, Li_xFePO_4 with x = 0 to 1, have been synthesized. The as recorded FTIR absorption spectrum of Li_xFePO_4 from x = 0.00 to x = 0.75 are shown **in** the appendix. The observed bands are tabulated in table 2 and a comparison is made with the FTIR spectrum of $LiFePO_4$. And the corresponding observed pattern is shown in figure 4.

4.5.1 High-frequency region (700–1300cm^{-1}):

In the PO_4^{3-} antisymmetric stretching region of $LiFePO_4$, the sharp and strong band at 1138 cm^{-1} (ν_3) also appears in $Li_{0.25}FePO_4$, $Li_{0.50}FePO_4$ and $Li_{0.75}FePO_4$ and disappears in $Li_{0.00}FePO_4$, which clearly indicates the formation of orthorhombic phase of $LiFePO_4$ with the presence of lithium as low as 25%.

The presence or absence of Li^+ ions in Fe^{2+}phosphate structure resulted in dramatic changes in ν_3 and ν_1 modes of stretching vibrations of $LiFePO_4$. In the PO_4^{3-} antisymmetric stretching region of $LiFePO_4$, the sharp but weak bands at 1049 cm^{-1} and 1102 cm^{-1} (both ν_3 modes) move to low frequency side in $Li_{0.50}FePO_4$ and $Li_{0.75}FePO_4$ and disappear in $Li_{0.00}FePO_4$ and $Li_{0.25}FePO_4$. In the PO_4^{3-} antisymmetric stretching region of $LiFePO_4$, the sharp but weak band at 1064 cm^{-1} (ν_3) appears in $Li_{0.25}FePO_4$, $Li_{0.50}FePO_4$ and $Li_{0.75}FePO_4$ and absent in $Li_{0.00}FePO_4$, which clearly indicates the formation of orthorhombic phase of $LiFePO_4$ with the presence of lithium as low as 25%.

Table 2: Observed FTIR bands in nanoparticles of C-Li_xFePO_4.

S. No.	x = 0.00	x = 0.25	x = 0.50	x = 0.75	x = 1.00	Assign-ment
1	—	1136	1135	1140	1138	ν_3
2	—	—	1095	1098	1102	ν_3
3	1084	1066	1064	1064	1064	ν_3
4	—	—	1035	—	1049	ν_3
5	958	968	950	962	957	ν_1
6	720	712	710	705	—	—
7	—	—	—	660	660	ν_4
8	615	627	635	635	635	ν_4
9	577	581	577	577	577	$\nu_4+\nu_2$
10	548	548	547	547	549	$\nu_4+\nu_2$
11	528	528	526	—	—	—
12	—	—	498	500	497	$\nu_4+\nu_2$
13	—	465	465	467	468	$\nu_4+\nu_2$
14	428	428	428	428	428	$\nu_4+\nu_2$

In the high frequency region, the band at 957 cm^{-1} (ν_1) corresponding to symmetric stretching mode is present in all Li_xFePO_4 (x = 0 to 1) compositions, which shows that this mode is independent of the crystal structure and could arise in IR spectra by the mere presence of phosphate ion. The band at 720 cm^{-1} in $Li_{0.00}FePO_4$ slowly moves to lower frequencies with reducing intensity as 'x' varies from 0.0 to 0.75 and disappears in $Li_{1.00}FePO_4$. This band cannot arise from the $LiFePO_4$ internal vibrations. Also this band cannot be attributed to the asymmetric 'ν_{as}' stretching mode of P−O−P bridges of $LiFeP_2O_7$, as it should be observed at around 740 cm^{-1} **[17]**.

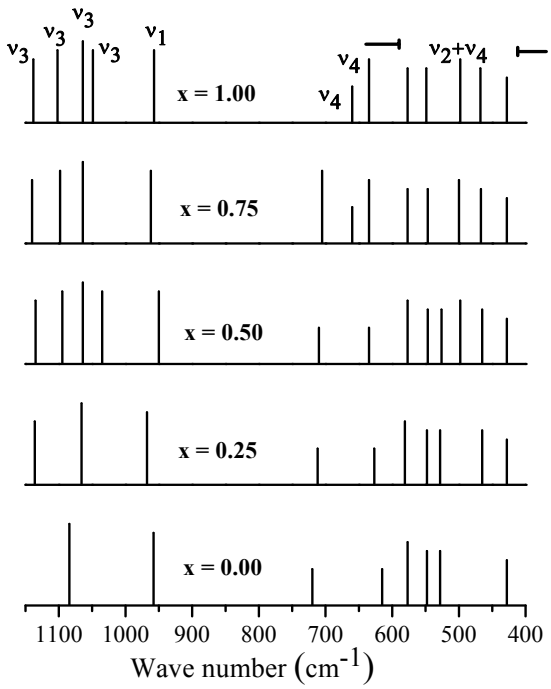

Figure 4. Observed pattern of FTIR bands in nanoparticles of C-Li_xFePO_4.

4.5.2 Low frequency region (400–700cm^{-1}):

In the low frequency region, assignment of the bands due to symmetric and antisymmetric bending modes of phosphate ion (ν_2 and ν_4) is rather difficult as they are strongly coupled **[16]**. The following conclusions are drawn for these modes for Li_xFePO_4.

One of the important modes that characterize the internal PO_4^{3-} bending modes of orthorhombic $LiFePO_4$ is the band observed at 660cm^{-1} (ν_4). It is also observed in $Li_{0.75}FePO_4$ but absent in all other Li_xFePO_4 (x = 0.00 to 0.50). The two other modes which are specific and only can be observed due to internal symmetric and antisymetric bending modes of phosphate ion in $LiFePO_4$ are the bands at 498 and 468 cm^{-1} (both $\nu_2 - \nu_4$ modes). It is evident from the table that these modes are absent in $Li_{0.00}FePO_4$, and thus not a characteristic band of the phosphate ion of ferrous phosphate. In the low frequency region, it has been found that a band observed at 528 cm^{-1} is the characteristic band for monoclinic ferrous phosphate and also observed for $Li_{0.25}FePO_4$ and $Li_{0.50}FePO_4$. The bands at 635 cm^{-1} (ν_4), 577 cm^{-1}, and 428 cm^{-1} (both $\nu_2 - \nu_4$ modes) characterize the internal bending modes of phosphate ion that exist in both monoclinic and orthorhombic crystal structures. The band observed at 635 cm^{-1} is constant up to x = 1.00 to 0.50 and decreases below x = 0.50.

4.5 Mössbauer spectroscopy of Li_xFePO_4:

As discussed in the previous chapter on $Na_xLi_{1-x}FePO_4$, during electrochemical lithiation and/or delithiation of $LiFePO_4$, changes at the Fe site takes place **[1]** and the high spin octahedral Fe^{2+} sites with high spin and low electron density in olivine $LiFePO_4$ change to Fe^{3+} with low spin and high electron density in heterosite $FePO_4$ (in completely charged state). This was observed as a doublet in Mossbauer spectra (with IS = 0.424 mm/sec and QS = 1.52mm/sec) developing in between the doublet obtained for Fe^{2+} of Olivine $LiFePO_4$ (with IS = 1.222 mm/sec and QS = 2.963mm/sec). Mid way between either charging (or discharging), a dynamical equilibrium exists with two phases $LiFePO_4$ and $FePO_4$. Thus, one may understand that the percentage of lithium present in Li_xFePO_4 affects the electric field gradient (EFG) at the Fe site.

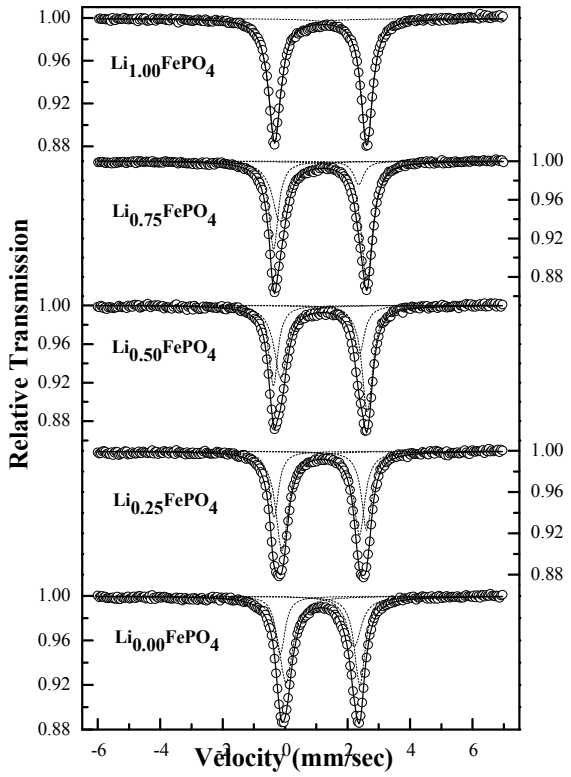

Figure 5. Room temperature Mössbauer spectra of Li_xFePO_4 (x = 0.00 to 1.00). The open circles show the raw data, the black line shows the non-linear least square fit of the spectrum and the dashed line show the lorentzians fit of the individual line of the spectra.

Table 3: The full width at half maximum (FWHM) values $\omega_1$and ω_2 of monoclinic and orthorhombic phases.

S. No.	'x' in Li_xFePO_4	FWHM of Fe site of orthorhombic phase		FWHM of Fe site of monoclinic phase	
		ω_1 (mm/sec)	ω_2 (mm/sec)	ω_3 (mm/sec)	ω_4 (mm/sec)
1	0.00	–	–	0.35826	0.41104
2	0.25	0.48111	0.41403	0.34056	0.39125
3	0.50	0.52221	0.39386	0.34542	0.41108
4	0.75	0.58475	0.38114	0.35036	0.44579
5	1.00	0.47628	0.43958	–	–

Table 4: The hyperfine parameters of monoclinic and orthorhombic phases.

S. No.	'x' in Li_xFePO_4	Hyperfine Parameters for Fe site of orthorhombic phase		Hyperfine Parameters for Fe site of monoclinic phase	
		IS δ (mm/sec)	QS Δ (mm/sec)	IS δ (mm/sec)	QS Δ (mm/sec)
1	0.00	–	–	1.2250	2.5485
2	0.25	1.2340	2.9666	1.2453	2.4812
3	0.50	1.2346	3.0085	1.2270	2.5142
4	0.75	1.2309	2.9861	1.2009	2.5230
5	1.00	1.2469	2.9469	–	–

Room temperature Mössbauer spectra of Li_xFePO_4 ($0.00 \leq x \leq 1.00$) are recorded in transmission mode using ^{57}Co γ-ray source in a Rhodium matrix and multi-channel analyzer. Figure 5 shows the Mössbauer spectra of Li_xFePO_4 (for x = 0.00, 0.25, 0.50, 0.75, and 1.00) plotted with velocity of the channel along the x-axis and relative transmission of the γ-rays through the sample along Y-axis. In the fig.1, the circles show the raw data, the thick black line shows the best non-linear least squares fit obtained after fitting the data to lorentzians and the dashed line shows the lorentzians fit of the individual line of the spectrum. The full width at half maximum (FWHM) values ω_1 and ω_2 of the two different Fe sites are tabulated in table 3 while the corresponding isomer shift (δ) and quadrupole splitting (Δ) of the doublets obtained for two different Fe sites in Li_xFePO_4 are given in table 4.

Initially, when x = 0.00, the sample is nothing but ferrous phosphate for which there are three different Fe sites. Out of them, two Fe sites are irregularly coordinated by five oxygen atoms in the form of a incomplete octahedra (irregularly coordinated by five oxygen atoms) while one Fe site has six nearest oxygen atoms in the shape of highly distorted octahedron. The Mössbauer spectrum of this sample could be fitted to a set of two quadrupoles. The hyperfine parameters obtained from the non-linear least square fit for the first quadrupole are given by δ = 1.225 mm/sec, Δ = 2.1847mm/sec (not given in table2), while for the second quadrupole δ = 1.225 mm/sec and Δ = 2.549 mm/sec. The isomer shift and quadrupole split for these two quadrupoles shows the Fe sites are occupied with high spin Fe^{2+} ions. The quadrupole splitting Δ = 2.1847mm/sec obtained for the first quadrupole strongly suggests it is due to the high spin Fe^{2+} located in a incomplete octahedra while the quadrupole splitting Δ = 2.5485mm/sec obtained for the second quadrupole shows it is due to the high spin Fe^{2+} located in a highly distorted octahedra. For the sample for which x = 1.00 (also $LiFePO_4$), the spectrum could be fitted to a doublet as explained in previous chapters, for which the isomer shift (δ) and quadrupole splitting (Δ) are given by δ = 1.2469mm/sec and Δ = 2.9469 mm/sec. These values are typical for highly distorted octahedrally coordinated high spin Fe^{2+}.

For all the samples for which $0.00 < x < 1.00$, the room temperature Mössbauer spectra could be fitted to a pair of doublets as done for the ferrous phosphate sample. The isomer shift (δ) and quadrupole splitting (Δ) obtained for these samples are given in table 2. The values of 'δ' and 'Δ' for these three samples show a demarcation from those of ferrous phosphate. These values show that these two doublets corresponds to highly distorted octahedrally bonded high spin Fe^{2+} environment. While the difference in quadrupole splitting for the two doublets may be ascribed to the difference in bond lengths of Fe–O and Fe–P due to the coexistence of monoclinic ferrous phosphate and orthorhombic $LiFePO_4$. It is important to note that for $0.00 < x < 1.00$, three different Fe sites are expected (Two different Fe sites of ferrous phosphate and one of $LiFePO_4$), which supposed to give rise to three different doublets. These results show that for $x \geq 0.25$, the doublet expected due to the high spin Fe^{2+} located in an incomplete octahedra, is absent. This reveals that as 'x' increases from 0.00, the incomplete octahedral Fe sites irregularly coordinated by five oxygen atoms in (typical for) ferrous phosphate are being bonded to another oxygen atom to attains octahedral environment and this octahedral bonding at Fe site is complete for x = 1.00, whose Mössbauer spectrum contains a single doublet, corresponding to highly distorted octahedral high spin Fe^{2+}. This reveals that as 'x' is increased from 0.00 to 1.00, a phase transition from monoclinic ferrous phosphate to orthorhombic $LiFePO_4$ has been observed.

4.7 Conclusions

The two-phase system (1-x)$Fe^{2+}PO_4$:(x)$LiFePO_4$ (0.00<x<1.00) is investigated through XRD, FTIR spectroscopy and Mossbauer spectroscopy in order to gain insight into the structural transitions in the olivine structure and This preliminary study has probably opened the door for a detailed structural investigation in future.

References:

1. Anderson A.S., Thomas J. O., Kalaska B., and Häggström L., *Electrochemistry and Solid State letters, **3**, p66 (2000)*.
2. Yamada, A., Koizumi, H., Nishimura, S. I., Sonoyama, N., Kanno, R., Yonemura, M., Nakamura, T., Kobayashi, Y., *Nature Materials, **5**, p357 (2006)*.
3. Delacourt, C., Poizot, P., Tarascon, J. M., Masquelier, C., *Nature Materials, **4**, p254 (2005)*.
4. Dodd, J. L., Yazami, R., and Fultz, B., *Electrochemical and Solid-State Letters, **9(3)**, pA151 (2006)*.
5. Burba, C. M., and Frech, R., *Journal of Electrochemical Society, **151(7)**, pA1032 (2004)*.
6. Zhou, F., Marianetti, C., Cococcioni, M., Morgan, D., Ceder, G., *Physical Review B, **69**, p201101 (2004)*.
7. Padhi, A. K., Nanjundaswamy, K. S., Masquelier, C., Okada, S., Goodenough, J. B., *Journal of Electrochemical Society, **144**, p1609 (1997)*.
8. Yamada, A., Chung, S. C., Hinikuma, K., *Journal of Electrochemical Society, **148**, pA224 (2001)*.
9. Padhi, A. K., Nanjundaswamy, K. S., Masquelier, C., Goodenough, J. B., *Journal of Electrochemical Society, **144**, p2581 (1997)*.
10. Masquelier, C., Padhi, A. K., Nanjundaswamy, K. S., Goodenough, J. B., *Journal of Solid State Chemistry, **135**, p228 (1998)*.
11. Sundarayya, Y., Kumaraswamy, K. C., Sunandana, C. S., *MRS proceedings, 1023-JJ03-06*.
12. Kostiner, E., and Rea, J. R., *Inorganic Chemistry, **13(12)**, 2876 (1974)*.
13. Yakubovich, O. V., Simonov, M. A., Belov, N. V., *Akad. Nauk. SSSR, **93** (1997) 235.* JCPDS (Joint committee on powder diffraction standards) XRD data base 83-2092 of PCPDFWIN version 2.02 May 1999, ©JCPDS-ICDD, 1999.
14. Warner, J. K., Cheetham, A. K., and Cox, D. E., *Journal of Applied Crystallography, **28**, p494 (1995)*. JCPDS (Joint committee on powder diffraction standards) XRD data base 83-0801 of PCPDFWIN version 2.02 May 1999, ©JCPDS-ICDD, 1999.
15. Cullity, B. D., *Elements of X-ray diffraction*, Addisson-Wiley, Massachusetts (1978).
16. Paques-Ledent, M.T., and Tarte, P., *Spectrochim. Acta A, 30 (1974) 673–689*.

17. Ravet, N., Gauthier, M., Zaghib, K., Goodenough, J. B., Mauger, A., Gendron, F., and Julien, C. M., *Chemistry of Materials, **19** (2007) p.2595*.

--- O ---

Chapter 5

$Na_xLi_{1-x}FePO_4$ – A two phase system

5.1 Introduction

The successful application of $LiFePO_4$ is hindered by its intrinsic low electronic and ionic conductivity **[1]**, because the electronic and ionic conductivity must be simultaneously large to maintain a fast electrochemical reaction as for high power batteries. Many studies have focused on improving its electrochemical performance via decreasing the particle size or improving electronic contact **[2-5]**. However, these efforts did not improve the intrinsic electronic conductivity of the material itself. One possible method is doping with high valance transition metal ions **[6]**. Shi et al **[7]** have reported that the electronic conductivity of Cr doped (at Li site) $LiFePO_4$ improved enormously, which could solve the problem of poor electronic conduction. However, the electrochemical performance of the high valance transition metal ion doped material was not improved as expected. The reason was that the doped high valance transition metal ions would block the one dimensional diffusion pathway of Li ions, resulting in lower ionic conductivity than the undoped compound **[8]**. An interesting alternative to solve this problem is to try doping isovalent metal ions such as Na at the Li site in $LiFePO_4$, hoping it would improve the electronic conductivity but not block the diffusion pathway in the same time. Ouyang et al **[9]** have shown that both pure and Na doped $LiFePO_4$ show semiconductor band structures, and the Na-doped material (band gap 0.66 eV) has narrower band width than that of the pure $LiFePO_4$ (band gap 0.93 eV), whether spin polarization is considered or not. This indicates that Na-doped material should have better electronic conductivity than pure $LiFePO_4$ material. The projected density of states (PDOS) shows that the states around Fermi level are mainly contributed by Fe 3d electrons. It means that the doped Na atom does not change the band gap directly, but it changes the band gap through an indirect effect on the electronic structure of Fe atoms.

Two phases of $NaFePO_4$ have been described in the literature. Yakubovich et al. **[10]** and Birdson et al. **[11]** used X-ray diffraction data to identify a phase of $NaFePO_4$ that is isostructural with the phospho-olivine mineral maricite (space group Pnma, D_{2h}^{16}) **[12]**. Though this phase of $NaFePO_4$ is a structural analogue of $LiFePO_4$, the two differ in many respects. This probably due to the larger ionic radius of Na^+ (102 pm) compared to Li^+ (76 pm). Additionally, the average Na-O bond length in $NaFePO_4$ (2.46 Å) is significantly longer than the Li-O bonds (2.14Å) in $LiFePO_4$, yet the average Fe-O (2.17 Å) and P-O bond lengths are nearly identical in the two compounds. In this regard it is very important to understand the structural changes of $Na_xLi_{1-x}FePO_4$ (as x tends from 0 to 1), the variation in the local structure at phosphate tetrahedra and to follow the changes that take place at the Fe site on an atomic scale.

5.2 Synthesis

Stoichiometric amounts of Lithium acetate dihydrate, Sodium acetate, Ferrous oxalate diHydrate and Ammonium dihydrogen phosphate were mixed in minimum amount of Ethylene glycol and samples of $Na_xLi_{1-x}FePO_4$ (x = 0.00, 0.25, 0.50, 0.75 and 1.00) were synthesized by non-aqueous sol-gel synthesis as explained in chapter 2. The samples are examined by X-ray diffraction for characterization of the crystal structure and lattice parameters, Infrared spectroscopy to observe the variation in the local molecular structure, and Mössbauer spectroscopy to understand the changes in electronic structure at/local environment around the Fe site.

5.3 Structural characterization by XRD:

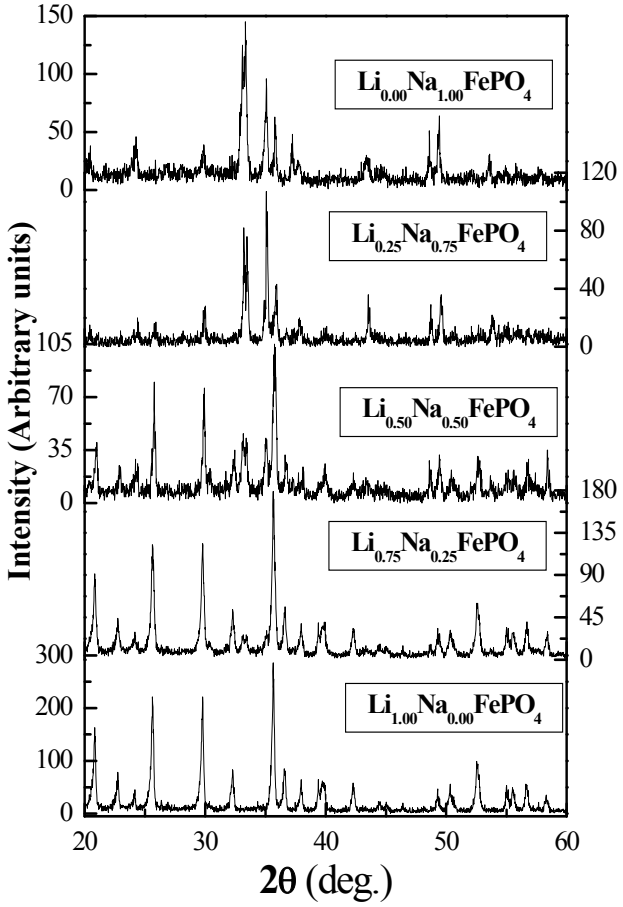

Figure 1. As-recorded X-ray diffractograms of $Na_xLi_{1-x}FePO_4$ (x = 0.00 to 1.00).

All the samples $Na_xLi_{1-x}FePO_4$ were characterized by X-ray diffraction using PHILLIPS X-ray diffractometer with Cu-K_α radiation (1.54056Å). The diffraction patterns were recorded in the angle (2θ) range 20^o – 60^o with a step size of 0.02^o. Figure 1 shows the as recorded X-ray

diffratograms of $Na_xLi_{1-x}FePO_4$ (x = 0.00 to 1.00). A comparison of the as recorded X-ray diffractograms with the JCPDS cards of the possible combinations of Li, Na, Fe, P and O permitted the identification of tryphilite $LiFePO_4$ with orthorhombic phase and space group P*nma* **[13]** for the sample with x = 0, while Maricite $NaFePO_4$ with orthorhombic phase and space group P*mnb* **[14]** for the sample with x = 1. And both the phases have been observed for samples of intermediate composition $Na_xLi_{1-x}FePO_4$ with x = 0.25, 0.50 and 0.75. A gradual phase transformation from orthorhombic $LiFePO_4$ to orthorhombic $NaFePO_4$ was observed as x varies from 0 to 1. Figure 2 shows the X-ray diffractograms of $Na_xLi_{1-x}FePO_4$ (x = 0.00 to 1.00) and the respective non-linear least square fits in the angle (2θ) range $31^o – 41^o$.

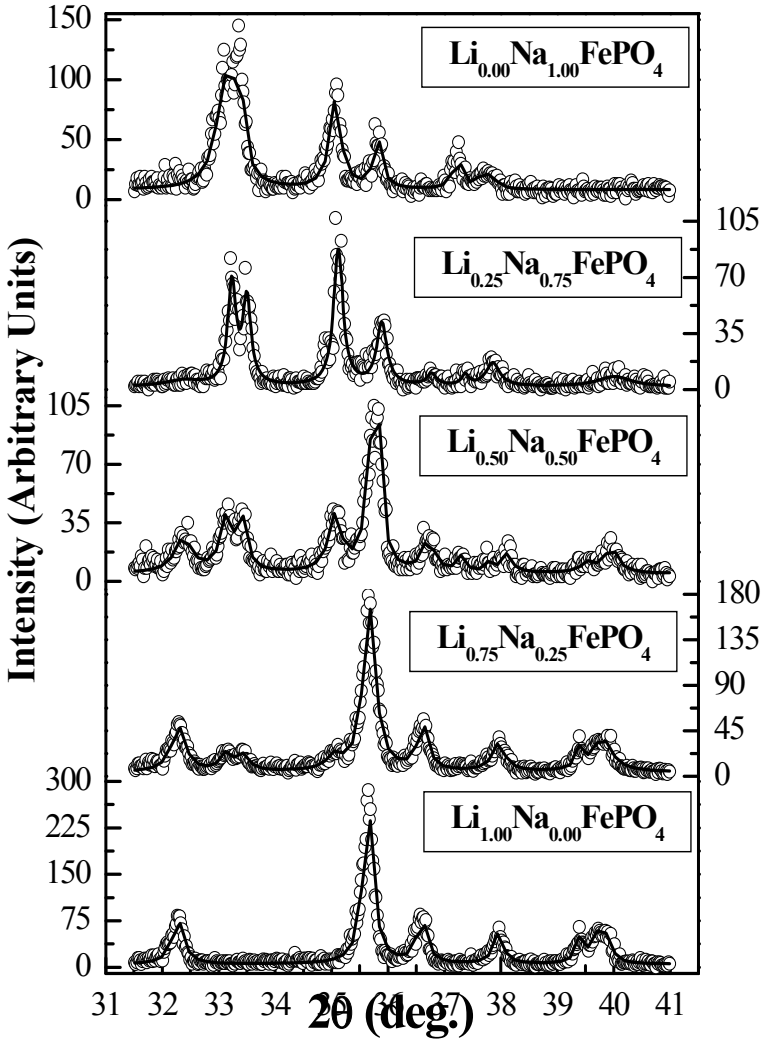

Figure 2. X-ray diffractograms of $Na_xLi_{1-x}FePO_4$ (x = 0.00 to 1.00) and the respective non-linear least square fits in the angle (2θ) range $31^o – 41^o$.

Table 1: The calculated unit cell parameters of $Na_xLi_{1-x}FePO_4$ (x = 0 to 1).

S. No.	Sample Na_xLi_{1-x}-$FePO_4$	Calculated cell parameters For $LiFePO_4$ phase			Calculated cell parameters For NaFePO4 phase			Volume of the Unit cell $(Å)^3$	
		a (Å)	b(Å)	c (Å)	a (Å)	b(Å)	c (Å)	LIP phase	NIP phase
1	x = 0	10.3154	5.9966	4.6858	–	–	–	289.85	–
2	x = 0.25	10.2941	5.9944	4.6893	6.8868	8.7747	5.0379	289.36	304.44
3	x = 0.50	10.2978	5.9716	4.6866	6.8078	8.9219	5.0121	288.20	304.43
4	x = 0.75	10.3374	5.9655	4.6632	6.8087	8.9997	4.9097	287.57	300.85
5	x = 1	–	–	–	6.8348	8.9332	5.0167	–	306.30

The phase transformation is identified by the scattering angle (2θ) of the peak with highest intensity as it shifts from 35.7° (for x = 0) to 33.4° (for x = 1). The observed values of '2θ' and 'd' obtained from the X-ray diffractograms of $Na_xLi_{1-x}FePO_4$, for all x (= 0 to 1) are processed by 'method of least squares' **[15]** to prove all the reflections are from either orthorhombic $LiFePO_4$ phase or orthorhombic $NaFePO_4$. The calculated values of '2θ' and 'd' are compared with the observed values and found to be in good agreement with the literature **[10, 11]**. The values of observed and calculated values of '2θ and d' with the assigned Miller indices for all the samples $Na_xLi_{1-}xFePO_4$ are tabulated. The calculated cell parameters obtained from 'method of least square' for all the samples in discussion are given in table1. The average crystallite size calculated using Scherrer's formula **[15]** for $Na_xLi_{1-x}FePO_4$ are 44(9) nm, 30(9) nm, 41(18) nm, 52(16) nm and 39(16) nm for x = 0.00, 0.25, 0.50, 0.75 and 1.00 respectively.

5.4 Vibrational spectroscopy of $Na_xLi_{1-x}FePO_4$:

To determine the effect of the bigger monovalent cation on the vibrational modes of the phosphor-olivine compounds, infrared spectroscopic measurements have been carried out at 300 K in the range from 2000 – 400 cm^{-1}. As discussed in the previous section, $NaFePO_4$ and $LiFePO_4$ are structurally analogous, and thus it is expected that the IR spectra of $Na_xLi_{1-x}FePO_4$ resemble one another. In these compounds, the degenerate internal modes of a phosphate anion may split whenever the symmetry of the electric crystal field is lower than the tetrahedral symmetry of the anion. Fortunately, the phosphate anions occupy 4(c) Wyckoff sites in $LiFePO_4$ and $NaFePO_4$. Hence, the selection rules for the internal modes of these compounds are identical.

The magnitude of the splitting of IR absorption peaks in a crystalline compound is controlled by specific interactions between the ions in the unit cell. Phosphate anions that interact strongly with neighboring cations will exhibit large factor group splitting effects **[16]**. Crystallographic data show that the Fe-O bond lengths are nearly identical in $LiFePO_4$ and $NaFePO_4$, but the Na-O bonds are longer than the Li-O bonds **[10, 11, and 17]**. Thus, difference in the factor group splitting of the internal modes may be primarily due to interactions between the monovalent cations and phosphate anions. Lithium ions have a relatively larger charge density and can form stronger bonds with the phosphate anions than sodium ions. Therefore, the Li^+ ions exert a stronger perturbation on the vibrational modes of the phosphate anions, which results in greater factor group splitting effects for $LiFePO_4$ compared to$NaFePO_4$.

5.4.1 High – frequency region:

In the high-frequency region, in which the symmetric and antisymmetric stretching modes are responsible for the observed bands, $NaFePO_4$ and $LiFePO_4$ are expected to show similar IR patterns as proposed by Paques-Ledent et al **[18]**. Due to the presence of less charge density in $NaFePO_4$ relative to $LiFePO_4$, a systematic change in factor group is expected in $Na_xLi_{1-x}FePO_4$ and the effect of substitution of sodium for lithium, is as follows.

The sharp band with strong intensity due to asymmetric stretching mode (ν_3) observed at 1138 cm^{-1} in $LiFePO_4$ becomes weaker in $Na_{0.25}Li_{0.75}FePO_4$ and merges with the next band at 1100 cm^{-1}. It was observed only as slope variation in the broad peak in the case of $Na_{0.50}Li_{0.50}FePO_4$ and $Na_{0.75}Li_{0.25}FePO_4$ but disappears completely in $NaFePO_4$.

The band at 1102 cm^{-1} observed as a distinct band in $LiFePO_4$ exists in all $Na_xLi_{1-x}FePO_4$ for all x lies between 1 and 0.25 but loses its identity and becomes a part in the broad peak formed with nearest bands.

The very weak but sharp band observed at 1064 cm^{-1} in $LiFePO_4$ becomes much stronger and broader as the partial substitution of sodium for lithium increases and this band takes the peak position of the broad band observed due to the merging of all other bands corresponding to asymmetric stretching modes (ν_3).

Table 2: Observed FTIR bands (cm^{-1}) in nanoparticles of C-$Na_xLi_{1-x}FePO_4$.

S. No.	x = 0.00	x = 0.25	x = 0.50	x = 0.75	x = 1.00	Assignment With respect to $LiFePO_4$
1	1138	1140	1130	1140	—	ν_3
2	1102	1094	1093	1098	1102	ν_3
3	1064	1060	1063	1063	1061	ν_3
4	1049	—	—	—	—	ν_3
5	—	1003	1011	1009	1007	ν_3
6	—	975	—	—	—	—
7	957	953	953	953	953	ν_1
8	—	—	—	—	840	—
9	—	741	—	—	—	—
10	—	—	—	—	700	—
11	660	655	—	—	—	ν_4
12	635	633	629	631	627	ν_4
13	—	—	590	588	586	—
14	577	577	577	577	577	$\nu_4+\nu_2$
15	549	554	556	556	556	$\nu_4+\nu_2$
16	498	502	—	—	—	$\nu_4+\nu_2$
17	468	467	467	469	467	$\nu_4+\nu_2$
18	428	421	421	420	420	$\nu_4+\nu_2$

While the band at 1049 cm^{-1} in $LiFePO_4$ is completely absent (or hides in the broad band) in all Na substituted compounds, the band at 1007 cm^{-1} in $NaFePO_4$ is observed in all $Na_xLi_{1-x}FePO_4$ compositions(except for x = 0.00). Thus these two bands are typical and can be used to differentiate between the asymmetric stretching modes in $LiFePO_4$ and $NaFePO_4$.

The band due to symmetric stretching vibration (ν_1) at 957 cm^{-1} is present in $Na_xLi_{1-x}FePO_4$ for all 'x' (from 0 to 1). A very weak but distinct band at 975 cm^{-1} observed in $Na_{0.25}Li_{0.75}FePO_4$ is again a marker showing it is observable when the content of Li is more than Na in $Na_xLi_{1-x}FePO_4$ (not shown as a separate peak as it has been merged with the band at 953 cm^{-1} in $LiFePO_4$). The factor group splitting of asymmetric stretching vibrations (ν_3) for $Na_xLi_{1-x}FePO_4$ is $\Delta\nu_3$ = 95, 131, 119, 137 and 89 cm^{-1} for x = 0.00, 0.25, 0.50, 0.75, and 1.00 respectively.

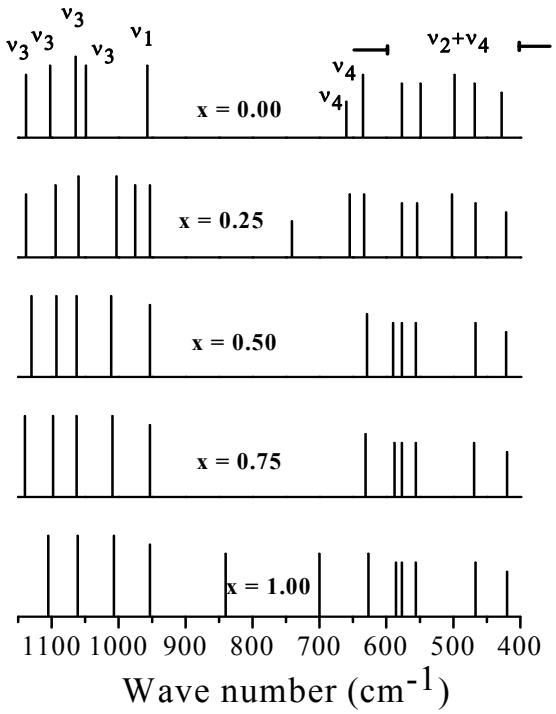

Figure 3. Observed pattern of FTIR bands in nanoparticles of C-$Na_xLi_{1-x}FePO_4$.

5.4.2 Low – frequency region (400–700cm^{-1}):

In low frequency region (400 – 700 cm^{-1}), the bands at 660 cm^{-1} and 635 cm^{-1} in $LiFePO_4$ are related to symmetric bending modes (ν_4). While the band at 660cm^{-1} in $LiFePO_4$ initially shifts to 655cm^{-1} in $Na_{0.25}Li_{0.75}FePO_4$ and then disappears in other $Na_xLi_{1-x}FePO_4$ (x = 0.50, 0.75, and 1.00), the band at 635cm^{-1} in $LiFePO_4$ shifts to lower frequencies (to a little extent) for $Na_xLi_{1-x}FePO_4$ for all x from 0.25 to 1.00. Further more; the relative intensities of the observed ν_4 bands in $Na_xLi_{1-x}FePO_4$ are nearly identical for all $0.0 < x < 1.0$.

Interestingly, the band at 498 cm^{-1} in the spectrum of $LiFePO_4$ is not recovered when Na is substituted for Li. And instead, there is only a weak feature near 500 cm^{-1} in $Na_{0.25}Li_{0.75}FePO_4$, which is completely absent in all other $Na_xLi_{1-x}FePO_4$ ($0.5 \leq x \leq 1.0$). The two bands at 577 cm^{-1} and 468 cm^{-1} are unaffected by the presence of either lithium or sodium showing that these two bands arise exclusively from the asymmetric bending modes of phosphate ion and could be the standard bending modes of $(PO_4)^{3-}$ whether the system is crystalline or an aqueous solution or a solid solution.

The asymmetric bending modes observed at 549 cm^{-1} and 428 cm^{-1} in $LiFePO_4$ varies to a very little as x changes from 0.0 to 1.0. While the band at 549 cm^{-1} shifts to higher frequencies, the band at 428 cm^{-1} shifts to lower frequencies. Interestingly the band observed at 586 cm^{-1} in $NaFePO_4$

shifts to higher frequencies (to a very less extent) and disappears in $Na_{0.25}Li_{0.75}FePO_4$ and $LiFePO_4$. This remarkable band differentiates $LiFePO_4$ from $NaFePO_4$.

As discussed above, the infrared spectrum of $LiFePO_4$ contains two broad bands centered at 498 and 468 cm^{-1} due to asymmetric bending modes. Previous research **[18, 19]** has shown that these two bands in $LiFePO_4$ contain a significant amount of lithium motion; the $^6Li/^7Li$ isotope effect was not large enough to confidently assign these bands solely as lithium cage modes. That is, the isotope effect could not completely rule out the possibility that the Li^+ ion translatory motions are mixed with phosphate bending modes (ν_2). Sodium ions have a larger mass than Li^+ ions so the Na^+ ion translatory modes are expected at much lower frequencies than the corresponding Li^+ ion translations. Thus Burba et al **[16]** have analyzed these modes to be lithium cage modes but not of the modes due to Li-ion translations and ν_4. Out of these two modes, the one at 468 cm^{-1} has also been observed for all values of x in $Na_xLi_{1-x}FePO_4$. Thus, we expect this mode may be due to Li-ion translation only.

5.5 Mössbauer spectroscopy of $Na_xLi_{1-x}FePO_4$:

It is known that during electrochemical lithiation and/or delithiation of $LiFePO_4$, local structural changes at the Fe site take place **[1]** and the high spin octahedral Fe^{2+} sites with high spin and low electron density in olivine $LiFePO_4$ change to Fe^{3+} with low spin and high electron density in heterosite $FePO_4$ (in completely charged state). These changes are most conveniently monitored by Fe^{57} Mossbauer spectroscopy. This presence of Fe^{3+} was observed as a doublet (with IS = 0.424 mm/sec and QS = 1.52mm/sec) developing in between the doublet obtained for Fe^{2+} of Olivine $LiFePO_4$ (with IS = 1.222 mm/sec and QS = 2.963mm/sec). Midway between charging (and discharging), a dynamical equilibrium exists with two phases $LiFePO_4$ and $FePO_4$. Thus, one may understand that the percentage of lithium present in $LiFePO_4$ affects the electron field gradient (EFG) at the Fe site. With this back ground, one may expect the changes at the Fe sites by the substitution of low monovalent metal Na for Li in $LiFePO_4$. This would hopefully give clues to the electronic structure of $LiFePO_4$ indirectly, particularly the environment at the Fe site.

Room temperature Mössbauer spectra of $Na_xLi_{1-x}FePO_4$ ($0 \leq x \leq 1$) are recorded in transmission mode using ^{57}Co γ-ray source in a Rhodium matrix and multi-channel analyzer. Figure 4 shows the Mössbauer spectra of $Na_xLi_{1-x}FePO_4$ (for x = 0.00, 0.25, 0.50, 0.75 and 1.00) plotted with velocity of the channel along the x-axis and relative transmission of the γ-rays through the sample along Y-axis. In the fig.4, the circles show the raw data, the thick black line shows the best non-linear least squares fit obtained after fitting the data to lorentzians and the dashed line shows the lorentzians fit of the individual line of the spectrum.

Initially, when x = 0.00 ($Na_xLi_{1-x}FePO_4$), the sample is nothing but lithium iron phosphate, in which Fe exists in the form of high spin Fe^{2+} in highly distorted octahedra FeO_6. The Mössbauer spectrum of this sample could be fitted to a pair of two lorentzians, as explained in previous chapters. The hyperfine parameters obtained from the non-linear least square fit for the first quadrupole are given by δ = 1.2469 mm/sec, Δ = 2.9499mm/sec. The isomer shift and quadrupole split for this quadrupole shows the Fe sites are occupied with high spin Fe^{2+} ions. For the sample for which x = 1.00 (also $NaFePO_4$), the spectrum could be fitted to a doublet, for which the isomer shift (δ) and quadrupole splitting (Δ) are given by δ = 1.2237 mm/sec and Δ = 2.2346 mm/sec. These values are also typical for highly distorted octahedrally coordinated high spin Fe^{2+}. The hyperfine parameters obtained from the non-linear least square fit for $Na_xLi_{1-x}FePO_4$ (0 < x < 1) are given in table 3. And the full width at half maximum (FWHM) values ω_1 and ω_2 of the two different Fe sites are tabulated in table 4.

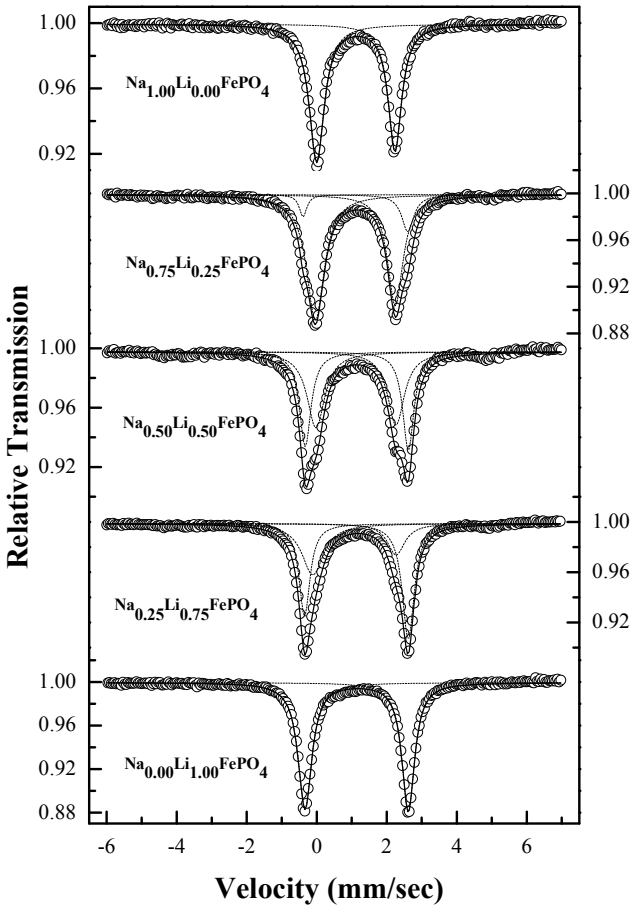

Figure 4. Room temperature Mössbauer spectra of $Na_xLi_{1-x}FePO4$ (x = 0.00 to 1.00). The open circles show the raw data, the black line shows the non-linear least square fit of the spectrum and the dashed line show the lorentzians fit of the individual line of the spectra.

Table 3: The hyperfine parameters for the two phase system $Na_xLi_{1-x}FePO_4$.

S. No.	'x' in $Na_xLi_{1-x}FePO_4$	Hyperfine Parameters for Fe site of $LiFePO_4$ phase		Hyperfine Parameters for Fe site of $NaFePO_4$ phase	
		IS δ (mm/sec)	QS Δ (mm/sec)	IS Δ (mm/sec)	QS Δ (mm/sec)
1	0.00	1.2469	2.9499	–	–
2	0.25	1.2394	2.9635	1.1842	2.3806
3	0.50	1.2498	2.9456	1.2270	2.2847
4	0.75	1.2106	2.9845	1.2090	2.2817
5	1.00	–	–	1.2237	2.2346

Table 4: The full width at half maximum (FWHM) values $\omega_1$and ω_2 of two phase system $Na_xLi_{1-x}FePO_4$.

S. No.	'x' in $Na_xLi_{1-x}FePO_4$	FWHM of Fe site of $LiFePO_4$ phase		FWHM of Fe site of $NaFePO_4$ phase	
		ω_1 (mm/sec)	ω_2 (mm/sec)	ω_3 (mm/sec)	ω_4 (mm/sec)
1	0.00	0.4763	0.4396	–	–
2	0.25	0.3746	0.4167	0.7444	0.6011
3	0.50	0.4007	0.3882	0.6097	0.5831
4	0.75	0.2521	0.4139	0.6158	0.5424
5	1.00	–	–	0.5194	0.4694

Existence of two-phase system:

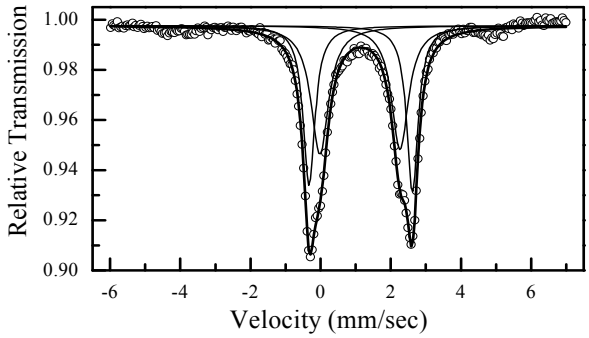

Figure 5. Room temperature Mössbauer spectrum of $Na_{0.50}Li_{0.50}FePO_4$.

As is evident from XRD and IR of $Na_xLi_{1-x}FePO_4$, there exists a two phase region (x)$NaFePO_4$:(1-x) $LiFePO_4$ for $0 \leq x \leq 1$. Figure 5 shows the Mössbauer spectrum recorded of

$Na_{0.50}Li_{0.50}FePO_4$ at room temperature, with a non-linear least square fit of the two quadruples. Out of two, while the outer quadrupole doublet is fitted with a pair of lorentzians, the inner quadruple is fitted with another pair of lorentzians. The FWHM of the outer doublet are found to be $\omega_{outer\ 1}$ = 0.40074 mm/sec and $\omega_{outer\ 2}$ = 0.38818 mm/sec, and for the inner doublet these values are given by $\omega_{inner\ 1}$ = 0.60973 mm/sec and $\omega_{inner\ 2}$ = 0.58311 mm/sec, show these two doublets are asymmetric doublets. The isomer shift (IS) and quadruple splitting (QS) for outer doublet are given by IS_{outer} = 1.2496 mm/sec and 2.9456 mm/sec respectively, while for inner doublet these values are IS_{inner} = 1.2270 mm/sec and QS_{inner} = 2.2847 mm/sec. The IS and QS values of the outer and inner doublets thus obtained correspond to the IS and QS values of $LiFePO_4$ and $NaFePO_4$ respectively, as shown in table1.Thus, this spectrum shows very clearly that a two phase system of $LiFePO_4$ and $NaFePO_4$ exists in this sample. A two phase system exists even for x = 0.25 and 0.75, which was observed with a line broadening relative to the parent systems.

5.6 Conclusions

The two-phase system $Na_xLi_{1-x}FePO_4$ ($0.00<x<1.00$) is investigated through XRD, FTIR spectroscopy and Mossbauer spectroscopy in order to gain insight into the alkali site occupancy in the olivine structure and the role of Na on the electronic properties of $LiFePO_4$. This preliminary study has probably opened the door for a detailed structural investigation in future.

References

1. Anderson A.S., Thomas J. O., Kalaska B., and Häggström L., *Electrochemistry and Solid State letters, **3**, p66 (2000)*.
2. Franger S., Cras F., Bourbon C., and Rouault H., *Electrochemistry and Solid State letters, **5**, pA231 (2002)*.
3. Parka K. S., Son J. T., Chung H. T., Kim S. J., Lee C. H., Kang K. T., and Kim H. G., *Sold State Communications, **129**, p311 (2004)*.
4. Yamada A., Chung S. C., and Hinokuma K., *Journal of Electrochemical Society, **148**, pA224 (2001)*.
5. Huang H., Yin S. C., Nazar F., *Electrochemistry and Solid State letters, **4**, pA170 (2001)*.
6. Chung S. Y., Bloking J., and Chiang Y. M., *Nature Materials, **1**, p123 (2002)*.
7. Shi S. Q., Liu L. J., Ouyang C. Y., Wang D. S., Wang Z. X., Chen L. Q., and Huang X. J., *Physical Review B, **69**, p104303 (2004)*.
8. Ouyang C. Y., Shi S. Q., Wang Z. X., Li, H., Huang X. J., and Chen L.Q., *Journal of Physics: Condensed Matter, **16**, p2265 (2004)*.

9. Ouyang, C. Y., Wang, D. Y., Shi, S. Q., Wang, Z. X., Li H., Huang X. J., and Chen L.Q., *Chinese Physics Letters,* ***23(1)****, p61 (2006)*.
10. O.V. Yakubovich, E.L. Belokoneva, V.G. Tsirel'son, V.S. Urusov, Vestn. *Mosk. Univ. Ser. 4: Geol. 6 (1992) 54–65*.
11. J.N. Birdson, S.E. Quinlan, P.R. Tremaine, *Chemistry of Materials,* ***10*** *(1998) p763–768*.
12. Y. Le Page, G. Donnay, *Can. Mineral.* ***15*** *(1977) p518–521*.
13. Yakubovich, O. V., Simonov, M. A., Belov, N. V., *Akad. Nauk. SSSR,* ***93*** *(1997) 235*. JCPDS (Joint committee on powder diffraction standards) XRD data base 83-2092 of PCPDFWIN version 2.02 May 1999, ©JCPDS-ICDD, 1999.
14. Struman, B., Mandarino, J., and Corlett, M., *Can. Mineral., 15 (1977) 396*. JCPDS (Joint committee on powder diffraction standards) XRD data base 29 – 1216 of PCPDFWIN version 2.02 May 1999, ©JCPDS-ICDD, 1999.
15. B. D. Cullity, *Elements of X-ray diffraction, Addisson-Wiley, Massachusetts (1978)*.
16. Christopher M. Burba., Roger Frech, *Spectrochimica Acta A,* ***65*** *(2006) 44-50*.
17. A.S. Andersson, B. Kalska, L. H¨aggstr¨om, J.O. Thomas, *Solid State Ionics* ***130*** *(2000) 41–52*.
18. M.T. Paques-Ledent, P. Tarte, *Spectrochim. Acta A,* ***30*** *(1974) 673–689*.
19. C. M. Burba, R. Frech, *Journal of Electrochemical Society,* ***151*** *(2004) A1032-A1038*.

--- O ---

Chapter 6

Phospho-Vanadate ($LiFe(VO_4)_x(PO_4)_{1-x}$)System

6.1 Introduction

In phospho-olivines, ($LiFe(VO_4)_x(PO_4)_{1-x}$) in particular, four oxygens are strongly covalent bonded to P^{+5} forming the $(PO_4)^{3-}$ tetrahedral poly anion and consequently difficult to extract. The DSC trace of the fully charged state with electrolyte as shown by Yamada et al **[1]** is consistent with this expectation. The total, gradual heat evolution detected over a wide temperature range of 250 – 360^{o}C is only 147 J/gm, while much larger and more abrupt heat evolution with significant oxygen loss is observed at lower temperatures in charged $LiNiO_2$, $LiCoO_2$ and $LiMn_2O_4$ **[2]**. This guarantees safety against combustion and adds greatly to the attractiveness of $LiFePO_4$ as a cathode. The extremely stable nature of the olivine structure will produce batteries with high tolerance to unusual conditions. Here we present an attempt made to disturb and destructure the close network formed due to FeO_6 octahedra and PO_4 tetrahedra.

6.2 Synthesis

Stoichiometric amounts of Lithium acetate dihydrate, Ferrous oxalate dihydrate, Ammonium dihydrogen phosphate and Ammonium mono vanadate were mixed in minimum amount of Ethylene glycol and samples of $LiFe(VO_4)_x(PO_4)_{1-x}$ (x = 0.00, 0.05, 0.10, 0.20, 0.30 and 0.50) were synthesized by non-aqueous sol-gel synthesis as was explained in chapter 3. The samples were examined by X-ray diffraction for characterization of the crystal structure, Infrared spectroscopy to observe the variation in the local structure, and Mössbauer spectroscopy to examine whether or not valence/coordination changes occur at the Fe site.

6.3 Structural characterization by XRD

All the samples $LiFe(VO_4)_x(PO_4)_{1-x}$ (x = 0.00, 0.05, 0.10, 0.20, 0.30 and 0.50) were characterized by X-ray diffraction using PHILLIPS X-ray diffractometer with Cu-K_α radiation (1.54056Å). The diffraction patterns were recorded in the angle (2θ) range 20^o–60^o with a step size of 0.02^o. Fig.1 shows the as recorded X-ray diffractograms of $LiFe(VO_4)_x(PO_4)_{1-x}$ (x = 0.00 to 0.50). As discussed in the previous chapters, the identification of tryphilite $LiFePO_4$ with orthorhombic phase and space group Pnma has been done for the sample for which x = 0.00. Fig.2 shows the X-ray diffractograms of $LiFe(VO_4)_x(PO_4)_{1-x}$ (x = 0.00 to 0.50) in the scattering angle (2θ) range 20^o–41^o . The circles in the figure show the raw data and the line shows the non-linear least square fit of lorentzians obtained. The observed values of '2θ' and lattice parameter 'd' obtained from the X-ray diffractograms of $LiFe(VO_4)_x(PO_4)_{1-x}$, for all x (= 0.00 to 0.50) are processed by the 'method of least squares' **[3]**, the calculated values of '2θ' and 'd' thus obtained, are compared with the observed

values and found to be in good agreement with the literature **[4]**. The values for 'Δ2θ' and 'Δd' are also calculated, found to be with in the experimental limits and all the values of $2\theta_{obs}$, $2\theta_{cal}$, d_{obs}, d_{cal}, Δ2θ and Δd for all $LiFe(VO)_4(PO_4)_{1-x}$ ($0 \leq x \leq 0.50$) are tabulated and are given in an appendix. The calculated cell parameters obtained from 'method of least squares' for all the samples in discussion are given in table 1.

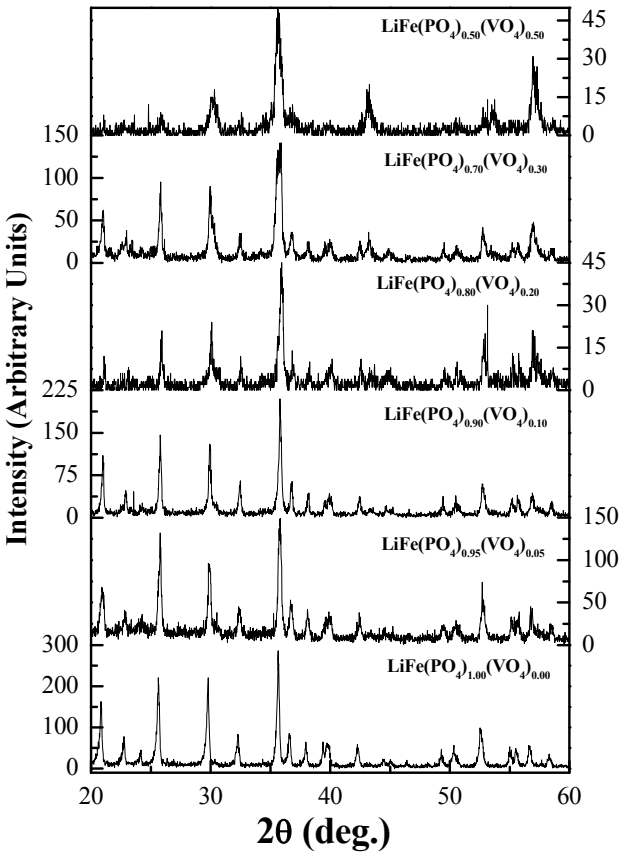

Figure 1. As-recorded X-ray diffractograms of $LiFe(VO_4)_x(PO_4)_{1-x}$ (x = 0.00 to 0.50).

Interestingly, besides a number of Bragg diffraction peaks which may be accounted for by an olivine structure, we find some extra (but quite reproducible) peaks which would forbid the olivine space group, observed from our own XRD data. However, the structure of $LiFe(VO_4)_x(PO_4)_{1-x}$, retains the same orthorhombic phase with little changes observed, as the percentage of vanadate substituted for phosphate (i.e., x) is varied from 0.00 to 0.50. As 'x' is varied from 0.00 to 0.20, there is essentially no change in the orthorhombic structure of $LiFePO_4$, while broadening of peaks is observed. A new peak at $2\theta = 30.6^o$, has been observed for 5% of vanadate substituted sample and it is observed to be developing with increasing 'x' up to 0.30 and remarkably shown as a peak with the almost equal intensity relative to the peak (of orthorhombic phase) at $2\theta = 29.9^o$. Another important

feature to be noted is the high intensity peak [(3 1 1) reflection] of orthorhombic $LiFePO_4$ at $2\theta = 35.65^o$, which gradually broadens with increase in 'x' and splits in to two peaks at x = 0.30 ($2\theta = 35.6^o$ and 35.8^o) and broadened further. From x = 0.30 onwards, a new unknown phase started developing (other than orthorhombic $LiFePO_4$), the formation of which is incomplete. The average crystallite sizes calculated using Scherrer's formula **[5]** for $LiFe(VO_4)_x(PO_4)_{1-x}$ are 40(1) nm, 39(1) nm, 36(1) nm, 26(1) nm, 23(1) nm and 20(1) nm for x = 0.00, 0.05, 0.10, 0.20, 0.30 and 0.50 respectively and figure 4 depicts the variation of average crystallite size with 'x' in $LiFe(VO_4)_x(PO_4)_{1-x}$.

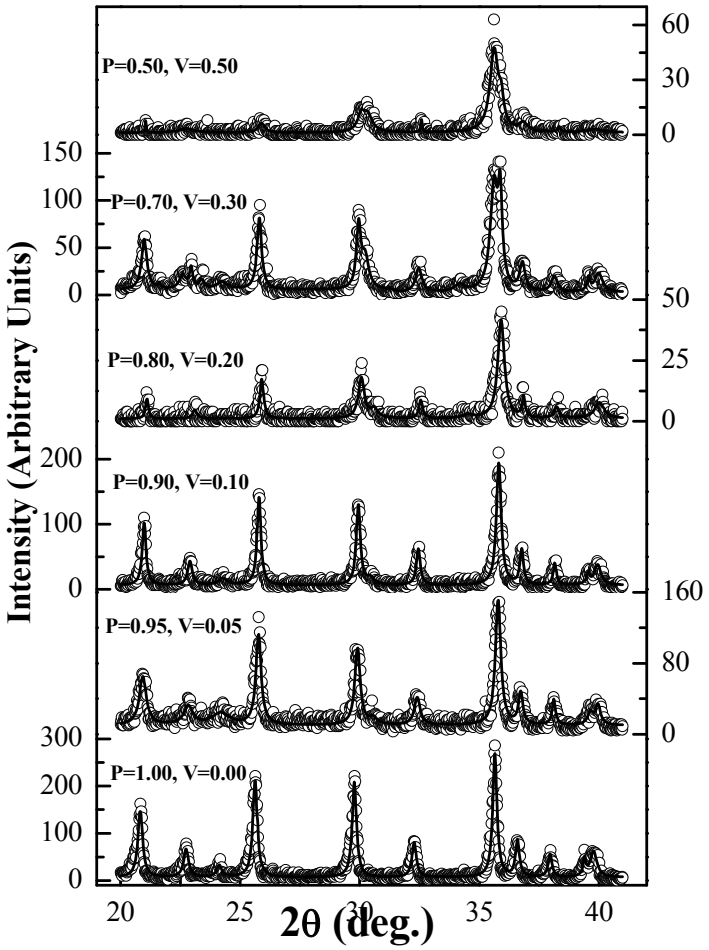

Figure 2. X-ray diffractograms of $LiFe(VO_4)_x(PO_4)_{1-x}$ (x = 0.00 to 0.50) and the respective non-linear least square fits in the angle (2θ) range $20^o - 41^o$.

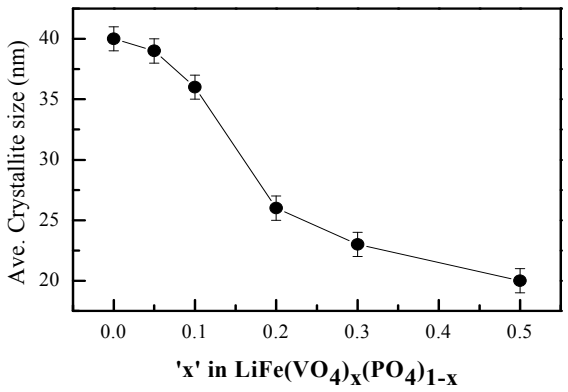

Figure 3. Variation of average crystallite size with 'x' in $LiFe(VO_4)_x(PO_4)_{1-x}$.

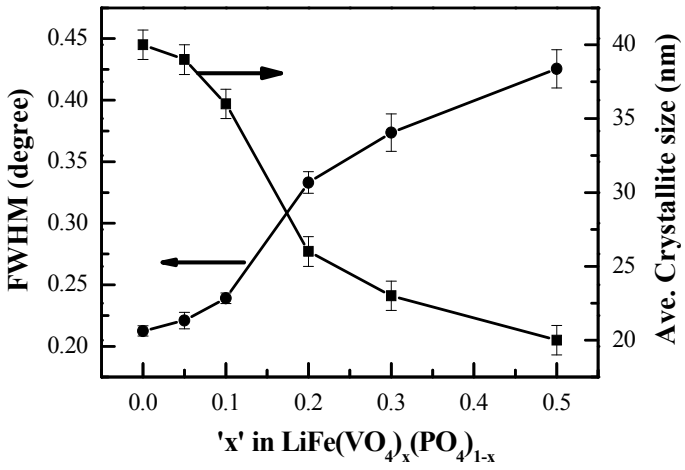

Figure 4. The FWHM values of the (3 1 1) reflection of $LiFePO_4$ phase as a function of 'x' in $LiFe(VO_4)_x(PO_4)_{1-x}$ and the corresponding change in average crystallite size.

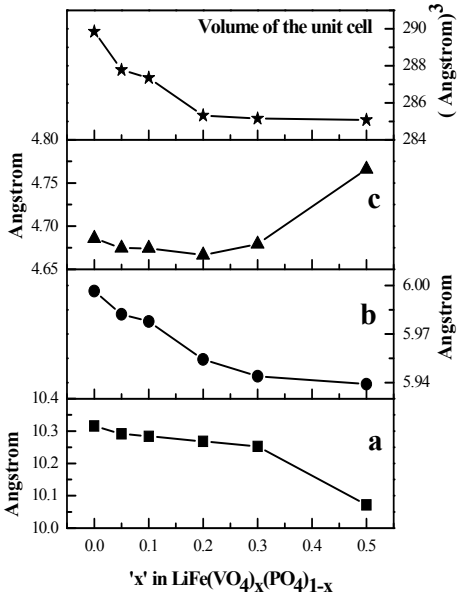

Figure 5. Variation of lattice parameters a, b, c and volume of the unit cell with 'x' in $LiFe(VO_4)_x(PO_4)_{1-x}$.

Table 1: The calculated unit cell parameters of $LiFe(VO_4)_x (PO_4)_{1-x}$ (x = 0.00 to 0.50).

S. No.	'x' in $LiFe(VO_4)_x (PO_4)_{1-x}$	Calculated cell parameters For $LiFePO_4$ phase			Volume of the Unit cell $(Å)^3$
		a (Å)	b(Å)	c (Å)	
1	0.00	10.3154	5.9966	4.6858	289.85
2	0.05	10.2908	5.9822	4.6746	287.78
3	0.10	10.2839	5.9778	4.6743	287.35
4	0.20	10.2682	5.9543	4.6666	285.32
5	0.30	10.2525	5.9439	4.6792	285.15
6	0.50	10.0718	5.9391	4.7659	285.08

Figure 4 shows the full width at half maximum (FWHM) values of the (3 1 1) reflection of $LiFePO_4$ phase as a function of 'x' in $LiFe(VO_4)_x (PO_4)_{1-x}$ and the corresponding changes in the average crystallite size. The variation of lattice parameter a, b, c and the volume of the unit cell is shown as a function of vanadate fraction(x) in $LiFe(VO_4)_x(PO_4)_{1-x}$. The volume of the unit cell in $LiFePO_4$ depends on the Fe–O and P–O distances. One needs to consider the effect of partial replacement of P by V and the consequent changes in the Fe-O and P-O distances. In the absence of a detailed crystal structural analysis it may be said that there is a limit- say solubility limit- for V in $LiFePO_4$ beyond which phase separation seems to occur. The variation of a,b,c parameters with increasing x strongly suggests that the orthorhombic lattice of $LiFe(VO_4)_x(PO_4)_{1-x}$ especially for x>0.3 becomes metastable.

6.4 Vibrational spectroscopy of $LiFe(VO_4)_x(PO_4)_{1-x}$:

The olivine structure is not limited to some orthosilicates and germanates of the type $X_2^{2+}SiO_4$, but is also represented in a fairly large number of compounds, which may be derived from Mg_2SiO_4 formula, either by the double substitution $2Mg^{II} \rightarrow 1A^{I} + 1B^{III}$, viz. $A^{I}B^{III}SiO_4$ or $A^{I}B^{III}GeO_4$, or by the double substitution $Mg^{II}Si^{IV} \rightarrow A^{I}X^{V}$, viz. $A^{I}B^{II}X^{V}O_4$ (X^{V} = P, As, or V). Due to the fairly low symmetry of these compounds, the interpretation of the vibrational spectra of these compounds is difficult **[6]**. A few compounds are characterized by an olivine – like X-ray powder pattern; but the occurrence of some reproducible extra – lines (not allowed in the olivine space group) strongly suggests that, despite some structural analogies, the space group of these compounds is different from that of olivines. This is the case for $LiMgAsO_4$, $LiB^{II}VO_4$ with B^2 = Mg, Mn, Cd and $NaB^{II}VO_4$ with B^{2+} = Cd, Ca **[7]**.

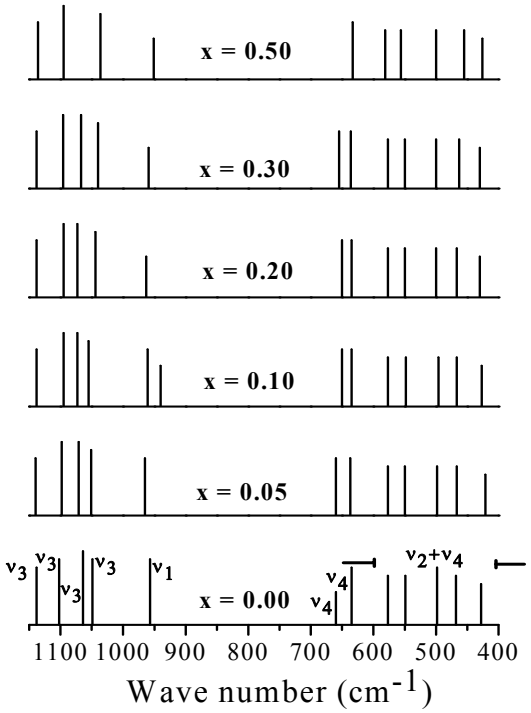

Figure 6. Observed pattern of FTIR bands in nanoparticles of C- $LiFe(VO_4)_x(PO_4)_{1-x}$.

Paques et al **[6]** have suggested that the stretching frequencies of the tetrahedral XO_4 anion may be considered as internal modes, but the corresponding bending frequencies can be considered as "internal" only for the phosphates and for the sodium compounds. For the arsenates and vanadates where A is lithium, the ^6Li–^7Li isotopic shifts reveal important interactions between the Li translations and the AsO_4 or VO_4 bending vibrations. It has also been possible to evidence a number of vibrational interactions in the case of the external vibrations. We have made an attempt to see whether the

changes in the stretching and bending modes occur when vanadate is partially substituted for the phosphate in $LiFePO_4$.

The FTIR spectra recorded on $LiFe(VO_4)_x(PO_4)_{1-x}$ ($0.00 \leq x \leq 0.50$) is given in appendix – III. The wave numbers of various absorption maxima obtained from the observed pattern of $LiFe(VO_4)_x(PO_4)_{1-x}$ are shown in figure 6 and these numbers are tabulated in table 2. Though $LiFeVO_4$ is also supposed to belong to olivine family, we find some extra lines (but quite reproducible) which would be forbidden olivine space group, besides a number of diffraction lines which may be accounted for olivine structure, observed from our own X-ray data. However, the FTIR spectra recorded on $LiFe(VO_4)_x(PO_4)_{1-x}$ samples yielded almost similar patterns for both stretching and bending modes. The tentative explanation for the changes in the modes, for the two regions is as follows.

6.4.1 High – frequency region

The high – frequency region corresponding to the symmetric and asymmetric stretching vibrations of the $LiFe(VO_4)_x(PO_4)_{1-x}$, as 'x' increases is characterized by a very broad absorption with a few well-defined bands. However, observed pattern does not show any appreciable systematic changes. The peculiar shape of the bands, especially when x = 0.50, cannot be ascribed to the crystal structure, since a similar behavior has been observed for the corresponding spinels $LiCoVO_4$ and $LiNiVO_4$ **[8]**, and for some other orthovanadates.

Table 2: Observed FTIR bands in nanoparticles of C- $LiFe(VO_4)_x(PO_4)_{1-x}$.

S. No.	x = 0.00	x = 0.05	x = 0.10	x = 0.20	x = 0.30	x = 0.50
1	1138	1140	1138	1138	1138	1136
2	1102	1098	1095	1095	1096	1095
3	1064	1071	1073	1073	1067	—
4	1049	1051	1055	1044	1040	1036
5	957	965	961	963	959	951
6	—	—	940	—	—	—
7	660	660	650	650	655	—
8	635	637	635	635	636	633
9	577	577	577	577	577	581
10	549	550	548	550	550	556
11	498	498	496	500	500	500
12	468	467	467	467	463	455
13	428	421	427	430	430	426

Thus, this seems to be related to some property of the V–O bonds in the VO_4 group. The factor group splitting of asymmetric stretching vibrations (ν_3) for $LiFe(VO_4)_x(PO_4)_{1-x}$ is calculated and found to be $\Delta\nu_3$ = 89, 89, 83, 94, 98 and 100cm^{-1} for x = 0.00, 0.05, 0.10, 0.20, 0.30 and 0.50 respectively. The variation is also shown in figure 6.

6.4.2 Low – frequency region:

In the low frequency region, corresponding to the bending modes, the spectra do not show any variation as a whole, but appears to exhibit a reduced number of bands, as seen for the x = 0.50 composition. For this region too, there is not much change in the observed modes. The modes are assigned as the combination of ν_2 and ν_4 as shown in figure 6, and are compared with the bending modes of $LiFePO_4$. The precise assignments for this vanadate system need to be ascertained from the observed patterns of $^6Li - ^7Li$ isotopic shifts.

Paques et al **[6]**, have shown that in the compounds of the type $A^IB^{II}X^VO_4$, the stretching frequencies of the tetrahedral XO_4 anion may be considered as internal modes, but the corresponding bending frequencies can be considered as "internal" only for the phosphates and for the sodium (mono–valent cation in $A^IB^{II}X^VO_4$) compounds. For the aresenates (AsO_4) and vanadates (VO_4), where A is lithium, at least a few of the bending vibrations of the anion are strongly mixed up with Li translational motions and thus are no longer internal modes. Thus, despite the isotypic character of these compounds, the separation of the vibrations in to internal and external modes is not valid for the whole family and does depend on the nature of the constitutive atoms. Nevertheless, owing to the complexity of the compounds investigated, these assignments remain essentially qualitative in nature. The only way to go deeper in to the problem would be the study of monocrystals which could be the subject of a future investigation.

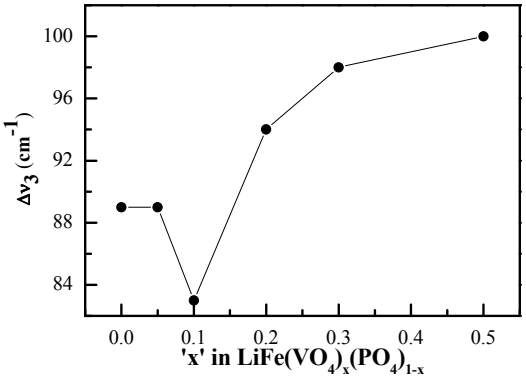

Figure 7. Factor group splitting ($\Delta\nu_3$ cm^{-1}) vs. x of $LiFe(VO_4)_x(PO_4)_{1-x}$.

6.5 Mössbauer spectroscopy of $LiFe(VO_4)_x(PO_4)_{1-x}$:

Room temperature Mössbauer spectra of $LiFe(VO_4)_x(PO_4)_{1-x}$ ($0 \leq x \leq 0.50$) are recorded in transmission mode using ^{57}Co γ-ray source in a Rhodium matrix and multi-channel analyzer. Fig.8 shows the Mössbauer spectra of $LiFe(VO_4)_x(PO_4)_{1-x}$ (for x = 0.00, 0.05, 0.10, 0.20, 0.30 and 0.50) plotted with velocity of the channel along the x-axis and relative transmission of the γ-rays through the sample along Y-axis. In the fig.8, the circles show the raw data, the thick black line shows the best non-linear least squares fit obtained after fitting the data to lorentzians and the dashed line shows the lorentzians fit of the individual line of the spectrum. The full width at half maximum (FWHM) values $\omega_1$and ω_2 are tabulated in table 3 while the corresponding isomer shift (δ) and quadrupole splitting (Δ) of the doublets obtained for Fe^{2+} and Fe^{3+} sites in $LiFe(VO_4)_x(PO_4)_{1-x}$ are given in table 4.

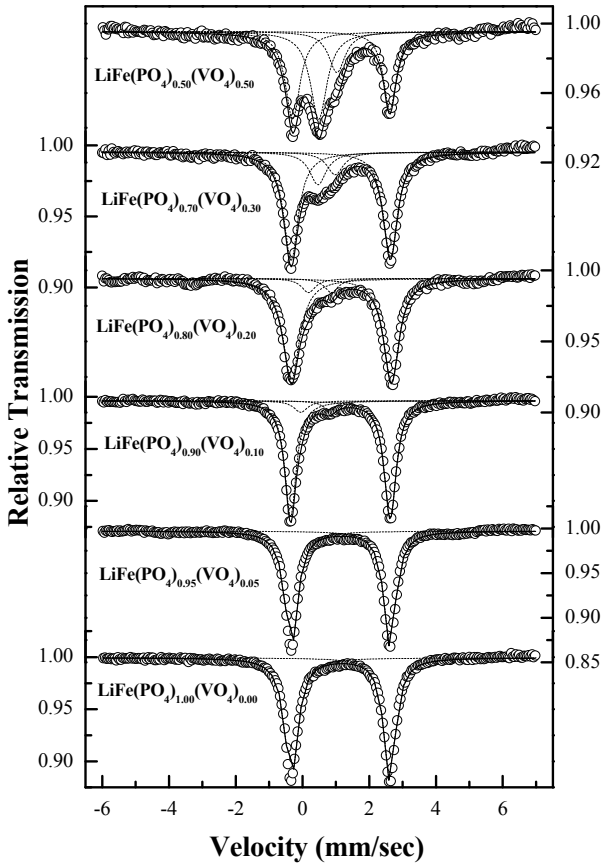

Figure 8. Room temperature Mössbauer spectra of $LiFe(VO_4)_x(PO_4)_{1-x}$ (x = 0.00 to 0.50). The open circles show the raw data, the black line shows the non-linear least square fit of the spectrum and the dashed line show the lorentzians fit of the individual line of the spectra.

Table 3: The full width at half maximum (FWHM) values $\omega_1$and ω_2 of Fe^{2+} and Fe^{3+} doublets.

S. No.	'x' in $LiFe(VO_4)_x(PO_4)_{1-x}$	FWHM of Fe^{2+} doublet		FWHM of Fe^{3+} doublet	
		ω_1 (mm/sec)	ω_2 (mm/sec)	ω_3 (mm/sec)	ω_4 (mm/sec)
1	0.00	0.4763	0.4396	–	–
2	0.05	0.4416	0.4322	–	–
3	0.10	0.4143	0.4363	0.5	0.5
4	0.20	0.6025	0.5565	0.5	0.5
5	0.30	0.5290	0.5148	0.6	0.6
6	0.50	0.5340	0.4662	0.6	0.6

Table 4: The hyperfine parameters of Fe^{2+} and Fe^{3+} doublets.

S. No.	'x' in $LiFe(VO_4)_x(PO_4)_{1-x}$	Hyperfine Parameters for Fe^{2+} doublet		Hyperfine Parameters for Fe^{3+} doublet	
		IS δ (mm/sec)	QS Δ (mm/sec)	IS δ (mm/sec)	QS Δ (mm/sec)
1	0.00	1.2468	2.9499	–	–
2	0.05	1.2480	2.9537	–	–
3	0.10	1.2405	2.9849	0.4819	0.8601
4	0.20	1.2712	2.9948	0.6289	0.6851
5	0.30	1.2516	2.9749	0.8257	0.5155
6	0.50	1.2672	2.9126	0.8640	0.5456

For the sample $LiFePO_4$, only a doublet of two lorentzians could be fitted, as discussed in the previous chapters and the isomer shift (IS) and quadruple splitting (QS) are δ = 1.2468 mm/sec and Δ = 2.9499 mm/sec. These values are typical for high spin Fe^{2+} ions of $LiFePO_4$. The asymmetric nature of the doublet shows that these Fe^{2+} exists in a distorted octahedral environment, as revealed from full width at half maximum values of the doublet given by ω_1 = 0.4763 mm/sec ω_2 = 0.4396 mm/sec. Furthermore even when 5% of vanadium is substituted for phosphorus in $LiFePO_4$, no appreciable change could be observed and the spectrum could still be fitted by a doublet with little asymmetry. The isomer shift and quadruple splitting values for this sample are given by δ = 1.2480 mm/sec and Δ = 2.9537 mm/sec. An observable change appears to initiate at the Fe site in $LiFePO_4$ for x = 0.10 which gets enhanced with further increase in 'x' of $LiFe(VO_4)_x(PO_4)_{1-x}$. For all the samples for which $0.10 \leq x \leq 0.50$, another doublet of lorentzians could be fitted in addition to the existing high spin Fe^{2+} doublet. The isomer shift (δ) and quadrupole splitting (Δ) values of this new doublet is found to be matching with that of high spin Fe^{3+}. And this new doublet becomes more visible as 'x' reaches 0.50.

The intensity of this Fe^{3+} doublet gradually increases (of course more asymmetric in nature) which in turn make the high spin Fe^{2+} doublet to be asymmetric. The FWHM of this doublet are constrained to the values, as given in table 3, to yield a fit with physical significance.

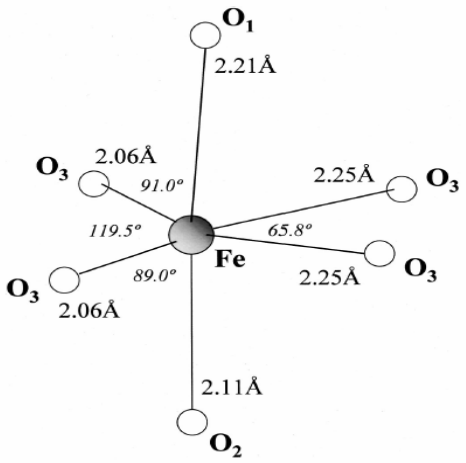

Figure 9. Highly distorted FeO_6 octahedra with C_s symmetry in $LiFePO_4$.

In phospho-olivines, all oxygens form strong covalent bonds with P^{+5} to form the $(PO_4)^{3-}$ tetrahedral poly anion and consequently difficult to extract [1]. This guarantees safety against combustion and adds greatly to the attractiveness of the $LiFePO_4$ cathode. The extremely stable nature of the olivine structure will produce batteries with high tolerance to unusual conditions and this lies in the stabilization of low valance (+2) at Fe site. It is very clear **[9]**; $LiFePO_4$ has olivine formula $MNXO_4$, where M and N are cations with different sizes. The olivine structure has a hexagonally close-packed oxygen array, in which the octahedra share both edges and faces. There is no continuous network of FeO_6 edge shared octahedra and the divalent Fe^{2+} ions occupy corner-shared octahedral positions. The phosphate ions are located in tetrahedral sites. The lithium ions residing in tunnels formed by chains of edge-shared octahedra become mobile during charging and discharging cycles.

Fig.9 shows the highly distorted FeO_6 octahedra **[1]** with C_s symmetry in $LiFePO_4$. As can be seen in fig.2, the Fe site has Cs symmetry. The eight Fe – O bonds differ by as much as 0.2Å in length and are categorized into four shells. The oxygen atoms can roughly be grouped into 'axial' and 'equatorial types'. The angle O_{axial}–Fe–O_{axial} is roughly 180^o. On the plane perpendicular to the O_{axial}–Fe–O_{axial} line, the O_2 – Fe – O_2 roughly form a scissor structure with O – Fe – O angles far from 90^o.

Now when vanadate is substituted for phosphate ion in $LiFePO_4$, by mixing the ammonium metavanadate (NH_4VO_3) during the precursor mixing stage, an appreciable change is observed in the

RT Mössbauer spectra. Another quadrupole in between the doublet of high spin Fe^{2+} begins to develop for x = 0.10 in $LiFe(VO_4)_x(PO_4)_{1-x}$, whose intensity grows with increasing 'x'. The isomer shift and quadrupole splitting values obtained for this doublet, shown in table 2, reveals that this is arising due to the formation of high spin Fe^{3+} ions/phase in the material. The root cause for this may be ascertained from the structural aspects of vanadate in the reactant and product as follows: The characteristic feature for the structure of ammonium metavanadate is the chain structure formed by the tetrahedra VO_4. Each tetrahedron contains two bonding oxygen atoms which join it to the neighboring tetrahedra of the chain. The chains are mutually bonded through electrostatic forces between the cations NH_4^+. The repulsive force between the positive charges of V^{5+} causes a lowering of stability of the chains. The positive charge of the vanadium ion causes the vanadium atoms to take up positions as far as possible from each other. For this reason the possible bond is through the single common oxygen atom. The positive charge of the vanadium ion also causes a slight mutual incline of the tetrahedral in the common chain. It must be noted here that the vanadate $(VO_3)^{1-}$ in NH_4VO_3 transforms to $(VO_4)^{3-}$ in $LiFe(VO_4)_x(PO_4)_{1-x}$. For this to this transformation to occur two electrons are required, which may be supplied by the formation of Fe^{3+} from the octahedral Fe^{2+}, the mechanism of which could be as follows.

$$\mathbf{2Fe^{2+} \rightarrow 2Fe^{3+} + 2e^-}$$

$$\mathbf{(VO_3)^{1-} + 2e^- \rightarrow (VO_4)^{3-}}$$

This results in the breaking of the chains of highly distorted FeO_6 octahedra of high spin Fe^{2+} ions present in $LiFePO_4$, thus producing trivalent Fe sites.

6.6 Conclusions

Sub-micron particles of carbon coated $LiFe(VO_4)_x(PO_4)_{1-x}$ are synthesized with 'x' varying from 0.00 to 0.50. The vanadate substituted for phosphate is perfectly fitting in the tetrahedral structure of phosphate ion of $LiFePO_4$ and no change in the FTIR spectra have been observed. But it is shown that the vanadate ion breaks the chains of highly distorted FeO_6 octahedra resulting the Fe at the edge to increase its oxidation state.

References:

1. Yamada, A., Chung, S. C., and Hinokuma, K., *Journal of the Electrochemical Society, **148(3)**, pA224 (2001)*.
2. Dahn, J. R., Fuller, E. W., Obrovac, M., Sacken, U. von, *Solid State Ionics, **69**, p26 (1994)*.
3. B. D. Cullity, *Elements of X-ray diffraction,* Addisson-Wiley, Massachusetts (1978).

4. Yakubovich, O. V., Simonov, M. A., Belov, N. V., *Akad. Nauk. SSSR,* ***93*** *(1997) 235.* JCPDS (Joint committee on powder diffraction standards) XRD data base 83-2092 of PCPDFWIN version 2.02 May 1999, ©JCPDS-ICDD, 1999.
5. B. D. Cullity, *Elements of X-ray diffraction, Addisson-Wiley, Massachusetts (1978)*.
6. Paques–Ledent, M. Th., Tarte, P., *Spectrochimica Acta,* ***30A****, p673 (1974)*.
7. Paques-Ledent, M. TH., *Compt. Rend.* ***274****, p1998 (1972)*.
8. Preudhomme, J., *Doctorate thesis*, Liège, Belgium (1970).
9. M. Thackeray, *Nature materials,* ***1,*** *p8 (2002)*.

--- O ---

Chapter 7

Order – disorder phase transition in $LiFePO_4$

7.1 Theoretical background of FTIR of Olivine –type structure

The vibrational spectrum of silicates and germanates of the olivine type has not been exhaustively investigated, despite the relative simplicity of their chemical composition **[1]**. This type of structure is not limited to some orthosilicates, and –germanates of the types $X_2^{II}SiO_4$, but is also represented in a fairly large number of compounds $AB^{II}X0_4$ (X = P, As, or V), which may be derived from the Mg_2SiO_4 formula. And the Infrared and Raman spectra of $AB^{II}X0_4$ phosphates, arsenates and vanadates of olivine structure have been investigated by Tarte's research group **[2]**. The interpretation of these spectra is difficult, as expected from a fairly low symmetry of these compounds and can be attempted only if a sufficient number of data available **[2]**. Still they had tried the interpretation of these spectra and have been discussed on both theoretical and experimental bases. Assignments have been deduced from the systematic investigation of pure compounds, solid solutions and isotopic species. For all the compounds investigated, the stretching frequencies of the tetrahedral XO_4 anion may be considered as internal modes, but the corresponding bending frequencies can be considered as "internal" only for the phosphates and for the sodium compounds. They have also investigated to what extent the internal stretching vibrations of the complex anion are modified by the chemical nature of the bivalent cation B^{II} and an original correlation with the second ionization potential of the B^{II} cation is proposed. Different types and activities of the normal modes of $ABXO_4$ compounds are shown in figure1 and are tabulated (Table 1).

Olivines, $LiFePO_4$ in particular belong to a general class of 'polyanion' compounds containing compact tetrahedral 'anion' structural units $(XO_4)^{n-}$ (X = P, As, Mo or W) with strong covalent bonding, networked to produce higher-coordination sites such as oxygen octahedra that are occupied by other metal ions **[3]**. The primitive unit cell, space group Pnma – D_{2h}^{16}, is centrosymmetric, with 4 formula units in the cell. There are 2 types of octahedral sites: the divalent cations Fe^{2+} are located on the largest one with C_6 symmetry, the monovalent cation Li^+ being located on the smaller one with C_4 symmetry. And the pentavalent cation P^{5+} is located in "isolated" tetrahedra PO_4 with the site symmetry C_4.

The local molecular structural features and different vibrational modes of carbon-coated $LiFePO_4$ at room temperature have been extensively studied by infrared spectroscopy **[4–7]**. However, the thermal behavior of $LiFePO_4$ especially at high temperatures has somehow failed to attract the attention of the research groups. It is expected that interesting and important changes occur in the local environment at the Fe site and also the bonding with in FeO_6 and PO_4. In this chapter, the effect

of temperature on the local structure of $LiFePO_4$, on the bending and stretching modes of the phosphate ion (also called internal modes), and the variation of the modes in terms of shift in the wave number and presence and/or absence of different modes with temperature has been discussed for the first time.

Table 1: Types and activities of the normal modes of $ABXO_4$ compounds (Except the A, modes, all u modes are IR active and the g modes are Raman active). (Courtesy: Ledent et al)

Atoms and site symmetry		Normal modes
		Translations
A^{I}	C_i	$\Gamma_A = 3A_u + 3B_{1u} + 3B_{2u} + 3B_{3u}$
B^{II}, X^{V}	C_s	$\Gamma_B = \Gamma_X = 2A_g + B_{1g} + 2B_{2g} + 1B_{3g} + 1A_u + 2B_{1u} + 1B_{2u} + 2B_{3u}$
		Rotations
$X^{V}O_4$	C_s	$\Gamma_{rot} = 1A_g + 2B_{1g} + 1B_{2g} + 2B_{3g} + 2A_u + 1B_{1u} + 2B_{2u} + 1B_{3u}$
		Internal modes
XO_4	C_s	$\Gamma_{int} = \Gamma_{\nu_1} + \Gamma_{\nu_2} + \Gamma_{\nu_3} + \Gamma_{\nu_4}$ $\Gamma_{\nu_1} = A_g + B_{2g} + B_{1u} + B_{3u}$ $\Gamma_{\nu_2} = A_g + B_{1g} + B_{2g} + B_{3g} + A_u + B_{1u} + B_{2u} + B_{3u}$ $\Gamma_{\nu_3} = \Gamma_{\nu_4} = 2A_g + B_{1g} + 2B_{2g} + B_{3g} + A_u + 2B_{1u} + B_{2u} + 2B_{3u}$

Before presenting and discussing the results, some general remarks should be made:

1) The number of predicted active fundamentals is 35 for the IR spectrum, rather large.
2) Most of the IR spectra are accordingly very complex (although the number of observed bands is smaller than the number of active fundamentals).

These spectra may be divided into 2 regions:

1) A series of high – frequency bands which are observed in the region 700 – 1200cm^{-1}, clearly related to stretching vibrations of the phosphate ion.
2) A rather complex pattern of bands in the region 400–700cm^{-1}, expected due to the bending vibrations of the tetrahedral phosphate group.

The resulting normal modes may consist of a mixture of contributions from different kinds of intramolecular motions. Fortunately, the bands originating in the intramolecular stretching motions of phosphate anion (ν_3 and ν_1) can be assigned with a high degree of confidence because they are highly decoupled. However, an unambiguous assignment of the phosphate anion bending modes (ν_2 and ν_4) in this system is some what problematic because these modes are strongly coupled **[2]** and involve some lithium ion motion as well.

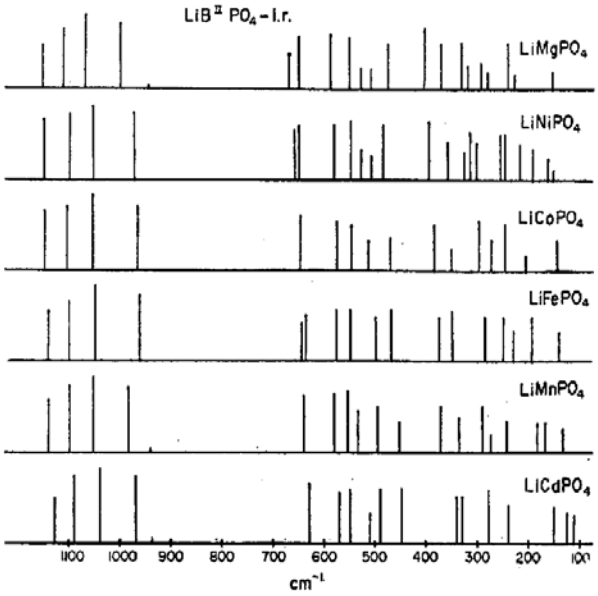

Figure 1. General pattern of IR spectra for the $LiB^{2+}PO_4$ compounds.

In view of the complexity of the spectra and since powder data only are available, the assignment of the bands to the different symmetry classes is ruled out. Nevertheless, with the help of the different techniques (namely the comparative study of pure compounds, isotopic species and solid solutions) it is possible to investigate some aspects of the assignment problem, namely to determine to what extent a given cation or coordinated group is participating in a vibration of a given frequency.

The results and conclusions arrived at for some compounds can be extended with out too much difficulty to the remaining compounds of the same family (here the Olivine family), at least in some spectral regions, since most of the spectra are very similar. This is in accordance with the well-recognized fact that compounds which are both chemically and structurally related generally give similar vibrational spectra. Significant modifications are observed principally in the low-frequency region, in connection with the modification of the chemical nature of the cation.

7.2 Assignment of the bands of the IR spectra

7.2.1 The high-frequency region: internal stretching vibrations

The IR pattern is rather similar for all phosphates and is characteristic of the PO_4 anion engaged in an olivine structure. The four strong, moderately broad, bands of the 700 – 1200cm^{-1} region are assigned to components originating from the ν_3 antisymmetric stretching mode, whereas the weak, sharp band observed on the low frequency side of this absorption is assigned to ν_1. This last assignment is proposed on the basis of low intensity, the results of solid solutions, the sharpness and, finally, of the frequency of this band. However the labeling "ν_1" and "ν_3" has no strict significance since both ν_1 and ν_3 of the free phosphate are split under the influence of both side and factor groups

into a series of modes, some of which belong to the same representations and thus are liable to interact. The reality and importance of such a mixing between the split components of ν_1 and ν_3 modes has been demonstrated in the case of Mg_2SiO_4 on the basis of isotopic shifts of silicon. This kind of experimental proof is impossible in the case of phosphates, since there is only one isotope of phosphorus.

7.2.2 The medium and low frequency regions

This part of the spectrum is expected to correspond to the internal bending modes of the phosphate ion and to the external modes (rotations and translations). The distinction between internal and external modes is a satisfactory approximation; and if this is the case, to propose the right type of assignment for the numerous bands which are observed in this region.

7.3 TG – DTA analysis

A certain amount (32mg) of the nanosized powder of C-$LiFePO_4$, synthesized from non–aqueous sol–gel synthesis route has been taken in an alumina crucible and dynamic calcinations were carried out in the furnace of a thermo-gravimetric analysis (TG) device (NETZSCH STA 409 PC/PG). The sample was dynamically heated from room temperature to 1270K **at** a heating rate of 10^oCmin^{-1}. Figure 2 shows the TG–DTA recorded on $LiFePO_4$ sample. To prevent the oxidation of the precursor, a continuous flow of nitrogen was maintained in the furnace during heating.

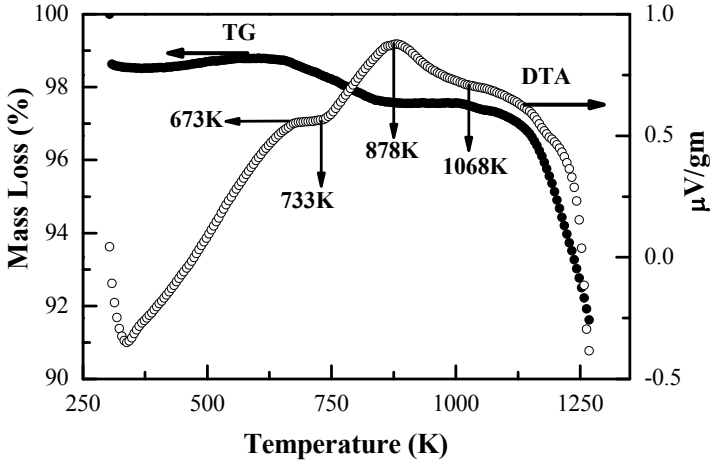

Figure 2. TG – DTA of in-situ carbon coated nano particles of $LiFePO_4$.

A careful perusal of the above figure indicates that an order–disorder phase transition apparently occurs in the temperature range 273–1270K in general, and at 673K, 733K, 878K and

1068K in particular. These changes are accompanied by a mass loss of ~10% in the sample with increase in temperature (up to 1270K) as observed from thermo gravimetric analysis.

7.4 FTIR studies

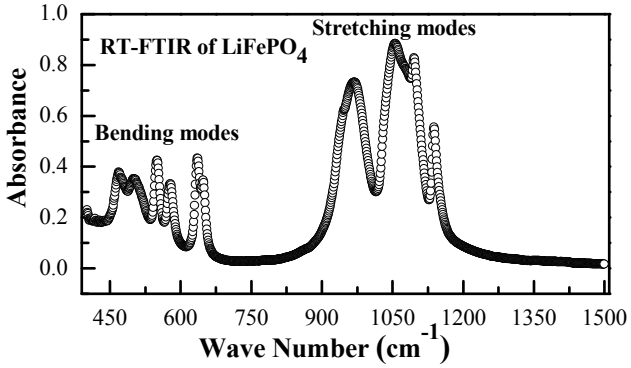

Figure 3. Room temperature Fourier transform of infrared (FTIR) spectrum of $LiFePO_4$.

With the TG – DTA of $LiFePO_4$ in hand, Infrared spectroscopic studies were carried out on a NEXUS FTIR spectrometer from Thermo–Nicolet, using a thermo–electrically cooled deuterated tri–glycene sulphate (DTGS) detector and an extended range KBr (XT – KBr) beam splitter, capable of working in the wavenumber range 400–1500 cm^{-1}. Spectra at above ambient temperatures were collected using a specially fabricated environmental chamber. This chamber can be used to increase the temperature of the sample under study up to 950^{o}K with an accuracy of ±2K. Running tap water was used to cool the outer jacket of the chamber, which includes the infrared transparent windows. Conventional KBr pellet technique was adapted to record FTIR spectra and the spectra reported are the resultant of 256 scans, with a resolution of 2 cm^{-1} and aperture of 25. Typical uncertainties in the peak positions are about 2 cm^{-1} for the sharper and stronger modes, while that for the weak and overlapping modes could be about 5 cm^{-1}. We restrict our investigations to the internal modes of phosphate ion of $LiFePO_4$, which involves bending modes in the low-wave number region (400–700cm^{-1}) and stretching vibrations in the high-wave number region (700–1300cm^{-1}).

Figure 3 shows the Fourier transform of infrared (FTIR) spectrum recorded at room temperature, in the wave number range 400–1500cm^{-1}. The figure clearly shows the bending modes of the phosphate ion in the wave number region 400–700 cm^{-1} and the stretching modes in the wave number region 700–1300cm^{-1}. The vibrations of the PO_4^{3-} units are split in to many components due to the correlation effect induced by the coupling with of Fe–O units in the $LiFePO_4$ sample. In $LiFePO_4$, the FeO_6 and PO_4 are part of a 'train'- a molecular ions' train- providing a framework for

the structure. While bending modes (υ_2 & υ_4) are more susceptible to small structural changes–being less localized than stretching modes (υ_1 & υ_3), the latter modes show order–disorder transition in the form of variations in the bond lengths of the phosphate ion.

7.5 Results and Discussion

FTIR spectra of nano particles of C-$LiFePO_4$ were recorded from room temperature to 898K at different steps of temperature, guided by TG–DTA shown in figure 2. The spectra on this sample were also recorded while cooling the sample, to explore the nature (reversibility) of the order–disorder phase transition. For convenience, the spectra have been divided into different wave number regions. Also the spectra corresponding to heating and cooling runs are shown separately.

7.5.1 Bending modes

a) 400 – 530 cm^{-1} region:

Figures 4, 5 and 6 show the in-situ FTIR spectra recorded on C-$LiFePO_4$ in the wave number region 400 – 530 cm^{-1}, in the temperature range 300K–623K, 653K–773K and 823K–898K respectively, during increase of temperature of the sample. While figure 7 represents the in-situ FTIR spectra of the same sample from RT – 898K while cooling. From these figures, it is clear that the bending modes in this region undergoes a random variation with increase in temperature and retain the room temperature infrared spectrum upon cooling. This may be due to the reversible order-disorder transition in the sample with the temperature. This transition is more systematic as would be explained in the forth coming sections of this chapter.

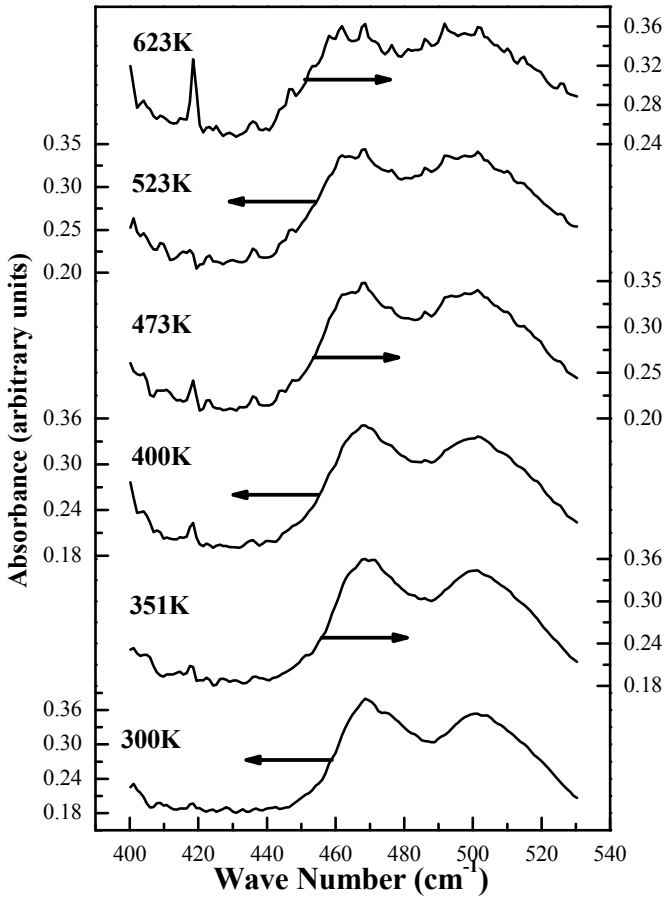

Figure 4In–situ FTIR spectra of $LiFePO_4$ in the wave number region 400 cm^{-1}–530 cm^{-1} from 300K– 623K.

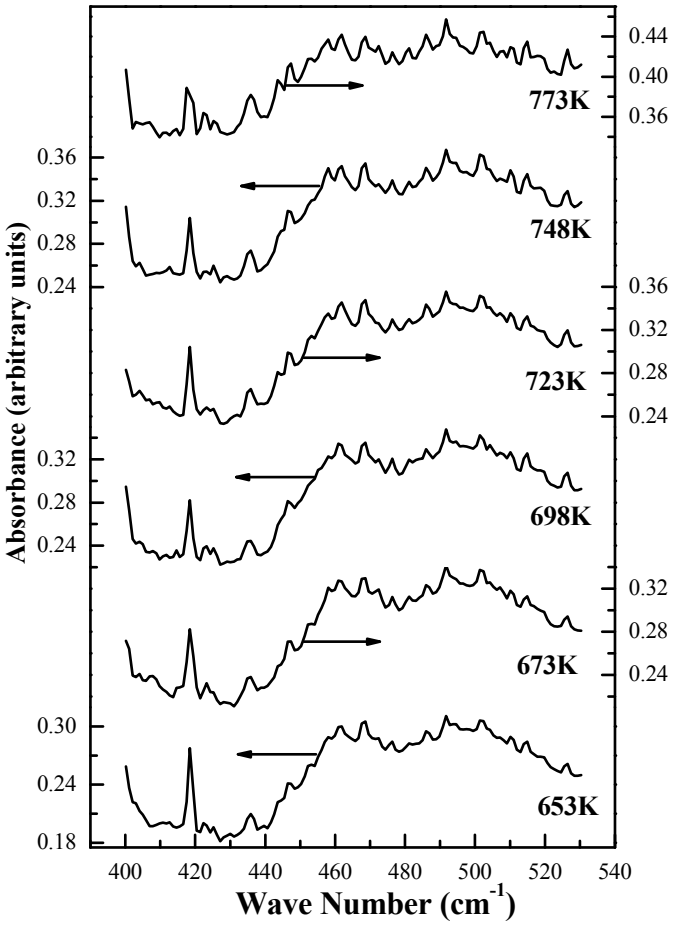

Figure 5In–situ FTIR spectra of $LiFePO_4$ in the wave number region 400 cm^{-1}–530 cm^{-1} from 653K–773K.

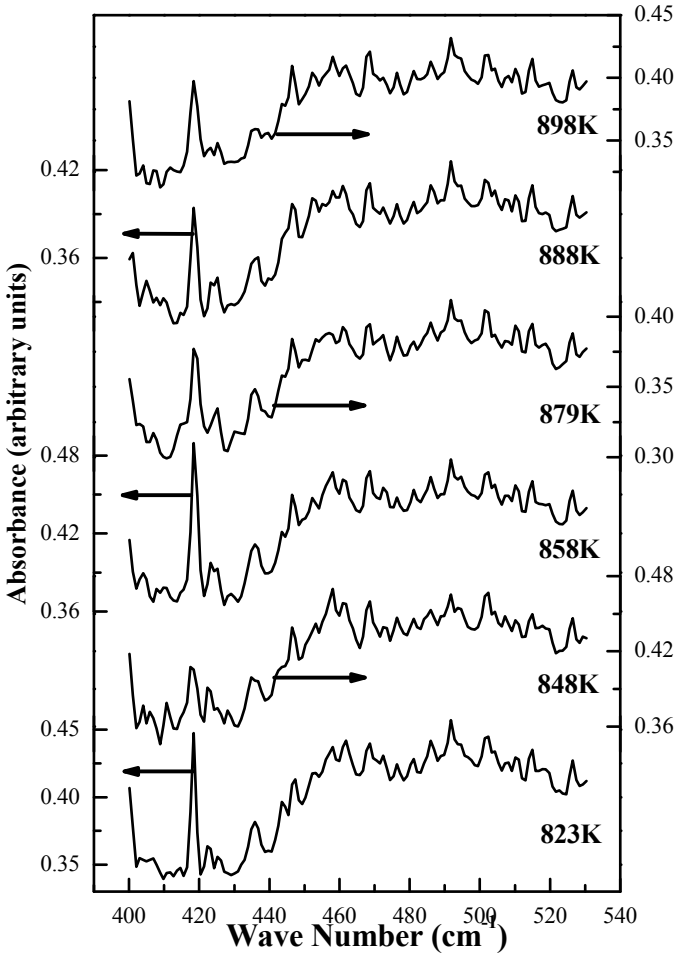

Figure 6In–situ FTIR spectra of $LiFePO_4$ in the wave number region 400 cm^{-1}–530 cm^{-1} from 823K–898K.

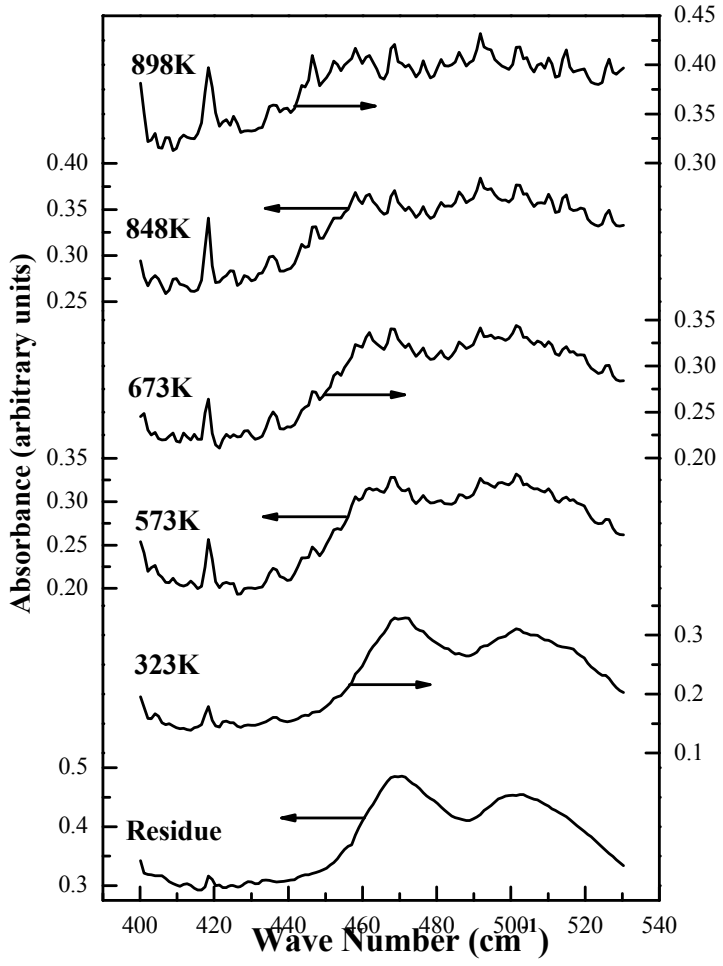

Figure 7In–situ FTIR spectra of $LiFePO_4$ in the wave number region 400 cm^{-1}–530 cm^{-1} from 300K–898K.

b) 530 – 700 cm^{-1} region:

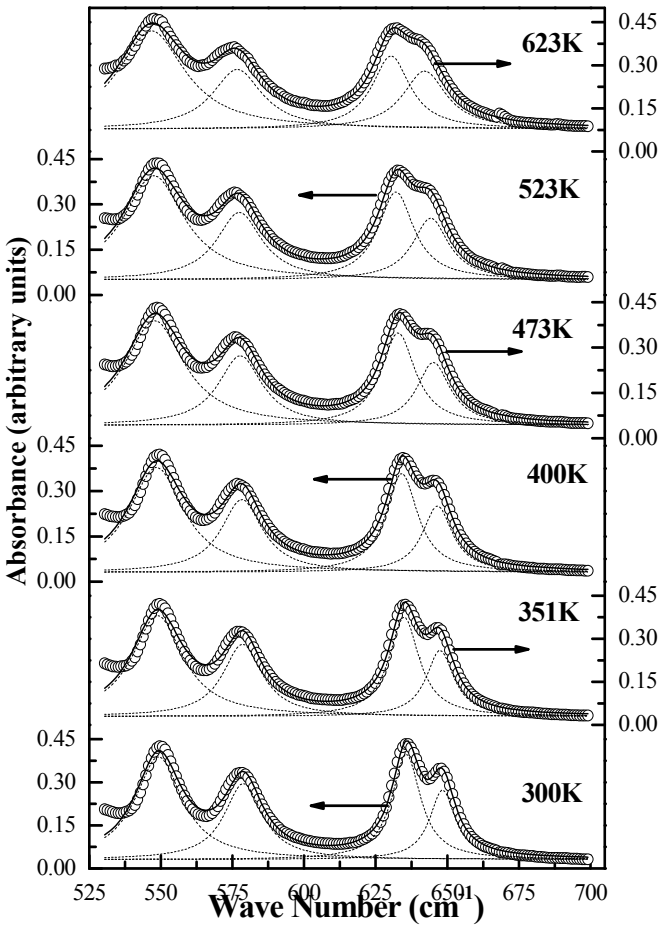

Figure 8In–situ FTIR spectra of $LiFePO_4$ in the wave number region 530 cm^{-1}–700 cm^{-1} from 300K–623K.

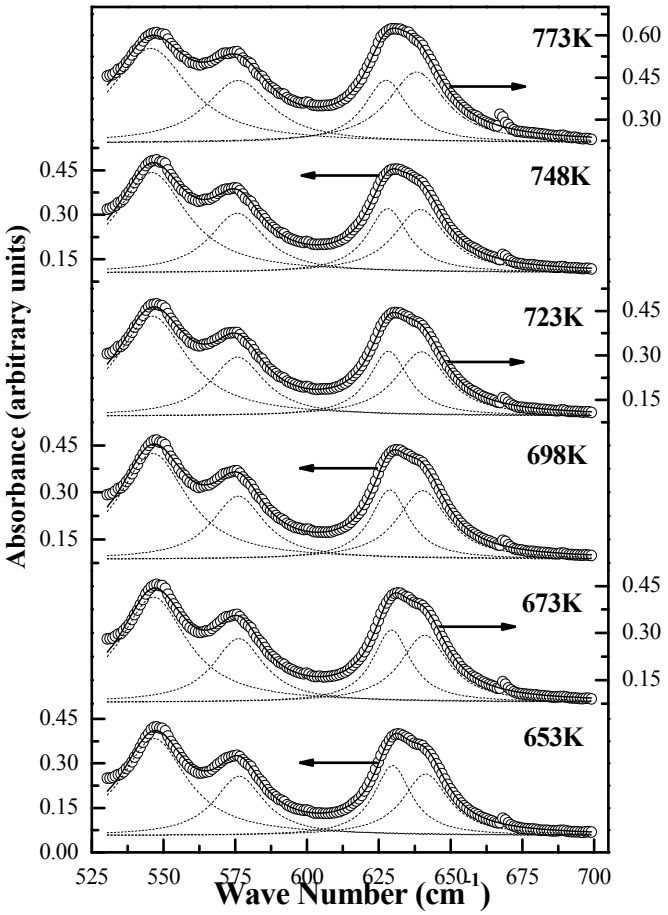

Figure 9In–situ FTIR spectra of $LiFePO_4$ in the wave number region 530 cm^{-1}–700 cm^{-1} from 653K–773K.

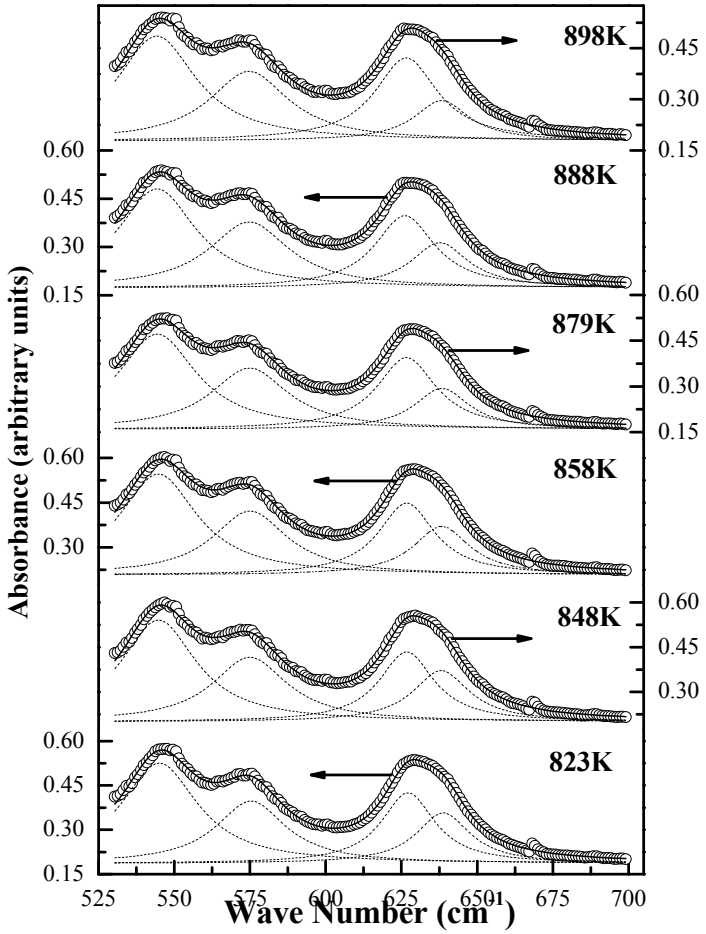

Figure10In–situ FTIR spectra of $LiFePO_4$ in the wave number region 530cm^{-1}–700 cm^{-1} from 823K–898K.

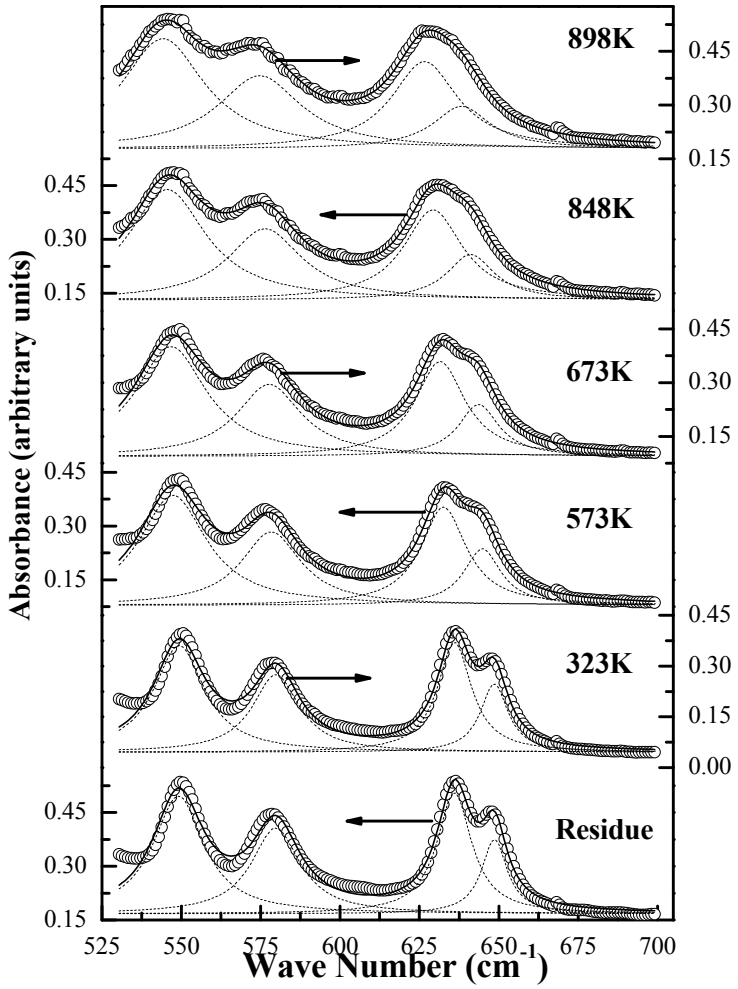

Figure 11. In–situ FTIR spectra of C-LiFePO$_4$ in the region 530 cm^{-1}–700 cm^{-1} from 300K–898K during cooling

.

Table 2: The four bending IR modes of PO_4 in $LiFePO_4$ in the region 530–700 cm^{-1}, obtained from non-linear least square fit.

S.No.	Temperature		Mode1 (cm^{-1})	Mode 2 (cm^{-1})	Mode 3 (cm^{-1})	Mode 4 (cm^{-1})
	(^oC)	(K)				
1	27	300	549.2	578.8	635.7	648.3
2	50	323	549	578.7	635.3	647.9
3	78	351	548.9	578.5	634.9	647.5
4	127	400	548.5	578.3	634.1	646.6
5	155	428	548.2	578.1	633.7	646.1
6	200	473	547.8	577.7	632.9	645.2
7	250	523	547.5	577.4	632.1	644.2
8	323	596	547	576.8	630.9	642.8
9	350	623	546.7	576.7	630.4	642.1
10	380	653	546.7	576.3	629.8	641.3
11	400	673	546.5	576.2	629.4	640.9
12	425	698	546.3	576	628.8	640.3
13	450	723	546	575.8	628.4	639.9
14	475	748	545.9	575.6	628.1	639.4
15	500	773	545.5	576	627.5	638.2
16	550	823	545.1	575.3	627.2	638.8
17	575	848	544.8	574.9	626.7	638.1
18	585	858	544.7	575	626.7	638.2
19	606	879	544.4	574.8	626.7	638.3
20	615	888	544.3	574.7	626.1	637.6
21	625	898	544.2	574.7	626.6	638.3

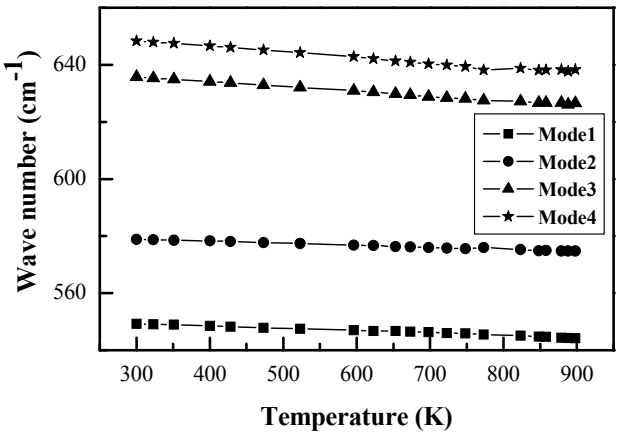

Figure 12. The variation of bending modes with temperature in the region 530 – 700 cm^{-1} while heating the sample.

Table 3: The four IR active bending modes in the region 530 – 700 cm^{-1}, observed while cooling the sample.

S.No.	Temperature		Mode1 (cm^{-1})	Mode 2 (cm^{-1})	Mode 3 (cm^{-1})	Mode 4 (cm^{-1})
	(^oC)	(K)				
1	27	300	549.3	579.8	636.1	648.6
2	50	323	549.1	579.7	636	648.6
3	300	573	547.4	578.3	632.6	644.8
4	400	673	546.7	577.6	631.5	643.6
5	575	848	545.5	576.3	629.3	641.1
6	625	898	544.2	574.7	626.6	638.3

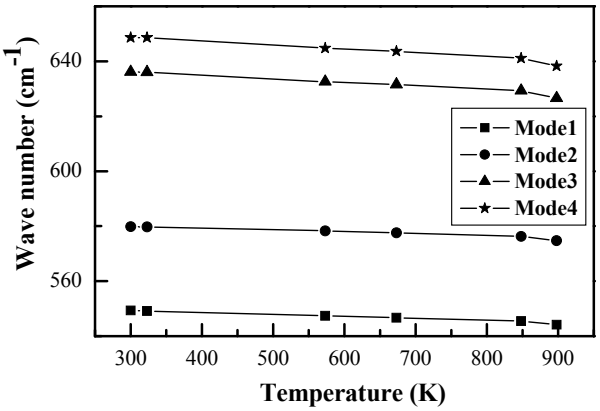

Figure 13. The variation of bending modes with temperature in the region 530 – 700 cm^{-1} while cooling the sample.

Table 4: The full width at half maximum (Δω) of the four active bending modes in the region 530 – 700 cm^{-1}.

S.No.	Temperature		$\Delta\omega_1$ (cm^{-1})	$\Delta\omega_2$ (cm^{-1})	$\Delta\omega_3$ (cm^{-1})	$\Delta\omega_4$ (cm^{-1})
	(^oC)	(K)				
1	27	300	19.8	16	12.1	10.8
2	50	323	20.8	16.4	12.3	11.4
3	78	351	21.6	16.6	12.6	11.7
4	127	400	23.2	17.4	13.4	12.7
5	155	428	23.8	17.8	13.8	13.8
6	200	473	25.1	18.6	14.4	14.1
7	250	523	26	19.2	15	15.2
8	323	596	27.4	20.6	16	17.1
9	350	623	28.5	21.2	16.1	18.4
10	380	653	27.7	20.9	15.7	19.4
11	400	673	28.4	21.7	16	20.5
12	425	698	29	22.4	16.2	21.2
13	450	723	29.8	23.1	16.8	21.8
14	475	748	30	23.5	17.4	22.1
15	500	773	32.8	28	18.5	24.5
16	550	823	30.9	28.2	21.4	21.6
17	575	848	30.3	30.1	22	22.7
18	585	858	31.4	30	22.7	22.6
19	606	879	31.4	31.1	23.8	21.9
20	615	888	31.5	32.1	24.1	23
21	625	898	31.9	32	25.2	22

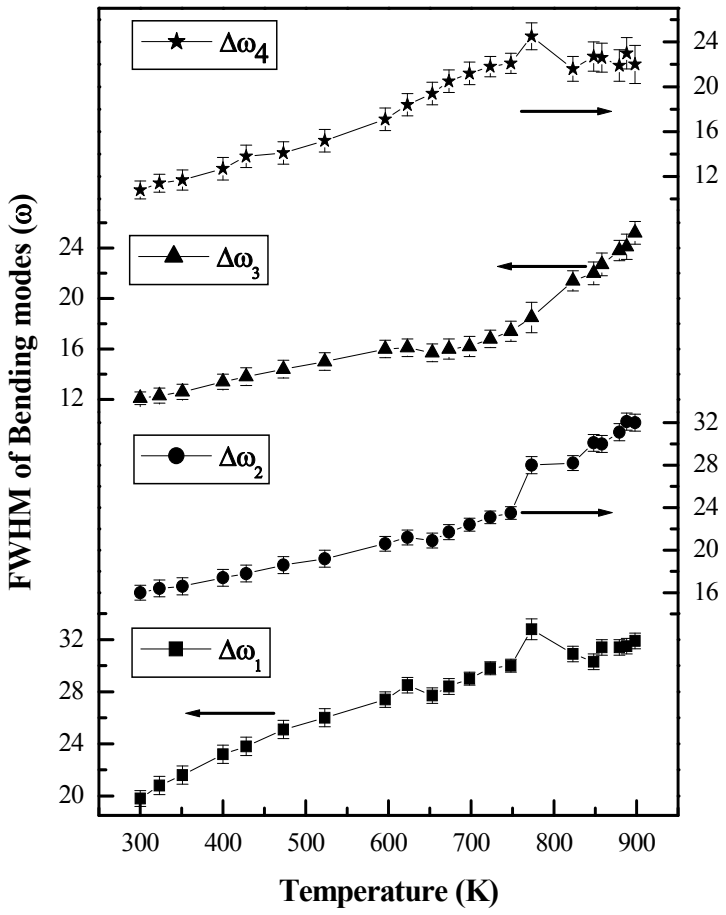

Figure 14. Temperature dependence of FWHM values of each of the four bending modes in the wave number region 530–700cm^{-1} while heating the sample.

Table 5: The full width at half maximum (Δω) of the four active bending modes in the region 530 – 700 cm^{-1}, while cooling the sample.

S.No.	Temperature		$\Delta\omega_1$ (cm^{-1})	$\Delta\omega_2$ (cm^{-1})	$\Delta\omega_3$ (cm^{-1})	$\Delta\omega_4$ (cm^{-1})
	(^{o}C)	(K)				
1	Residue	300	19.4	18.6	13.2	9.8
2	50	323	19.4	17.9	13.0	10.5
3	300	573	25.9	23.0	17.4	14.2
4	400	673	27.3	24.8	19.1	15.4
5	575	848	29.7	28.3	22.5	18.2
6	625	898	31.9	32.0	25.2	22.0

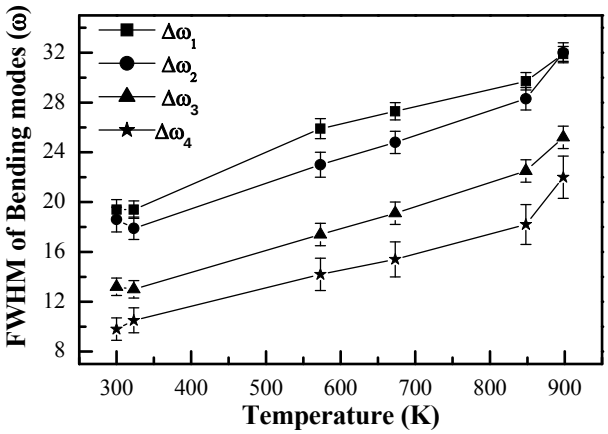

Figure 15. FWHM values of each of the four bending modes with temperature in the wave number region 530–700cm^{-1} while cooling the sample.

Bending modes (530–700 cm^{-1}):

Figures 8, 9 and 10 show the in-situ FTIR spectra recorded on C-$LiFePO_4$ in the wave number region 530 – 700cm^{-1}, in the temperature range 300K – 623K, 653K – 773K and 823K – 898K respectively. While figure 11 represents the in-situ FTIR spectra of the same sample from RT – 898K while cooling. In this region, the symmetric bending mode (υ_2), the anti symmetric bending modes (υ_4) and the mixed bending modes ($\upsilon_2+\upsilon_4$) of phosphate ion are active and these spectra show four such active modes (of this region). All the spectra shown in the figures 8–11 have been analysed by fitting each spectrum to non-linear least square fit, which consists of a set of four lorentzians. In all these figures, black circles show the raw data while the black solid line through the circles shows the non-linear least square fit and the dashed line shows the lorentzian fit for individual peaks.

The wave numbers of the four such active modes thus obtained from the room temperature FTIR spectrum of $LiFePO_4$ are observed to be 549.2 cm^{-1}, 578.8 cm^{-1}, 635.7 cm^{-1}, and 648.3 cm^{-1}. And the bending modes in the wave number region 530 – 700 cm^{-1} obtained at temperatures above room temperature, obtained from the fitting procedure have been tabulated (table2). The variation of the bending modes with increase in temperature is plotted in figure 12. Significantly *all* the four bending modes in this region shift to *lower* wave numbers upon *heating*. The shift in the wave number of the four modes for the increase in temperature form 300K – 898K is found to be 5cm^{-1}, 4.1 cm^{-1}, 9.1cm^{-1}, and 10cm^{-1} respectively.

The wave numbers of the four modes are found to be increasing with decrease of temperature, while cooling the sample. These values are tabulated in table 3 and are plotted in figure 13. The wave numbers of the four modes obtained from the room temperature FTIR spectrum of residual $LiFePO_4$ are observed to be 549.3 cm^{-1}, 579.8 cm^{-1}, 636.1 cm^{-1}, and 648.6 cm^{-1}, and are nothing but the room temperature bending modes of $LiFePO_4$ before heat treatment of the sample, with in the experimental limits.

While increasing the temperature of the sample, it is observed that the shoulder mode 4 (648.3 cm^{-1}) on the mode 3 (635.7 cm^{-1}) in the room temperature spectrum starts merging with the latter at 473K. These two modes appear to be a single degenerate mode after merging with broadened width. However, the lorentzian fit could resolve this mode in to well two distinct modes. And it has been noticed that these two modes are getting separated, while cooling the sample to room temperature, as shown in figure 11.

Another very weak but still observable mode starts developing at 668.2 cm^{-1} at 623K as shown in figure 8 and which remains to be one of the bending modes up to 898K. This mode has been observed while cooling the sample, even for the room temperature FTIR spectrum of residual $LiFePO_4$.

Significantly, all the four bending modes in this region shift to lower wave numbers upon heating. The shift in the wave number of the four modes for the increase in temperature form 300K – 898K is found to be 5cm^{-1}, 4.1cm^{-1}, 9.1cm^{-1}, and 10cm^{-1} respectively.

The full width at half maximum (FWHM) values obtained from the non – linear least square fit, are found to be increasing with increase in temperature from 300K – 898K, for all the bending modes in this wave number region. This implies that the modes are getting thermally broadened with increase in temperature. The full width at half maximum values denoted as $\Delta\omega_1$, $\Delta\omega_2$, $\Delta\omega_3$, and $\Delta\omega_4$ for the four active bending modes, obtained from the non-linear least square fit in this region, with increase in temperature are given in table 4, and are plotted as shown in figure 14. The systematic increase in the values of $\Delta\omega_1$, $\Delta\omega_2$, $\Delta\omega_3$, and $\Delta\omega_4$ indicate the disorder in the bending modes set in the sample with increase in temperature.

The FWHM values $\Delta\omega_1$, $\Delta\omega_2$, $\Delta\omega_3$, and $\Delta\omega_4$ obtained from the non-linear least square fit, change abruptly at around 653K and 773K, with increase in temperature. This may be attributed to

sudden changes in the P–O bond lengths of the phosphate ion. These structural changes in the phosphate ion are found to be reversible upon cooling.

Finally the following conclusions may be drawn based on the observed trends in IR spectra in the wave number region 530–700 cm^{-1}.

1. The FTIR spectra of C-$LiFePO_4$ as shown in figures 7–9, in the temperature range 300K – 623K, 653K – 773K and 823K – 898K are show a reversible temperature dependence with respect to a heat-cool cycle as revealed from the figure 11.

2. a) The shift in the wave number of the bending modes to lower values observed with increase in temperature indicates that the energy required for excitation of the bending modes decrease, at higher temperatures. And the modes are observed to be shifting to higher wave numbers, while cooling the sample reflects the reversibility of the excitation phenomenon of the bending modes with temperature and thereby a robust 'molecular structure'.

   b) The different bending vibrations (the symmetric bending modes (υ_2) anti symmetric bending modes (υ_4) and mixed bending modes ($\upsilon_2+\upsilon_4$)) of phosphate ion, exhibit vibrational disorder due to increase in temperature. This is revealed from the increase in the increase in full width at half maximum values of all the bending modes. And it is found that the order could set in the sample upon decreasing the temperature. This shows the *order – disorder transition* observed for the *bending modes* of the phosphate ion in C-$LiFePO_4$ is *reversible.*

3. The abrupt structural changes of the phosphate ion at temperatures around 653K and 773K are found to be reversible.

7.5.2 Stretching modes (850 – 1250 cm^{-1})

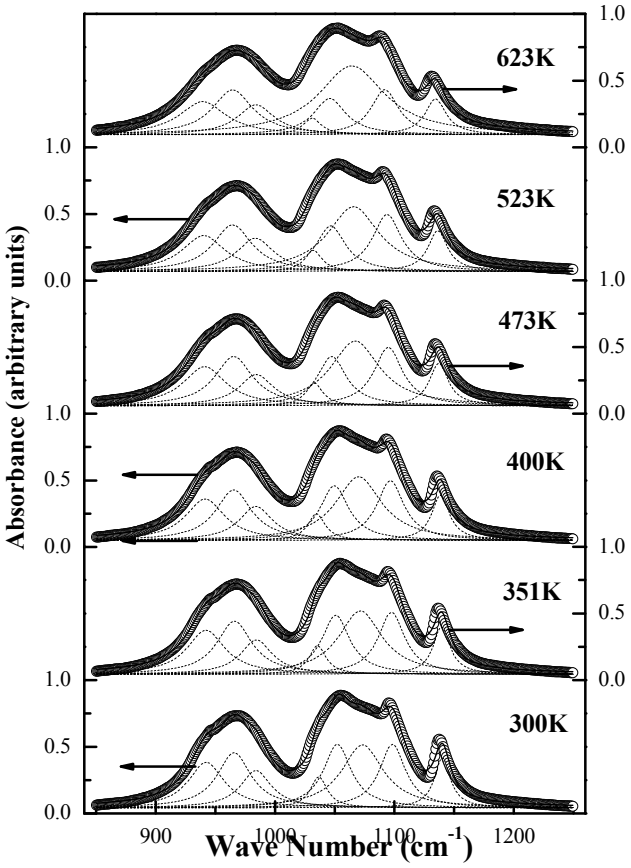

Figure 16. In–situ FTIR spectra of $LiFePO_4$ in the wave number region 850 cm^{-1}–1250 cm^{-1} from 300K–623K.

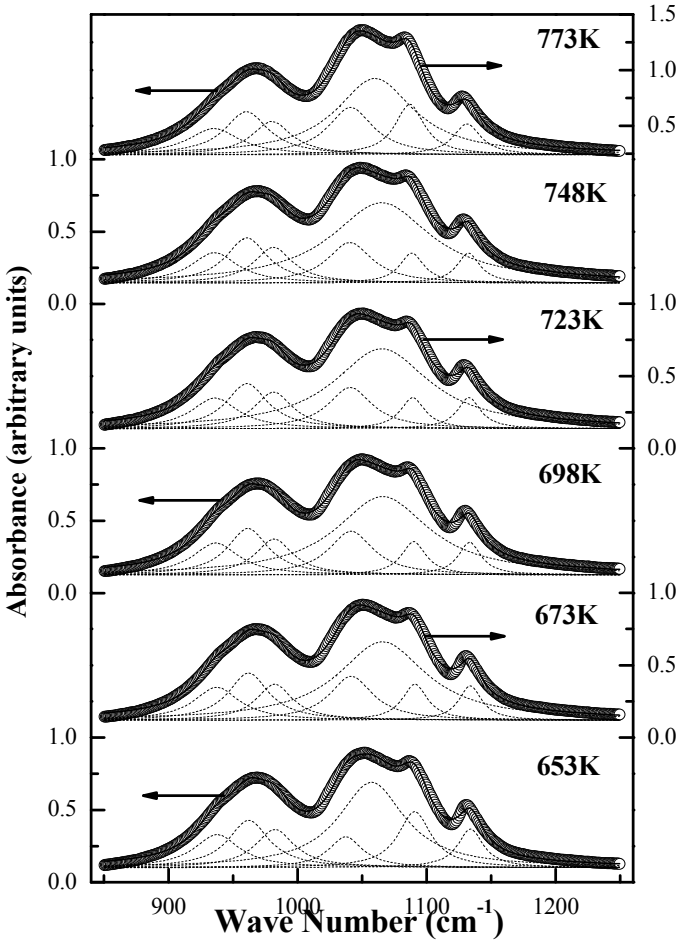

Figure 17. In–situ FTIR spectra of $LiFePO_4$ in the wave number region 850 cm^{-1}–1200 cm^{-1} from 653K–773K.

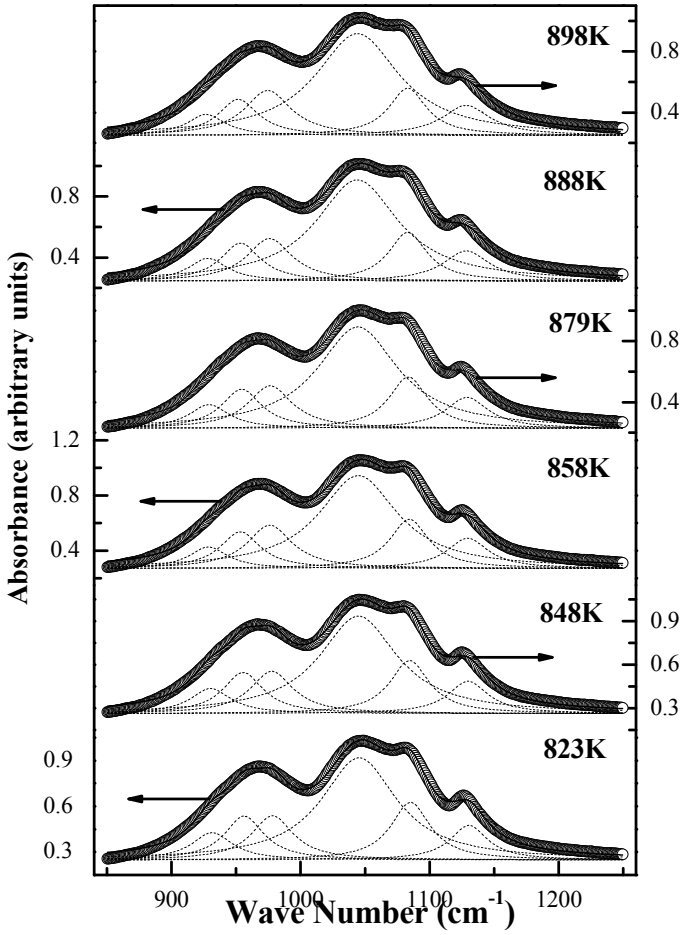

Figure 18. In–situ FTIR spectra of $LiFePO_4$ in the wave number region 830 cm^{-1}–1250 cm^{-1} from 823K–898K.

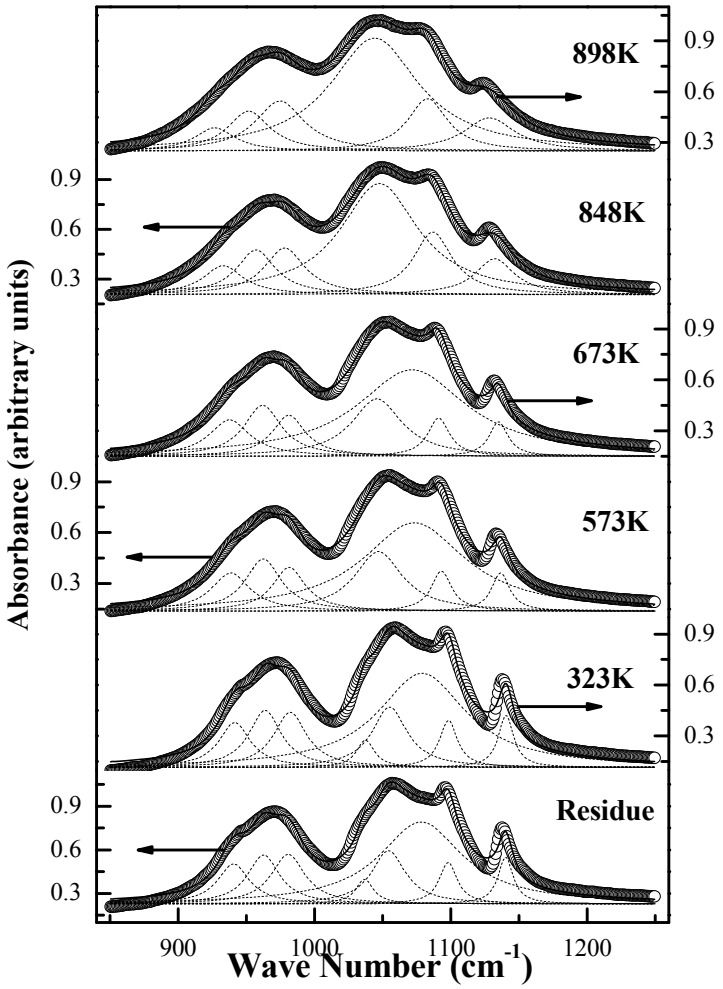

Figure 19. In–situ FTIR spectra of C-LiFePO$_4$ in the region 850 cm^{-1}–1250 cm^{-1} from 300K–898K during cooling .

Table 6: The stretching modes of PO_4 in $LiFePO_4$ in the region 850–1250 cm^{-1}, while heating the sample.

S.No.	Temperature		Mode1 (cm^{-1})	Mode 2 (cm^{-1})	Mode 3 (cm^{-1})	Mode 7 (cm^{-1})	Mode8 (cm^{-1})
	(^oC)	(K)					
1	27	300	942.2	965.6	983.9	1098.4	1140.2
2	50	323	942.1	965.7	984.1	1098	1139.9
3	78	351	942.1	965.9	984.3	1097.6	1139.5
4	127	400	941.3	965.3	983.9	1096.7	1138.7
5	155	428	941.2	965.4	984.1	1096.1	1138.2
6	200	473	940.8	965.3	984.2	1094.9	1137.3
7	250	523	940	964.3	983.5	1093.9	1136.4
8	323	596	939.2	963.9	983.3	1092.3	1134.9
9	350	623	939.3	964.3	983.9	1091.9	1134.5
10	380	653	937.6	962.1	982.2	1091.2	1134
11	400	673	937.2	961.9	982.2	1090.9	1133.9
12	425	698	936.5	961.5	981.8	1090	1133.3
13	450	723	935.8	960.7	981.2	1089.3	1132.8
14	475	748	935.4	960.6	981.2	1088.5	1132.4
15	500	773	935.9	961.4	981.2	1086.2	1131.3
16	550	823	931.3	956.3	978.2	1085.2	1130.4
17	575	848	930.2	955.4	977.6	1084.5	1129.8
18	585	858	928.5	953.3	976.1	1084.3	1129.4
19	606	879	929	954.3	976.4	1083.5	1128.8
20	615	888	928.1	953.4	975.9	1083.1	1128.4
21	625	898	926.7	951.6	974.6	1082.9	1128.2

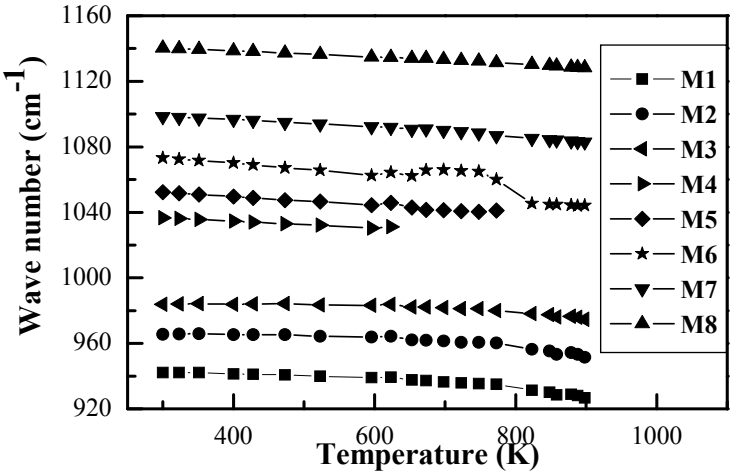

Figure 20. The variation of stretching modes with temperature in the region 850–1250 cm^{-1} while cooling the sample.

Table 7: The stretching modes in the region 850–1250 cm^{-1}, obtained while cooling the sample.

S.No.	Temperature		Mode1 (cm^{-1})	Mode 2 (cm^{-1})	Mode 3 (cm^{-1})	Mode 7 (cm^{-1})	Mode8 (cm^{-1})
	(^oC)	(K)					
1	27	300	941.6	963.7	982.3	1098.3	1140.5
2	50	323	941.4	963.6	982.2	1098.1	1140.2
3	300	573	938.5	962.3	981.3	1093.1	1136.6
4	400	673	937.6	961.9	981.1	1091.1	1135.1
5	575	848	932.9	957.1	978	1086.8	1132.2
6	625	898	926.7	951.6	974.6	1082.9	1128.2

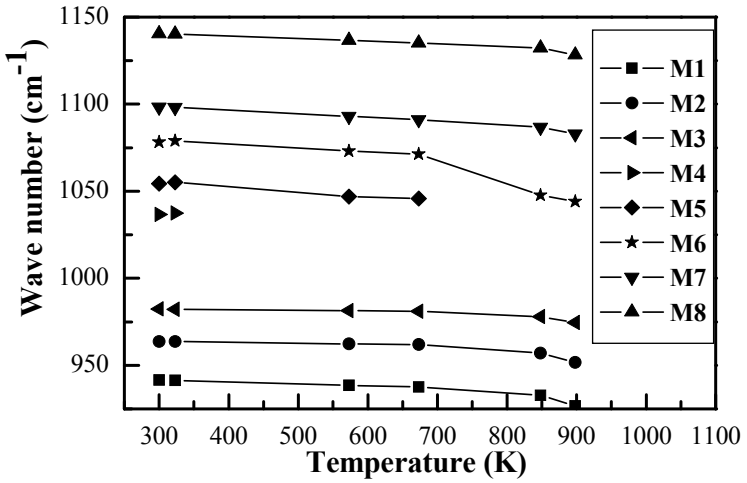

Figure 21. The variation of stretching modes with temperature in the region 850–1250 cm^{-1} while cooling the sample.

Table 8: The full width at half maximum (Δω) of the stretching modes in the region 850–1250 cm^{-1}.

S.No.	Temperature		$\Delta\omega_1$ (cm^{-1})	$\Delta\omega_2$ (cm^{-1})	$\Delta\omega_3$ (cm^{-1})	$\Delta\omega_7$ (cm^{-1})	$\Delta\omega_8$ (cm^{-1})
	(^oC)	(K)					
1	27	300	36(3)	35(7)	31(5)	27(2)	16(1)
2	50	323	38(2)	35(9)	32(5)	27(2)	17(1)
3	78	351	39(3)	36(9)	32(5)	27(2)	17(1)
4	127	400	40(3)	37(10)	34(5)	28(2)	18(1)
5	155	428	41(3)	38(10)	35(6)	28(2)	19(1)
6	200	473	43(3)	39(10)	36(6)	29(1)	19(1)
7	250	523	44(3)	40(11)	38(6)	30(1)	20(1)
8	323	596	46(3)	41(11)	40(6)	30(1)	22(1)
9	350	623	48(3)	41(10)	38(6)	28(2)	22(1)
10	380	653	44(4)	40(10)	39(6)	31(1)	22(1)
11	400	673	43(4)	38(9)	34(5)	24(2)	21(1)
12	425	698	43(4)	39(9)	35(5)	23(2)	21(1)
13	450	723	44(4)	39(10)	36(5)	23(2)	22(1)
14	475	748	44(4)	39(10)	36(5)	23(2)	22(1)
15	500	773	49(4)	42(10)	39(6)	28(1)	26(1)
16	550	823	38(4)	37(9)	39(4)	37(2)	35(1)
17	575	848	38(4)	38(9)	40(4)	37(2)	38(1)
18	585	858	37(5)	38(10)	42(4)	37(2)	39(1)
19	606	879	38(4)	38(10)	42(5)	37(2)	40(2)
20	615	888	37(5)	38(10)	42(5)	36(2)	44(2)
21	625	898	36(5)	38(10)	44(5)	36(2)	45(2)

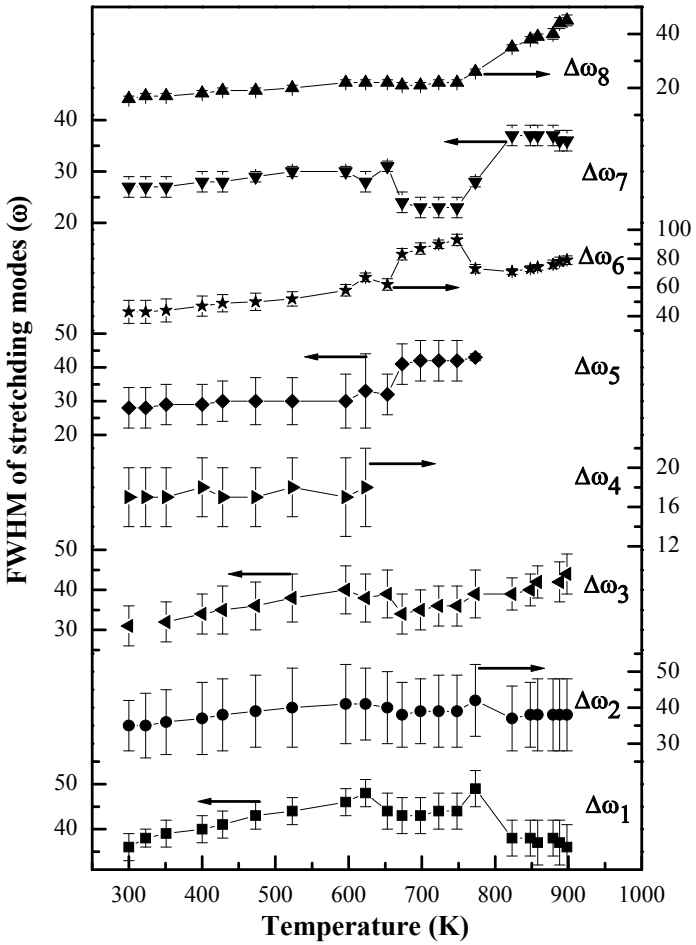

Figure 22. FWHM values of different stretching modes with temperature in the wave number region 850–1250cm^{-1} while heating the sample.

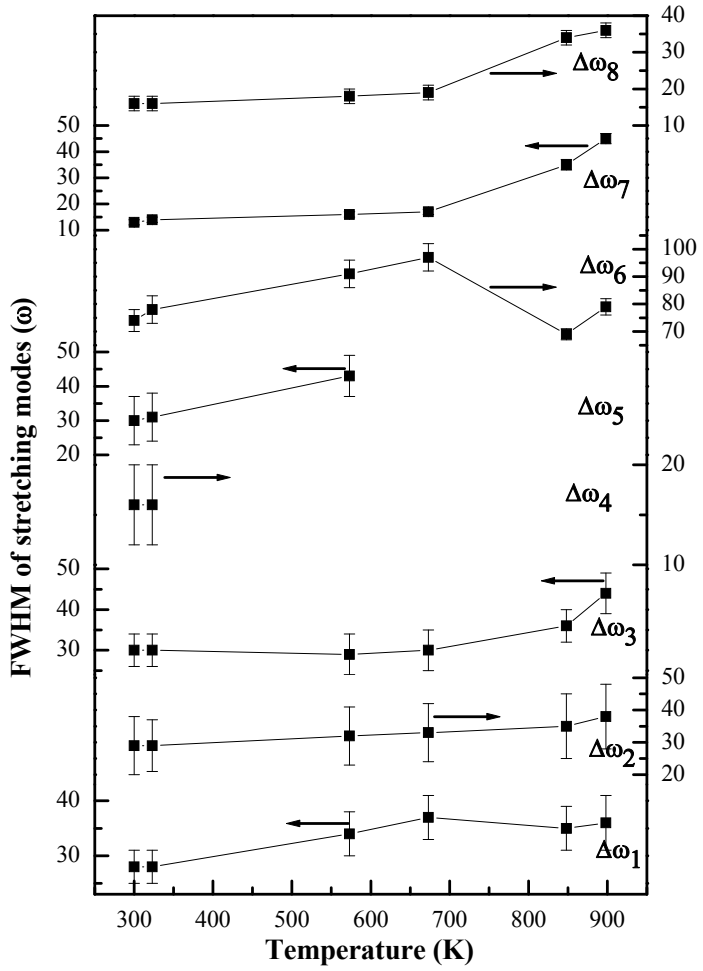

Figure 23. FWHM values of stretching modes with temperature in the wave number region 850–1250cm^{-1} while cooling the sample.

Table 9: The FWHM values (Δω) of the stretching modes in the region 850–1250 cm^{-1}, while cooling.

S.No.	Temperature		$\Delta\omega_1$ (cm^{-1})	$\Delta\omega_2$ (cm^{-1})	$\Delta\omega_3$ (cm^{-1})	$\Delta\omega_7$ (cm^{-1})	$\Delta\omega_8$ (cm^{-1})
	(^{o}C)	(K)					
1	27	300	28(3)	29(9)	30(4)	16(2)	13(1)
2	50	323	28(3)	29(8)	30(4)	16(2)	14(1)
3	300	573	34(4)	32(9)	29(5)	18(2)	16(1)
4	400	673	37(4)	33(9)	30(5)	19(2)	17(1)
5	575	848	35(4)	35(10)	36(4)	34(2)	35(2)
6	625	898	36(5)	38(10)	44(5)	36(2)	45(2)

Stretching modes (850–1250 cm^{-1}):

Figures 16, 17 and 18 show the in-situ FTIR spectra recorded on C-$LiFePO_4$ in the wave number region 850 – 1250cm^{-1}, in the temperature range 300K – 623K, 653K – 773K and 823K – 898K respectively. While figure 19 represents the in-situ FTIR spectra of the same sample from RT – 898K while cooling. In this region, the symmetric stretching modes (υ_1) and anti symmetric stretching modes (υ_3) and of phosphate ion are active and these spectra show eight such active modes (of this region) at room temperature as shown in figure 16. All the spectra shown in the figures 16–19 have been analyzed by fitting each spectrum to a non-linear least square fit to a set of 6–8 lorentzians. The spectra from300K – 623K, could be fitted to a set of *eight* lorentzians as shown in figure 16, while the spectra from 653K–773K and 823K–898K were fitted to a set of *seven* and *six* lorentzians respectively, as shown in figures 17 and 18. During cooling, the FTIR spectra at 898K and 848K are fitted to a set of six lorentzians, spectra at 673K and 57K are fitted to a set of seven lorentzians and spectra at 323K and residual $LiFePO_4$ are fitted to eight lorentzians respectively. In all these figures, black circles show the raw data while the black solid line through the circles shows the non-linear least square fit and the dashed line shows the lorentzian fit for individual peaks.

The wave numbers of the stretching modes thus obtained from the room temperature FTIR spectrum of $LiFePO_4$ are observed to be 942.2 cm^{-1}, 965.6 cm^{-1}, 983.9 cm^{-1}, 1036.6 cm^{-1}, 1052.2 cm^{-1}, 1073.3 cm^{-1}, 1098.4 cm^{-1}, and 1140.2 cm^{-1}. And the different stretching modes in the wave number region 850–1250 cm^{-1} obtained at above room temperature, obtained from the fitting procedure have been tabulated as given in table6. The variation of the bending modes with increase in temperature is plotted in figure 20.

Significantly, all the stretching modes in this wave number region shift to *lower* wave numbers upon *heating*. The shift in the wave number of the stretching modes for the increase in temperature form 300K – 898K is found to be 15.5cm^{-1}, 14cm^{-1}, 9.3cm^{-1}, 15.5 cm^{-1} and 12cm^{-1} for the modes M1, M2, M3, M7 and M8 respectively.

The wave numbers of the stretching modes are found to be increasing with decrease of temperature, while cooling the sample. These values are tabulated in table 7 and are plotted in figure 21. The wave numbers of the stretching modes obtained from the room temperature FTIR spectrum of residual $LiFePO_4$ are observed to be 941.6 cm^{-1}, 963.7 cm^{-1}, 982.3 cm^{-1}, 1036.7 cm^{-1}, 1054.3 cm^{-1}, 1078.1 cm^{-1}, 1098.3 cm^{-1} and 1140.5 cm^{-1} and are nothing but the room temperature bending modes of $LiFePO_4$ before heat treatment of the sample, with in the experimental limits.

Through out the temperature range 300K–898K, over which the FTIR spectra of C-$LiFePO_4$, have been recorded in the wave number region 850–1250 cm^{-1}, the first three modes M1, M2 and M3 i.e., symmetric stretching modes (υ_1) give rise to a *single* very broad peak, during both increase and decrease of temperature. While the asymmetric stretching modes M4, M5, M6, M7 and M8 observed in the room temperature spectrum, merges upon heating and results in reduction in the number of modes and as a result few modes tends to disappear as shown in figures 16–18. And the same has been noticed while cooling the sample down to room temperature, by observing all the five asymmetric stretching modes in the FTIR spectrum of residual C-$LiFePO_4$. This may be explained as follows. At room temperature, the sample gives rise to eight stretching modes, each having a definite excitation energy, which may reflect the different stretching vibrations of the P–O bonds in the phosphate ion. As the sample temperature increases above room temperature, the energy required for the stretching modes decreases, which results in the shift of the modes towards lower wave numbers. At around 653K, the thermal energy overcomes the excitation energy of mode M4 and hence it disappears from the spectrum. Hence the phosphate ion undergoes structural changes; the stretching vibrations (which are dependent on the structure of phosphate ion) are altered and reduced to only seven modes. Similarly, at around 823K, another mode M5 vanishes, resulting the FTIR spectrum with six modes. These structural changes are found to be reversible with decrease of temperature, as shown in figure 19. And the FTIR spectrum of the residual $LiFePO_4$ is shown to be consisting of eight stretching modes.

Figure 22 shows the variation full width at half maximum values of the stretching modes $\mathbf{\Delta}\omega_1$ – $\mathbf{\Delta}\omega_8$ obtained from non-linear least square fit in the temperature range 300K–898K, while heating the sample and these values are tabulated in table 8. Figure 23 shows the variation full width at half maximum values of the stretching modes $\mathbf{\Delta}\omega_1$ – $\mathbf{\Delta}\omega_8$ in the temperature range 300K–898K, while cooling the sample and these values are tabulated in table 9. It has been observed that these values (as denoted) increase steadily with temperature, which shows the disorder developing in the stretching vibrations. Due to the disappearance of the modes M4 and M5 at temperatures 653K and 823K respectively, the FWHM values undergo abrupt changes, with increase in temperature. This may be attributed to sudden changes in the P–O bond lengths of the phosphate ion. The FWHM values are shown to be decreasing with temperature, revealing the ordering of the stretching modes. This shows these structural changes in the phosphate ion are found to be reversible upon cooling in a heat-cool cycle.

The factor group splitting $\Delta\nu_3$ of asymmetric stretching vibrations (ν_3) of $LiFePO_4$, during heating are found to be 103.6, 103.7, 103.9, 104, 104.2, 104.4, 104.3, 104.5, 103.4, 91, 92.3, 91.9,

92.1, 92, 90.2, 85, 85, 84.6, 84.5, 84.5 and 84.1 cm^{-1} at temperatures 300K – 898K as shown in figures 16–18 respectively. While these values are found be 103.5, 103.1, 89.6, 89.4, 84.6, and 84.1 for the temperatures 300K, 323K, 573K, 673K, 848K and 898K respectively.

Finally the following conclusions may be drawn for the stretching modes in the wave number region 850–1250 cm^{-1}.

1. The FTIR spectra of C-$LiFePO_4$ as shown in figures 15–17, in the temperature range 300K – 623K, 653K – 773K and 823K – 898K are shown to be reversible upon cooling the sample in a heat-cool cycle, as revealed from the figure19.

2. a) The shift in the wave number of the stretching modes to lower values observed with increase in temperature indicates the energy required for excitation of the stretching modes decrease, at higher temperatures. And the modes are observed to be shifting to higher wave numbers, while cooling the sample reflects the reversibility of the excitation phenomenon of the stretching modes with temperature.

   b) The disappearance of two of the antisymmetric stretching modes M4 and M5 at temperatures 653K and 823K respectively during heating the sample are found to be restored while cooling with the presence of all the eight modes in the FTIR spectrum of residual $LiFePO_4$.

   c) The different stretching vibrations (the symmetric stretching modes (υ_1) antisymmetric stretching modes (υ_3)) of phosphate ion reflect 'molecular-structural' disorder due to thermal origin. This is revealed from the increase in the increase in full width at half maximum values of all the bending modes. And it is found that the order could be restored in the sample with decrease in temperature. This shows the order – disorder transition observed for the bending modes of the phosphate ion in C-$LiFePO_4$ is reversible.

   3. The abrupt structural changes of the phosphate ion at temperatures around 653K and 773K are found to be reversible.

7.5.3 Further Analysis

The mode (M_x) observed at room temperature (300K) has been assumed to be 'υ_o' and the corresponding mode at any given temperature above 300K be 'υ_x'. Then the shift in the mode M_x at a given temperature with respect to room temperature is defined as '$\delta\upsilon$', from which ($\delta\upsilon/\upsilon_o$) values have been calculated. A plot is drawn between (1/T) versus ($\delta\upsilon/\upsilon_o$). The plot thus obtained shows that the values of ($\delta\upsilon/\upsilon_o$) decay exponentially with (1/T). Hence the following equation has been assumed to analyse the data further.

$$\delta\upsilon = \upsilon_o e^{\left(-E_a/kT\right)} \qquad \text{- - -} \qquad (1)$$

$$\left(\frac{\delta\upsilon}{\upsilon_o}\right) = e^{\left(-E_a/kT\right)} \qquad \text{- - -} \qquad (2)$$

Taking natural logarithm on both sides,

$$\log_e\left(\frac{\delta\upsilon}{\upsilon_o}\right) = -\left(E_a/k\right)\left(1/T\right) \qquad \text{- - -} \qquad (3)$$

where 'E_a' is assumed to be the 'activation energy of the mode (either bending or stretching)', and 'k' is Boltzmann's constant. The plot (1/T) versus ($\delta\upsilon/\upsilon_o$) has been fitted to a straight line to find the temperature T(υ_o) of the initial mode υ_o provided ($\delta\upsilon/\upsilon_o$) varies linearly with (1/T). The data has also been fitted to equation (3) to find the activation energy of the corresponding mode (either bending mode or stretching mode) 'E_a' with (1/T) along X-axis and natural logarithm of ($\delta\upsilon/\upsilon_o$) on Y-axis.

Bending modes:

Heating (530–700 cm^{-1} region):

A plot between (1/T) and ($\delta\upsilon/\upsilon_o$) of each of the four bending modes (black circles), obtained from the non-linear least square fit is drawn as depicted in figure 24. The solid line through the circles shows the limited linear fit. The expected temperature T(υ_o) of the mode υ_o, obtained from the linear fit are given in table 10.

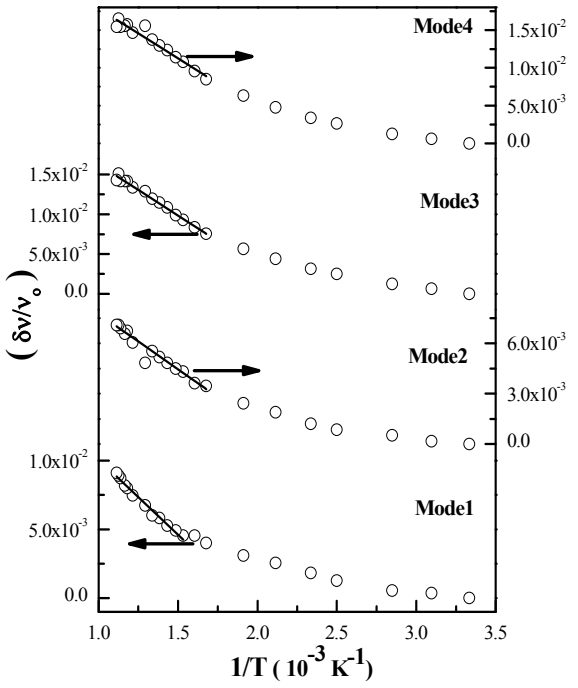

Figure 24. The variation of ($\delta\upsilon/\upsilon_o$) of the bending modes (black circles) with (1/T) in the region 530 – 700 cm^{-1}, while heating the sample.

Table 10: The values of $T(\upsilon_o)$ corresponding to the four bending modes in the region 530 – 700 cm^{-1}.

	Mode 1	**Mode 2**	**Mode 3**	**Mode 4**
$T(\upsilon_o)$	521(22)	474(15)	430(13)	425(29)

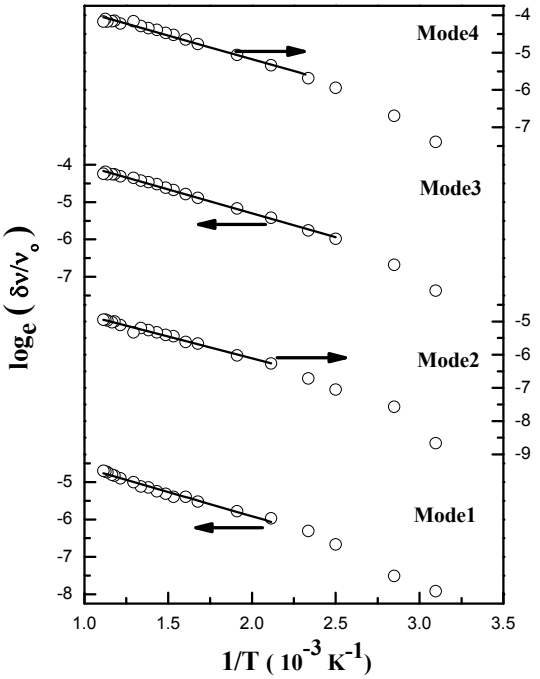

Figure 25. The variation of $log_e(\delta\upsilon/\upsilon_o)$ with (1/T) of the bending modes during increase of temperature in the wave number region 530 - 700cm^{-1}.

Figure 25 shows the variation of $\log_e(\delta\upsilon/\upsilon_o)$ with (1/T) of each of the bending modes, obtained from non-linear least square fit in the wave number region 530 – 700cm^{-1}. The solid line through the circles shows the linear fit for the plot, obtained after fitting the data to equation 3. The values of activation energies 'E_a' thus for each of the bending modes are given in the following table 11.

Table 11: The values of 'E_a' corresponding to the four bending modes in the region 530 – 700 cm^{-1}.

	Mode 1	**Mode 2**	**Mode 3**	**Mode 4**
E_a (eV)	0.112(4)	0.113(4)	0.110(2)	0.109(4)

Cooling (530–700 cm^{-1} region):

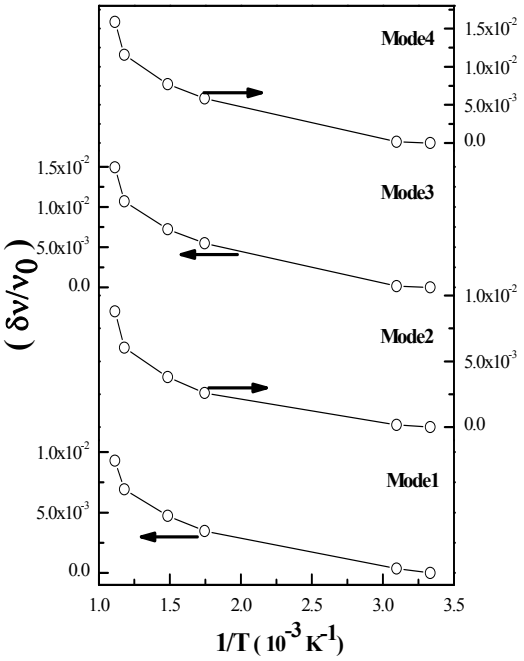

Figure 26. The variation of ($\delta\upsilon/\upsilon_o$) of the bending modes (black circles) with (1/T) in the region 530–700 cm^{-1}, while cooling the sample. The solid line is a guide to the variation.

A plot between (1/T) and ($\delta\upsilon/\upsilon_o$) of each of the four bending modes (black circles), obtained, while cooling the sample to room temperature, is drawn in figure 26. The solid line through the circles **is** a guide to the eye, to observe the variation. Due to insufficient acquisition of the data during cooling, further analysis has not been done. But the plot is shown for a comparison with the data during heating, as shown in figure 24.

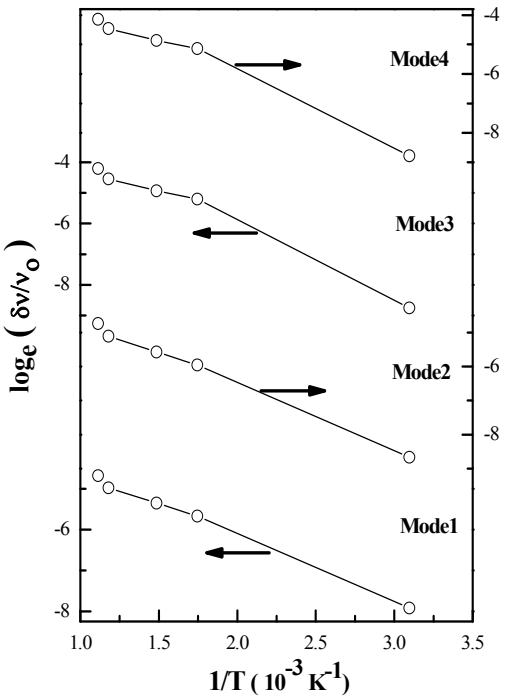

Figure 27. The variation of $\log_e(\delta\upsilon/\upsilon_o)$ with (1/T) of the bending modes with decrease of temperature of the sample in the wave number region 530–700 cm^{-1}.

Figure 27 shows the variation of $\log_e(\delta\upsilon/\upsilon_o)$ with (1/T) of each of the bending modes, obtained, while cooling the sample to room temperature in the wave number region 530–700cm^{-1}. The solid line through the circles acts a guide to the eye, to observe the variation. The plot is shown for a comparison with the data during heating, as shown in figure 25.

Stretching modes (850–1250 cm^{-1})

Heating

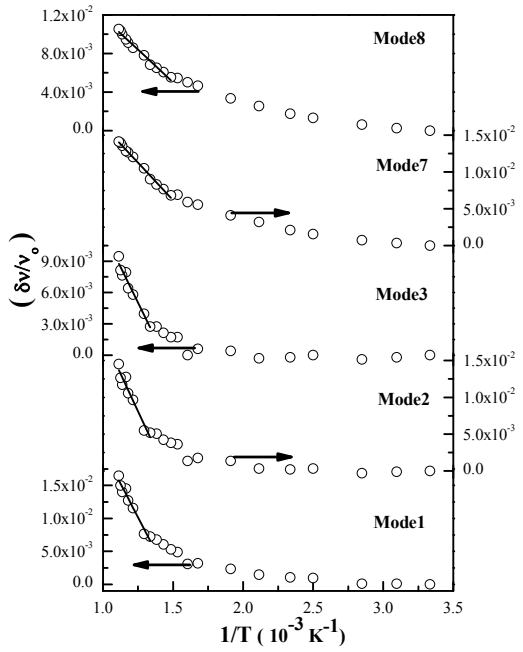

Figure 28. The variation of (δυ/υ$_o$) of the stretching modes (black circles) with (1/T) in the region 850–1250 cm^{-1}, while heating the sample.

A plot between (1/T) and (δυ/υ$_o$) of stretching modes (black circles), obtained from the non-linear least square fit is drawn as depicted in figure 28. The solid line through the circles shows the linear fit. The expected temperature T(υ$_o$) of the mode υ$_o$, obtained from the linear fit are given in table 12.

Table 12: The values of T(υ$_o$) corresponding to the stretching modes in the region 850–1250 cm^{-1}.

	Mode 1	**Mode 2**	**Mode 3**	**Mode 7**	**Mode 8**
T(υ$_o$)	683(55)	678(68)	683(58)	507(15)	540(24)

Figure 29 shows the variation of log$_e$(δυ/υ$_o$) with (1/T) of each of the bending modes, obtained from non-linear least square fit in the wave number region 850 – 1250cm^{-1}. The solid line through the circles shows the linear fit for the plot, obtained after fitting the data to equation 3. The values of activation energies 'E$_a$' thus for each of the bending modes are given in the following table 13.

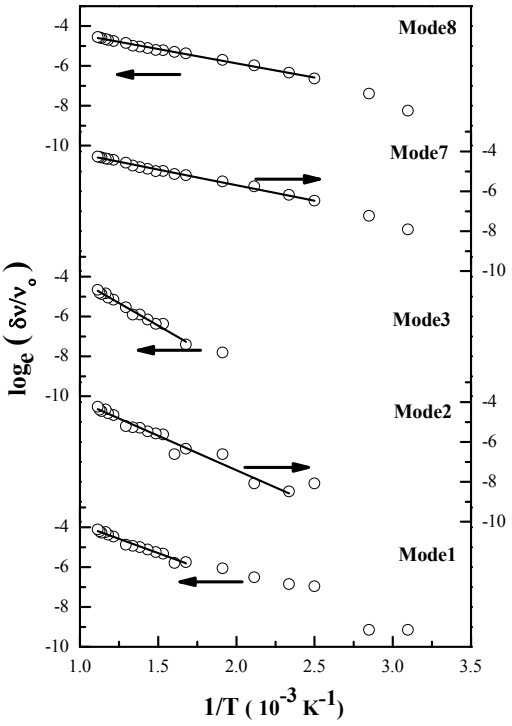

Figure 29. The variation of $\log_e(\delta\upsilon/\upsilon_o)$ with (1/T) for the stretching modes during increase of temperature in the wave number region 850–1250 cm^{-1}.

Table 13: The values of 'E_a' corresponding to the four stretching modes in the region 850 – 1250 cm^{-1}.

	Mode 1	**Mode 2**	**Mode 3**	**Mode 4**	
E_a (eV)	0.24(1)	0.30(1)	0.39(1)	0.135(3)	0.124(2)

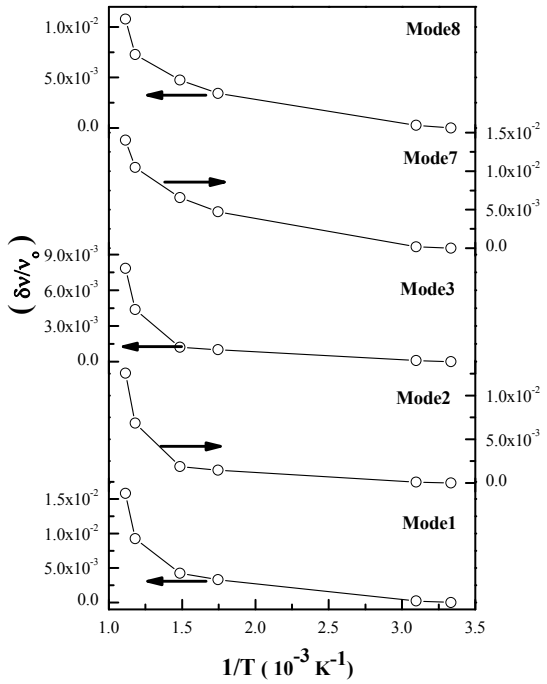

Figure 30. The variation of ($\delta\upsilon/\upsilon_o$) of the stretching modes (black circles) with (1/T) in the region 850–1250 cm^{-1}, while cooling the sample. The solid line is a guide to the variation.

A plot between (1/T) and ($\delta\upsilon/\upsilon_o$) of each of the stretching modes (black circles), obtained, while cooling the sample to room temperature, is drawn in figure 30. The solid line through the circles acts a guide to the eye, to observe the variation. Due to insufficient acquisition of the data during cooling, further analysis has not been done. But the plot is shown for a comparison with the data during heating, as shown in figure 28.

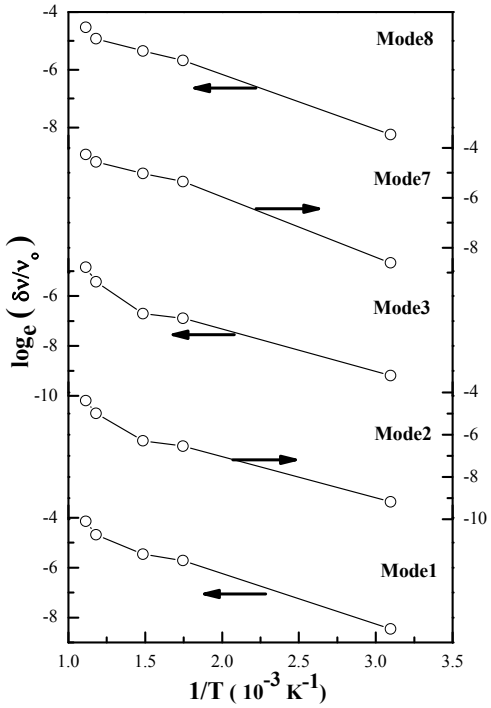

Figure 31. The variation of $\log_e(\delta\upsilon/\upsilon_o)$ with (1/T) of the stretching modes with decrease of temperature of the sample in the wave number region 850–1250 cm^{-1}.

Figure 31 shows the variation of $\log_e(\delta\upsilon/\upsilon_o)$ with (1/T) of each of the stretching modes, obtained, while cooling the sample to room temperature in the wave number region 850–1250cm^{-1}. The solid line through the circles is a guide to the eye, to observe the variation. The plot is shown for a comparison with the data during heating, as shown in figure 29.

Further studies and analysis need to be considered for understanding these systematic variations due to the temperature dependent reversible order – disorder transition set in the sample.

References

1. Paques-Ledent, M. Th., and Tarte, P., *Spectrochimica Acta, **29A**, p1007 (1973)*.
2. Paques-Ledent, M. Th., and Tarte, P., *Spectrochimica Acta, **30A**, p673 (1974)*.
3. Chung, S, -Y., Bloking, J. T., Chiang, Y. –M., *Nature Materials, **1**, p123 (2002)*.
4. Zaghib, K., Ravet, N., Gauthier, M., Gendron, F., Mauger, A., Goodenough, J. B., and Julien, C. M., *Journal of power sources, **163** (2006) p560*.
5. Julien, C. M., Zaghib, K., Mauger, A., Massot, M., Ait-Salah, A., Selmane, M., and Gendron, F., *Journal of Applied Physics, **100**, p063511, 2006*.

6. Lemos, V., Guerini, S., Filho, J. M., Lala, S. M., Montoro, L. A., and Rosolen, J. M., *Solid State Ionics, **177** (2006) p1021*.
7. Ravet, N., Gauthier, M., Zaghib, K., Goodenough, J. B., Mauger, A., Gendron, F., and Julien, C. M., *Chemistry of Materials, **19** (2007) p.2595*.

--- O ---

Chapter 8

Magnetic Phase transition and Relaxation effects in $LiFePO_4$

8.1 Introduction

When two adjacent electronic magnetic moments (spins) in a paramagnetic crystalline lattice are spontaneously aligned parallel (↑↑) below a critical temperature, the Curie temperature T_c, there is a ferromagnetic order and the material is said to be ferromagnetic. When two such neighboring magnetic moments having same magnitude are anti-parallel (↑↓) aligned, and the net magnetic moment in the material is zero, the material is said to have attained an antiferromagnetic state/order. This ordered magnetic state is usually attained through a cooperative second-order phase transition. This transition is usually probed through a magnetic susceptibility measurement which shows a characteristic cusp at a temperature called Neel temperature (T_N). The origin of (anti)ferromagnetism is quantum-mechanical and the most interesting experimental observation in magnetism is the gradual appearance of a spontaneous magnetization in a solid. This fascinating subject is treated in many textbooks **[1–4]**. The concept of a molecular field developed by Weiss sustains to this day and forms the basis of many important models for magnetism. The origin of magnetism in $LiFePO_4$ must be traced to the Fe^{2+} moments stabilized in the orthorhombic lattice and the highly temperature –sensitive microscopic crystalline environments in which they exist.

In this Chapter we describe and discuss our experimental efforts to understand the nature of magnetism and magnetic phase transitions and relaxation in $LiFePO_4$ through DC magnetization and Mossbauer spectroscopy. We begin with a brief theoretical background.

8.2 Molecular field theory of Antiferromagnetism

Let us assume an antiferromagnetic material with two sublattices A and B, with the A lattice consisting of the corner positions and the lattice B, the body-centre positions in a bcc lattice. An atom at an A site then has nearest neighbors that all lie on B sites and next nearest neighbors that all lie on A sites. A similar situation holds for an atom at a B site. The molecular field H_{mA} acting on an atom at an A site may be written as

$$H_{mA} = -N_{AA}M_A - N_{AB}M_B \qquad (1)$$

where M_A and M_B are the magnetizations of the A and B sub lattices, N_{AB} is a molecular field constant for the nearest neighbor interaction, and N_{AA} is a molecular field constant for the next nearest neighbor interaction. Similarly H_{mB} acting on an atom at a B site may be written as

$$H_{mB} = -N_{BA}M_A - N_{BB}M_B \qquad (2)$$

Since the same type of atoms occupy the A and B lattice sites, $N_{AA} = N_{BB} = N_{ii}$ and $N_{AB} = N_{BA}$. Then, if a field H is also applied, the fields H_A and H_B at an atom on the A and B lattices, respectively, are given by

$$H_A = H - N_{ii}M_A - N_{AB}M_B \tag{3}$$

And

$$H_B = H - N_{AB}M_A - N_{ii}M_B \tag{4}$$

The interaction between nearest neighbors is antiferromagnetic and therefore the molecular field constant N_{AB} must be positive. On the other hand, it is conceivable that N_{ii} may be positive, negative or even zero, depending on the particular material.

At thermal equilibrium the magnetizations of the sublattices are given by

$$M_A = \frac{1}{2}Ng\mu_B SB_S(x_A) \tag{5}$$

where
$$x_A = \frac{Sg\mu_B}{kT}H_A \tag{6}$$

and
$$B_S(x_A) = \frac{2S+1}{2S}\coth\frac{2s+1}{2s}x_A - \frac{1}{2S}\coth\frac{x_A}{2S} \tag{7}$$

is the Brillouin function

Similarly
$$B_S(x_B) = \frac{2S+1}{2S}\coth\frac{2s+1}{2s}x_B - \frac{1}{2S}\coth\frac{x_B}{2S} \tag{8}$$

Here N is the total number of atoms (or ions) with a permanent dipole moment per unit volume, and J has been set equal to S.

8.2.1 Behavior above the Néel temperature

The Néel temperature, T_N, is the temperature at which an antiferromagnetic material becomes paramagnetic — that is, the thermal energy becomes large enough to destroy the macroscopic magnetic ordering within the material. Although there is no antiferromagnetic ordering above the Néel temperature, a small magnetization is induced by the applied field. For the usual values of applied field, saturation effects are negligible and the Brillouin function **[5]** can be replaced by the first term of the series expansion in x, namely, $B_S(x) = [(S+1)/3S]x$. Then the above equations 5-8 become

$$M_A = \frac{Ng^2\mu_B{}^2 S(S+1)}{6kT}H_A \tag{9}$$

and

$$M_B = \frac{Ng^2\mu_B{}^2 S(S+1)}{6kT} H_B \qquad (10)$$

Now

$$H_A = \left| H - N_{ii} M_A - N_{AB} M_B \right|$$

$$\Rightarrow H_A = H - N_{ii} M_A - N_{AB} M_B \qquad (11)$$

since H, M_A and M_B are parallel in the paramagnetic region. Similarly

$$H_B = H - N_{ii} M_B - N_{AB} M_A \qquad (12)$$

Substitution of these values of H_A and H_B into the foregoing equations for M_A and M_B gives

$$M_A = \frac{Ng^2\mu_B{}^2 S(S+1)}{6kT} (H - N_{ii} M_A - N_{AB} M_B) \qquad (13)$$

and

$$M_B = \frac{Ng^2\mu_B{}^2 S(S+1)}{6kT} (H - N_{ii} M_B - N_{AB} M_A) \qquad (14)$$

Addition of equations 13 and 14 gives

$$M = M_A + M_B = \frac{Ng^2\mu_B{}^2 S(S+1)}{6kT} [2H - (N_{ii} - N_{AB})M] \qquad (15)$$

Hence the susceptibility $\chi = M/H$ is given by

$$\chi = \frac{C}{T + \Theta} \qquad (16)$$

Where

$$C = \frac{Ng^2\mu_B{}^2 S(S+1)}{6kT} \qquad (17)$$

And

$$\Theta = \frac{1}{2} C(N_{ii} + N_{AB}) \qquad (18)$$

Since, generally, $N_{AB} > N_{ii}$, Θ is positive. Equation (16) may be compared to $\chi = C/(T - \Theta)$, the Curie-Weiss law.

8.2.2 The Néel temperature

Below the Néel temperature, both sublattices possess a spontaneous magnetization (H=0) of equal magnitude but pointing in opposite directions. The critical temperature at which the spontaneous magnetization of one of these sublattices vanishes can be found from eq. 5-8.

Alternatively, the critical temperatures can be found by approaching from the high temperature side ($T > T_N$). Equations (13) and (14) are valid in the vicinity of T_N, for saturation effects are still unimportant. With H = 0, these equations become

$$M_A = \frac{C}{2T}(-N_{ii}M_A - N_{AB}M_B) \tag{19}$$

$$M_B = \frac{C}{2T}(-N_{ii}M_B - N_{AB}M_A) \tag{20}$$

For nonzero values of the magnetizations M_A and M_B the determinant of the coefficients of M_A and M_B must be zero. Application of this condition yields the Néel temperature, namely,

$$T_N = \frac{1}{2}C(N_{AB} - N_{ii}) \tag{21}$$

Hence the Néel temperature is higher, the stronger the AB interaction and the weaker the AA or BB interaction, as is to be expected on physical grounds. Substitution for C from eq. (16) then gives

$$\frac{\Theta}{T_N} = \frac{N_{AB} + N_{ii}}{N_{AB} - N_{ii}} \tag{22}$$

If $N_{ii} = 0$, $T_N = \Theta$, where as if $N_{ii} > 0$, $\Theta > T_N$. if N_{ii} is becomes too large in comparison to N_{AB}, the two sublattice arrangement is assumed unstable.

8.2.3 Susceptibility below the Néel temperature

In the absence of any applied magnetic field the sublattice magnetizations M_A and M_B are antiparallel to one another below the Néel temperature. The crystalline anisotropy, assumed for simplicity to be uniaxial, determines the common direction of M_A and M_B, since these sublattice magnetizations will be collinear with the easy direction. In general, the applied field may make any arbitrary angle with the easy axis. Now let us suppose the applied field H is parallel to H_{mA} and antiparallel to H_{mB}. Then x_A and x_B equations may be written as

$$x_A = \frac{g\mu_B S}{kT}(H - N_{ii}M_A + N_{AB}M_B) \tag{23}$$

And

$$x_B = \frac{g\mu_B S}{kT}(-H - N_{ii}M_B + N_{AB}M_A) \tag{24}$$

On the other hand, when H = 0, $M_A = -M_B = M_0$, it follows from equations 5-8, that $x_A = -x_B = x_0$, where

$$x_0 = \frac{g\mu_B S}{kT}[(N_{AB} - N_{ii})M_0] \tag{25}$$

The Brillouin function may be expanded as a Taylor series in H. If only the first-order term is retained, we have

$$B_S(x_A) = B_S(x_0) + \frac{g\mu_B S}{kT}[H + N_{ii}(M_0 - M_A) + N_{AB}(M_B - M_0)] \times B_S{}^1(x_0) \tag{26}$$

And

$$B_S(x_B) = B_S(x_0) - \frac{g\mu_B S}{kT}[H + N_{ii}(M_B - M_0) + N_{AB}(M_0 - M_A)] \times B_S{}^1(x_0) \tag{27}$$

where $B_S{}^1(x_0)$ is the derivative of the Brillouin function with respect to its argument. The coefficient $B_S{}^1(x_0)$ in eq. (26) is the difference of Eqs. (23) and (24). Multiplication of eqs. (26) and (27) by $\frac{1}{2}g\mu_B SN$ yields the sublattice magnetizations M_A and M_B, respectively. The magnetization M induced by the field is then $M = M_A - M_B$. From this equation it is easy to show that the susceptibility $\chi_{11}(T) = M/H$ is given by

$$\chi_{11}(T) = \frac{n\mu_B{}^2 g^2 S^2 B_S{}^1(x_0)}{kT + \frac{1}{2}(N_{ii} + N_{AB})\mu_B{}^2 g^2 S^2 N B_S{}^1(x_0)} \tag{28}$$

At absolute zero, this equation predicts $\chi_{11} = 0$. The physical reason is that in the approximation of the molecular field theory all the atomic moments are either parallel or antiparallel to the applied field at $T = 0^oK$. Hence the field does not exert any torque on the moments and the induced magnetization is zero. As the temperature increases, the χ_{11} also increases until at the Néel temperature $\chi_{11}(T_N)$ becomes equal to the susceptibility $\chi(T)$ given by eq. (16). For $T > T_N$, eq. (28) reduces to eq. (16).

8.3 Paramagnetic – Antiferromagnetic Phase transition:

Although the magnetic moment of a body is zero both in paramagnetic and antiferromagnetic states, their magnetic characteristics are quite different. At high temperatures the magnetic susceptibility is governed by Curie-Weiss law, and at the Néel point it reaches maximum; as temperature is lowered further, the magnetic susceptibility diminishes. When temperature passes through the Néel point, the heat capacity of an antiferromagnetic undergoes a jump wise change; this

effect is typical of the phase transitions of the second order. Such a phase transition is a "disorder-to-order" transition when the Neel point is approached from above.

In this particular case, the 'disorder' is found in the absolute identity of all lattice sites in which magnetic atoms are located so that the mean magnetic moment is zero at each site. Beginning with the Néel point (at $T \leq T_N$), an 'order' appears and lattice sites grow to be different; in some of them the mean magnetic moment points in one direction , and in the others it points in the opposite direction. The transition is smooth (and it must be for any phase transition of the second order) because at the Neel temperature the mean magnetic moment in a lattice site is zero, and reaches its maximum possible value at T = 0 K. This behavior imparts more physical meaning to conclude that an antiferromagnetic is composed of two (or more in general) ferromagnetic sublattices inserted in to each other. It is known that both in antiferromagnetics and ferromagnetics, the main role is played by the exchange interaction.

8.4 Antiferromagnetism in $LiFePO_4$

Even though $LiFePO_4$ was found to be electrochemically active material much later (in 1997) by Padhi et al **[6]**, but its magnetic structure has been determined as early as in 1967 by Santoro and Newnham **[7]**. They have discovered that $LiFePO_4$ undergoes a magnetic structural transition from paramagnetic to antiferromagnetic state. They found that the reciprocal susceptibility of $LiFePO_4$ shows a minimum at 50 ± 2^oK, the Néel temperature. It is known that the magnetic properties are determined by the electronic states and may thus reflect the potential advantage of $LiFePO_4$. After Goodenough's group **[6]** proposed the electrochemical nature of the material, the research on this material has shot up. Particularly, extensive work by Julien's group **[8–10]** on magnetic measurements has given a picture of magnetic structure of $LiFePO_4$. Luo Zhi et al **[11]** have done the low temperature Mössbauer measurements of $LiFePO_4$ and evaluated the hyperfine parameters above and below the Néel temperature. Rousse et al **[12]** have solved the magnetic structures using neutron diffraction on polycrystalline samples of $LiFePO_4$. A comparison has been made between the magnetic structures of $LiFePO_4$ and $FePO_4$ and the difference in Néel temperatures have been discussed both in terms of super and super-super exchange interactions and anisotropy of Fe^{2+}.

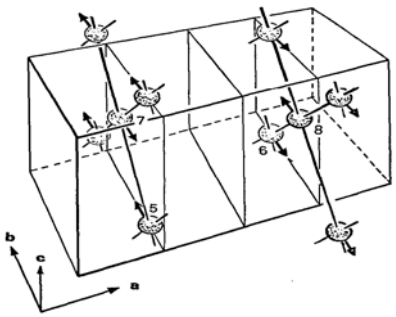

Figure 1. Magnetic structure of $LiFePO_4$. Only the iron positions are shown. (Courtesy: R. P. Santoto et al)

In 1969, Ok **[13]** had shown that the antiferromagnetic ferrous carbonate undergoes slow electron relaxation, that is spin-lattice relaxation phenomena, with Mössbauer spectra recorded at low temperatures. Also, electron-spin relaxation phenomena have been observed by many investigators **[14–19]**. However, most of these studies in iron compounds were restricted to the ferric (Fe^{3+}) ions. Though, Luo Zhi et al **[11]** have done the Mössbauer studies of $LiFePO_4$, they were not aimed at the relaxation effects in it. And to the best of our knowledge, no relaxation effects in the Fe^{2+} ions in the antiferromagnetic $LiFePO_4$ have been discussed. Among all experimental probes, Mossbauer spectroscopy effectively combines and optimizes both electrical (electrostatic) and magnetic aspects of the magnetic response through isomer shift, quadrupole splitting and magnetic hyperfine interactions. In an Fe^{2+} system such as $LiFePO_4$ these parameters are all expected to be sensitive to temperature as mentioned earlier. Furthermore as a direct probe of low-temperature magnetism DC magnetization reveals in a sensitive manner the basic changes $LiFePO_4$ undergoes as it orders antiferromagnetically and enables the temperature-dependence of magnetic susceptibility to be accurately measured and used to test qualitatively the models for antiferromagnetism.

8.5 DC Magnetisation measurements

In the zero-field-cooled (ZFC) case, the sample was cooled in zero magnetic field to 5^oK ($T << T_N$), and magnetisation, M(T), was measured as a function of temperature while heating the sample to temperatures above room temperature. While in the field-cooled (FC) case, a field of H = 100 Oe was applied on the sample and the sample was cooled to 5^oK. Magnetisation M(T) of the sample was measured in the same field from 5^oK to above room temperature. These measurements were carried out using SQUID magnetometer. All the above said measurements were carried out on 5.14 mg of C-$LiFePO_4$ sample.

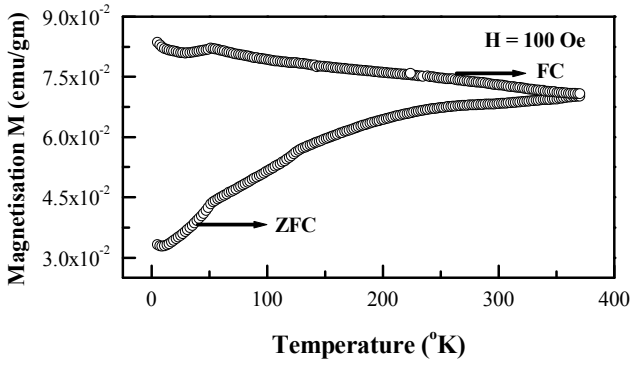

Figure 2. Temperature variations of the zero-field-cooled (ZFC) and field-cooled (FC) magnetizations at an applied filed of H = 100 Oe for C-LiFePO₄.

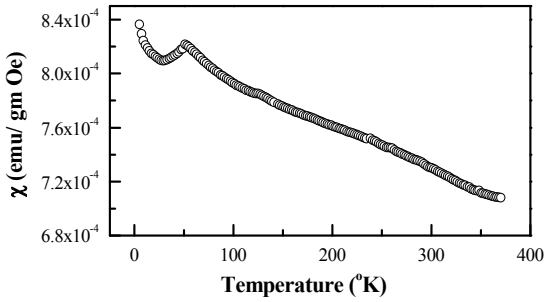

Figure 3. The DC magnetic susceptibility $\chi(T)$ of C-LiFePO₄.

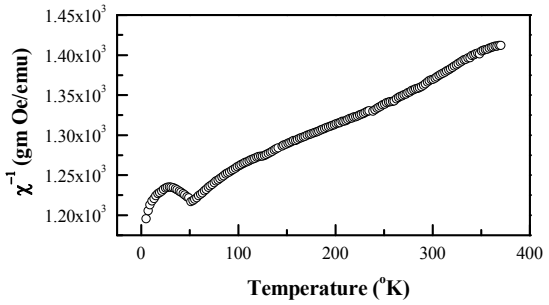

Figure 4. The reciprocal magnetic susceptibility $\chi^{-1}(T)$ of C-LiFePO₄.

Figure 2 shows the zero-field-cooled (ZFC) and field-cooled (FC) magnetisation at an applied field of H = 100 Oe on C-LiFePO$_4$. While Figures 3 and 4 depicts the DC magnetic susceptibility $\chi(T)$ and reciprocal magnetic susceptibility $\chi^{-1}(T)$ with temperature. From figure 3, it is evident

that the magnetic susceptibility $\chi(T)$ increases down to 50°K, and suddenly undergoes a decrease. The temperature at which the fall in $\chi(T)$ was observed is identified as Néel temperature and is found to be 50.9°K. The magnetic susceptibility shows a deviation from the linear behavior at this temperature suggesting that the sample is well crystallized and neither structural defects nor the impurities can impede the propagation of long-range spin correlations that are responsible for the onset of the antiferromagnetic ordering. And also this spin correlation length is limited by thermal fluctuations. We note that the temperature dependence of the magnetic susceptibility does not follow the dependence predicted for the 2D square lattice of classical spins as it does not show a typical broad maximum **[20]**.

Figure 5 shows the variation of reciprocal magnetic susceptibility $\chi^{-1}(T)$ down to temperature 50°K, the Néel temperature observed for C-$LiFePO_4$. As is evident, at temperatures above Néel temperature, the DC magnetic susceptibility obeys eq. (16), which may be compared to Curie-Weiss law $\chi = C/(T-\Theta)$. The reciprocal magnetic susceptibility $\chi^{-1}(T)$, shown as circles in the figure 5 is fitted to Curie-Weiss law and the thick line through the circles shows the fit. Due to the continuous variation of the slope of the curve shown in figure 5, Curie temperature could not be reported here and further investigations are under consideration.

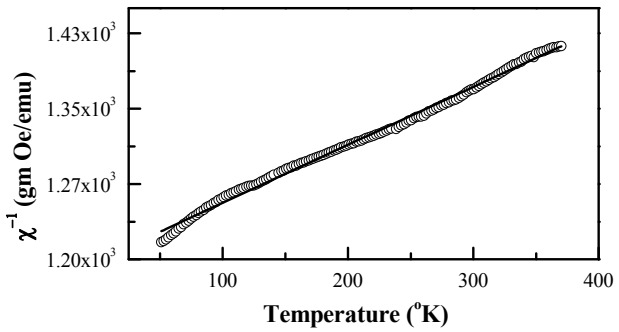

Figure 5. The reciprocal magnetic susceptibility $\chi^{-1}(T)$ of C-$LiFePO_4$ above Néel temperature.

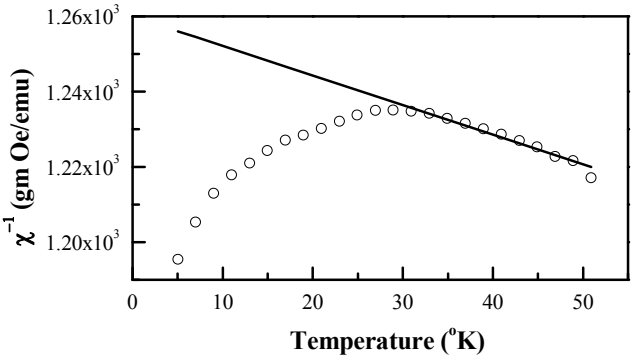

Figure 6. The reciprocal magnetic susceptibility $\chi^{-1}(T)$ of C-LiFePO$_4$ below Néel temperature.

The variation of reciprocal susceptibility $\chi^{-1}(T)$ below the Néel temperature is shown in figure 6. An anomalous feature observed for the C-LiFePO$_4$ sample in question is that the $\chi^{-1}(T)$ curve at around 27°K is characterized by a sharp decrease in $\chi^{-1}(T)$ upon cooling through this temperature. This feature signals the onset of a spontaneous magnetisation at this temperature **[10]**, which is the signature of the weak ferromagnetic component of $Li_3Fe_2(PO_4)_3$ at this temperature **[21, 22]**. This was proposed by showing a narrow doublet in the room temperature Mössbauer spectrum of Anderson et al **[22]**. This narrow doublet is conspicuously absent in the room temperature Mössbauer spectrum of LiFePO$_4$ shown in chapter 2 and also in the forthcoming sections of this chapter rules out the presence of $Li_3Fe_2(PO_4)_3$ in our sample demonstrating the power of Mossbauer spectroscopy. Thus the origin of the slight rise in the susceptibility around 27 K cannot possibly be traced to the existence of a ferromagnetic phase. More work is necessary to clarify this feature. The reciprocal magnetic susceptibility $\chi^{-1}(T)$ below Néel temperature has been fitted to a straight line. The thick line in figure 6 shows the fit. The fit has been extrapolated down to 0°K to obtain $\chi^{-1}(T)$ at absolute zero. The reciprocal susceptibility was found to be 1.26×10^3 gm Oe/emu and the magnetic susceptibility $\chi\ (T)$ of C-LiFePO$_4$ at absolute zero was determined to be 7.937×10^{-4} emu/gm Oe.

8.6 Relaxation effects in Mössbauer spectroscopy:

Relaxation effects in Mössbauer line shape arise when the nucleus is subject to fluctuations in its surroundings occasioned by spin-lattice/spin-spin interaction, time-varying electric field gradients, and a host of other dynamical processes. Quite generally, the effect of relaxation is to cause shift, broadening, narrowing and sometimes collapse of the spectra. We shall present here, a qualitative picture of the relaxation phenomenon in Mössbauer studies with more emphasis on the physical concepts rather than mathematical details. Most theoretical treatments of relaxation effects in

Mössbauer spectra necessarily involve certain formal techniques which often obscure the essential physical insight.

While looking at Mössbauer line shape consider just a single nucleus which is part of a many body system consisting of the surrounding electrons and other elementary excitations including phonons, magnons. One of the features observed upon cooling the sample is the increase in width of the Mössbauer lines, due to Debye-Waller factor.

The basics of the relaxation phenomenon is shown in the following figure. It shows the nucleus in *direct* interaction with its surrounding electrons. The latter, in turn, interact with the other degrees of freedom which constitute the heat bath. Relaxation effects occur whenever there is time-fluctuation in the direct interaction between the nucleus and its surrounding electrons within the lifetime of the Mössbauer state. Thus relaxation phenomenon may arise from any of the following three events.

1. *Fluctuations in the Isomer shift*

   A common example of this case is that of a point defect, e.g., an interstitial or vacancy which undergoes jump diffusion in the vicinity of the Mössbauer nucleus. As a result the electronic wave function is modulated abruptly leading to a fluctuating isomer shift. A case in point is the study of hydrogen diffusion in tantalum **[23, 24]**. From an analysis of the spectra, quantities such as the concentration and the diffusivity of hydrogen interstitials can be extracted.

2. *Fluctuations in the Magnetic Hyperfine Interaction*

   There are innumerable instances of this case because the electronic component of the magnetic hyperfine coupling between the nucleus and its surrounding electrons is likely to interact with a host of other degrees of freedom e.g., the other electrons via the dipolar mechanism **[25]**, phonons **[26, 27]**, conduction electrons **[28, 29]**, spin waves **[30]**, etc. As a result of this interaction, the local field created by the electrons at the site of the nucleus fluctuates randomly. Denoting the local field by H(t) the Hamiltonian for the nucleus may be written as

$$H(t) = g\mu_N I_z H(t) \qquad (29)$$

   where g is the g-factor, μ_N the nuclear magneton and Iz the z-component of the nuclear spin. In view of this interaction, an isolated Mössbauer line (for ^{57}Fe, say) with a natural line width, splits into a six-finger pattern if the local field is static. That is, during the lifetime of the Mössbauer state the local field remains almost constant in time. On the other hand, when the local field varies on a time-scale comparable to the lifetime one sees a relaxation pattern characterized by broadening and shift of the resonance line. From an analysis of the spectra the statistical properties of the internal field can be determined.

In writing down Eq. (29) two assumptions have been made. First, the field is taken to lie along the z-axis and second, the field is assumed to be a classical variable. One example of this simple-minded situation is that of a magnet consisting of various domains in which the internal field is pointed along positive (or negative) z-axis. If an oscillatory magnetic field is imposed on the system externally, the domains begin to move. A Mössbauer nucleus embedded inside the system will find the local field 'switch' between the ± z-axes at random.

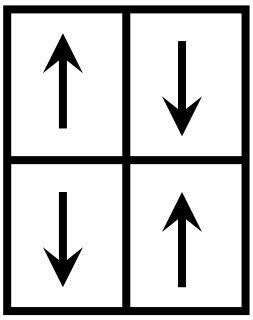

Figure 7. The arrows indicate the directions of the magnetization and hence the internal fielding different domains.

From a microscopic viewpoint the local field H arises from the spin angular momentum of the electron. Thus the Hamiltonian in Eq. (29) may equally describe a uniaxial magnetic hyperfine interaction.

$$H(t) = AI_z S_z(t) \qquad (30)$$

where A is the hyperfine constant. The time fluctuating electronic spin can be decomposed as

$$S_z(t) = \overline{S}_z + \left(S_z(t) - \overline{S}_z\right) \qquad (31)$$

where the bar denotes a time average. If the system is ergodic (which means having zero probability that any of its states will never recur) as most systems are, $\overline{S}_z$ may also be interpreted as the ensemble-averaged spin angular momentum of a many electron system which, in fact, is proportional to the magnetization of the specimen.

3. Fluctuations in the Electric Quadrupolar Interactions

The third important instance of relaxation effect occurs in the case of time varying electric field gradients (EFG) leading to a fluctuating quadrupolar interaction.

8.7 Low Temperature Mössbauer Experimental setup

A Mössbauer spectrometer with an electromechanical drive system manufactured by Elron Co. and stabilized up to ±0.001 mm/sec was used with 10-mCi Co^{57} source in rhodium matrix which

was kept at room temperature. Temperature measurement and control were carried out by a platinum resistance and a heater above 50K with an accuracy of 0.5K. A carbon resistance thermometer calibrated at liquid-nitrogen, liquid hydrogen and liquid-helium temperatures was used for temperature measurement and control below 50K with an accuracy of 0.1K. The temperature near the antiferromagnetic transition temperature was controlled manually with a stability of 0.01K using a highly sensitive galvanometer and a heater. The $LiFePO_4$ sample used for the Mössbauer measurements contained $10mg/cm^2$ of the iron, and the uniformity was obtained by thoroughly grinding. The sample was sandwiched between the sheets of high-purity aluminium foil (~0.2 mm thick) and mounted in a variable temperature insert (for a helium cryostat), in which the sample temperature may be maintained as desired.

8.8 Analysis of Mössbauer Spectra

The Mössbauer spectra of $LiFePO_4$ at various temperatures are shown in figure 8 and these spectra are fitted to static full Hamiltonian and the fits are shown by thick line passing through the data. This static full Hamiltonian properly calculates the line positions and intensities for any combination of hyperfine magnetic filed B_{hf} and electric field gradient (EFG) tensor. Below 48 K, the spectra consists of six lines, which can be analysed by diagnolising the 4×4 magnetic hyperfine and quadrupole-interaction matrix **[31]** for the first excited state of Fe^{57} to give magnetic hyperfine field and quadrupole splitting. And all the spectra at and below 45K are fitted with one doublet and a sextet.

On the basis of the temperature dependence of the magnetic hyperfine field B_{hf}, the transition point of antiferromagnetic phase may be determined. The temperature dependence of the hyperfine field is shown in figure 9. From the figure, it is evident that, the spectra did not change as the temperature is increased from 20 to 45 K. The magnetic hyperfine field of the sample at 20K was found to be 12.32(1) Tesla, and found to decrease to two-third value (of 12.32 T) at 45 K. And it showed a sudden fall at 48 K and reaches the minimum value (roughly 0.1 T) as the temperature approaches to 50K. So, the transition temperature for antiferromagnetic to paramagnetic transition is less than 48 K, the Néel temperature. While the hyperfine field observed by Zhi et al **[11]** at the Neel temperature 50K (their claim) was around 53kOe, little less than the half of the hyperfine field (115kOe) observed at 20 K.

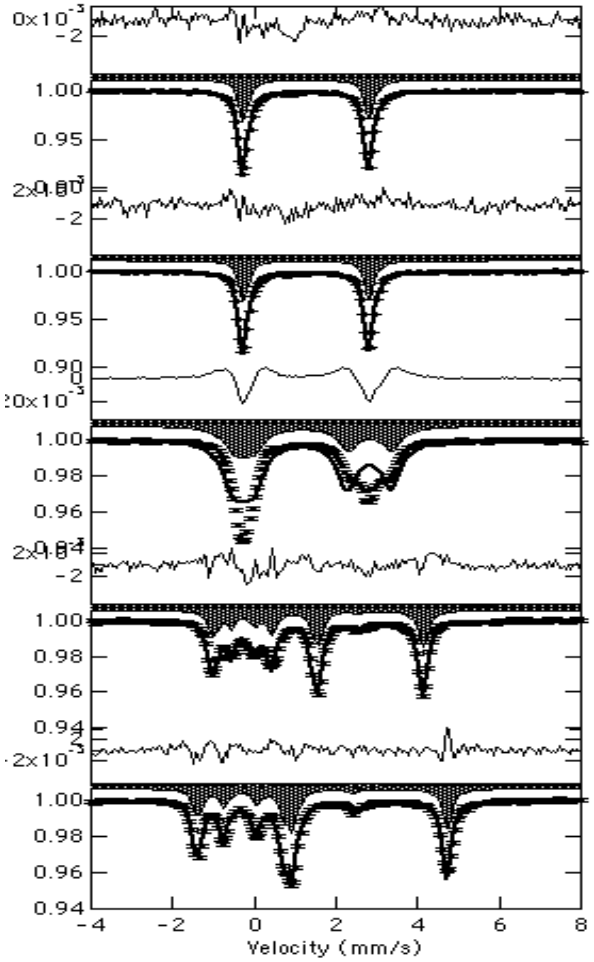

Figure 8. The Mössbauer spectra recorded at temperatures 300, 50, 48, 45 and 20 K, from top to bottom. The thick line being the fit obtained from Static full Hamiltonian.

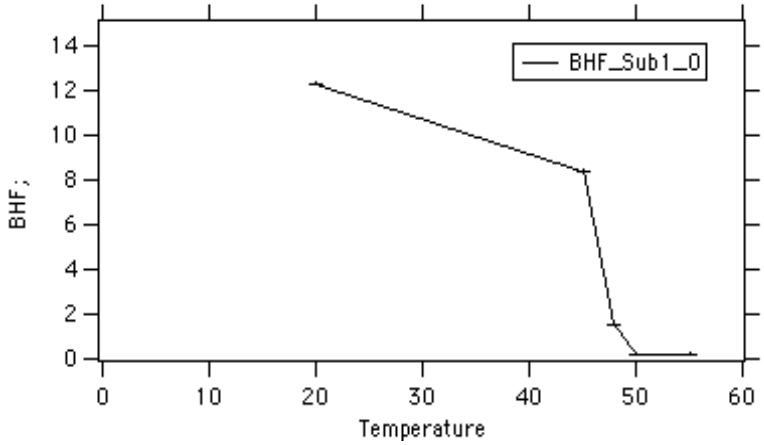

Figure 9. Temperature dependence of Hyperfine field B_{hf} (in Tesla). The line is a guide for the eye.

Another interesting point evident from the fits shown in figure 8 is that as the temperature is increased above 20°K towards T_N the highest-energy line (the extreme right line) broadens much more

than the other lines. To begin with note that this asymmetric broadening does not come from a non uniform temperature distribution across the sample or from any other instrumental effects. This has been proved by mounting an iron foil in the same place as the $LiFePO_4$ sample, which did not show any instrumental effects on the line broadening.

Another noteworthy point is the asymmetric line broadening of the doublet in the paramagnetic state above T_N, as shown in figure 8. This kind of asymmetric line broadening of a doublet has been observed for paramagnetic Fe^{3+} ions in some materials **[32]**, and was interpreted as evidence of slow electron-spin relaxation as compared to the nuclear–precession frequency.

The angle between the magnetic hyperfine field B_{hf} and the direction of the maximum electric field gradient is defined as θ, and η is defined to be asymmetry parameter of the electric field gradient (EFG). The line positions and relative intensities shown in the figure 8 are calculated for θ = 0 i.e., the hyperfine field B_{hf} is along the principal axis of the electric field gradient. This is due to the fact that the EFG axis must be perpendicular to the mirror symmetry plane, so are the magnetic moments. The asymmetry parameter η is found to be 0.766(6). Since this value is in the range of 0 to 1, it means that the fitted angles between x-y-z of the electric field gradient (EFG) tensor and the hyperfine magnetic field B_{hf} are corrected (not necessarily to reorder the axis system of the EFG).

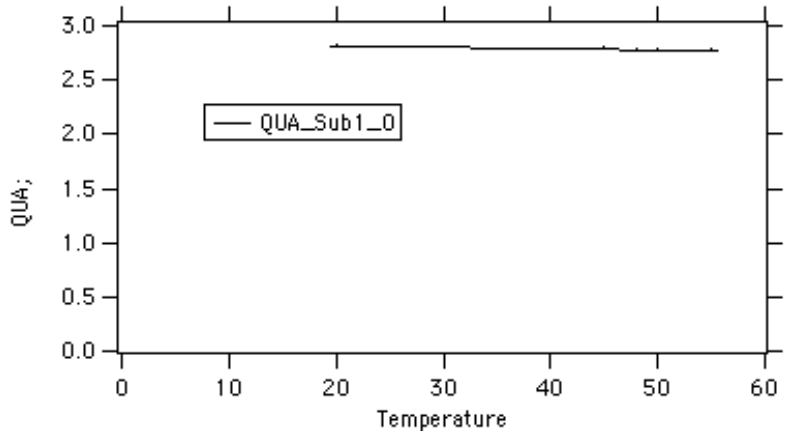

Figure 10. Temperature dependence of quadrupole splitting Δ.

The temperature dependence of the quadrupole splitting Δ is shown in figure 10. The change in Δ is caused by the influence of hyperfine field. Under the first-order perturbation, the quadrupole splitting may be expressed as

$$\Delta(T < T_N) = \frac{eQV_{zz}}{2}(3\cos^2\theta) \qquad (32)$$

where θ is the angle between the hyperfine field and the principal component of the electric field gradient. And this is evaluated to be 2.82(6) mm/sec and found to be a constant (within error limits) at all temperatures.

8.9 Conclusions

DC magnetization and low-temperature (up to 20 K) Mossbauer spectroscopy measurements on nanocrystalline $LiFePO_4$ have established the antiferromagnetic ordering in this compound which begins at ~50 K but is not apparently complete at the lowest of temperatures employed in this work. These measurements have also revealed interesting relaxation phenomena. Extended measurements of Mossbauer spectra at sub-helium temperatures as well as neutron diffraction measurement would probably give a more definitive quantitative picture of this fascinating phenomenon.

References

1. Kittel, C., *Introduction to Solid State Physics*, Chapter 16,7th Edn, Wiley publishers.
2. Animalu, A. O. E., *Intermediate Quantum Theory of Crystalline Solids*, Prentice Hall India, New Delhi,1978, Chapter 10,p 353.
3. Lev Kantarovich, *Quantum Theory of the Solid State: An Introduction*, Kluwer Academic, Dordrecht, 2004, Chapter 6, p.299.
4. Feng Duan and Jin Guojun, *Introduction to Condensed Matter Physics*, Volume 1, World Scientific Pub, Singapore, 2005, Chapter 7, p.449.
5. Morrish, A. H., *The physical principles of magnetism*, Robert E. Krieger publishing company, Inc., Huntington, Newyork (1980).
6. Padhi, A. K., Nanjundaswamy K. S., Goodenough J. B., *Journal of Electrochemical Society, **144**, p1188 (1997)*.
7. Santoro, R. P., and Newnham, R. E., *Acta Crystallography, **22**, p344 (1967)*.
8. Ait-Salah, A., Zaghib, K., Mauger, A., Gendron, F., and Julien, C. M., *Physica Status Solidi (A) **203(1)**, R1 (2006)*.
9. Zagbib, K., Ravet, N., Gauthier, M., Gendron, F., Mauger, A., Goodenough, J. B., and Julien, C. M., *Journal of Power Sources, **163**, p560 (2006)*.
10. Ravet, N., Gauthier, M., Zagbib, K., Goodenough, J. B., Mauger, A., Gendron, F., and Julien, C. M., *Chemistry of Materials, **19**, p2595 (2007)*.
11. Luo Zhi, Di Nai-Li, Kou Zhi-Qi, Cheng Zhao-Hua, Liu Li-Jun, Chen Li-Quan, and Huang Xue-Jie, *Chinese Physics, **13(12)**, p2158 (2004)*.
12. Rousse, G., Rodriguez-Carvajal, J., Patoux, S., and Masquelier, C., *Chemistry of Materials, **15**, p4082 (2003)*.

13. Hang Nam Ok, *Physical Review, **185(2)**, p472 (1969)*.
14. Wertheim, G. K., and Remeika, J. P., *Physics Letters, **10**, p14 (1964)*.
15. Blume, M., *Physical Review Letters, **14**, p96 (1965)*.
16. Blume, M., and Tjon, J. A., *Physical Review, **165**, p446 (1968)*.
17. Campbell, L. E., and Debenedetti, S., *Physical Review, **167**, p556 (1968)*.
18. Wichman, H. H., Klein, M. P., and Shirley, *Physical Review, **152**, p345 (1966)*.
19. Vander Woode, F., and Dekker, A. J., *Physica Status Solidi, **9**, p977 (1965)*.
20. Curely, J., and Rouch, J., *Physica B, **254**, p298 (1998)*.
21. Goni, A., Lezama, L., Moreno, N. O., Fournes, L., Olazcuaga R., Barberis, G. E., and Tojo, T., *Chemistry of Materials, **12**, p62 (2000)*.
22. Anderson, A.S., Kalaska, B., Jonsson, P., Haggstrom, L., Nordblad, P., Tellgren, R., and Thomas, J. O., *Journal of Materials Chemistry, **10**, p2545 (2000)*.
23. Heidemann, A., Kaindl, G., Saloman, D., Wipf, H., and Wortmann, G., *Physical Review Letters, **36**, p213 (1976)*.
24. Wipf, H., and Heidemann, A., *Journal of Physics, **C13**, p5757 (1980)*.
25. Shenoy, G. K., Dunlap, B. D., Dattagupta, S., and Asch, L., *Physical Review Letters, **37**, p539 (1976)*.
26. Afanas'ev, A. M., and Yu. Kagan, *Soviet Physical JETP, **18**, p1139 (1964)*.
27. Gabriel, H., Bosse, J., and Rander, K., *Physica Status Solidi, **27**, p301 (1968)*.
28. Hirst, L. L., *Journal of Physics and Chemistry of Solids, **31**, p655 (1970)*.
29. Hartmann-Boutron, F., *Annals of Physics, Paris **9**, p285, (1975)*.
30. Kagan, Yu, and Afanas'ev, A. M., *Soviet Physics JETP, **20**, p743 (1965)*.
31. Ok, H. N., and Mullen, J. G., *Physical Reviews, **168**, p563 (1968)*.
32. Bradford, E., and Marshall, W., *Proceedings of Physics Society (London), **87**, p731 (1966)*.

--- O ---

Chapter 9

Electrochemical Characterization of $LiFePO_4$

9.1 Test cell construction

Electrochemical measurements on nanocrystalline C-$LiFePO_4$ were conducted by assembling standard R2032 coin-type test cells. Working electrodes for the cells were made by mixing 70-85 wt% of active powder, 0-15 wt% carbon black, and 8-15 wt% polyvinylidene difluoride (PVdF) in a mortar and pestle. The dry powder mix was blended with N-methylpyrolidinone (NMP) to make a slurry, which was then spread uniformly on a 1 cm^2 aluminium or copper substrate current collector. The choice of a material to be used as a current collector relates to its reactivity and surface chemistry. Copper is the preferred substrate to be coated in the preparation of anodes. Although copper does not dissolve electrochemically in non-aqueous lithium salt solutions in the operating potential range (0–4 V), it is reactive in the battery electrolyte solutions **[1]**. Specifically, redox reactions between the copper and salt anions form a surface coating that is electrically conducting and can allow electron transfer to the active mass. In the case of cathode materials, aluminium is the substrate material of choice. Despite being thermodynamically unstable at operating voltages greater than 3 V, aluminium also derives a form of pseudo-stability due to passivation effects afforded by the formation of species such as aluminium fluoride **[2]**.

The completed electrodes were dried in a vacuum oven for 12hr at 80^oC and cold pressed at 300 kg/cm^2 in a uniaxial hydraulic press. All electrodes contained no more than 2 mg of the active material and were assembled into a coin cell in a high purity argon-filled glove box where the concentration of water and oxygen are less than 5 and 10 ppm respectively. Battery grade lithium foil was used as both the counter and reference electrode. Celgard® 2400 (Celgard LLC, USA) was used as a separator or membrane after soaking in a 1:1 by volume mixture of ethylene carbonate (EC) and diethyl carbonate (DEC) electrolyte solution. The lithium salt used for the purpose of this research was lithium hexaflourophosphate ($LiPF_6$) at a concentration of 1 M. Figure 1 shows a schematic of a typical completed coin test cell.

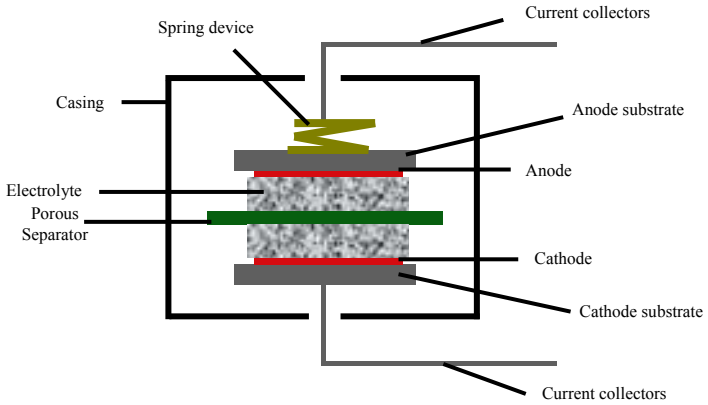

Figure 1. Basic design of Test cells for Charge-Discharge

9.2 Galvanostatic Charge/Discharge Cycling

Charge/discharge cycles of the coin cells were measured using various cut-off on a Neware battery test system at a constant current of 0.01-0.35 mA. The rate of charge and discharge was selected depending upon the theoretical capacity of the material under investigation. The theoretical capacity was calculated using the relationship between the number of moles of lithium in the reaction product and the molar mass of the lithium host:

$$TheoreticalCapacity = \frac{Fn}{3.6M}$$

where F is Faraday's constant,

n is the number of moles of lithium in the reaction product, and

M is the molar mass in grams of the lithium host.

The C rate is a method of expressing the constant current applied to an electrode in relation to its theoretical capacity. The specific capacity of the cell tested was calculated by considering only the active mass in the electrode.

9.3 Cell Electrochemical Tests

9.3.1 Charge/Discharge Testing

Most battery researchers incorporate Charge-Discharge testing in their suite of performance tests of battery materials or construction designs. In principle, this needs only an adjustable voltage/current source (preferably 'Constant-current' variety) for re-charging the test cell, plus the equipment of figure 2 for monitoring and controlling discharge. The amounts of charge and discharge are very easy to keep tract of if the currents both ways are kept constant – in such a case, total charge accumulated or spent is proportional to time spent charging or recharging. For the discharge half of the cycle, this means using a variable load resistance which must be periodically adjusted in step with diminishing cell voltage.

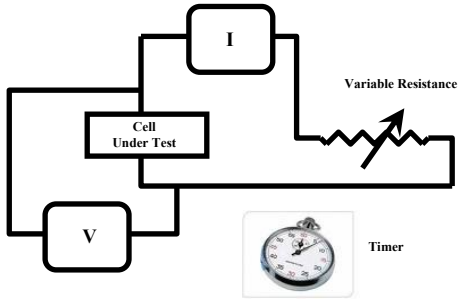

Figure 2. The essentials of Discharge testing

It is tedious and labour-intensive to keep trimming the value of load resistance to preserve accurate charge estimates while a cell test is in progress, so most battery test labs have long since switched to automatically-controlled charge-discharge equipment. In the present case, this takes the form of a personal computer interfaced to the coin cell test equipment.

9.4 Results and discussion

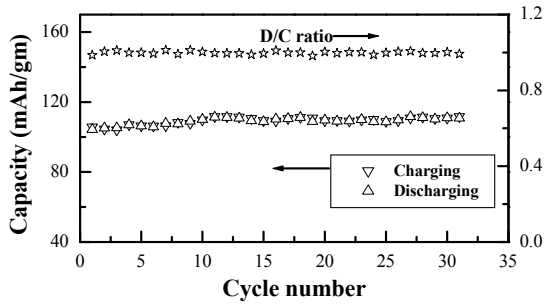

Figure 3. The specific capacity of C-$LiFePO_4$ with the cycle number. A line of stars shown in the figure depicts the discharge to charge ratio of the capacity.

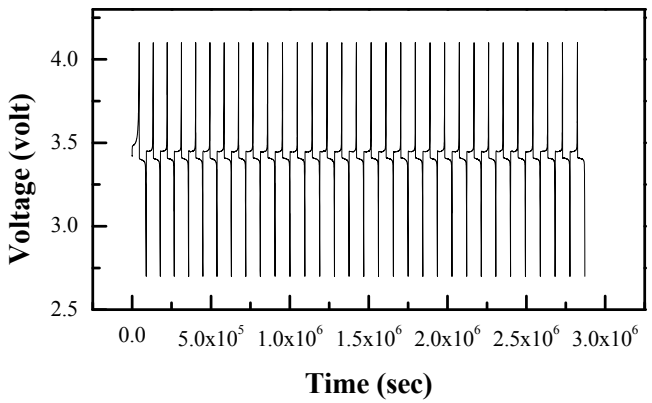

Figure 4. The voltage peaks with time during the 31 cycles.

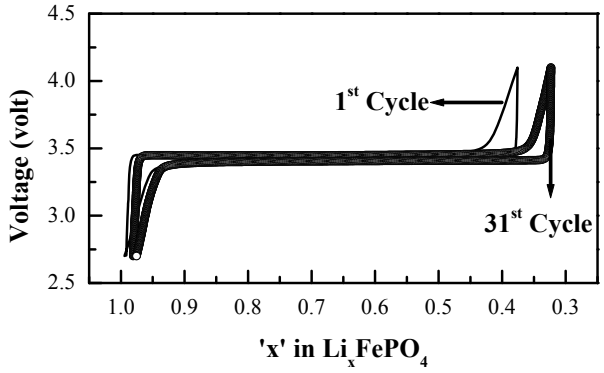

Figure 5. The variation of voltage with 'x' in $LiFePO_4$ of 1 and 31 cycle.

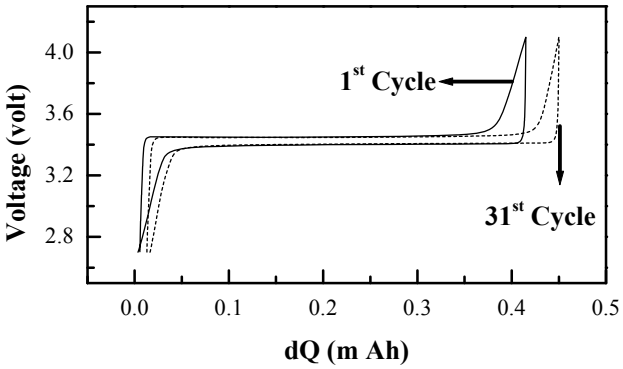

Figure 6. The variation of dQ (=Q-Q_0) with cycle number.

The electrochemical performance of coin cell was evaluated by galvanostatic cycling with potential limitation from 2.7 – 4.1 V over 31 cycles as shown in figure 3. The electrochemical testing was done at ambient temperature. The coin cell exhibited an open circuit voltage (OCV) between 2.5 – 4.5 V, a high first charge in the range of 110 mAh/gm, with the extent of no loss in capacity between the first charge and first discharge. The experiments have 'benchmarked' the material $LiFePO_4$ to possess 65% (~110mAh/gm) of the theoretical capacity (170mAh/gm) **[3]** of the material. Figure 3 shows the specific capacity during charge and/or discharge of the carbon coated nanocrystalline $LiFePO_4$. Figure 4 shows the stability in the voltage peaks during charge and discharge with time. Figure 5 shows the variation in the open circuit voltage (OCV) with 'x' in Li_xFePO_4 for the 1^{st} and 31^{st} cycles. While figure 6 shows the variation in the charging and discharging capacities Q and Q_0 with cycles.

9.5 Conclusions

The electrochemical performance of $LiFePO_4$ as cathode has been evaluated by fabricating a coin-type cell and performing charging-discharging cycles. $LiFePO_4$ synthesized in this work is found to possess 65% of the theoretical capacity of 170mAh/gm. Upscaling of materials synthesis (~100 gm batches) with control of particle size and phase purity appear achievable goals to ultimately realize Li batteries.

References

1. Kawakita, J., and Kobayashi, K., Journal of Power Sources, **101**, p47 (2001).
2. Braithwaite, J. W., Gonzales, A., Nagsubramanian, G., Lucero, S. J., Peebles, D. E., Ohlhausen, J. A., and Cieslak, W. R., Journal of Electrochemical Society, **146**, p448 (1999).
3. Padhi, A. K., Nanjundaswamy, K. S., and Goodenough, J. B., *Journal of Electrochemical Society, **144** (1997) p1188*.

--- O ---

List of Publications

1. Oxalate based non-aqueous sol-gel synthesis of phase pure sub-micron $LiFePO_4$
Y. Sundarayya, K. C. Kumaraswamy and C. S. Sunandana
(*Materials Research Bulletin, Vol.42 (10), p1942, 2007*)

2. Sudden olivine $LiFePO_4$ nanocrystallisation by progressive introduction of Li into Ferrous phosphate structure
Y. Sundarayya, K. C. Kumaraswamy and C. S. Sunandana
(*MRS proceedings, 1023-JJ03-06, 2007*)

3. Optimal synthesis and characterization of Nanoscale $LiFePO_4$.
Y. Sundarayya and C. S. Sunandana
(*Solid State Ionics: New Materials for Polution free Energy Devices, p197, Edited by B. V. R. Chowdari et al, World Scientific, Singapore 2008*)

Papers to be communicated

1. Synthesis and Electrochemical Evaluation of Nanophase $LiFePO_4$.
2. A Detailed High-Temperature FTIR Absorption Study of Order-Disorder Phase Transitions in C-$LiFePO_4$.
3. Magnetic Phase transitions and Relaxation in $LiFePO_4$: A Low-Temperature Mossbauer Spectroscopic and SQUID Magnetometric Investigation.
4. Structural, IR and Mossbauer Spectral Study of Phase Evolution in the Na-substituted $LiFePO_4$.
5. Phosphate –chain Stability in Olivine $LiFePO_4$: Effect of anion-substitution.
6. $LiFePO_4$ Nanocathode- A Physics Perspective.

Publications not related to this thesis

4. Experimental observation of quantum corrections to electrical resistivity in nanocrystalline soft magnetic alloys.
Balakrishnan. K., **Sundarayya. Y.**, Naidu. M. K., and Kaul. S. N.
(*PRAMANA: Journal of Physics, Vol.60, No.3, March 2003, 521-524*).

5. Investigation of structure and electrical transport in partially nanocrystallised amorphous soft magnetic alloys.
Balakrishnan. K., **Sundarayya. Y.**, Naidu. M. K., and Kaul. S. N.
(*International journal of Modern Physics–B, Vol.16, No.26, (2002) 4003-4016*).

6. Reactively Radio frequency sputtered silver oxide thin films: Phase evolution and Phase stability.
M. N. V. Ramesh, **Y. Sundarayya**, and C. S. Sunandana
(*Modern Physics Letters B, Vol.21, No.28 (2007)1933-1944*)

7. Structure, Thermal Stability and Effect of Cu substitution in Ag_2O nanopowders.
Y. Sundarayya and C. S. Sunandana
(*Proceedings of Nano-2005, Sivakasi, Tamilnadu, INDIA*).

--- O ---

Appendix I

FTIR spectra of (1-x)$Fe^{2+}PO_4$:(x)$LiFePO_4$

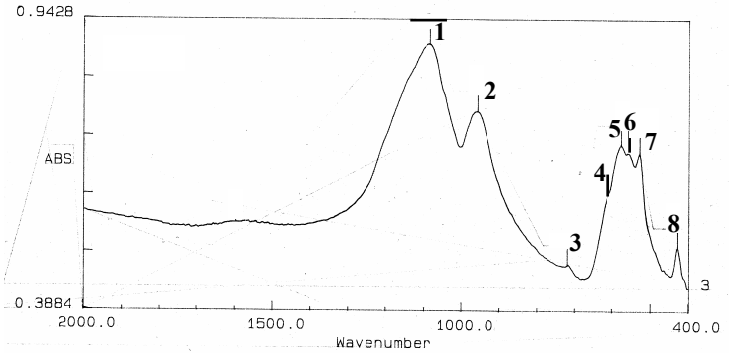

x = 0.00

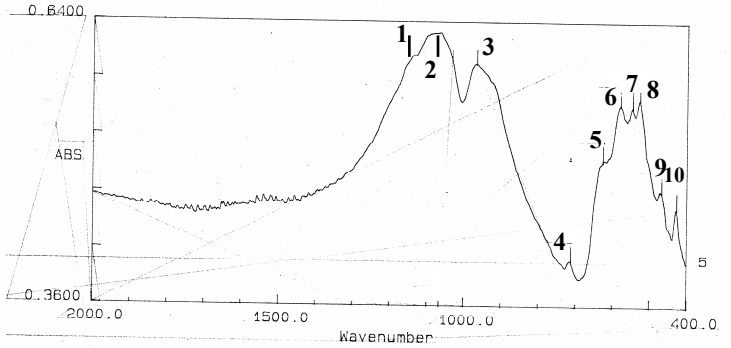

x = 0.25

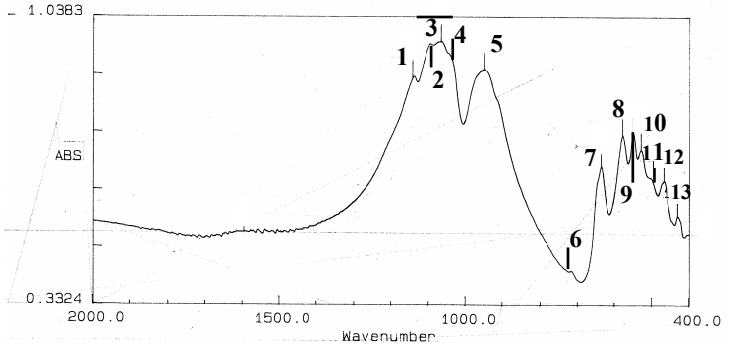

x = 0.50

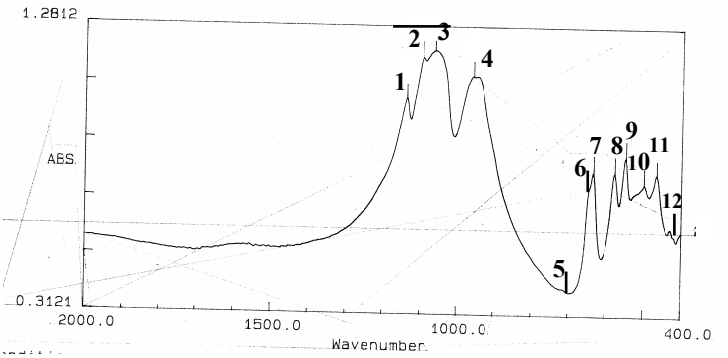
1.2812
ABS.
0.3121
2000.0
1500.0
1000.0
400.0
Wavenumber
1
2
3
4
5
6
7
8
9
10
11
12

x = 0.75

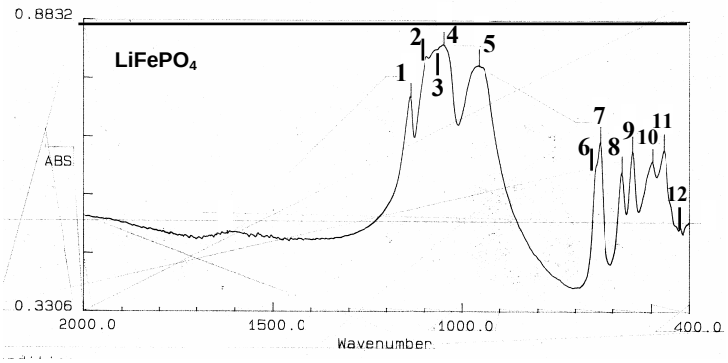
0.8832
LiFePO4
ABS.
0.3306
2000.0
1500.0
1000.0
400.0
Wavenumber
1
2
3
4
5
6
7
8
9
10
11
12

x = 1.00

Appendix-II

FTIR spectra of $Na_xLi_{1-x}FePO_4$

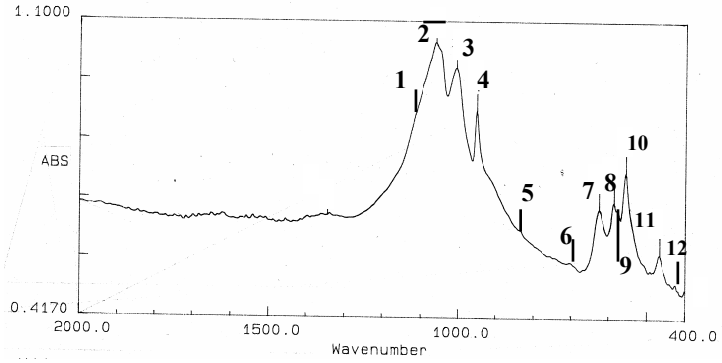

x = 1.00

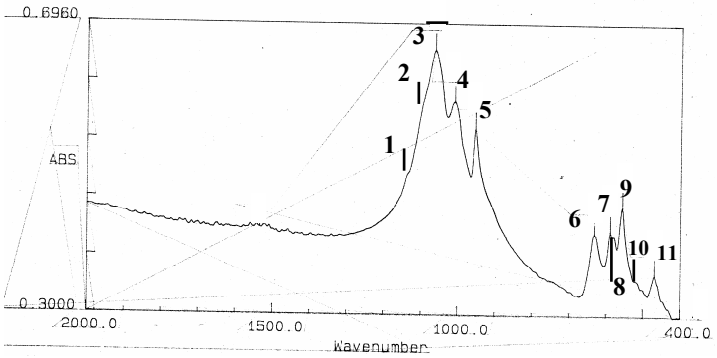

x = 0.75

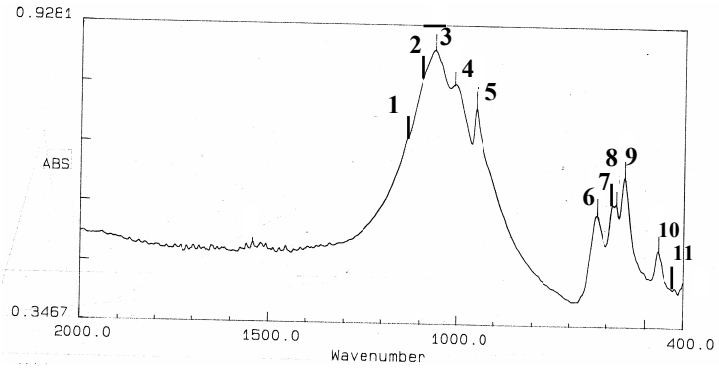

x = 0.50

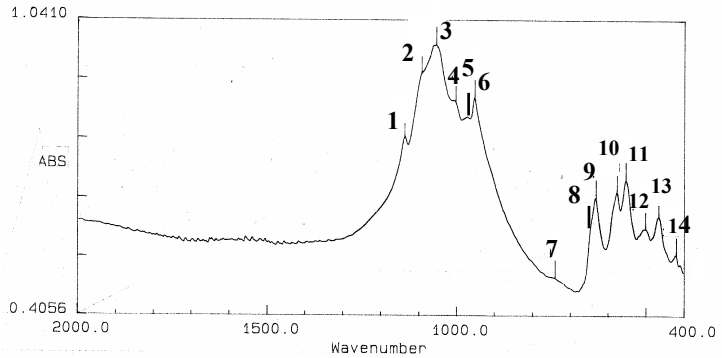
1.0410
ABS
0.4056
2000.0
1500.0
1000.0
400.0
Wavenumber
1
2
3
4
5
6
7
8
9
10
11
12
13
14

x = 0.25

Appendix – III

FTIR Spectra of $LiFe(VO_4)_x(PO_4)_{1-x}$

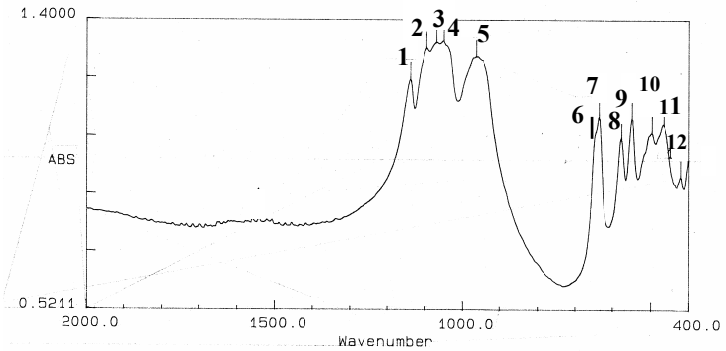

x = 0.05

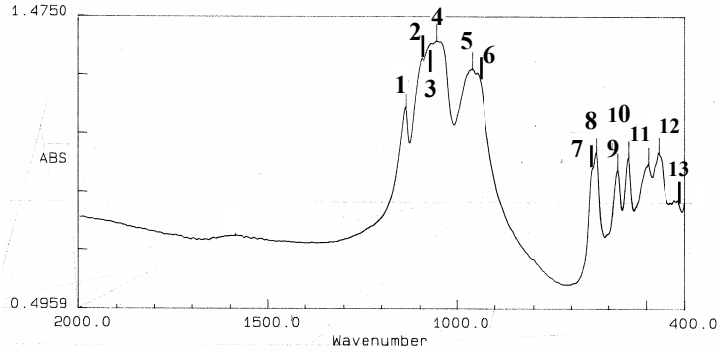

x = 0.10

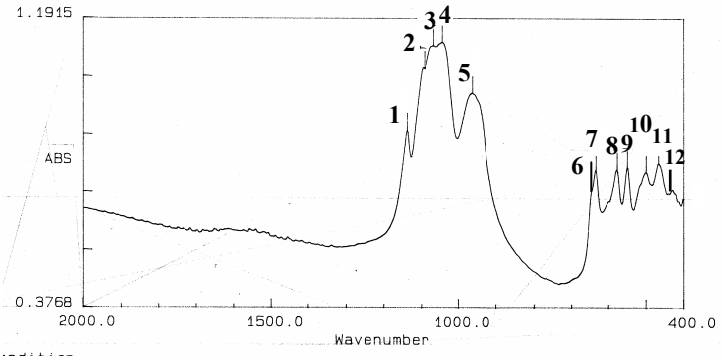

x = 0.20

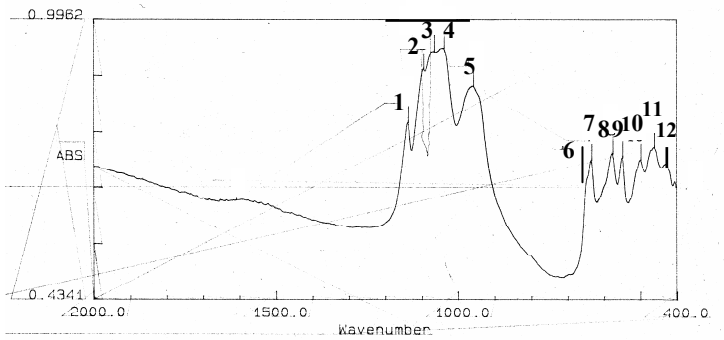
0.9962
ABS
0.4341
2000.0
1500.0
1000.0
400.0
Wavenumber
1
2
3
4
5
6
7
8
9
10
11
12

x = 0.30

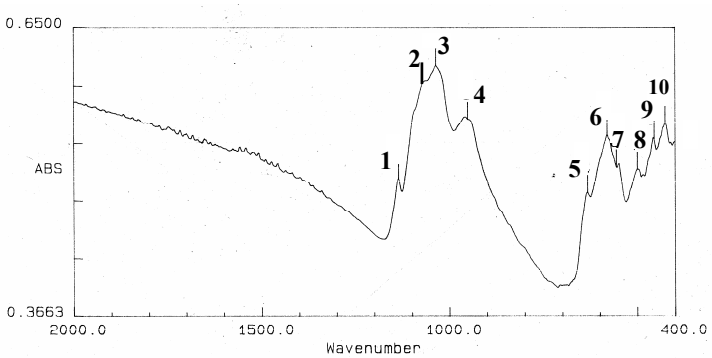
0.6500
ABS
0.3663
2000.0
1500.0
1000.0
400.0
Wavenumber
1
2
3
4
5
6
7
8
9
10

x = 0.50

Appendix – IV

Table1: The values of $2\theta_{obs}$, $2\theta_{cal}$, d_{obs}, d_{cal}, $\Delta 2\theta$ and Δd for monoclinic phase $Li_{0.00}FePO_4$ sample.

S. No.	$2\theta_{obs}$	$2\theta_{cal}$	$\Delta 2\theta$	d_{obs}	d_{cal}	Δd	Miller indices
1	20.471	20.456	0.015	4.3357	4.3388	-0.0032	(0 1 1)
2	26.021	25.982	0.039	3.4221	3.4272	-0.0051	(1 3 0)
3	29.338	29.252	0.086	3.0423	3.0511	-0.0088	(1b 1 2)
4	29.420	29.439	0.019	3.0340	3.0321	-0.0019	(0 0 2)
5	29.619	29.546	0.073	3.0141	3.0214	-0.0073	(1b 0 2)
6	30.422	30.356	0.066	2.9364	2.9426	-0.0062	(0 1 2)
7	31.533	31.495	0.038	2.8354	2.8387	-0.0033	(2 3 0)
8	32.866	32.765	0.101	2.7234	2.7315	-0.0082	(3b 1 1) / (1 0 2)
9	34.181	34.172	0.009	2.6215	2.6222	-0.0007	(2b 0 2)
10	34.764	34.678	0.086	2.5789	2.5851	-0.0062	(2 0 2)
11	35.450	35.347	0.103	2.5305	2.5377	-0.0071	(0 4 1)
12	41.774	41.674	0.100	2.1609	2.1659	-0.0050	(1 5 0)
13	43.128	43.122	0.006	2.0962	2.0964	-0.0003	(0 5 1)
14	44.219	44.130	0.089	2.0469	2.0509	-0.0039	(1b 4 2)
15	47.299	47.245	0.054	1.9206	1.9227	-0.0021	(3 1 2)
16	49.486	49.412	0.074	1.8407	1.8433	-0.0026	(2b 2 1)
17	52.292	52.200	0.092	1.7483	1.7512	-0.0029	(3b 5 1)
18	56.412	56.361	0.051	1.6300	1.6314	-0.0014	(4 1 2)
19	57.302	57.205	0.097	1.6068	1.6093	-0.0025	(2 5 2)
20	58.698	58.677	0.021	1.5724	1.5724	-0.0005	(5b 2 2) / (1 7 0)

Table2: The values of $2\theta_{obs}$, $2\theta_{cal}$, d_{obs}, d_{cal}, $\Delta 2\theta$ and Δd for monoclinic phase $Li_{0.25}FePO_4$ sample.

S. No.	$2\theta_{obs}$	$2\theta_{cal}$	$\Delta 2\theta$	d_{obs}	d_{cal}	Δd	Miller indices
1	20.498	20.456	0.042	4.3300	4.3388	-0.0088	(0 1 1)
2	25.681	25.982	-0.301	3.4667	3.4272	0.0395	(1 3 0)
3	29.366	29.252	0.114	3.0395	3.0511	-0.0116	(1b 0 2)
4	30.393	30.356	0.037	2.9391	2.9426	-0.0035	(0 1 2)
5	31.887	31.833	0.054	2.8047	2.8093	-0.0046	(0 1 3)
6	34.210	34.172	0.038	2.6194	2.6222	-0.0028	(2b 0 2)
7	35.627	35.347	0.280	2.5184	2.5377	-0.0193	(0 4 1)
8	41.639	41.674	-0.035	2.1676	2.1659	0.0017	(1 5 0)
9	43.211	43.122	0.089	2.0923	2.0964	-0.0041	(0 5 1)
10	44.245	44.130	0.115	2.0458	2.0509	-0.0051	(1b 4 2)
11	49.155	49.412	-0.257	1.8523	1.8433	0.0090	(2b 2 1)
12	52.438	52.200	0.238	1.7438	1.7512	-0.0074	(3b 5 1)
13	56.565	56.361	0.204	1.6260	1.6314	-0.0054	(4 1 2)
14	57.251	57.205	0.046	1.6081	1.6093	-0.0012	(2 5 2)
15	58.662	58.677	-0.015	1.5727	1.5724	0.0004	(5b 2 2) / (1 7 0)

Table3: The values of $2\theta_{obs}$, $2\theta_{cal}$, d_{obs}, d_{cal}, $\Delta 2\theta$ and Δd for orthorhombic phase $Li_{0.25}FePO_4$ sample.

S. No.	$2\theta_{obs}$	$2\theta_{cal}$	$\Delta 2\theta$	d_{obs}	d_{cal}	Δd	Miller indices
1	20.858	20.7585	0.0995	4.2553	4.2755	-0.0202	(1 0 1)
2	22.759	22.7030	0.0560	3.9040	3.9135	-0.0095	(2 1 0)
3	24.154	24.0229	0.1311	3.6816	3.7014	-0.0198	(0 1 1)
4	25.437	25.6291	-0.1921	3.4987	3.4729	0.0258	(2 0 1)
5	25.437	25.5477	-0.1107	3.4987	3.4838	0.0149	(1 1 1)
6	29.738	29.6855	0.0525	3.0018	3.0069	-0.0052	(2 1 1)
7	29.738	29.7064	0.0316	3.0018	3.0049	-0.0031	(0 2 0)
8	32.354	32.2390	0.1150	2.7648	2.7744	-0.0096	(3 0 1)
9	36.486	36.5191	-0.0331	2.4606	2.4584	0.0022	(1 2 1)
10	37.876	37.9415	-0.0655	2.3734	2.3695	0.0039	(4 1 0)
11	39.567	39.3037	0.2633	2.2758	2.2904	-0.0146	(1 0 2)
12	42.191	42.1882	0.0028	2.1401	2.1403	-0.0001	(1 1 2)
13	42.191	42.2405	-0.0495	2.1401	2.1377	0.0024	(2 0 2)
14	55.005	54.9987	0.0063	1.6680	1.6682	-0.0002	(4 1 2)

Table4: The values of $2\theta_{obs}$, $2\theta_{cal}$, d_{obs}, d_{cal}, $\Delta 2\theta$ and Δd for monoclinic phase $Li_{0.50}FePO_4$ sample.

S. No.	$2\theta_{obs}$	$2\theta_{cal}$	$\Delta 2\theta$	d_{obs}	d_{cal}	Δd	Miller indices
1	29.551	29.546	0.005	3.0209	30.0214	-0.0005	(1b 0 2)
2	30.570	30.356	0.214	2.9225	2.9426	-0.0201	(0 1 2)
3	32.165	32.013	0.152	2.7811	2.7940	-0.0129	(0 4 0)
4	34.419	34.172	0.247	2.6040	2.6222	-0.0183	(2b 0 2)
5	41.863	41.674	0.189	2.1565	2.1659	-0.0093	(1 5 0)
6	43.350	43.122	0.228	2.0859	2.0964	-0.0105	(0 5 1)
7	44.501	44.130	0.371	2.0346	2.0509	-0.0162	(1b 4 2)
8	57.440	57.205	0.235	1.6033	1.6093	-0.0060	(2 5 2)
9	58.727	58.677	0.050	1.5712	1.5724	-0.0012	(5b 2 2) / (1 7 0)

Table5: The values of $2\theta_{obs}$, $2\theta_{cal}$, d_{obs}, d_{cal}, $\Delta 2\theta$ and Δd for orthorhombic phase $Li_{0.50}FePO_4$ sample.

S. No.	$2\theta_{obs}$	$2\theta_{cal}$	$\Delta 2\theta$	d_{obs}	d_{cal}	Δd	Miller indices
1	20.985	20.8587	0.1263	4.2298	4.2552	-0.0253	(1 0 1)
2	22.945	22.7806	0.1644	3.8727	3.9003	-0.0276	(2 1 0)
3	24.319	24.1524	0.1666	3.6570	3.6818	-0.0248	(0 1 1)
4	25.791	25.7288	0.0622	3.4515	3.4597	-0.0082	(2 0 1)
5	25.791	25.6759	0.1151	3.4515	3.4667	-0.0152	(1 1 1)
6	29.953	29.8125	0.1405	2.9807	2.9944	-0.0137	(2 1 1)
7	29.953	29.8661	0.0869	2.9807	2.9892	-0.0085	(0 2 0)
8	32.472	32.3436	0.1284	2.7550	2.7656	-0.0106	(3 0 1)
9	35.829	35.7423	0.0867	2.5042	2.5101	-0.0059	(3 1 1)
10	36.829	36.7117	0.1173	2.4385	2.4460	-0.0075	(1 2 1)
11	38.155	38.0397	0.1153	2.3567	2.3636	-0.0069	(4 1 0)
12	39.578	39.5158	0.0622	2.2752	2.2786	-0.0034	(1 0 2)
13	39.984	39.9639	0.0201	2.2530	2.2541	-0.0011	(4 0 1)
14	42.458	42.4177	0.0403	2.1273	2.1292	-0.0019	(1 1 2)
15	42.458	42.4517	0.0063	2.1273	2.1276	-0.0003	(2 0 2)
16	49.416	49.5608	-0.1448	1.8428	1.8378	0.0050	(3 1 2)
17	49.416	49.4703	-0.0543	1.8428	1.8409	0.0019	(0 2 2)
18	50.489	50.5323	-0.0433	1.8061	1.8047	0.0014	(1 3 1)
19	52.738	52.7684	-0.0304	1.7343	1.7333	0.0009	(2 2 2)
20	55.159	55.2334	-0.0744	1.6637	1.6617	0.0021	(4 1 2)
21	55.662	55.6972	-0.0352	1.6499	1.6489	0.0010	(6 1 0)
22	56.818	56.6992	0.1188	1.6190	1.6222	-0.0031	(3 2 2)

Table6: The values of $2\theta_{obs}$, $2\theta_{cal}$, d_{obs}, d_{cal}, $\Delta 2\theta$ and Δd for orthorhombic phase $Li_{0.75}FePO_4$ sample.

S. No.	$2\theta_{obs}$	$2\theta_{cal}$	$\Delta 2\theta$	d_{obs}	d_{cal}	Δd	Miller indices
1	20.8590	20.8155	0.0435	4.2551	4.2639	-0.0088	(1 0 1)
2	22.7810	22.7329	0.0481	3.9003	3.9084	-0.0082	(2 1 0)
3	24.2180	24.0982	0.1198	3.6720	3.6900	-0.0180	(0 1 1)
4	25.6690	25.6193	0.0497	3.4676	3.4742	-0.0066	(1 1 1)
5	25.6690	25.6772	-0.0082	3.4676	3.4665	0.0011	(2 0 1)
6	29.8090	29.7491	0.0599	2.9948	3.0007	-0.0059	(2 1 1)
7	29.8090	29.7928	0.0162	2.9948	2.9964	-0.0016	(0 2 0)
8	32.3050	32.2800	0.0250	2.7689	2.7709	-0.0021	(3 0 1)
9	35.7010	35.6684	0.0326	2.5129	2.5151	-0.0022	(3 1 1)
10	36.6530	36.6249	0.0281	2.4498	2.4516	-0.0018	(1 2 1)
11	38.0050	37.9642	0.0408	2.3657	2.3681	-0.0024	(4 1 0)
12	39.4690	39.4302	0.0388	2.2812	2.2834	-0.0022	(1 0 2)
13	39.8270	39.8855	-0.0585	2.2615	2.2584	0.0032	(4 0 1)
14	42.3600	42.3235	0.0365	2.1320	2.1337	-0.0018	(1 1 2)
15	42.3600	42.3607	-0.0007	2.1320	2.1319	0.0001	(2 0 2)
16	49.3410	49.3538	-0.0128	1.8454	1.8450	0.0004	(0 2 2)
17	50.4150	50.4060	0.0090	1.8086	1.8089	-0.0003	(1 3 1)
18	52.6620	52.6454	0.0166	1.7366	1.7371	-0.0005	(2 2 2)
19	55.0790	55.1134	-0.0344	1.6660	1.6650	0.0010	(4 1 2)
20	55.5970	55.5843	0.0127	1.6517	1.6520	-0.0003	(6 1 0)
21	56.7320	56.7658	-0.0338	1.6213	1.6204	0.0009	(3 3 1)
22	57.3390	57.6754	-0.3364	1.6056	1.5970	0.0086	(5 2 1)
23	58.4000	58.3956	0.0044	1.5789	1.5790	-0.0001	(4 3 0)

Table7: The values of $2\theta_{obs}$, $2\theta_{cal}$, d_{obs}, d_{cal}, $\Delta 2\theta$ and Δd for orthorhombic phase $LiFePO_4$ sample.

S. No.	$2\theta_{obs}$	$2\theta_{cal}$	$\Delta 2\theta$	d_{obs}	d_{cal}	Δd	Miller indices
1	20.8230	20.7948	0.0302	4.2624	4.2685	-0.0061	(1 0 1)
2	22.7410	22.7369	0.0041	3.9070	3.9077	0.0007	(2 1 0)
3	24.1330	24.0740	0.0590	3.6847	3.6936	-0.0089	(0 1 1)
4	25.6230	25.6633	-0.0403	3.4737	3.4684	0.0054	(1 1 1)
5	25.6230	25.5980	0.0250	3.4737	3.4771	-0.0033	(2 0 1)
6	29.7730	29.7347	0.0383	2.9983	3.0021	-0.0038	(2 1 1)
7	29.7730	29.7836	-0.106	2.9983	2.9973	0.0010	(0 2 0)
8	32.2920	32.2750	0.0170	2.7699	2.7714	-0.0014	(3 0 1)
9	35.6470	35.6618	-0.0149	2.5165	2.5155	0.0010	(3 1 1)
10	36.6580	36.6038	0.0542	2.4494	2.4529	-0.0035	(1 2 1)
11	37.9530	37.9800	-0.0270	2.3688	2.3672	0.0016	(4 1 0)
12	39.3950	39.3762	0.0188	2.2853	2.2864	-0.0011	(1 0 2)
13	39.8990	39.8887	0.0103	2.2576	2.2582	-0.0006	(4 0 1)
14	42.2910	42.2708	0.202	2.1353	2.1363	-0.0010	(1 1 2)
15	42.2910	42.3127	-0.0217	2.1353	2.1342	0.0010	(2 0 2)
16	44.4600	44.4876	-0.0276	2.0360	2.0348	0.0012	(3 2 1)
17	45.0530	45.0525	0.0005	2.0106	2.0106	0.0000	(2 1 2)
18	46.4120	46.4366	-0.0246	1.9548	1.9539	0.0010	(4 2 0)
19	49.2960	49.4132	-0.1172	1.8470	1.8429	0.0041	(3 1 2)
20	49.2960	49.3016	-0.0056	1.8470	1.8468	0.0002	(0 2 2)
21	50.3290	50.3823	-0.0533	1.8115	1.8097	0.0018	(1 3 1)
22	50.6210	50.5653	0.557	1.8017	1.8036	-0.0019	(4 2 1)
23	50.6210	50.6748	-0.0538	1.8017	1.7999	0.0018	(5 1 1)
24	52.5740	52.5990	-0.0250	1.7393	1.7385	0.0008	(2 2 2)
25	52.7480	52.7410	0.0070	1.7340	1.7342	-0.0002	(4 0 2)
26	55.0060	55.0826	-0.0766	1.6680	1.6659	0.0021	(4 1 2)
27	55.1560	55.0826	0.0734	1.6638	1.6659	-0.0020	(4 1 2)
28	55.5100	55.6125	-0.1025	1.6541	1.6513	0.0028	(6 1 0)
29	55.6590	55.6125	0.0465	1.6500	1.6513	-0.0013	(6 1 0)
30	56.6600	56.5280	0.1320	1.6232	1.6267	-0.0035	(3 2 2)
31	56.8070	57.7505	0.0565	1.6193	1.6208	-0.0015	(3 3 1)
32	57.6470	57.6797	-0.0327	1.5977	1.5969	0.0008	(5 2 1)
33	58.2960	58.3963	-0.1003	1.5815	1.5790	0.0025	(4 3 0)

Appendix – V

Table1: The values of $2\theta_{obs}$, $2\theta_{cal}$, d_{obs}, d_{cal}, $\Delta 2\theta$ and Δd for orthorhombic phase $Na_{1.00}Li_{0.00}FePO_4$ sample.

H	K	L	DOBS	DCALC	DELD	2TH-O	2TH-C	DEL2TH
1	1	1	3.6747	3.6843	-.0096	24.2000	24.1360	.0640
1	2	1	2.9895	2.9979	-.0085	29.8630	29.7768	.0862
1	3	0	2.7158	2.7299	-.0141	32.9540	32.7788	.1752
2	2	0	2.7056	2.7141	-.0086	33.0820	32.9748	.1072
2	1	1	2.6831	2.6930	-.0099	33.3670	33.2412	.1258
0	3	1	2.5570	2.5606	-.0036	35.0640	35.0133	.0507
0	0	2	2.5050	2.5084	-.0034	35.8170	35.7672	.0498
0	1	2	2.4130	2.4150	-.0019	37.2310	37.2001	.0309
2	2	1	2.3807	2.3872	-.0064	37.7550	37.6497	.1053
1	2	2	2.0835	2.0830	.0005	43.3940	43.4049	-.0109
3	2	0	2.0275	2.0295	-.0021	44.6580	44.6104	.0476
2	4	0	1.8714	1.8695	.0019	48.6120	48.6643	-.0523
2	2	2	1.8437	1.8421	.0016	49.3900	49.4351	-.0451
4	0	0	1.7090	1.7087	.0003	53.5810	53.5898	-.0088 \
0	4	2	1.6705	1.6680	.0025	54.9160	55.0069	-.0909
0	1	3	1.6434	1.6437	-.0003	55.9030	55.8905	.0125
4	1	1	1.5931	1.5916	.0015	57.8300	57.8903	-.0603

Table2: The values of $2\theta_{obs}$, $2\theta_{cal}$, d_{obs}, d_{cal}, $\Delta 2\theta$ and Δd for NIP phase in $Na_{0.75}Li_{0.25}FePO_4$ sample.

H	K	L	DOBS	DCALC	DELD	2TH-O	2TH-C	DEL2TH
1	1	1	3.7003	3.6417	.0586	24.0300	24.4223	-.3923
2	0	0	3.4487	3.4044	.0444	25.8120	26.1543	-.3423
1	2	1	2.9795	2.9822	-.0027	29.9650	29.9376	.0274
2	2	0	2.6935	2.7149	-.0214	33.2340	32.9648	.2692
2	1	1	2.6728	2.6715	.0012	33.5000	33.5161	-.0161
0	3	1	2.5701	2.5599	.0102	34.8800	35.0241	-.1441
0	3	1	2.5530	2.5599	-.0068	35.1210	35.0241	.0969
0	0	2	2.5001	2.4549	.0453	35.8890	36.5741	-.6851
0	1	2	2.4044	2.3683	.0361	37.3700	37.9604	-.5904
2	2	1	2.3747	2.3759	-.0012	37.8550	37.8353	.0197
1	2	2	2.0771	2.0546	.0225	43.5350	44.0375	-.5025
1	2	2	2.0721	2.0546	.0176	43.6450	44.0375	-.3925
2	4	0	1.8676	1.8770	-.0094	48.7170	48.4564	.2606
2	4	0	1.8630	1.8770	-.0141	48.8460	48.4564	.3896
2	2	2	1.8376	1.8209	.0167	49.5650	50.0520	-.4870
2	2	2	1.8330	1.8209	.0122	49.6970	50.0520	-.3550
4	0	0	1.7011	1.7022	-.0011	53.8490	53.8117	.0373
3	3	1	1.6968	1.6982	-.0014	53.9950	53.9470	.0480
0	4	2	1.6863	1.6587	.0276	54.3600	55.3427	-.9827

Table 3: The values of $2\theta_{obs}$, $2\theta_{cal}$, d_{obs}, d_{cal}, $\Delta 2\theta$ and Δd for LIP phase in $Na_{0.75}Li_{0.25}FePO_4$ sample.

H	K	L	DOBS	DCALC	DELD	2TH-O	2TH-C	DEL2TH
0	1	1	3.7003	3.6739	.0264	24.0300	24.2051	-.1751
2	0	1	3.4487	3.4623	-.0136	25.8120	25.7088	.1032
1	1	1	3.4487	3.4618	-.0131	25.8120	25.7130	.0990
2	1	1	2.9795	2.9945	-.0150	29.9650	29.8116	.1534
0	2	0	2.9795	2.9827	-.0032	29.9650	29.9322	.0328
3	1	1	2.5001	2.5133	-.0132	35.8890	35.6943	.1947
1	2	1	2.4428	2.4416	.0012	36.7610	36.7799	-.0189
4	1	0	2.3747	2.3714	.0033	37.8550	37.9097	-.0547
4	0	1	2.2520	2.2604	-.0084	40.0020	39.8473	.1547
0	2	2	1.8376	1.8370	.0007	49.5650	49.5839	-.0189
3	1	2	1.8376	1.8372	.0004	49.5650	49.5767	-.0117
4	2	1	1.8012	1.8015	-.0003	50.6360	50.6266	.0094
5	1	1	1.8012	1.8018	-.0005	50.6360	50.6195	.0165

Table 4: The values of $2\theta_{obs}$, $2\theta_{cal}$, d_{obs}, d_{cal}, $\Delta 2\theta$ and Δd for NIP phase in $Na_{0.50}Li_{0.50}FePO_4$ sample.

H	K	L	DOBS	DCALC	DELD	2TH-O	2TH-C	DEL2TH
1	1	1	3.6623	3.6774	-.0151	24.2830	24.1818	.1012
1	2	1	2.9848	2.9930	-.0082	29.9110	29.8275	.0835
2	2	0	2.7006	2.7061	-.0055	33.1450	33.0756	.0694
2	1	1	2.7006	2.6853	.0153	33.1450	33.3387	-.1937
2	1	1	2.6786	2.6853	-.0067	33.4250	33.3387	.0863
0	3	1	2.5574	2.5576	-.0002	35.0590	35.0558	.0032
0	0	2	2.5033	2.5060	-.0027	35.8420	35.8014	.0406
0	1	2	2.4092	2.4127	-.0034	37.2920	37.2368	.0552
2	2	1	2.3643	2.3812	-.0169	38.0280	37.7478	.2802
1	2	2	2.0817	2.0804	.0013	43.4350	43.4634	-.0284
3	2	0	2.0235	2.0226	.0009	44.7500	44.7710	-.0210
2	4	0	1.8696	1.8656	.0040	48.6610	48.7719	-.1109
2	2	2	1.8418	1.8387	.0031	49.4450	49.5337	-.0887
4	0	0	1.7043	1.7019	.0024	53.7390	53.8199	-.0809
0	4	2	1.6662	1.6661	.0001	55.0700	55.0734	-.0034
0	1	3	1.6499	1.6422	.0077	55.6630	55.9474	-.2844

Table 5: The values of $2\theta_{obs}$, $2\theta_{cal}$, d_{obs}, d_{cal}, $\Delta 2\theta$ and Δd for LIP phase in $Na_{0.50}Li_{0.50}FePO_4$ sample.

H	K	L	DOBS	DCALC	DELD	2TH-O	2TH-C	DEL2TH
1	0	1	4.2398	4.2656	-.0258	20.9350	20.8069	.1281
2	1	0	3.8764	3.8995	-.0231	22.9230	22.7854	.1376
0	1	1	3.6623	3.6868	-.0245	24.2830	24.1194	.1636
2	0	1	3.4544	3.4659	-.0115	25.7690	25.6821	.0869
1	1	1	3.4544	3.4710	-.0166	25.7690	25.6433	.1257
0	2	0	2.9848	2.9858	-.0010	29.9110	29.9008	.0102
3	0	1	2.7622	2.7693	-.0071	32.3850	32.3000	.0850
3	1	1	2.5033	2.5123	-.0090	35.8420	35.7097	.1323
1	2	1	2.4459	2.4461	-.0002	36.7130	36.7098	.0032
4	1	0	2.3643	2.3641	.0002	38.0280	38.0308	-.0028
1	0	2	2.2794	2.2849	-.0055	39.5010	39.4028	.0982
4	0	1	2.2542	2.2564	-.0022	39.9620	39.9209	.0411
1	1	2	2.1338	2.1340	-.0002	42.3210	42.3175	.0035
3	2	1	2.0235	2.0304	-.0069	44.7500	44.5897	.1603
3	1	2	1.8418	1.8411	.0007	49.4450	49.4657	-.0207
1	3	1	1.8058	1.8038	.0020	50.5000	50.5588	-.0588
2	2	2	1.7364	1.7355	.0009	52.6680	52.6976	-.0296
4	1	2	1.6662	1.6643	.0020	55.0700	55.1400	-.0700
6	1	0	1.6499	1.6495	.0003	55.6630	55.6757	-.0127
3	3	1	1.6144	1.6163	-.0019	56.9970	56.9231	.0739
4	3	0	1.5786	1.5747	.0038	58.4140	58.5697	-.1557

Table 6: The values of $2\theta_{obs}$, $2\theta_{cal}$, d_{obs}, d_{cal}, $\Delta 2\theta$ and Δd for NIP phase in $Na_{0.25}Li_{0.75}FePO_4$ sample.

H	K	L	DOBS	DCALC	DELD	2TH-O	2TH-C	DEL2TH
1	1	1	3.6826	3.6892	-.0066	24.1470	24.1031	.0439
1	1	1	3.6377	3.6892	-.0516	24.4500	24.1031	.3469
2	0	0	3.4715	3.4434	.0281	25.6400	25.8525	-.2125
1	2	1	2.9965	2.9823	.0143	29.7910	29.9369	-.1459
2	2	0	2.7010	2.7088	-.0077	33.1390	33.0420	.0970
2	1	1	2.6789	2.7044	-.0255	33.4210	33.0966	.3244
0	3	1	2.5585	2.5295	.0290	35.0430	35.4586	-.4156
0	0	2	2.5150	2.5189	-.0039	35.6690	35.6122	.0568
2	2	1	2.3706	2.3858	-.0152	37.9230	37.6727	.2503
1	1	2	2.2666	2.2841	-.0175	39.7350	39.4171	.3179
1	2	2	2.0847	2.0822	.0024	43.3690	43.4222	-.0532
3	2	0	2.0362	2.0340	.0022	44.4570	44.5066	-.0496
2	4	0	1.8686	1.8501	.0185	48.6880	49.2072	-.5192
2	2	2	1.8476	1.8446	.0030	49.2780	49.3643	-.0863
2	2	2	1.8415	1.8446	-.0031	49.4520	49.3643	.0877
0	5	1	1.6682	1.6573	.0110	54.9980	55.3932	-.3952
0	4	2	1.6538	1.6543	-.0005	55.5210	55.5016	.0194
0	1	3	1.6497	1.6494	.0004	55.6690	55.6820	-.0130
1	0	3	1.6229	1.6315	-.0086	56.6710	56.3460	.3251
1	5	1	1.6229	1.6113	.0116	56.6710	57.1173	-.4463
4	1	1	1.6019	1.6018	.0001	57.4830	57.4857	-.0027
3	2	2	1.5818	1.5825	-.0007	58.2840	58.2545	.0295

Table 7: The values of $2\theta_{obs}$, $2\theta_{cal}$, d_{obs}, d_{cal}, $\Delta 2\theta$ and Δd for LIP phase in $Na_{0.25}Li_{0.75}FePO_4$ sample.

H	K	L	DOBS	DCALC	DELD	2TH-O	2TH-C	DEL2TH
1	0	1	4.2603	4.2674	-.0070	20.8330	20.7983	.0347
2	1	0	3.9050	3.9050	.0000	22.7530	22.7527	.0003
0	1	1	3.6826	3.6934	-.0108	24.1470	24.0752	.0718
2	0	1	3.4715	3.4664	.0051	25.6400	25.6783	-.0383
1	1	1	3.4715	3.4764	-.0050	25.6400	25.6027	.0373
2	1	1	2.9965	3.0008	-.0042	29.7910	29.7479	.0431
0	2	0	2.9965	2.9972	-.0007	29.7910	29.7840	.0070
3	0	1	2.7852	2.7692	.0161	32.1100	32.3013	-.1913
3	0	1	2.7694	2.7692	.0003	32.2980	32.3013	-.0033
3	1	1	2.5150	2.5139	.0012	35.6690	35.6861	-.0171
1	2	1	2.4523	2.4527	-.0004	36.6140	36.6074	.0066
4	1	0	2.3706	2.3648	.0058	37.9230	38.0194	-.0964
1	0	2	2.2856	2.2861	-.0005	39.3900	39.3814	.0086
4	0	1	2.2666	2.2561	.0105	39.7350	39.9271	-.1921
4	0	1	2.2564	2.2561	.0003	39.9220	39.9271	-.0051
1	1	2	2.1350	2.1360	-.0010	42.2970	42.2758	.0212
2	0	2	2.1350	2.1337	.0013	42.2970	42.3244	-.0274
3	2	1	2.0362	2.0339	.0022	44.4570	44.5079	-.0509
2	1	2	2.0107	2.0101	.0005	45.0510	45.0637	-.0127
4	2	0	1.9548	1.9525	.0023	46.4120	46.4703	-.0583
0	2	2	1.8476	1.8467	.0009	49.2780	49.3043	-.0263
1	3	1	1.8108	1.8096	.0012	50.3500	50.3854	-.0354
4	2	1	1.8011	1.8025	-.0014	50.6400	50.5974	.0426
2	2	2	1.7391	1.7382	.0008	52.5820	52.6092	-.0272
4	0	2	1.7335	1.7332	.0003	52.7650	52.7737	-.0087
4	1	2	1.6682	1.6650	.0032	54.9980	55.1143	-.1163
4	1	2	1.6639	1.6650	-.0011	55.1540	55.1143	.0397

6	1	0	1.6538	1.6494	.0043	55.5210	55.6785	-.1575
6	1	0	1.6497	1.6494	.0003	55.6690	55.6785	-.0095
3	2	2	1.6229	1.6262	-.0033	56.6710	56.5467	.1243
3	3	1	1.6192	1.6204	-.0012	56.8120	56.7678	.0442
5	2	1	1.5818	1.5957	-.0140	58.2840	57.7252	.5588
5	2	1	1.5785	1.5957	-.0173	58.4170	57.7252	.6918

Appendix – V

Table1: The values of $2\theta_{obs}$, $2\theta_{cal}$, d_{obs}, d_{cal}, $\Delta 2\theta$ and Δd for orthorhombic phase $LiFe(VO_4)_{0.05}(PO_4)_{0.95}$ sample.

H	K	L	DOBS	DCALC	DELD	2TH-O	2TH-C	DEL2TH
1	0	1	4.2408	4.2561	-.0152	20.9300	20.8542	.0758
2	1	0	3.8893	3.9009	-.0116	22.8460	22.7771	.0689
0	1	1	3.6697	3.6834	-.0136	24.2330	24.1419	.0911
1	1	1	3.4668	3.4679	-.0011	25.6750	25.6666	.0084
2	0	1	3.4477	3.4599	-.0122	25.8200	25.7270	.0930
2	1	1	2.9846	2.9951	-.0105	29.9130	29.8061	.1069
0	2	0	2.9846	2.9911	-.0065	29.9130	29.8465	.0665
3	0	1	2.7607	2.7655	-.0048	32.4030	32.3447	.0583
3	1	1	2.5131	2.5103	.0029	35.6970	35.7391	-.0421
3	1	1	2.5038	2.5103	-.0064	35.8340	35.7391	.0949
1	2	1	2.4487	2.4472	.0015	36.6700	36.6928	-.0228
4	1	0	2.3591	2.3634	-.0043	38.1140	38.0427	.0713
1	0	2	2.2734	2.2792	-.0059	39.6110	39.5047	.1063
4	0	1	2.2567	2.2539	.0028	39.9160	39.9678	-.0518
4	0	1	2.2479	2.2539	-.0060	40.0790	39.9678	.1112
1	1	2	2.1276	2.1299	-.0023	42.4520	42.4036	.0484
2	0	2	2.1276	2.1280	-.0005	42.4520	42.4424	.0096
0	2	2	1.8414	1.8417	-.0003	49.4560	49.4478	.0082
1	3	1	1.8048	1.8057	-.0009	50.5280	50.5019	.0261
5	1	1	1.7957	1.7967	-.0010	50.8020	50.7729	.0291
2	2	2	1.7350	1.7340	.0010	52.7150	52.7483	-.0333
4	0	2	1.7330	1.7300	.0031	52.7790	52.8798	-.1008
4	1	2	1.6631	1.6619	.0013	55.1810	55.2267	-.0457
6	1	0	1.6488	1.6487	.0001	55.7040	55.7059	-.0019
3	3	1	1.6178	1.6175	.0004	56.8650	56.8790	-.0140
4	3	0	1.5767	1.5761	.0006	58.4900	58.5150	-.0250

Table2: The values of $2\theta_{obs}$, $2\theta_{cal}$, d_{obs}, d_{cal}, $\Delta 2\theta$ and Δd for orthorhombic phase $LiFe(VO_4)_{0.10}(PO_4)_{0.90}$ sample.

H	K	L	DOBS	DCALC	DELD	2TH-O	2TH-C	DEL2TH
1	0	1	4.2306	4.2554	-.0248	20.9810	20.8575	.1235
2	1	0	3.8799	3.8982	-.0183	22.9020	22.7931	.1089
0	1	1	3.6617	3.6822	-.0205	24.2870	24.1495	.1375
2	0	1	3.4520	3.4588	-.0068	25.7870	25.7357	.0513
1	1	1	3.4520	3.4667	-.0147	25.7870	25.6757	.1113
2	1	1	2.9819	2.9938	-.0119	29.9410	29.8192	.1218
3	0	1	2.7587	2.7643	-.0056	32.4270	32.3597	.0673
3	0	1	2.7535	2.7643	-.0108	32.4900	32.3597	.1303
3	1	1	2.5053	2.5090	-.0037	35.8120	35.7576	.0544
3	1	1	2.5012	2.5090	-.0078	35.8730	35.7576	.1154
1	2	1	2.4422	2.4459	-.0036	36.7700	36.7133	.0567
4	1	0	2.3570	2.3618	-.0048	38.1500	38.0695	.0805
1	0	2	2.2777	2.2791	-.0013	39.5320	39.5080	.0240
4	0	1	2.2547	2.2527	.0020	39.9530	39.9896	-.0366
1	1	2	2.1275	2.1295	-.0020	42.4530	42.4108	.0422
2	0	2	2.1275	2.1277	-.0002	42.4530	42.4493	.0037
3	2	1	2.0175	2.0294	-.0119	44.8910	44.6126	.2784
0	2	2	1.8425	1.8411	.0014	49.4240	49.4641	-.0401
1	3	1	1.8057	1.8046	.0011	50.5030	50.5358	-.0328
4	2	1	1.7971	1.7990	-.0019	50.7610	50.7039	.0571
5	1	1	1.7971	1.7956	.0014	50.7610	50.8045	-.0435
2	2	2	1.7354	1.7334	.0020	52.7020	52.7681	-.0661
4	0	2	1.7308	1.7294	.0014	52.8520	52.8986	-.0466
4	1	2	1.6629	1.6613	.0016	55.1900	55.2484	-.0584
6	1	0	1.6483	1.6476	.0007	55.7210	55.7467	-.0257
3	3	1	1.6170	1.6164	.0006	56.8950	56.9185	-.0235
3	2	2	1.6170	1.6220	-.0049	56.8950	56.7057	.1893

3	3	1	1.6141	1.6164	-.0023	57.0080	56.9185	.0895
5	2	1	1.6012	1.5929	.0082	57.5110	57.8361	-.3251
4	3	0	1.5767	1.5750	.0017	58.4910	58.5604	-.0694

Table 3: The values of $2\theta_{obs}$, $2\theta_{cal}$, d_{obs}, d_{cal}, $\Delta 2\theta$ and Δd for orthorhombic phase $LiFe(VO_4)_{0.20}(PO_4)_{0.80}$ sample.

H	K	L	DOBS	DCALC	DELD	2TH-O	2TH-C	DEL2TH
1	0	1	4.2003	4.2485	-.0481	21.1340	20.8919	.2421
2	1	0	3.9335	3.8883	.0452	22.5860	22.8522	-.2662
1	1	1	3.4371	3.4584	-.0213	25.9010	25.7387	.1623
2	0	1	3.4371	3.4533	-.0162	25.9010	25.7775	.1235
2	1	1	2.9695	2.9872	-.0178	30.0690	29.8859	.1831
0	2	0	2.9695	2.9772	-.0077	30.0690	29.9895	.0795
3	0	1	2.7485	2.7600	-.0115	32.5510	32.4120	.1390
3	1	1	2.4989	2.5040	-.0052	35.9080	35.8312	.0768
1	2	1	2.4368	2.4381	-.0013	36.8550	36.8344	.0206
4	1	0	2.3517	2.3573	-.0056	38.2390	38.1450	.0940
4	0	1	2.2512	2.2492	.0020	40.0170	40.0546	-.0377
1	1	2	2.1229	2.1254	-.0025	42.5500	42.4970	.0530
2	0	2	2.1229	2.1242	-.0013	42.5500	42.5219	.0281
3	2	1	2.0170	2.0240	-.0070	44.9020	44.7380	.1640
4	2	0	1.9449	1.9441	.0008	46.6630	46.6826	-.0196
3	1	2	1.8366	1.8342	.0024	49.5940	49.6637	-.0696
0	2	2	1.8366	1.8365	.0001	49.5940	49.5973	-.0033
1	3	1	1.8038	1.7982	.0056	50.5590	50.7268	-.1678
4	2	1	1.7914	1.7946	-.0033	50.9350	50.8356	.0994
5	1	1	1.7914	1.7925	-.0011	50.9350	50.9007	.0343
2	2	2	1.7306	1.7292	.0014	52.8590	52.9052	-.0462
4	0	2	1.7306	1.7266	.0040	52.8590	52.9896	-.1306
4	1	2	1.6605	1.6583	.0022	55.2750	55.3551	-.0801
6	1	0	1.6459	1.6448	.0012	55.8080	55.8506	-.0426
3	2	2	1.6160	1.6183	-.0022	56.9340	56.8480	.0860
5	2	1	1.6074	1.5894	.0180	57.2670	57.9774	-.7104
3	3	1	1.6074	1.6114	-.0040	57.2670	57.1133	.1537

4	3	0	1.5741	1.5702	.0039	58.5970	58.7559	-.1589

Table 4: The values of $2\theta_{obs}$, $2\theta_{cal}$, d_{obs}, d_{cal}, $\Delta 2\theta$ and Δd for orthorhombic phase $LiFe(VO_4)_{0.30}(PO_4)_{0.70}$ sample.

H	K	L	DOBS	DCALC	DELD	2TH-O	2TH-C	DEL2TH
1	0	1	4.2290	4.2533	-.0243	20.9890	20.8679	.1211
2	1	0	3.8734	3.8969	-.0235	22.9410	22.8008	.1402
0	1	1	3.6553	3.6781	-.0228	24.3300	24.1770	.1530
2	0	1	3.4502	3.4585	-.0083	25.8010	25.7379	.0631
1	1	1	3.4502	3.4635	-.0134	25.8010	25.6996	.1014
2	1	1	2.9808	2.9923	-.0115	29.9520	29.8345	.1175
0	2	0	2.9808	2.9837	-.0029	29.9520	29.9222	.0298
3	0	1	2.7554	2.7649	-.0095	32.4670	32.3530	.1140
3	1	1	2.5186	2.5087	.0099	35.6170	35.7628	-.1458
1	2	1	2.4402	2.4426	-.0024	36.8020	36.7640	.0380
4	1	0	2.3577	2.3626	-.0049	38.1380	38.0566	.0814
1	0	2	2.2760	2.2775	-.0016	39.5640	39.5355	.0285
4	0	1	2.2528	2.2535	-.0008	39.9880	39.9741	.0139
1	1	2	2.1262	2.1278	-.0016	42.4800	42.4467	.0333
2	0	2	2.1262	2.1266	-.0004	42.4800	42.4713	.0087
3	2	1	2.0175	2.0280	-.0105	44.8910	44.6453	.2457
3	1	2	1.8409	1.8368	.0041	49.4700	49.5888	-.1188
0	2	2	1.8409	1.8391	.0019	49.4700	49.5234	-.0534
1	3	1	1.8022	1.8018	.0004	50.6070	50.6181	-.0111
4	2	1	1.8022	1.7983	.0039	50.6070	50.7253	-.1183
2	2	2	1.7341	1.7318	.0024	52.7430	52.8201	-.0771
4	0	2	1.7283	1.7292	-.0009	52.9330	52.9034	.0296
4	1	2	1.6615	1.6609	.0006	55.2400	55.2611	-.0211
6	1	0	1.6481	1.6485	-.0003	55.7270	55.7149	.0121
3	2	2	1.6183	1.6208	-.0026	56.8480	56.7498	.0982

3	3	1	1.6183	1.6147	.0036	56.8480	56.9856	-.1376
3	3	1	1.6141	1.6147	-.0006	57.0080	56.9856	.0224
3	3	1	1.6091	1.6147	-.0056	57.2030	56.9856	.2174
4	3	0	1.5753	1.5737	.0016	58.5470	58.6135	-.0665

Table 5: The values of $2\theta_{obs}$, $2\theta_{cal}$, d_{obs}, d_{cal}, $\Delta 2\theta$ and Δd for $LiFe(VO_4)_{0.50}(PO_4)_{0.50}$ sample.

H	K	L	DOBS	DCALC	DELD	2TH-O	2TH-C	DEL2TH
1	0	1	4.2215	4.3079	-.0865	21.0270	20.6003	.4267
2	1	0	3.8903	3.8410	.0493	22.8400	23.1375	-.2975
2	0	1	3.4379	3.4615	-.0237	25.8950	25.7150	.1800
1	1	1	3.4379	3.4872	-.0493	25.8950	25.5226	.3724
2	1	1	2.9693	2.9906	-.0214	30.0710	29.8512	.2198
0	2	0	2.9693	2.9695	-.0003	30.0710	30.0683	.0027
3	0	1	2.7514	2.7446	.0068	32.5150	32.5978	-.0828
3	1	1	2.4991	2.4915	.0076	35.9050	36.0182	-.1132
1	2	1	2.4384	2.4449	-.0066	36.8300	36.7277	.1023
4	1	0	2.3415	2.3182	.0233	38.4130	38.8138	-.4008
4	1	1	2.0924	2.0847	.0078	43.2000	43.3692	-.1692
1	3	1	1.8015	1.7988	.0027	50.6270	50.7080	-.0810
4	2	1	1.8015	1.7813	.0202	50.6270	51.2433	-.6163
4	0	2	1.7313	1.7308	.0005	52.8360	52.8536	-.0176
6	1	0	1.6154	1.6153	.0001	56.9570	56.9599	-.0029
5	2	1	1.5707	1.5735	-.0028	58.7330	58.6186	.1144

--- O ---